

Stochastic uncertainty quantification for multiscale modeling of polymeric nanocomposites

DISSERTATION

Zur Erlangung des akademischen Grades eines
Doktor-Ingenieur
an der Fakultät Bauingenieurwesen
der Bauhaus Universität Weimar

vorgelegt von

M.E., Nam Vu-Bac
geboren am 29. März 1981
in Ho Chi Minh City, Vietnam

Mentor:

Prof. Dr.-Ing. Timon Rabczuk, Bauhaus Universität Weimar

Gutachter:

Prof. Dr.-Ing. habil. Carsten Könke, Bauhaus Universität Weimar

Prof. Dr. Pedro Miguel Almeida Areias, Universidade de Évora

Weimar, 11 November 2015

This thesis is dedicated to my parents

Acknowledgements

The thesis guidelines allow only a single author, but I want to clarify that this dissertation has been done with the help and support of a great number of people. First and foremost, the individual to whom I am most indebted is Professor Timon Rabczuk, the best supervisor I could have wished for. There are no proper words to express strongly enough that this study would not have been possible without his invaluable guidance and support throughout my years of graduate study. Quite simply, had I not worked in his group I do not think that I would have completed this degree. Looking back on the entire process of my graduate program, I feel that I was fortunate to have been a member of his group at Bauhaus Universität Weimar.

My sincere thanks also go to the members of my thesis advisory and exam committee: Professor Casten Koënke, Professor Pedro Areias, Professor Tom Lahmer and Dr. Sebastian Bock for their patience in reading this manuscript and for the comments they provided to improve it. Professor Tom Lahmer in particular was instrumental in providing initial guidance into my work with sensitivity analysis and related stochastic modeling methods, and was always willing to share his expertise in the field of stochastic modeling and uncertainty quantification.

I would also like to thank Professor Roham Rafiee, Dr. Yangchen Zhang and Dr. Mohammad Silani for providing precious materials used in this work. In addition, there have been a number of people at Institute for Structural Mechanics such as Dr. Junhua Zhao, Dr. Xiaoying Zhuang, Dr. Cosmin Anitescu, Dr. Nguyen Thanh Nhon, Dr. Hossein Talebi, Dr. Pattabhi Ramaiah Budarapu and Dr. Holger Keitel whose assistance has been greatly appreciated. I am also thankful to Albrecht Schmidt, Michael Schwedler, Daniel Arnold who maintained networks or computer systems so efficiently. I have especially benefited from them. I feel that they are the greatest system administrators in the world. I would also like to extend my thanks to all members of the Institute for Structural Mechanics with whom I have had the pleasure of interacting.

I am grateful for the financial support of the Deutscher Akademischer Austauschdienst (DAAD).

Most of all, I would like to thank my family, especially my parents for their unconditional support as I pursued this goal. To them I dedicate this thesis.

Abstract

Nanostructured materials are extensively applied in many fields of material science for new industrial applications, particularly in the automotive, aerospace industry due to their exceptional physical and mechanical properties. Experimental testing of nanomaterials is expensive, time-consuming, challenging and sometimes unfeasible. Therefore, computational simulations have been employed as alternative method to predict macroscopic material properties.

The behavior of polymeric nanocomposites (PNCs) are highly complex. The origins of macroscopic material properties reside in the properties and interactions taking place on finer scales. It is therefore essential to use multiscale modeling strategy to properly account for all large length and time scales associated with these material systems, which across many orders of magnitude. Numerous multiscale models of PNCs have been established, however, most of them connect only two scales. There are a few multiscale models for PNCs bridging four length scales (nano-, micro-, meso- and macro-scales). In addition, nanomaterials are stochastic in nature and the prediction of macroscopic mechanical properties are influenced by many factors such as fine-scale features. The predicted mechanical properties obtained by traditional approaches significantly deviate from the measured values in experiments due to neglecting uncertainty of material features. This discrepancy is indicated that the effective macroscopic properties of materials are highly sensitive to various sources of uncertainty, such as loading and boundary conditions and material characteristics, etc., while very few stochastic multiscale models for PNCs have been developed. Therefore, it is essential to construct PNC models within the framework of stochastic modeling and quantify the stochastic effect of the input parameters on the macroscopic mechanical properties of those materials.

This study aims to develop computational models at four length scales (nano-, micro-, meso- and macro-scales) and hierarchical upscaling approaches bridging length scales from nano- to macro-scales. A framework for uncertainty quantification (UQ) applied to predict the mechanical properties of the PNCs in dependence of material features at different scales is studied. Sensitivity and uncertainty analysis are of great helps in quantifying the effect of input parameters, considering both main and interaction

effects, on the mechanical properties of the PNCs. To achieve this major goal, the following tasks are carried out:

At nano-scale, molecular dynamics (MD) were used to investigate deformation mechanism of glassy amorphous polyethylene (PE) in dependence of temperature and strain rate. Steered molecular dynamics (SMD) were also employed to investigate interfacial characteristic of the PNCs. *At mico-scale*, we developed an atomistic-based continuum model represented by a representative volume element (RVE) in which the SWNT's properties and the SWNT/polymer interphase are modeled *at nano-scale*, the surrounding polymer matrix is modeled by solid elements. Then, a two-parameter model was employed *at meso-scale*. A hierarchical multiscale approach has been developed to obtain the structure-property relations at one length scale and transfer the effect to the higher length scales. In particular, we homogenized the RVE into an equivalent fiber. The equivalent fiber was then employed in a micromechanical analysis (i.e. Mori-Tanaka model) to predict the effective *macroscopic* properties of the PNC. Furthermore, an averaging homogenization process was also used to obtain the effective stiffness of the PCN *at meso-scale*.

Stochastic modeling and uncertainty quantification consist of the following ingredients:

- Simple random sampling, Latin hypercube sampling, Sobol' quasi-random sequences, Iman and Conover's method (inducing correlation in Latin hypercube sampling) are employed to generate independent and dependent sample data, respectively.
- Surrogate models, such as polynomial regression, moving least squares (MLS), hybrid method combining polynomial regression and MLS, Kriging regression, and penalized spline regression, are employed as an approximation of a mechanical model. The advantage of the surrogate models is the high computational efficiency and robust as they can be constructed from a limited amount of available data.
- Global sensitivity analysis (SA) methods, such as variance-based methods for models with independent and dependent input parameters, Fourier-based techniques for performing variance-based methods and partial derivatives, elementary effects in the context of local SA, are used to quantify the effects of input parameters and their interactions on the mechanical properties of the PNCs. A bootstrap technique is used to assess the robustness of the global SA methods with respect to their performance.

In addition, the probability distribution of mechanical properties are determined by using the probability plot method. The upper and lower bounds of the predicted Young's modulus according to 95 % prediction intervals were provided.

The above-mentioned methods study on the behaviour of intact materials. Novel numerical methods such as a node-based smoothed extended finite element method (NS-XFEM) and an edge-based smoothed phantom node method (ES-Phantom node) were developed for fracture problems. These methods can be used to account for crack at *macro-scale* for future works.

The predicted mechanical properties were validated and verified. They show good agreement with previous experimental and simulations results.

Contents

1	Introduction	1
2	Literature review	7
2.1	Molecular dynamics simulations	7
2.1.1	United atom model and Dreiding potential	7
2.1.2	AIREBO potential	8
2.1.3	MD simulations for polymer	9
2.1.4	Steered molecular dynamics	11
2.2	Continuum methods	12
2.2.1	Nano-scale model	12
2.2.2	Micro-scale model	14
2.2.3	Meso-scale model	15
2.2.4	Macro-scale model	16
2.3	Homogenization technique	18
2.3.1	Equivalent fiber	18
2.3.2	Rule of mixture (ROM) and inverse rule of mixture (IROM)	19
2.3.3	Effective elastic material properties	20
2.4	Finite element method for fracture mechanics	20
2.4.1	A short review of finite element method	20
2.4.2	A brief description of XFEM	21
2.4.3	A brief description of phantom-node method	22
2.4.4	Brief on the node-based smoothed FEM (NS-FEM)	24
2.4.5	Brief on edge-based strain smoothing method in finite elements	27
2.5	Design of experiments (DOE)	28
2.5.1	Monte Carlo sampling (MCS)	28
2.5.2	Latin hypercube sampling (LHS)	29
2.5.3	Sobol' quasi-random sequences	29
2.5.4	Inducing correlation in Latin hypercube sampling	30
2.6	Scatter plots	31
2.7	Sensitivity analysis	31
2.7.1	The ANOVA-representation	32

CONTENTS

2.7.2	The variance-based sensitivity indices	32
2.8	Sensitivity analysis of model response with uncorrelated input parameters	33
2.8.1	Best practices for computing S_i and S_{T_i}	33
2.8.2	Computational scheme for S_{T_i}	35
2.8.3	The method of slices	36
2.8.4	Fourier amplitude sensitivity test (FAST)	36
2.8.5	Extended Fourier amplitude sensitivity test (EFAST)	38
2.8.6	Random balance design method	39
2.8.7	Effective algorithm for sensitivity indices	40
2.8.7.1	First-order sensitivity indices	40
2.8.7.2	Higher order effects	41
2.9	Sensitivity analysis of model response with correlated input parameters	42
2.9.1	Correlated input parameters	42
2.9.2	Improvements of Fourier amplitude sensitivity test to models with correlated parameters (IFAST)	43
2.9.3	Variance decomposition by regression with correlated input	44
2.9.4	Sampling from the conditional distribution (reordering)	46
2.9.5	Extension of the matrix combination approach	46
2.9.6	Extension for regression based indices	48
2.9.7	Extension of Sobol' approach for models with correlated inputs (ESACIs)	48
2.9.8	Variance-based sensitivity indices for models with correlated inputs (VBCIs)	50
2.9.8.1	Dependences among random inputs	50
2.9.8.2	Orthogonalization of the correlated inputs	50
2.9.8.3	Interpretation of the sensitivity indices	51
2.9.8.4	Computational issues	51
2.10	Sensitivity analysis based on coefficients of determination	51
2.11	Partial derivatives	52
2.12	Elementary effects	54
2.12.1	The sampling strategy for elementary effects	55
2.12.2	The computation of the sensitivity measures	55
2.13	Surrogate models	55
2.13.1	Polynomial regression model	56
2.13.2	Moving least squares (MLS)	58
2.13.3	Hybrid algorithm	59
2.13.4	Kriging regression	59
2.13.4.1	Maximum likelihood estimation	59
2.13.4.2	Kriging prediction	60
2.13.5	Nonparametric regression model	61

CONTENTS

2.13.5.1	Cross-Validation	61
2.13.5.2	Penalized spline regression	62
2.14	Normalization of the input	64
3	Stochastic predictions of bulk properties of amorphous polyethylene based on molecular dynamics simulations	65
3.1	Introduction	65
3.2	Molecular dynamics method	66
3.3	Molecular dynamics simulation results	66
3.4	Numerical results	72
3.4.1	Scatter plots	72
3.4.2	Surrogate model	77
3.4.3	Partial derivatives	81
3.4.4	Elementary effects	84
3.4.5	Global sensitivity analysis	85
3.5	Conclusions	90
4	Stochastic predictions of interfacial characteristic of polymeric nanocomposites	91
4.1	Introduction	91
4.2	Molecular dynamics model	93
4.2.1	Potential functions and parameters	93
4.2.2	Pull-out simulations	94
4.3	Molecular dynamics simulation results	97
4.4	Numerical results	98
4.4.1	Derivative-based approach	102
4.4.2	Elementary effects	107
4.4.3	Sensitivity analysis based on coefficients of determination	111
4.4.4	Global sensitivity analysis	112
4.5	Conclusions	113
5	Uncertainty quantification for multiscale modeling of polymer nanocomposites with correlated parameters	115
5.1	Introduction	115
5.2	Multiscale model	117
5.2.1	Nano-scale model	117
5.2.2	Micro-scale model	118
5.2.3	Meso-scale model	120
5.2.4	Macro-scale model	121
5.3	Stochastic modeling	122
5.4	Numerical results	123

CONTENTS

5.4.1	Scatter plots	123
5.4.2	Covariance matrix	128
5.4.3	Surrogate model	128
5.4.4	FAST and IFAST methods	129
5.4.5	Variance decomposition by regression with correlated input	130
5.4.6	Sampling from the conditional distribution (reordering)	131
5.4.7	Extension of the matrix combination approach	132
5.4.8	Extension for regression based indices	132
5.4.9	Extension of Sobol' approach for models with correlated inputs (ESACIs)	133
5.4.10	Variance-based sensitivity indices for models with correlated inputs (VBCIs)	134
5.4.11	Discussion	134
5.5	Conclusions	137
6	A unified framework for stochastic predictions of mechanical properties of polymeric nanocomposites	139
6.1	Introduction	139
6.2	Model for PCN	140
6.2.1	RVE definition	141
6.2.2	Boundary conditions	142
6.2.3	RVE generation algorithm	143
6.2.4	Output	143
6.3	Stochastic input parameters	145
6.4	Global sensitivity analysis	145
6.5	Numerical results	145
6.6	Conclusions	159
7	A node-based smoothed extended finite element method (NS-XFEM) for fracture analysis	163
7.1	Introduction	163
7.2	Nodal-based smoothed extended finite element method (NS-XFEM)	165
7.2.1	Displacement and Strain Field	165
7.2.2	Weak form and discrete equation	168
7.2.3	Numerical integration	169
7.2.3.1	Numerical integration for the XFEM.	169
7.2.3.2	Numerical integration for the NS-XFEM.	170
7.2.4	Stress intensity factor	171
7.3	Numerical results	173
7.3.1	Plate with edge-crack under tension	173
7.3.2	Plate with edge-crack under shear	176

CONTENTS

7.4	Conclusions	176
8	A phantom-node method with edge-based strain smoothing for linear elastic fracture mechanics	181
8.1	Introduction	181
8.2	Edge-based strain smoothing phantom node method	183
8.2.1	Displacement and strain field	183
8.2.2	Weak formulation and discretized equation	187
8.2.3	Crack growth and stress intensity factor	187
8.3	Numerical examples	188
8.3.1	Sheet with an edge-crack under uniaxial tension	188
8.3.2	Sheet with edge-crack under shear	193
8.3.3	Crack growth simulation in a double cantilever beam	198
8.4	Conclusions	203
9	Conclusions	205
9.1	Summary of achievements	205
9.2	Future works	206
	References	208
	Curriculum Vitae	230

List of Figures

1.1	Multiscale modeling diagram for PNCs.	3
2.1	Undeformed (left) and deformed (right) (100% strain) representative volume elements built for PE.	10
2.2	Stress-strain curves for a glassy PE system (10 chains, 1000-units) deformed in uniaxial tension at a strain rate of 10^{-5} 1/fs and temperature of 250 K.	10
2.3	Pull-out SWCNT from PE matrix using SMD simulations. The green boxes show the edges.	11
2.4	Energy variation during the pull-out of the SWCNT: (top) Total potential energy, and (bottom) Pull-out energy (PMF).	12
2.5	Modeling of nanotubes by the molecular structural mechanics approach. Molecular mechanics model (top row) and structural mechanics model (bottom row) (LC03).	13
2.6	Representative volume element (RVE) with completely randomly oriented, straight fibers (left) and a SWNT with a global and local coordinate system (right).	15
2.7	RVE of SWNTs reinforced polymer at meso-scale.	16
2.8	Finite element model of half of the RVE at micro-scale and the development of the equivalent fiber.	18
2.9	(a) Normal and tangential coordinates for a crack; (b) Polar coordinate system associated with a crack tip.	22
2.10	A two dimensional body containing a crack and boundary conditions.	23
2.11	The decomposition of a cracked element into two superimposed elements.	24
2.12	Division of problem domain Ω into non-overlapping smoothing domains Ω_k^s for x_k	25
2.13	Construction of node-based strain smoothing domains and support domain w_i	25
2.14	Construction of edge-based strain smoothing domains.	27
2.15	(a) Monte Carlo, (b) Latin Hypercube and (c) Sobol' sampling.	30

LIST OF FIGURES

2.16	Scatter plots of sampling points in a two-parameters case obtained from the transformation given by: (a) Equation (2.78), (b) Equation (2.87), $N_r = 1$, (c) Equation (2.87), $N_r = 2$	39
2.17	Sorting-and-shuffling strategy.	41
2.18	(a) Conventional independent FAST sample; (b) reordered sample values based on X_1 's original sample order; (c) reordered sample values based on X_2 's original sample order; and (d) response values from the reordered sample (based on X_1 's original sample order).	44
2.19	Flowchart of partial derivatives of the surrogate model output w.r.t X_i (a) when we fix the others and (b) when we vary the others.	53
3.1	Undeformed (left) and deformed (right) (100% strain) representative volume elements built for PE	67
3.2	Plot of the relationship between volume evolution and temperature during cooling process.	67
3.3	Stress-strain curves for a glassy PE system (10 chains, 1000 units) and (100 chains, 100 units), respectively, deformed in uniaxial tension at a temperature of 250 K and strain rate of 10^{-5} 1/fs.	69
3.4	Stress-strain curves for a glassy PE system (10 chains, 1000-units) deformed in uniaxial tension at a strain rate of 10^{-5} 1/fs and temperature of 250 K and 100 K, respectively.	69
3.5	Stress-strain curves for a glassy PE system (10 chains, 1000 units) deformed in uniaxial tension at temperature of 250 K, strain rates of 10^{-5} 1/fs and 5×10^{-6} 1/fs, respectively.	70
3.6	Stress-strain curves for glassy PE systems (10 chains, 1000 units) at a strain rate of 10^{-5} 1/fs and temperature of 250 K.	70
3.7	Stress-strain curves at (a) 250 K and (b) 280 K for quasi-static and dynamics techniques	71
3.8	Schematic diagram of all sensitivity assessment methods presented in this paper.	72
3.9	Scatter plots of the yield stress (Y) versus the chain length (X_1), temperature (X_2) and strain rate (X_3), respectively.	73
3.10	Scatter plots of the Young's modulus versus (Y) the chain length (X_1), temperature (X_2) and strain rate (X_3), respectively.	74
3.11	Histogram of the Young's modulus and assumed probability density functions (PDFs) for different distribution types.	74
3.12	Normal probability plot for the distribution of the Young's modulus.	75
3.13	Weibull probability plot for the distribution of the Young's modulus.	75
3.14	Log-normal probability plot for the distribution of the Young's modulus.	76

LIST OF FIGURES

3.15	The plot of R^2 versus the number of samples when polynomial regression and MLS are used in both cases: the output model are yield stress (a) and Young's modulus (b).	78
3.16	Scatter points and projection surface yield	79
3.17	Scatter points and projection surface mod	80
3.18	Stress-strain curves of two trajectories (left) trajectory 1 and (right) trajectory 2	85
3.19	Stress-strain curves of two trajectories (left) trajectory 3 and (right) trajectory 4	86
3.20	Stress-strain curves of two trajectories (left) trajectory 5 and (right) trajectory 6	86
3.21	Stress-strain curves of two trajectories (left) trajectory 7 and (right) trajectory 8	87
4.1	Cross section of SWCNT/PE composite	93
4.2	Snap shots of CNT pull-out from SWCNT/PE composite	94
4.3	The ISS for SWCNT(5,5), SWCNT(10,10) and SWCNT(15,15) at 100 K and a pulling velocity of 0.1 \AA/ps	95
4.4	The ISS at a pulling velocity of 0.1 \AA/ps for the temperature of 100K, 200K and 300K.	95
4.5	The ISS at 100 K for the pulling velocity of 0.1, 0.5 and $0.75 (\text{ \AA/ps})$	95
4.6	The ISS at 100 K for the simulation boxes with 10^4 , 1.5×10^4 and 2×10^4 monomeric units.	96
4.7	The ISS at 200 K for the chain length of 100 – <i>units</i> , 500 – <i>units</i> and 1000 – <i>units</i>	96
4.8	Stress–strain response at (a) different temperatures (b) different strain rates of pure PE system.	97
4.9	The schematic of PE region of interaction with an a carbon atom on the SWCNT (ZWX+11).	98
4.10	Schematic diagram of all sensitivity assessment methods presented in this paper.	99
4.11	Scatter plots of the ISS (Y) versus the SWCNT radius (X_1), temperature (X_2) and pulling velocity (X_3), respectively.	100
4.12	The plot of R^2 versus the number of samples when polynomial regression, MLS and hybrid models are used	101
4.13	Scattered points and projection surface quadratic	103
4.14	Scattered points and projection surface mls	104
4.15	Scatter points and projection surface hybrid	105
4.16	Reduced pull-out energy of three trajectories (a) trajectory 1, (b) trajectory 2 and (c) trajectory 3	108

LIST OF FIGURES

4.17	Reduced pull-out energy of three trajectories (a) trajectory 4, (b) trajectory 5 and (c) trajectory 6	109
4.18	Reduced pull-out energy of three trajectories (a) trajectory 7, (b) trajectory 8 and (c) trajectory 9	110
4.19	Sensitivity indices (a) First-order (b) Total effect	114
5.1	Multiscale modeling scheme	117
5.2	Finite element model of half of the RVE at micro-scale.	118
5.3	The tensile stress–strain curves versus the SWNT length.	119
5.4	Regression model for $E_{LEF}^{straight}$ with respect to L_{SWNT}	119
5.5	The effective stiffness of the wavy EFs in longitudinal and transverse directions is generated between two bounding values.	121
5.6	Finite element analysis of partitioned material region (MR)	122
5.7	Scatter plot matrix for input parameters.	124
5.8	Schematic diagram of sensitivity assessment methods.	125
5.9	Scatter plots of input parameters with the Young’s modulus including subset averages.	126
5.10	Scatter plots of input parameters with the Poisson’s ratio including subset averages.	127
5.11	First-order and total-effect sensitivity indices for the Young’s modulus of different methods.	135
5.12	First-order and total-effect sensitivity indices for the Poisson’s ratio of different methods.	136
6.1	A detailed view of the mesh.	141
6.2	Boundary conditions imposed on the RVE: (left) an undeformed RVE and (right) a deformed RVE.	142
6.3	Flowchart of the proposed stochastic modeling.	144
6.4	Scatter plot matrix for input parameters.	147
6.5	Schematic diagram of sensitivity assessment methods.	148
6.6	Histogram of the Young’s modulus E of the PCNs and assumed probability density functions (PDFs) for different distribution types.	149
6.7	Normal probability plot for the distribution of the Young’s modulus E	149
6.8	Weibull probability plot for the distribution of the Young’s modulus E	150
6.9	Log-normal probability plot for the distribution of the Young’s modulus E	150
6.10	Scatter plots of input parameters versus the Young’s modulus including the penalized spline regression.	152
6.11	The plot of R^2 versus sample size when QDR and KR models are used	153

LIST OF FIGURES

6.12 First-order and total-effect sensitivity indices w.r.t. the penalized spline regression, the matrix combination method, Saltelli/Sobol', Jansen's method and MOS. 156

6.13 First-order and total-effect sensitivity indices w.r.t. FAST, EFAST, RBD and EASI. 157

6.14 Total sensitivity indices estimated via Saltelli/Sobol' for all pairs of parameters X_i & X_j with $j \neq i$ 159

6.15 The total-effect indices and 95% CIs estimated for the parameter $V_f(X_5)$ via Monte Carlo method. The indices were evaluated using the matrix combination method and formulas (a), (b), (c), (d), and (f) in Table 2.2 with 1000 bootstrapping replicas. 160

6.16 The sensitivity indices and 95% CIs estimated for the parameter $V_f(X_5)$ via Monte Carlo method. The indices were evaluated using FAST and EFAST methods with 1000 bootstrapping replicas. 160

6.17 The first-order indices and 95% CIs estimated for the parameter $V_f(X_5)$ via Monte Carlo method. The indices were evaluated using MOS, RBD and EASI methods with 1000 bootstrapping replicas. 162

7.1 Illustration of node-based smoothing domain (sd) and node categories in NS-XFEM in terms of the support domain of nodal shape function. 166

7.2 Partitioning split smoothing domain into triangular sub-domains (triangles). 172

7.3 Partitioning tip smoothing domain into triangular sub-domains (triangles). 172

7.4 Division of a sub-smoothing domain into sub-smoothing cells (a) $n_{sc} = 1$; (b) $n_{sc} = 2$; (c) $n_{sc} = 3$; (d) $n_{sc} = 4$; (e) $n_{sc} = 6$; (f) $n_{sc} = 8$ 173

7.5 Plate with edge crack under tension. 173

7.6 Strain energy for the plate with edge crack under tension. 175

7.7 The convergence in the energy norm vs. h (mesh size) for the plate with edge crack under tension. 175

7.8 The convergence in the stress intensity factor K_I vs. h (mesh size) for the plate with edge crack under tension. 176

7.9 Plate with edge crack under shear. 177

7.10 Strain energy for plate with edge crack under shear. 177

7.11 The convergence in the energy norm vs. h (mesh size) for plate with edge crack under shear. 178

7.12 The convergence in the stress intensity factor K_I vs. h (mesh size) for plate with edge crack under shear. 179

7.13 The convergence in the stress intensity factor K_{II} vs. h (mesh size) for plate with edge crack under shear. 179

LIST OF FIGURES

8.1	The decomposition of a completely cracked smoothing domain into two superimposed smoothing domains.	184
8.2	The decomposition of a cracked smoothing domain containing crack tip into two superimposed smoothing domains.	184
8.3	The decomposition of a completely cracked smoothing domain into two superimposed smoothing domains.	185
8.4	The decomposition of a cracked smoothing domain containing crack tip into two superimposed smoothing domains.	185
8.5	Sheet with edge crack under tension.	188
8.6	Strain energy for the sheet with edge crack under tension.	189
8.7	The convergence in the energy norm vs. h (mesh size) for the sheet with an edge crack under tension.	190
8.8	The convergence in the energy norm of XFEM vs. h (mesh size) for the sheet with an edge crack under tension.	190
8.9	The convergence in the stress intensity factor K_I vs. h (mesh size) for the sheet with edge crack under tension.	191
8.10	The convergence in the stress intensity factor K_I of XFEM vs. h (mesh size) for the sheet with edge crack under tension.	191
8.11	Computational efficiency of energy norm for the problem of a sheet with an edge crack under remote tension.	192
8.12	Computational efficiency of mode I SIF K_I for the problem of a sheet with an edge crack under remote tension.	192
8.13	Sheet with edge crack under shear.	194
8.14	Strain energy for a sheet with an edge crack under shear.	194
8.15	The convergence in the energy norm vs. h (mesh size) for a sheet with an edge crack under shear.	195
8.16	The convergence in the energy norm of XFEM vs. h (mesh size) for a sheet with an edge crack under shear.	195
8.17	The convergence in the stress intensity factor K_I vs. h (mesh size) for a sheet with an edge crack under shear.	196
8.18	The convergence in the stress intensity factor K_I of XFEM vs. h (mesh size) for a sheet with an edge crack under shear.	196
8.19	Error sif2 norm shear	197
8.20	The convergence in the stress intensity factor K_{II} of XFEM vs. h (mesh size) for sheet with edge crack under shear.	197
8.21	Double cantilever beam with an edge crack.	198
8.22	(a) Deformed shape of the double cantilever beam (structured mesh) and (b) Crack path simulated by ES-Phantom node method (structured mesh) after ten-step growing in which the filled circles are the new crack tip after each step.	199

LIST OF FIGURES

8.23	(a) Deformed shape of the double cantilever beam (unstructured mesh) and (b) Crack path simulated by ES-Phantom node method (unstructured mesh) after ten-step growing in which the filled circles are the new crack tip after each step.	200
8.24	Stress (a) σ_{xx} and (b) σ_{yy} contours in the sheet (structured mesh) after the crack propagates.	201
8.25	Stress (a) σ_{xx} and (b) σ_{yy} contours in the sheet (unstructured mesh) after the crack propagates.	202
9.1	Model selection based on graph theory and sensitivity analysis.	207

List of Tables

2.1	United atom model and parameters of the force field, (TWBH11). . .	9
2.2	Formulas to compute S_i and S_{Ti}	35
2.3	Radial (left-hand) and Winding stairs (right-hand) designs.	35
3.1	Model uncertainties	68
3.2	Statistical results for the ISS	77
3.3	Uncertainties of mechanical output using various distributions	77
3.4	Regression coefficient, COD R^2 and adjusted COD R_{adj}^2 in case the output is yield stress	81
3.5	Regression coefficient, COD R^2 and adjusted COD R_{adj}^2 in case the output is Young's modulus	82
3.6	Average of reduced NPD for the yield stress	84
3.7	Average of reduced NPD for the Young's modulus	84
3.8	Elementary effects for the yield stress	87
3.9	Elementary effects for the Young's modulus	88
3.10	First-order and total-effect sensitivity indices computed on the surrogate model of the input parameters contributing to the yield stress	88
3.11	First-order and total-effect sensitivity indices computed on the surrogate model of the input parameters contributing to the Young's modulus	89
4.1	Model uncertainties	101
4.2	Regression coefficient, COD R^2 and adjusted COD R_{adj}^2	102
4.3	Normalized average of reduced NPD for the ISS	107
4.4	Elementary effects for the ISS	111
4.5	The COD, adjusted COD, drop value of COD, and the coefficient of importance of the reduced quadratic polynomial, the reduced MLS and the reduced hybrid models	112
4.6	First-order and total effects sensitivity indices computed on the surrogate model of the input parameters contributing to the ISS	113
5.1	Effective properties of the EF (SR10b)	120
5.2	Model uncertainties	123

LIST OF TABLES

5.3 Linear regression model result summary 128

5.4 Quadratic polynomial without mixed terms regression model result summary 128

5.5 Sensitivity indices computed on the linear regression model with *uncorrelated parameters* of the Young’s modulus contributed by the input parameter X_i 129

5.6 Sensitivity indices computed on the linear regression model with *uncorrelated parameters* of the Poisson’s ratio contributed by the *uncorrelated* input parameter X_i 130

5.7 Sensitivity indices computed on the linear regression model of the Young’s modulus contributed by the input parameter X_i 130

5.8 Sensitivity indices computed on the linear regression model of the Poisson’s ratio contributed by the input parameter X_i 130

5.9 Sensitivity indices computed on the linear regression model of the Young’s modulus contributed by the input parameter X_i , the correlated part and uncorrelated part of the input parameter X_i 131

5.10 Sensitivity indices computed on the linear regression model of the Poisson’s ratio contributed by the input parameter X_i , the correlated part and uncorrelated part of the input parameter X_i 131

5.11 Main-effect indices computed on the quadratic without mixed terms regression model of the Young’s modulus with correlated input parameters. 131

5.12 Main-effect indices computed on the quadratic without mixed terms regression model of the Poisson’s ratio with correlated input parameters. 131

5.13 First-order and total-effect sensitivity indices computed on the quadratic without mixed terms regression model of the Young’s modulus with correlated input parameters. 132

5.14 First-order and total-effect sensitivity indices computed on the quadratic without mixed terms regression model of the Poisson’s ratio with correlated input parameters. 132

5.15 First-order and total-effect sensitivity indices computed on the quadratic without mixed terms regression model of the Young’s modulus with correlated input parameters. 132

5.16 First-order and total-effect sensitivity indices computed on the quadratic without mixed terms regression model of the Poisson’s ratio with correlated input parameters. 133

5.17 First-order and total-effect sensitivity indices computed on the quadratic without mixed terms regression model of the Young’s modulus with correlated input parameters. 133

LIST OF TABLES

5.18 First-order and total-effect sensitivity indices computed on the quadratic without mixed terms regression model of the Poisson’s ratio with correlated input parameters. 133

5.19 First-order and total-effect sensitivity indices computed on the quadratic without mixed terms regression model of the Young’s modulus with correlated input parameters. 134

5.20 First-order and total-effect sensitivity indices computed on the quadratic without mixed terms regression model of the Poisson’s ratio with correlated input parameters. 134

6.1 Statistical properties of model parameters 146

6.2 Statistical results for the Young’s modulus 147

6.3 Uncertainties of mechanical output using various distributions 147

6.4 QDR model result summary 151

6.5 KR model result summary 151

6.6 First-order sensitivity indices computed on the penalized cubic spline regression model of the Young’s modulus E 151

6.7 First-order and total-effect sensitivity indices computed by the combination method based on the QDR model of the Young’s modulus E . . . 153

6.8 First-order and total-effect sensitivity indices computed by the combination method based on the KR model of the Young’s modulus E . . . 154

6.9 First-order and total-effect sensitivity indices computed by the improved formulas in section 2.8.1 based on the QDR model of the Young’s modulus E 154

6.10 Total effects of pairs of parameters computed by the Saltelli/Sobol’ method based on the QDR model of the Young’s modulus E 155

6.11 First-order sensitivity indices computed by the MOS method based on the QDR model of the Young’s modulus E 155

6.12 First-order sensitivity indices computed by the FAST method based on the QDR model of the Young’s modulus E 155

6.13 First-order and total-effect sensitivity indices computed by the EFAST method based on the QDR model of the Young’s modulus E 158

6.14 First-order sensitivity indices computed by the RBD method based on the QDR model of the Young’s modulus E 158

6.15 First-order sensitivity indices computed by the EASI method based on the QDR model of the Young’s modulus E 158

6.16 Comparison of SA methods in terms of bootstrap CIs versus the number of model evaluations. 161

Nomenclature

Latin Symbols

A, B $N \times k$ sample matrices of input parameters

A_B⁽ⁱ⁾ Matrix, where column i comes from matrix **B** and all other $k - 1$ columns come from matrix **A**

a_i Acceleration of atom i in a system of N atoms

B_A⁽ⁱ⁾ Matrix, where column i comes from matrix **A** and all other $k - 1$ columns come from matrix **B**

C_{XX} Covariance function

C Desired correlation matrix of **X**

C_{XX} Covariance matrix of **X**

F_i Force on atom i

P Lower matrix of **C**

Q Lower matrix of **T**

R Matrix of k parameters generated by LHS

r_i Position of atom i in a system of N atoms

T Correlation matrix of **R**

X $N \times k$ matrix of input parameters

X Random variable vector $\mathbf{X} = [X_1, X_2, \dots, X_N]^T$

x Vector of design variables

X_{~i} $N \times (k - 1)$ matrix of all factors but X_i

LIST OF TABLES

\mathbf{Y}	Vector of responses at sampled design points
A	Cross-sectional area
E	Young's modulus of isotropic composite
$E(\cdot)$	Expected value of the quantity
E_b	Energy due to bond stretching
E_ϕ	Energy due to bond dihedral angle and out-of plane torsion
E_θ	Energy due to bond bending
E_{LEF}	Longitudinal modulus of equivalent fiber
E_{nb}	Energy due to non-bonded van der Waals interaction
E_{TEF}	Transverse modulus of equivalent fiber
E_{total}	Potential energy
EA	Tensile resistance
EI	Flexural rigidity
F	Cumulative distribution function
f	True function to be modeled
GJ	Torsional stiffness
k	Number of factors
k_b	Stiffness constant for bond length potential
k_i	Coefficients of dihedral multi-harmonic
k_θ	Stiffness constant for bond angle potential
L	Length of beam
m_i	Mass of atom i in a system of N atoms
N	Sample size
P	Probability density function
$Prob$	Probability value

LIST OF TABLES

R	Correlation matrix among the sampled design points
r	Distance between two atoms
r_0	Equilibrium distance between two atoms
r_c	Cutoff radius
r_u	Uniformly distributed random number
S_i	First-order sensitivity index of i th variable X_i
S_{ij}	Second-order sensitivity index of i th variable X_i and X_j
S_{T_i}	Total-effect sensitivity index of i th variable X_i
V	Total variance
v_f	Fiber volume fraction
V_i	Partial variance of i th variable X_i
v_m	Matrix volume fraction
$V_{\mathbf{X}_{\sim i}}(\cdot)$, $E_{\mathbf{X}_{\sim i}}(\cdot)$	Variance or mean of argument (\cdot) taken over all factors but X_i
$V_{X_i}(\cdot)$, $E_{X_i}(\cdot)$	Variance or mean of argument (\cdot) taken over X_i
X_i	Generic factor
x_{ji}	Generic value for factor X_i taken from row j of X_i
Cov	Covariance
LHS	Latin hypercube sampling
MCS	Monte Carlo sampling
MD	Molecular dynamics
MLS	Moving least squares
PDF	Probability density function
RSS	Residual sum of squares
SMD	Steered molecular dynamics

Greek Symbols

LIST OF TABLES

β	Vector of coefficients in polynomial regression
ϵ	Energy well depth
λ	Regularization parameter
$\langle \epsilon \rangle$	Average strain tensor
$\langle \sigma \rangle$	Average stress tensor
ϵ_f	Average strain tensor
ϵ_m	Average strain tensor
\mathbf{A}	Strain concentration tensor
\mathbf{C}	Elastic stiffness tensor of the composite
\mathbf{C}_f	Elastic stiffness tensor of fiber
\mathbf{C}_m	Elastic stiffness tensor of matrix
\mathbf{e}	Vector of errors in polynomial regression
\mathbf{I}	Identity tensor
\mathbf{S}	Eshelby's tensor
ω_i	The largest frequency among the set of ω_i
ω_{max}	The largest frequency among the set of ω_i
ϕ	Dihedral angle torsion
ρ_{ij}	Coefficient of correlation
σ	Distance at zero energy
σ^2	Variance of the response at sample design points
θ	Bond angle
θ_0	Initial bond angle

Chapter 1

Introduction

Motivation

New class of lightweight materials, such as polymers and polymeric nanocomposites (PNCs), are extensively used in a wide variety of industrial applications, particularly in the automotive, aerospace industry because of their exceptional physical and mechanical properties (Val08, BWH⁺09). Traditionally, polymer materials have been reinforced with carbon nanotubes (CNTs) or clays due to their high strength and high aspect ratio. Theoretical modeling (AJR⁺99, OGW⁺03) and experimental measurements (SGA98, QDAR00, ASGR00, KPL08) have shown that the mechanical properties of the resulting nanocomposites such as strength, modulus and fracture toughness, to name a few, have been enhanced even at low CNT or clay concentration. From the experimental point of view, a throughout structural characterization and tailored fabrication of nanomaterials at atomistic level are expensive, time-consuming, challenging and sometimes unfeasible. Computational simulations offer an excellent tool for the design of novel materials, and a *priori* prediction of their macroscopic mechanical properties.

The behavior of polymers and PNCs is highly complex. None of the single modeling strategy has properly accounted for all large length and time scales associated with these material systems, which across many orders of magnitude (BWH⁺09, TBW⁺14). Coarse grain methods (UT98, FMP02, FTD02, MP02), such as united atom (UA) models (PYS95, YSM93, LMV⁺06, MLLM07), have been employed to take various length and time scales into account in modeling of polymers. Molecular dynamics (MD) simulations using UA model are used to predict mechanical properties of polyethylene (PE) in dependence of temperature and strain rate by (CBR04, HTW⁺10). However, full molecular simulations are so computationally expensive that they are limited for the realistic system sizes. Even if state-of-the-art parallel supercomputers are used, we are only able to tackle for a system of less than one cubic micron according to a limited

number of atoms ($\sim 10^9$) (WM10). Therefore, a hierarchical multiscale approach is used to predict the macromechanical behavior of polymers and PNCs. Within the hierarchical modeling, the structure-property relationship at one length scale is established and their effect is passed to the higher length scales, the information of material from atomistic to macroscopic levels, hence, is incorporated through sequential simulations.

Numerous multiscale models of polymers and PNCs have been established, however, most of them connect only two scales, e.g, the equivalent-continuum model developed by Odegard *et al.* (OGW⁺03) incorporates the results of MD simulations to obtain microscale properties. A molecular structural mechanics approach was employed by Li and Chou (LC06) to obtain the atomistic structure-property relations in a continuum framework while reducing computational expense. Fermeglia *et al.* (FP07a) proposed a hierarchical procedure for bridging the gap between atomistic and macroscopic (FEM) modeling passing through mesoscopic simulations. His work is one of very few models for PNCs bridging more than two scales.

In addition, nanomaterials are stochastic in nature and the prediction of macroscopic mechanical properties is influenced by many factors such as fine-scale features (MCP⁺07). The effective macroscopic mechanical properties of different realizations of material structures are uncertain according to spatial distribution of the constituents, the material parameters, loading and boundary conditions, etc., while very few stochastic multiscale models for PNCs have been developed. Spanos *et al.* (SK08) developed a multiscale Monte Carlo method for determining mechanical properties of PNCs. However, in such a multiscale model, only phase volume fraction was considered as a random parameter. Also, no methods for uncertainty quantification (UQ) applied to predict the influence of input parameters at different scales on macroscopic properties of PNC have been derived so far. Therefore, it is essential to construct PNC models within the framework of stochastic modeling and quantify the stochastic effect of the input parameters at different length scales on the macroscopic mechanical properties of the PNCs.

Objective

The overall aim of this study is to develop computational models at four length scales (nano-, micro-, meso- and macro-scales) and hierarchical upscaling approaches bridging length scales from nano to macro-scales as shown in Figure 1.1. A framework for UQ applied to predict the mechanical properties of PNCs in dependence of material features at different scales is studied. To achieve this major goal, the following objectives are defined:

1. Obtain probability distributions of the model response given probability distributions of the input parameters;

2. Obtain upper and lower bounds of the predicted material responses;
3. Quantify the effects of input parameters and their interactions on the mechanical properties of the PNCs;
4. Assess the robustness of the methods in materials modeling via a bootstrap technique.

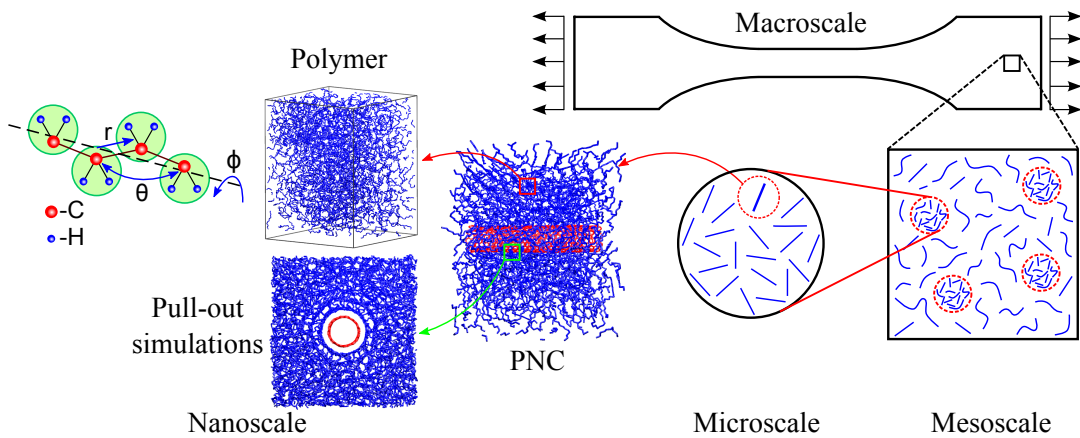


Figure 1.1: Multiscale modeling diagram for PNCs.

Dissertation structure

In chapter 2, theoretical background of methods that have been employed in our studies is described. At first, the interatomic force fields for the amorphous polyethylene (PE), the CNT, and the interface between the PE matrix and the CNT (van der Waals interactions) and the MD simulations applied to model PE and PNCs were briefly presented. Then, a brief description of the analytical and computational continuum modeling is provided. Finally, the stochastic part including design of experiments (DOE) followed by sensitivity analysis (SA) methods and aid tool surrogate models are presented.

In chapter 3, we present stochastic predictions of the bulk properties of amorphous polyethylene. Glassy amorphous polyethylene (PE) systems are simulated using MD simulations with the united atom model. The stress-strain response of amorphous PE systems were studied under uniaxial tension. The stress-strain curve was verified and it is shown that the results are quantitatively in agreement with the previous simulations and experimental results. The effect of the chain length, the temperature and the strain rate on the yield stress and the Young's modulus of glassy polyethylene is

systematically studied. Based on our results, the Young's modulus is best characterized by the Weibull distribution. Further, a sensitivity analysis (SA) is carried out in order to quantify the influence of the uncertain input parameters on the predicted yield stress and Young's modulus. The SA is based on response surface (RS) models (polynomial regression and moving least squares). We use partial derivatives (local SA) and variance-based methods (global SA) where we compute first-order and total-effect sensitivity indices. In addition, we use the elementary effects method on the mechanical model. All stochastic methods predict that the key parameter influencing the yield stress and Young's modulus is the temperature, followed by the strain rate.

In chapter 4, MD simulations are employed to predict interfacial characteristic of polymeric nanocomposites. The interfacial region is the key for load transfer mechanism between fiber and matrix. It is a crucial factor for reinforcing and strengthening the PNC. Thus, the interfacial properties were studied by single fiber pull-out simulations using steered molecular dynamics (SMD) method. The effect of the single-walled carbon nanotube (SWCNT) radius, the temperature and the pulling velocity on interfacial shear stress (ISS) is studied. We quantify the influence of the uncertain input parameters on the predicted ISS via sensitivity analysis (SA). First, partial derivatives in the context of averaged local SA are computed. The SA is based on surrogate models (polynomial regression, moving least squares (MLS) and hybrid of quadratic polynomial and MLS regressions). Next, the elementary effects are determined on the mechanical model to identify the important parameters in the context of averaged local SA. Finally, the approaches for ranking of variables (SA based on coefficients of determination) and variance-based methods are carried out based on the surrogate model in order to quantify the global SA. All stochastic methods predict that the key parameters influencing the ISS is the SWCNT radius followed by the temperature and the pulling velocity, respectively.

In chapter 5, we propose a stochastic multiscale method to quantify the correlated key-input parameters influencing the mechanical properties of polymer nanocomposites (PNCs). The variations of parameters at nano-, micro-, meso- and macro-scales are connected by a hierarchical multiscale approach. The first-order and total-effect sensitivity indices are determined first. The input parameters include the single-walled carbon nanotube (SWNT) length, the SWNT waviness, the agglomeration and volume fraction of SWNTs. Stochastic methods consistently predict that the key parameters for the Young's modulus of the composite are the volume fraction followed by the averaged longitudinal modulus of equivalent fiber (EF), the SWNT length, and the averaged transverse modulus of the EF, respectively. The averaged longitudinal modulus of the EF is estimated to be the most important parameter with respect to the Poisson's ratio followed by the volume fraction, the SWNT length, and the averaged transverse modulus of the EF, respectively. On the other hand, the agglomeration parameters have an insignificant effect on both Young's modulus and Poisson's ratio compared to other parameters. The SA also reveals the correlation between the input parameters and its

effect on the mechanical properties.

In chapter 6, we propose a stochastic framework based on sensitivity analysis (SA) methods to quantify the key-input parameters influencing the Young's modulus of polymer clay nanocomposites (PCNs). The input parameters include the clay volume fraction, clay aspect ratio, clay curvature, clay stiffness and epoxy stiffness. Finite element (FE) analysis is used to predict the stiffness of fully exfoliated PCNs. The obtained Young's modulus shows agreement with experimental results. The probability distribution of the Young's modulus is investigated and best characterized by the Log-normal distribution. Furthermore, the SA methods are performed. All stochastic methods predict that the key parameters for the Young's modulus are the epoxy stiffness followed by the clay volume fraction. On the other hand, the clay aspect ratio, clay curvature and the clay stiffness have an insignificant effect on the Young's modulus of PCNs. Besides the results on the sensitivity of the input parameters, this work includes a comparative study of a series of stochastic methods to predict mechanical properties of PCNs with respect to their performance.

In chapter 7 and chapter 8, we describe a node-based smoothed extended finite element method (NS-XFEM) and a phantom-node method with edge-based strain smoothing. These models are applied at macro-scale to analyze fracture problems of 2D elasticity. The node-based smoothed finite element method (NS-FEM) is incorporated into the extended finite element method (XFEM) to form a novel numerical method NS-XFEM. In this way, we avoid integration of the stress singularity at the crack tip. It is also not necessary to divide elements cut by cracks when we replace interior integration by boundary integration, simplifying integration of the discontinuous approximation. The key advantage of the NS-XFEM is that it provides more accurate solutions compared to the XFEM-T3 element. The phantom-node method with edge-based strain smoothing method is a numerical procedure based on the combination of an edge-based smoothed finite element (ES-FEM) with a phantom-node method. The phantom-node method allows modeling discontinuities at an arbitrary location in the mesh. The ES-FEM model owns a close-to-exact stiffness that is much softer than lower-order finite element methods (FEM). Taking advantage of both the ES-FEM and the phantom-node method, we introduce an edge-based strain smoothing technique for the phantom-node method. Numerical results show that the proposed methods achieve high accuracy compared with the extended finite element method (XFEM) and other reference solutions.

Chapter 2

Literature review

2.1 Molecular dynamics simulations

Molecular dynamics (MD) is a computer simulation technique that follows the physical movements of atoms and molecules through time and space. The trajectories of atoms and molecules are traced by numerically integrating Newton's equations of motions.

$$\mathbf{F}_i = m_i \mathbf{a}_i, \quad i = 1, \dots, N \quad (2.1)$$

where N is the number of atoms in the system, m_i is the mass of the atom i , $\mathbf{a}_i = d^2\mathbf{r}_i/d^2t$ is its acceleration, and \mathbf{F}_i denotes the time-dependent force on atom i . The forces acting on the atom i are determined from the gradient of the potential, E_{total} , with respect to (w.r.t.) the position vector for an atom pair, \mathbf{r}_i , as $\mathbf{F}_i = \partial E_{total} / \partial \mathbf{r}_i$.

Once the forces on each atom due to the interaction of the other atoms in the system are determined, the velocity-Verlet algorithm (Ver67) and Gear algorithm (AT87) are used to numerically integrate the corresponding equations of motion and the dynamics runs within microcanonical NVE (constant number of atoms, constant volume and constant energy), or canonical NVT (constant number of atoms, volume, and temperature) (Nos84, Hoo85) using a thermostat, isobaric-isothermic NPT (constant number of atoms, pressure, and temperature) with a barostat ensembles is performed.

2.1.1 United atom model and Dreiding potential

A united atom approximation is utilized in which the methyl groups (i.e., CH_2 monomer) are represented by a single "atom" or unit. The effect of the hydrogen atoms on the polymer configuration is accounted for in the present potentials, while the mass is included in the united atom.

In the present simulations, interatomic potential between atoms are described by the DREIDING potential (MOG90) that has 4 components: bond stretching (r), bond-

2.1 Molecular dynamics simulations

angle bending (θ), dihedral angle torsion (ϕ), and van der Waals non-bonded interactions. The total potential energy of the system can be expressed as

$$E_{total} = E_b(r) + E_\theta(\theta) + E_\phi(\phi) + E_{nb}(r). \quad (2.2)$$

The respective energies associated with bond stretching, bond-angle bending and bond torsion are

$$E_b = \frac{1}{2}k_b(r - r_0)^2; \quad (2.3)$$

$$E_\theta = \frac{1}{2}k_\theta(\cos(\theta) - \cos(\theta_0))^2; \quad (2.4)$$

$$E_\phi = \frac{1}{2} \sum_{i=0}^3 k_n \cos^i(\phi); \quad (2.5)$$

where k_b and k_θ are the respective stiffness constants for the bond length and bond angle potentials, r_0 and θ_0 are the equilibrium bond length and bond angle, respectively, and the variable k_i , $i = 1, \dots, 4$ are the coefficients for the dihedral multi-harmonic. The non-bonded or Van der Waals (vdWs) interactions are given by a Lennard-Jones potential

$$E_{nb} = \begin{cases} 4\epsilon \left[\left(\frac{\sigma}{r}\right)^{12} - \left(\frac{\sigma}{r}\right)^6 \right] & r \leq r_c \\ 0 & r > r_c \end{cases} \quad (2.6)$$

where r is the distance between the two united atoms for a particular simulation step, σ is the distance at zero energy, and ϵ is the energy (Lennard-Jones) well depth. A cutoff radius r_c of 10.5 Å was also applied to the potential. The interactions between united atoms are described by a force field, whose parameters are summarized in Table 2.1.

2.1.2 AIREBO potential

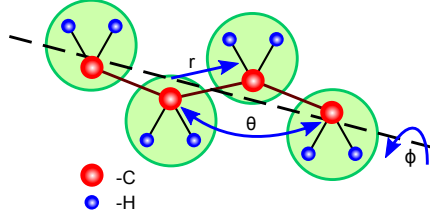
The adaptive intermolecular reactive empirical bond order (AIREBO) potential in (BSH⁺02, Pli95) is adopted to consider the intra-carbon nanotube interactions. The AIREBO potential (E) is an extension of the REBO potential (E^{REBO}) that additionally introduces intermolecular interactions between non-bonded atoms (E^{LJ}) and torsional interactions of four consecutive bonded atoms ($E^{TORSION}$).

$$E = \frac{1}{2} \sum_i \sum_{j \neq i} \left[E_{ij}^{REBO} + E_{ij}^{LJ} + \sum_{k \neq i, j} \sum_{l \neq i, j, k} E_{ijkl}^{TORSION} \right] \quad (2.7)$$

More details of this potential can be found in (STH00).

2.1 Molecular dynamics simulations

Table 2.1: United atom model and parameters of the force field, (TWBH11).



Parameters	Values
k_b	350 kcal/mol
r_0	1.53 Å
k_θ	60 kcal/mol/rad ²
θ_0	1.911 rad
k_ϕ	1.736 kcal/mol
k_1	-4.490 kcal/mol
k_2	0.776 kcal/mol
k_3	6.990 kcal/mol
σ	4.01 Å
ϵ	0.112 kcal/mol

2.1.3 MD simulations for polymer

According to Bouvard *et al.* (BWH⁺10), each generated structure (10,000 atoms) is equilibrated for 100 ps ($\Delta t = 1.0$ fs) so that the volume and energy of the system becomes stable, keeping both the temperature $T = 500$ K and the volume in the NVT ensemble controlled by the Nose-Hoover's thermostat (Nos84, Hoo85). Then, the system is kept at a temperature of $T = 500$ K and pressure $P = 0$ atm for 500 ps ($\Delta t = 0.5$ fs) in the NPT ensemble. After the process, the system is cooled down to the given temperature with a cooling rate of 0.8 K/ps by the same NPT process followed by further 500 ps NPT ensemble at the desired temperature. These structures are generated after the equilibration process in a cubic space in order to accurately calculate the mechanical properties. After the equilibration process, uniaxial tension tests are performed to obtain the stress-strain response in the NPT ensemble. Figure 2.1 illustrates the undeformed (left) and deformed (right) representative volume elements. The stress components were computed from the pressure tensor (BC91), which is defined to be symmetric given by

$$\mathbf{P} = \frac{1}{V} \sum_{i=1}^N \left[\frac{1}{m_i} \mathbf{p}_i \mathbf{p}_i + \mathbf{r}_i \mathbf{f}_i \right] \quad (2.8)$$

where V is the volume, m_i , \mathbf{p}_i , \mathbf{r}_i and \mathbf{f}_i are the respective mass, momentum, position, and the force on the atom i .

The stress-strain response for glassy amorphous PE system with 10 chains, 1000-units deformed in uniaxial tension at temperature of 250 K and strain rate of 1×10^{-5} 1/fs is shown in Figure 2.2.

2.1 Molecular dynamics simulations

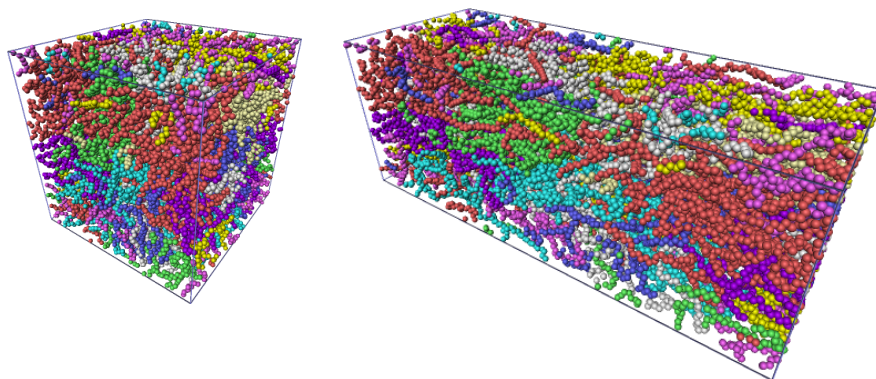


Figure 2.1: Undeformed (left) and deformed (right) (100% strain) representative volume elements built for PE.

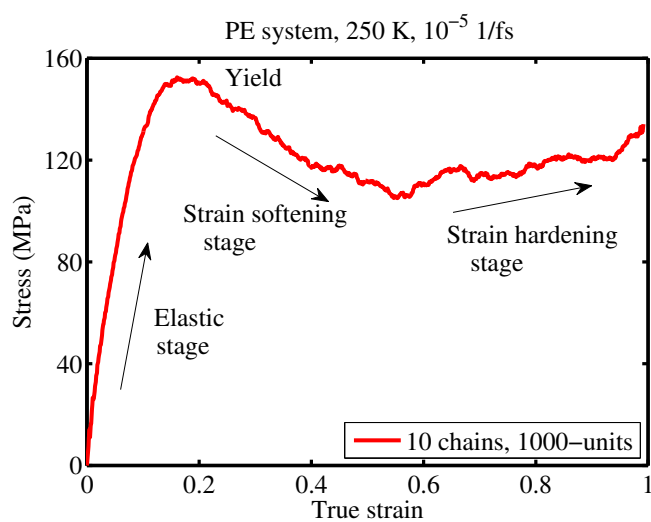


Figure 2.2: Stress-strain curves for a glassy PE system (10 chains, 1000-units) deformed in uniaxial tension at a strain rate of 10^{-5} 1/fs and temperature of 250 K.

2.1 Molecular dynamics simulations

2.1.4 Steered molecular dynamics

In the first step, LAMMPS (Pli95) was used to perform the equilibration process as presented above. The equilibration involves four different steps

1. Each generated structure is equilibrated for 100 ps ($\Delta t = 1 \times 10^{-4} ps$) so that the volume and energy of the system becomes stable.
2. The system is kept at a temperature of $T = 500K$ and pressure $P = 1 atm$ for 500 ps ($\Delta t = 5 \times 10^{-4} ps$) in the NPT ensemble
3. The system is cooled down to the desired temperature at a cooling rate of $0.8 K/ps$.
4. The system is further equilibrated for ($\Delta t = 5 \times 10^{-4} ps$) at the desired temperature in the NPT ensemble.

The main idea of steered molecular dynamics (SMD) simulations is to apply an external force to one or a group of atoms to cause a change in structure in a MD simulation. The atoms are reorganized in simulation process according to the forced change in structure. The potentials of mean force (PMF) are calculated as the force is acted upon the atoms. By applying a moving spring force to the center of mass of the SWCNT's atoms, the SWCNT is pulled along its axial (z-axis) direction at a constant speed while all longitudinal sides of the PE matrix are constrained as shown in Figure 2.3.

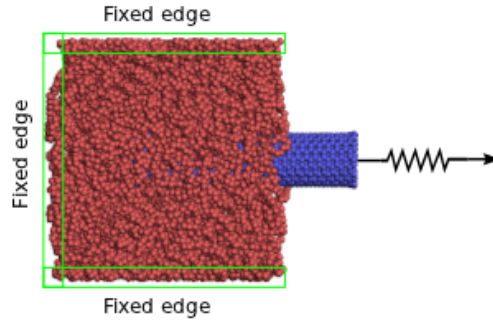


Figure 2.3: Pull-out SWCNT from PE matrix using SMD simulations. The green boxes show the edges.

The restoring force of magnitude is given by (ZZW⁺13):

$$F(t) = K_{spring} (\chi_{spring}(t) - \chi_{pull}(t)) \quad (2.9)$$

where the elastic spring ($K_{spring} = 100 eV/\text{\AA}^2$) is connected between the tether point and the center of mass of the SWCNT; χ_{spring} and χ_{pull} the spring and pulled group

2.2 Continuum methods

positions, respectively. For constant velocity pulling, the integral over time of the force projected on the pulling direction is accumulated and then used to compute the PMF by averaging over multiple independent trajectories along the same pulling path. More details can be found in (PS04).

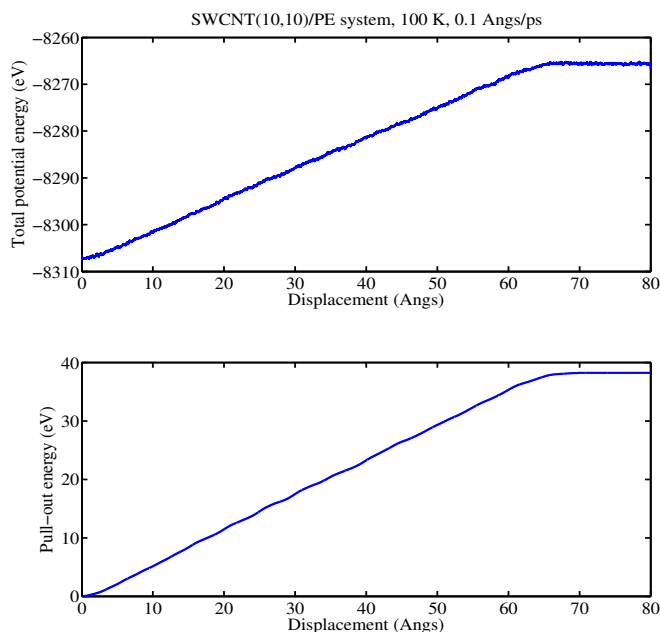


Figure 2.4: Energy variation during the pull-out of the SWCNT: (top) Total potential energy, and (bottom) Pull-out energy (PMF).

The PMF (pull-out energy) is computed and recorded during the pulling process. As shown in Figure 2.4, the total potential energy of SWCNT/PE system and pull-out energy increases linearly with displacement during the pull-out process and levels off after the SWCNT has been completely pulled out of the matrix. This trend is a good agreement with previous results in (LL01, GMW⁺04, LLP⁺11).

2.2 Continuum methods

2.2.1 Nano-scale model

A single-walled carbon nanotube (SWNT) is modeled as a space-frame structure. The $C-C$ covalent bonds in the frame-like structure are represented by 3D beam elements. Nodes representing carbon atoms are used to connect the beam elements to form the SWNT structure. For covalent systems, the total energy can be obtained as the sum of

2.2 Continuum methods

energies consisting of bonded and non-bonded interactions (RCC92)

$$U = \sum V_r + \sum V_\theta + \sum V_\phi + \sum V_{nb}. \quad (2.10)$$

where V_r , V_θ and V_ϕ are the energy associated with bond stretching, bond-angle bending, torsion (dihedral angle and out-of-plane), respectively; V_{nb} is the energy due to non-bonded van der Waals interactions, see also Figure 2.5.

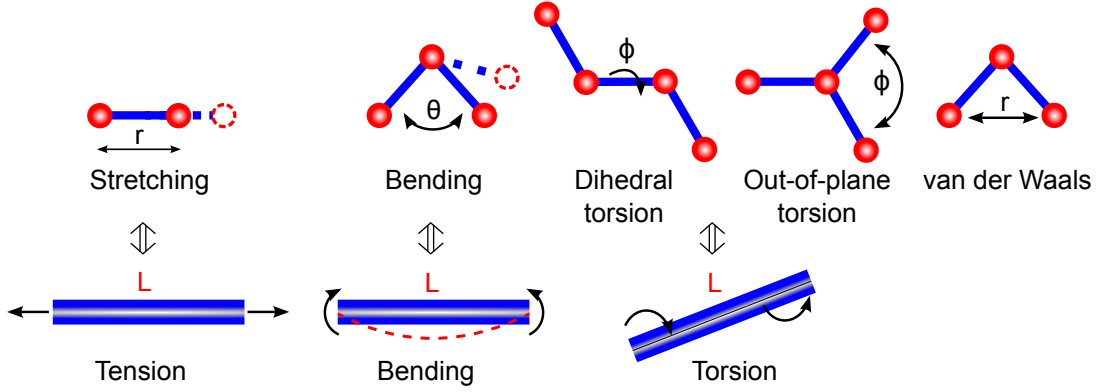


Figure 2.5: Modeling of nanotubes by the molecular structural mechanics approach. Molecular mechanics model (top row) and structural mechanics model (bottom row) (LC03).

Under the assumption of small deformation, simple harmonic approximations are adequate to describe the potential energy (Gel94):

$$V_r = \frac{1}{2}k_r(r - r_0)^2 = \frac{1}{2}k_r(\Delta r)^2, \quad (2.11a)$$

$$V_\theta = \frac{1}{2}k_\theta(\theta - \theta_0)^2 = \frac{1}{2}k_\theta(\Delta\theta)^2, \quad (2.11b)$$

$$V_\phi = \frac{1}{2}k_\phi(\Delta\phi)^2, \quad (2.11c)$$

where k_r , k_θ and k_ϕ are the bond stretching force constant, bond angle bending force constant and torsional resistance, respectively; Δr , $\Delta\theta$ and $\Delta\phi$ denote the bond stretching increment, the bond angle bending and the angle change of bond twisting, respectively.

Based on structural mechanics, the total strain energy of a uniform beam with length L , cross-sectional area A and moment of inertia I , subjected to axial load P ,

2.2 Continuum methods

bending moment M and twisting moment T , respectively, is given by

$$U = \int_0^L \frac{1}{2} \frac{EA}{(\Delta L)^2} dx + \int_0^L \frac{1}{2} \frac{EI}{(2\alpha)^2} dx + \int_0^L \frac{1}{2} \frac{GJ}{(\Delta\beta)^2} dx, \quad (2.12)$$

with ΔL , α and $\Delta\beta$ being the corresponding axial stretching deformation, the bending angle and the twist angle.

Figure 2.5 illustrates the equivalence of molecular mechanics (molecular forces) and structural mechanics (beam elements) for bonded interactions. It can be shown (LC03) that the parameters of the beam model (EA , EI and GJ) are related to the molecular mechanics constants (k_r , k_θ and k_ϕ) by

$$\frac{EA}{L} = k_r, \quad \frac{EI}{L} = k_\theta, \quad \frac{GJ}{L} = k_\phi, \quad (2.13)$$

where k_r , k_θ and k_ϕ are the bond stretching force constant, bond angle bending force constant and torsional resistance respectively.

A non-bonded vdW force of the truncated Lennard-Jones (LJ) 6-12 (SR10a, KGR+10) is used to describe the interphase between the SWNT and the polymer matrix. The vdW force field is expressed as:

$$F_{vdw} = 24 \frac{\epsilon}{\sigma} \left[2 \left(\frac{\sigma}{r} \right)^{13} - \left(\frac{\sigma}{r} \right)^7 \right] \quad (2.14)$$

2.2.2 Micro-scale model

Several micromechanical models which assume that the constituent phases are continuous, have been developed to predict the overall properties of a composite. We employ the micromechanical models to predict the average stiffness of the composite. The constitutive equation of polymer composite systems reinforced with fibers can be expressed in terms of the average strain and stress by

$$\langle \boldsymbol{\sigma} \rangle = \mathbf{C} \langle \boldsymbol{\epsilon} \rangle. \quad (2.15)$$

The effective average elastic moduli \mathbf{C} is given by (Ben87, SFH+04)

$$\mathbf{C} = (V_m \mathbf{C}_m + V_f \mathbf{C}_f \mathbf{A})(V_m \mathbf{I} + V_f \langle \mathbf{A} \rangle)^{-1} \quad (2.16)$$

with \mathbf{I} being the fourth-order tensor identity tensor; \mathbf{C}_f and \mathbf{C}_m denote the fourth-order elasticity tensor of the fiber and the polymer matrix, respectively; V_f and V_m denote the volume fractions of the fibers and the matrix. The Eshelby strain-concentration tensor \mathbf{A} relates the average strain $\boldsymbol{\epsilon}_f$ and $\boldsymbol{\epsilon}_m$ through the expression

$$\boldsymbol{\epsilon}_f = \mathbf{A} \boldsymbol{\epsilon}_m, \quad (2.17)$$

2.2 Continuum methods

and it is determined by

$$\mathbf{A} = [\mathbf{I} + \mathbf{S}(\mathbf{C}_m)^{-1}(\mathbf{C}_f - \mathbf{C}_m)]^{-1}. \quad (2.18)$$

where \mathbf{S} is the Eshelby tensor (Esh57). The micromechanics-based Mori Tanaka method (MT73) was used to predict the effective elastic moduli \mathbf{C} of the composite reinforced by randomly oriented, straight fiber. The orientation distribution of the fibers in a composite is characterized by a probability density function (PDF) $p(\alpha, \beta)$ given by

$$\int_0^{2\pi} \int_0^{\pi/2} p(\alpha, \beta) \sin \alpha d\alpha d\beta = 1 \quad (2.19)$$

with two Euler angles α and β as shown in Figure 2.6. If the fibers are completely randomly oriented, the PDF is $p(\alpha, \beta) = 1/2\pi$.

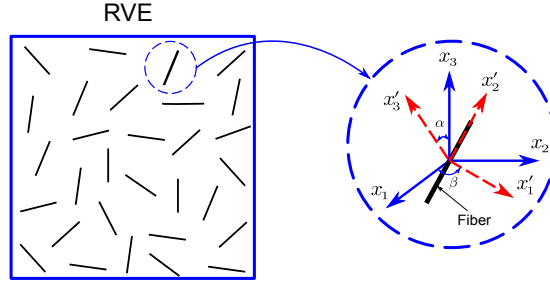


Figure 2.6: Representative volume element (RVE) with completely randomly oriented, straight fibers (left) and a SWNT with a global and local coordinate system (right).

For the composites reinforced with randomly oriented fibers, the effective elastic moduli \mathbf{C} is expressed by Equation (2.16).

2.2.3 Meso-scale model

The Mori-Tanaka method was extended to incorporate the agglomeration in composites reinforced with randomly oriented fibers illustrated in Figure 2.7. PNCs are considered as a two-phase media consisting of a hybrid matrix and spherical inclusions. Two parameters are used by (SFH⁺04) to describe the agglomeration of EFs:

$$\xi = \frac{V^{RVE}_{inclusion}}{V^{RVE}}, \quad \zeta = \frac{V^r_{inclusion}}{V^r}, \quad (2.20)$$

$$V^r = V^r_{inclusion} + V^r_m \quad (2.21)$$

2.2 Continuum methods

where ξ (agglomeration index) denotes the volume fraction of spherical inclusion with respect to (w.r.t.) the total volume of the RVE and ζ (dispersion index) denotes the volume ratio of fibers within the spherical inclusion w.r.t. the total volume of the fibers; $V_{inclusion}^{RVE}$ is the volume of the spherical inclusion in the RVE; $V_{inclusion}^r$ and V_m^r are the volume fibers in the spherical inclusion and in the hybrid matrix, respectively. According to (SFH⁺04) assuming the ratio $\zeta/\xi > 1$, the larger the value of ζ , the more heterogeneous the PNC. If $\zeta = \xi$, no agglomerations exist in the PNC. The average volume fraction, V_f of the fibers in the PNC is:

$$V_f = \frac{V^r}{V^{RVE}} \quad (2.22)$$

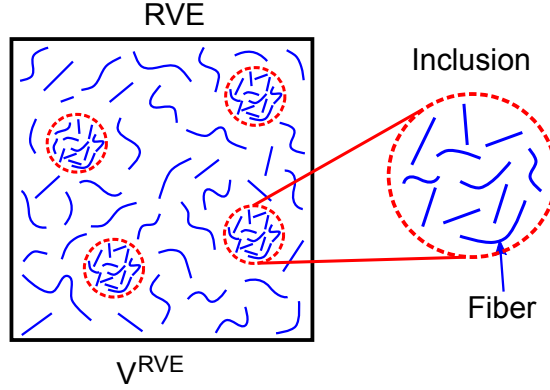


Figure 2.7: RVE of SWNTs reinforced polymer at meso-scale.

2.2.4 Macro-scale model

By assuming the transversely isotropic SWNTs are randomly oriented in the spherical inclusion as illustrated in Figure 2.7, the inclusions behave isotropically. The Mori-Tanaka method is used to calculate the elastic moduli of the two-phase media. The Eshelby's tensor for a spherical inclusion in an isotropic matrix is

$$\begin{aligned} S_{1111} = S_{2222} = S_{3333} &= \frac{7 - 5\nu_{out}}{15(1 - \nu_{out})}, \\ S_{1122} = S_{2233} = S_{3311} &= \frac{1 - 5\nu_{out}}{15(1 - \nu_{out})}, \\ S_{1212} = S_{2323} = S_{3131} &= \frac{4 - 5\nu_{out}}{15(1 - \nu_{out})} \end{aligned} \quad (2.23)$$

2.2 Continuum methods

where $\nu_{out} = \frac{(3K_{out}-2G_{out})}{2(3K_{out}+G_{out})}$ is the Poisson's ratio of the hybrid matrix. Substituting **S** into Equation (2.18) results in the strain concentration tensor **A** for the EF. The effective bulk moduli K_{in} and K_{out} and the effective shear moduli G_{in} and G_{out} of the effective elastic modulus **C** in Equation (2.16) are then expressed as:

$$\begin{aligned}
 K_{in} &= K_m + \frac{(\delta_r - 3K_m\alpha_r)V_f\zeta}{3(\xi - V_f\zeta + V_f\zeta\alpha_r)}, \\
 K_{out} &= K_m + \frac{V_f(\delta_r - 3K_m\alpha_r)(1 - \zeta)}{3[1 - \xi - V_f(1 - \zeta) + V_f(1 - \zeta)\alpha_r]}, \\
 G_{in} &= G_m + \frac{V_f\zeta(\eta_r - 2G\beta_r)}{2(\xi - V_f\zeta + V_f\zeta\beta_r)}, \\
 G_{out} &= G_m + \frac{V_f(1 - \zeta)(\eta_r - 2G_m\beta_r)}{2[1 - \xi - V_f(1 - \zeta) + V_f(1 - \zeta)\beta_r]}
 \end{aligned} \tag{2.24}$$

where δ_r , α_r , β_r , η_r are computed from the Hill's elastic moduli, k_r , l_r , p_r , m_r and n_r , for the fibers and the bulk and shear moduli of the polymer matrix, K_m and G_m , as given in (SFH⁺04).

$$\begin{aligned}
 \alpha_r &= \frac{3(K_m + G_m) + k_r - l_r}{3(G_m + k_r)} \\
 \beta_r &= \frac{1}{5} \left\{ \frac{4G_m + 2k_r + l_r}{3(G_m + k_r)} + \frac{4G_m}{G_m + p_r} + \frac{2[G_m(3K_m + G_m) + G_m(3K_m + 7G_m)]}{G_m(3K_m + G_m) + m_r(3K_m + 7G_m)} \right\} \\
 \delta_r &= \frac{1}{3} \left[n_r + 2l_r + \frac{(2k_r + l_r)(3K_m + 2G_m - l_r)}{G_m + k_r} \right] \\
 \eta_r &= \frac{1}{5} \left[\frac{2}{3}(n_r - l_r) + \frac{8G_m p_r}{G_m + p_r} + \frac{8m_r G_m(3K_m + 4G_m)}{3K_m(m_r + G_m) + G_m(7m_r + G_m)} + \frac{2(k_r - l_r)(2G_m + l_r)}{3(G_m + k_r)} \right]
 \end{aligned} \tag{2.25}$$

The effective Young's modulus E and Poisson's ratio ν of the PNC are obtained by:

$$E = \frac{9KG}{3K + G}, \quad \nu = \frac{3K - 2G}{6K + 2G} \tag{2.26}$$

where K , G are effective bulk and shear modulus of the composite, respectively. They

2.3 Homogenization technique

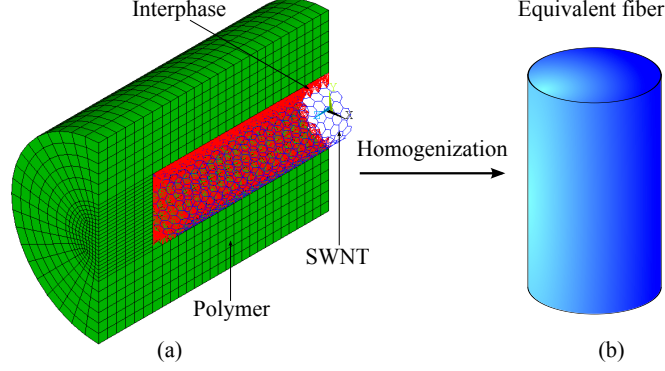


Figure 2.8: Finite element model of half of the RVE at micro-scale and the development of the equivalent fiber.

are given by:

$$\begin{aligned}
 K &= K_{out} \left[1 + \frac{\xi \left(\frac{K_{in}}{K_{out}} - 1 \right)}{1 + \alpha(1 - \xi) \left(\frac{K_{in}}{K_{out}} - 1 \right)} \right], \\
 G &= G_{out} \left[1 + \frac{\xi \left(\frac{G_{in}}{G_{out}} - 1 \right)}{1 + \beta(1 - \xi) \left(\frac{G_{in}}{G_{out}} - 1 \right)} \right],
 \end{aligned} \tag{2.27}$$

with $\alpha = \frac{(1+\nu_{out})}{3(1-\nu_{out})}$, $\beta = \frac{2(4-5\nu_{out})}{15(1-\nu_{out})}$; the effective bulk moduli K_{in} and K_{out} ; the effective shear moduli G_{in} and G_{out} are given in (SFH⁺04), respectively.

2.3 Homogenization technique

2.3.1 Equivalent fiber

After obtaining the mechanical properties of the SWNT as presented in subsection 2.2.1, we constructed a representative volume element (RVE) that includes a SWNT embedded in a polymer matrix modeled by a continuum mechanics approach (LC03). Isotropic solid elements are used to model the polymer matrix. 3-D nonlinear springs connecting the C atom on the SWNT and the nodes on the inner surface of the matrix are used to describe the interphase, see Figure 2.3.1. Subsequently, we homogenized the RVE into a equivalent fiber (EF) to obtain the micromechanical properties.

We employed the adaptive vdW interaction (AVI) model (SR10b, SR10a, SR10c) to determine the mechanical properties of the EF. The tensile stress–strain curve is

2.3 Homogenization technique

obtained from uniaxial tensile simulations by applying axial displacements to nodes at the left end and fix the nodes at the other end of the RVE. In this way, we obtained the longitudinal Young's modulus and the Poisson's ratio. To determine the shear modulus of the EF, we applied a uniform angular displacement at the left end while the nodes at the other end was fixed. The transverse Young's modulus is obtained by applying a uniform internal pressure upon nodes of the SWNT in radial direction.

2.3.2 Rule of mixture (ROM) and inverse rule of mixture (IROM)

Let us consider a model of a composite consisting of the EFs and matrix. The elastic properties are given by the rule of mixture (ROM) as

$$\begin{aligned}
 E_{11} &= V_f E_{11}^f + V_m E^m \\
 \nu_{12} &= V_f \nu_{11}^f + V_m \nu^m \\
 E_{22} &= \frac{E_{22}^f E^m}{E^m V_f + E_{22}^f V_m} \\
 G_{12} &= \frac{G_{12}^f G^m}{G^m V_f + G_{12}^f V_m}
 \end{aligned} \tag{2.28}$$

We use the inverse rule of mixture (**GHT03**) to obtain the elastic properties of the fiber as follows:

$$\begin{aligned}
 E_{11}^f &= \frac{E_{11}}{V_f} - \frac{E_m V_m}{V_f} \\
 \frac{1}{E_{22}^f} &= \frac{1}{E_{22} V_f} - \frac{V_m}{E_m V_f} \\
 \frac{1}{G_{12}^f} &= \frac{1}{G_{12} V_f} - \frac{V_m}{G_m V_f} \\
 \nu_{12}^f &= \frac{\nu_{12}}{V_f} - \frac{\nu_m V_m}{V_f}
 \end{aligned} \tag{2.29}$$

where E_{11}^f , E_{22}^f , G_{12}^f , ν_{12}^f are the longitudinal modulus, the transverse modulus, the shear modulus and the Poisson's ratio of the EF, respectively; E_{11} , E_{22} , G_{12} , ν_{12} are the longitudinal modulus, the transverse modulus, the shear modulus and the Poisson's ratio of the composite, respectively; E_m , G_m , ν_m are the Young's modulus, the shear modulus and the Poisson's ratio of the matrix, respectively; V_f , V_m are the volume fraction of the EF and the volume fraction of the matrix, respectively. The EF will be employed at the meso-scale where the micromechanics equations are applied.

2.4 Finite element method for fracture mechanics

2.3.3 Effective elastic material properties

Let ϑ be a macroscopic quantity of interest. The "effective" value of ϑ is determined by averaging the property over the RVE volume V as

$$\langle \vartheta \rangle = \frac{1}{V} \int_V \vartheta(\mathbf{x}) dV, \quad (2.30)$$

where \mathbf{x} is a position vector. Given a stress field $\sigma_{ij}(x_k)$ and strain field $\epsilon_{ij}(x_k)$, the volume average (homogenized) of the stress and strain are given by

$$\begin{aligned} \langle \sigma_{ij} \rangle &= \frac{1}{V} \int_V \sigma_{ij}(x_k) dV, \\ \langle \epsilon_{ij} \rangle &= \frac{1}{V} \int_V \epsilon_{ij}(x_k) dV, \end{aligned} \quad (2.31)$$

where x_k in index notation simply lists components of position. The effective stiffness for the RVE are defined as

$$\langle \sigma_{ij} \rangle = C_{ijkl} \langle \epsilon_{ij} \rangle \quad (2.32)$$

C_{ijkl} represents the effective stiffness tensor of an equivalent homogeneous material which has the same material properties as the original heterogeneous one (SS 9).

2.4 Finite element method for fracture mechanics

2.4.1 A short review of finite element method

The finite element method (FEM) is a numerical method that approximate the solutions of differential equations which describe the evolution of the material. The main idea of FEM is to discretize the continuum domain into a number of elements where adjacent elements are connected by nodes. By spatially discretizing the domain, partial differential equations are converted into a set of simultaneous algebraic equations at nodes. These equations then are solved in the context of Dirichlet (essential) and Neumann (natural) boundary conditions to find approximate solutions at nodes. Subsequently, we interpolate a field quantity over the entire structure in piecewise fashion based on the shape function.

Let us consider a two-dimensional domain discretized into a number of elements.

2.4 Finite element method for fracture mechanics

Displacement fields (u, v) can be interpolated using the same shape functions such as

$$\begin{aligned} u(\mathbf{x}) &= \sum_{I \in N^{fem}}^4 N_I(\mathbf{x}) u_I \\ v(\mathbf{x}) &= \sum_{I \in N^{fem}}^4 N_I(\mathbf{x}) v_I \end{aligned} \quad (2.33)$$

where I is set of all nodes whose support domain associated with a node of the standard FEM, u_I and v_I are the nodal degrees of freedom (DOFs), N_I are suitable shape functions. The element strain vector is given by

$$\boldsymbol{\epsilon}(\mathbf{x}) = \mathbf{B}(\mathbf{x}) \mathbf{d} \quad (2.34)$$

in which $\mathbf{d} = \{u_1 \ v_1 \ u_2 \ v_2 \ \dots\}^T$ is the nodal DOFs vector. The matrix \mathbf{B} is derivatives of shape functions, determined by

$$\mathbf{B} = \begin{bmatrix} \frac{\partial N_1}{\partial x} & 0 & \frac{\partial N_2}{\partial x} & 0 & \dots \\ 0 & \frac{\partial N_1}{\partial y} & 0 & \frac{\partial N_2}{\partial y} & \dots \\ \frac{\partial N_1}{\partial y} & \frac{\partial N_1}{\partial x} & \frac{\partial N_2}{\partial y} & \frac{\partial N_2}{\partial x} & \dots \end{bmatrix} \quad (2.35)$$

The element stiffness matrix \mathbf{k}_e can be determined as

$$\mathbf{k}_e = \int_{\Omega^e} \mathbf{B}^T \mathbf{C} \mathbf{B} d\Omega \quad (2.36)$$

where \mathbf{C} denotes the constitutive matrix involving material properties, Ω^e denotes the element domain.

2.4.2 A brief description of XFEM

XFEM is based on a local partition of unity. For the case of linear elastic fracture mechanics (LEFM), two sets of enrichment functions are utilized: (1) a Heaviside function to account for the jump across the crack faces and (2) asymptotic branch (near-tip) functions (BB99, RW06):

$$\mathbf{u}^h(\mathbf{x}) = \underbrace{\sum_{I \in N^{fem}} N_I(\mathbf{x}) \mathbf{d}_I}_{\mathbf{u}^{standard}} + \underbrace{\sum_{J \in N^c} N_J(\mathbf{x}) H(\mathbf{x}) \mathbf{a}_J + \sum_{K \in N^f} N_K(\mathbf{x}) \sum_{\alpha=1}^4 \Phi_\alpha(\mathbf{x}) \mathbf{b}_K^\alpha}_{\mathbf{u}^{enr}} \quad (2.37)$$

where $N_I(\mathbf{x})$, $N_J(\mathbf{x})$ and $N_K(\mathbf{x})$ are finite element shape functions, \mathbf{d}_I are nodal DOFs vector associated with node I , \mathbf{a}_J and \mathbf{b}_K are additional nodal DOFs corresponding

2.4 Finite element method for fracture mechanics

to the Heaviside function $H(\mathbf{x})$ and the near-tip functions, $\{\Phi_\alpha\}_{1 \leq \alpha \leq 4}$, respectively. Nodes in set N^c are such that their support is split by the crack and nodes in set N^f belong to the domains that contain a crack tip. These nodes are enriched with the Heaviside and asymptotic branch function fields. The $H(\mathbf{x})$ function is given by (MDB99, RB04).

$$H(\mathbf{x}) = \begin{cases} 1 & (\mathbf{x} - \mathbf{x}^*) \cdot \mathbf{n} \geq 0 \\ -1 & \text{otherwise} \end{cases} \quad (2.38)$$

where \mathbf{x}^* is a point on the crack surface, see Figure 2.9(a)

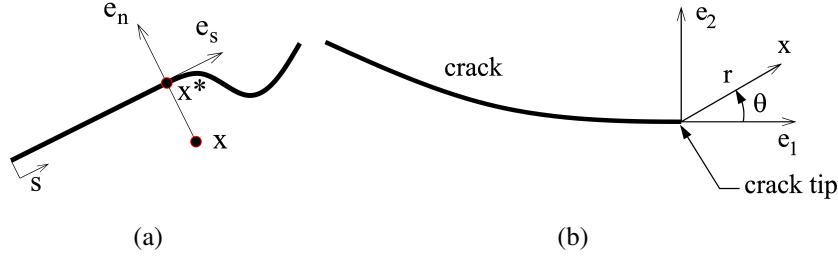


Figure 2.9: (a) Normal and tangential coordinates for a crack; (b) Polar coordinate system associated with a crack tip.

The near tip enrichment consist of functions which incorporate the radial and angular behaviours of the two-dimensional asymptotic crack-tip displacement field (MDB99, RBZ07, BRN⁺08):

$$\{\Phi_\alpha\}_{1 \leq \alpha \leq 4} = \sqrt{r} \left\{ \sin\left(\frac{\theta}{2}\right), \cos\left(\frac{\theta}{2}\right), \sin(\theta) \sin\left(\frac{\theta}{2}\right), \sin(\theta) \cos\left(\frac{\theta}{2}\right) \right\} \quad (2.39)$$

where r and θ are polar coordinates in the local crack-tip coordinate system, see Figure 2.9(b).

2.4.3 A brief description of phantom-node method

Consider a deformable body occupying domain Ω in motion, subjected to body forces \mathbf{b} , external applied traction \mathbf{t} on boundary Γ_t and displacement boundary conditions $\mathbf{u} = \bar{\mathbf{u}}$ on Γ_u containing a crack as shown in Figure 2.10 with the corresponding finite element discretization. In the phantom-node method, a completely cracked element is replaced by two partially active superimposed elements 1 and 2 whose nodes consist of real nodes and phantom nodes marked by solid and empty circles, respectively. The active part of element 1 (Ω_1), $\mathbf{u}^1(\mathbf{x})$, which holds for $f(\mathbf{x}) < 0$ and the other active part

2.4 Finite element method for fracture mechanics

(Ω_2) , $\mathbf{u}^2(\mathbf{x})$ which holds for $f(\mathbf{x}) > 0$. The two parts of the model do not share nodes, and therefore they displace (deform) independently. Areias and Belytschko (AB05) demonstrated that the Hansbo and Hansbo (HH04) formulation is equivalent to the XFEM formulation relying on discontinuous enrichment with the Heaviside function.

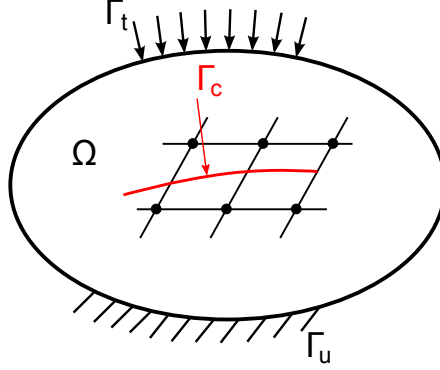


Figure 2.10: A two dimensional body containing a crack and boundary conditions.

The displacement field within an element Ω_e in Figure 2.11 is rewritten as (SAB06):

$$\forall \mathbf{x} \in \Omega_e, \mathbf{u}(\mathbf{x}) = \sum_{I \in S_1} \underbrace{\mathbf{u}_I^1 N_I(\mathbf{x})}_{\mathbf{u}^1(\mathbf{x})} H(-f(\mathbf{x})) + \sum_{I \in S_2} \underbrace{\mathbf{u}_I^2 N_I(\mathbf{x})}_{\mathbf{u}^2(\mathbf{x})} H(f(\mathbf{x})) \quad (2.40)$$

where S_1 and S_2 are the nodes of superimposed elements 1 and 2, respectively. As illustrated in Figure 2.11, each element contains real nodes and phantom nodes marked by solid and empty circles, respectively; N_I is the finite element shape function associated with node I, while \mathbf{u}_I^1 and \mathbf{u}_I^2 are nodal displacements of original nodes in superimposed element 1 and 2, respectively. H is the Heaviside function given in (BB99, RAB07, RB06, RB07a, BND⁺07) and defined by

$$H(x) = \begin{cases} 1 & x > 0 \\ 0 & x \leq 0 \end{cases} \quad (2.41)$$

Here, we choose the physical domain up to the crack line. Note that the crack line is a boundary in phantom node method. It is like the elements near the external boundary. So we avoid singularity in phantom node method. The corresponding strain terms are written the same.

The strain field is obtained as follows:

$$\forall \mathbf{x} \in \Omega_e, \boldsymbol{\epsilon}(\mathbf{x}) = \sum_{I \in S_1} \underbrace{\mathbf{B}_I(\mathbf{x}) \mathbf{u}_I^1}_{\boldsymbol{\epsilon}^1(\mathbf{x})} H(-f(\mathbf{x})) + \sum_{I \in S_2} \underbrace{\mathbf{B}_I(\mathbf{x}) \mathbf{u}_I^2}_{\boldsymbol{\epsilon}^2(\mathbf{x})} H(f(\mathbf{x})) \quad (2.42)$$

2.4 Finite element method for fracture mechanics

where \mathbf{B}_I is the standard strain-displacement matrix. The jump in the displacement field across the crack is calculated by

$$[[\mathbf{u}(\mathbf{x})]] = \mathbf{u}^1(\mathbf{x}) - \mathbf{u}^2(\mathbf{x}) \quad \text{on } \Gamma_c \quad (2.43)$$

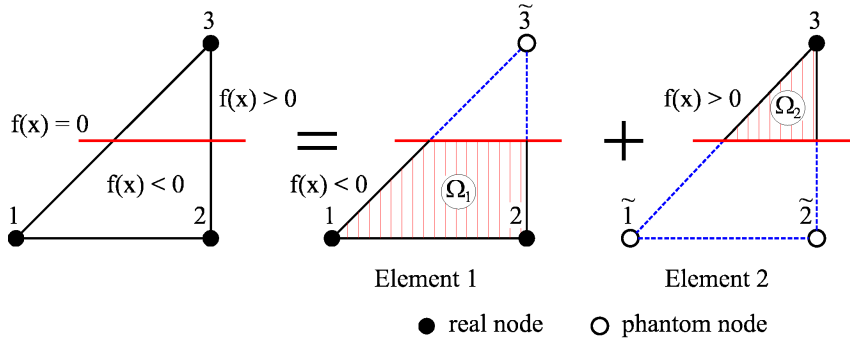


Figure 2.11: The decomposition of a cracked element into two superimposed elements.

$$I \text{ is a phantom node in } \begin{cases} \text{element 1} & \text{if } f(\mathbf{x}_I) > 0 \\ \text{element 2} & \text{if } f(\mathbf{x}_I) < 0 \end{cases} \quad (2.44)$$

In this chapter, the crack tip is forced to be located on the element's boundary.

2.4.4 Brief on the node-based smoothed FEM (NS-FEM)

In NS-FEM, the domain is discretized using elements, as in the FEM. However, instead of using the compatible strains, we utilize the "smoothed" strains over the domain Ω divided into a set of smoothing domains N_s as shown in Figure 2.12 associated with nodes bounded by Ω_k^s , which satisfy the conditions $\Omega = \bigcup_{k=1}^{N_n} \Omega_k^s$ and $\Omega_i^s \cap \Omega_j^s = \emptyset$, $\forall i \neq j$, in which N_n is the total number of nodes in the element mesh. In this case, $N_s = N_n$. The node-based smoothing domains are employed to smooth the strain field and calculate the stiffness matrix. For the triangular elements, the smoothing domains Ω_k^s associated with the node k are formed by connecting sequentially the mid-edge-point to the central points (centroids) of the surrounding triangular elements of the node k , as illustrated in Figure 2.13.

Introducing the node-based smoothing operation, the compatible strain $\epsilon = \nabla_s \mathbf{u}_k^h$

2.4 Finite element method for fracture mechanics

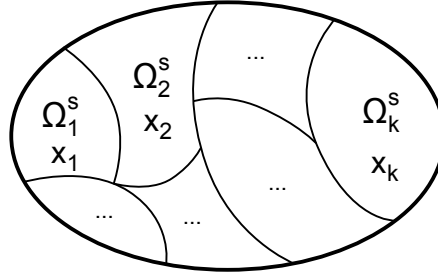


Figure 2.12: Division of problem domain Ω into non-overlapping smoothing domains Ω_k^s for x_k .

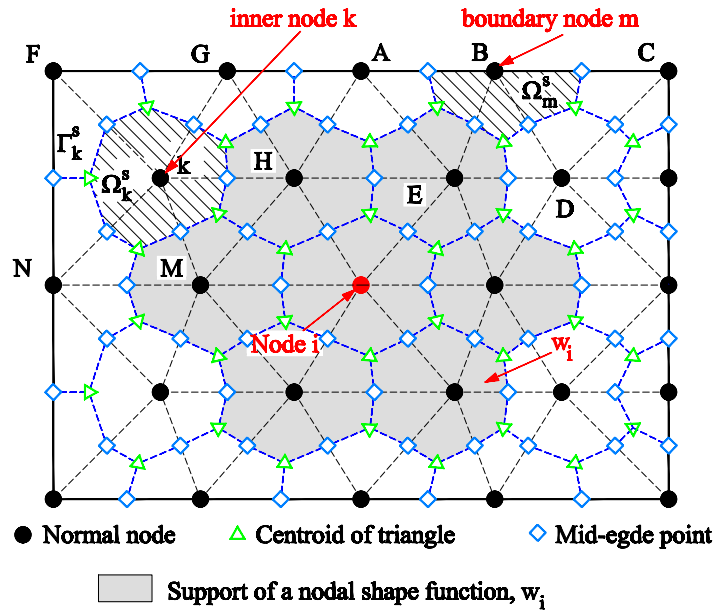


Figure 2.13: Construction of node-based strain smoothing domains and support domain w_i .

is smoothed over the cell Ω^k associated with node k :

$$\bar{\epsilon}_k = \int_{\Omega_k^s} \epsilon(\mathbf{x}) \Phi_k(\mathbf{x}) \, d\Omega = \int_{\Omega_k^s} \nabla_s \mathbf{u}^h(\mathbf{x}) \Phi_k(\mathbf{x}) \, d\Omega \quad (2.45)$$

2.4 Finite element method for fracture mechanics

where $\Phi_k(\mathbf{x})$ is a given smoothing function that satisfies the following property

$$\int_{\Omega_k^s} \Phi_k(\mathbf{x}) \, d\Omega = 1 \quad (2.46)$$

Using a constant smoothing function

$$\Phi = \begin{cases} 1/A_k^s & \mathbf{x} \in \Omega_k^s \\ 0 & \mathbf{x} \notin \Omega_k^s \end{cases} \quad (2.47)$$

It can be shown that

$$\bar{\epsilon}_k = \frac{1}{A_k^s} \int_{\Omega_k^s} \nabla_s \mathbf{u}^h(\mathbf{x}) \, d\Omega = \frac{1}{A_k^s} \int_{\Gamma_k^s} \mathbf{L}_n \mathbf{u}^h(\mathbf{x}) \, d\Gamma \quad (2.48)$$

where $A_k^s = \int_{\Omega_k^s} d\Omega$ is the area of the smoothing domain Ω_k^s , Γ_k^s is the boundary of the smoothing domain Ω_k^s , and L_n is a matrix comprising of normal components, and is expressed as:

$$\mathbf{L}_n = \begin{bmatrix} n_x & 0 \\ 0 & n_y \\ n_y & n_x \end{bmatrix} \quad (2.49)$$

The discretized strain field $\bar{\epsilon}_k$ is computed through the so-called smoothed discretized gradient operator or smoothed strain displacement operator, $\bar{\mathbf{B}}$.

$$\bar{\epsilon}_k = \sum_{I \in n_k^s} \bar{\mathbf{B}}_I(\mathbf{x}_k) \bar{\mathbf{d}}_I \quad (2.50)$$

where $\bar{\mathbf{d}}_I$ are the unknown displacement coefficients defined at the nodes of the finite element, n_k^s is the set of nodes associated to the smoothing domain Ω_k^s . The smoothed element stiffness matrix for element e is computed by the sum of the contributions of the subcells

$$\bar{\mathbf{K}}_{IJ} = \sum_{k=1}^{N_s} \bar{\mathbf{K}}_{IJ,k}^s = \sum_{k=1}^{N_s} \int_{\Omega_k^s} \bar{\mathbf{B}}_I^T \mathbf{D} \bar{\mathbf{B}}_J \, d\Omega = \sum_{k=1}^{N_s} \bar{\mathbf{B}}_I^T \mathbf{D} \bar{\mathbf{B}}_J A_k^s \quad (2.51)$$

where $\bar{\mathbf{B}}_I(\mathbf{x}_k)$ is the smoothed strain gradient matrix:

$$\bar{\mathbf{B}}_I(\mathbf{x}_k) = \begin{bmatrix} \bar{b}_{Ix}(\mathbf{x}_k) & 0 \\ 0 & \bar{b}_{Iy}(\mathbf{x}_k) \\ \bar{b}_{Iy}(\mathbf{x}_k) & \bar{b}_{Ix}(\mathbf{x}_k) \end{bmatrix} \quad (2.52)$$

2.4 Finite element method for fracture mechanics

with

$$\bar{b}_{Ih}(\mathbf{x}_k) = \frac{1}{A_k^s} \int_{\Gamma_k^s} n_h(\mathbf{x}) N_I(\mathbf{x}) d\Gamma; \quad h = x, y \quad (2.53)$$

Equation (2.53) is now evaluated by line integration along the boundary Γ_k^s of the smoothing domain Ω_k^s . Only the shape function itself is needed to compute the strain displacement matrix leading to simple computations for integration of discontinuous functions in XFEM.

2.4.5 Brief on edge-based strain smoothing method in finite elements

In the ES-FEM(LNL09), the domain Ω is partitioned into a set of non-overlapping no-gap smoothing domains constructed using element edges of the triangular elements. $\Omega^{(k)}$ satisfies the conditions $\Omega = \bigcup_{k=1}^{N_e} \Omega^{(k)}$ and $\Omega^{(i)} \cap \Omega^{(j)} = \emptyset, \forall i \neq j$, in which N_e is the total number of edges of elements in the problem domain. In Figure 2.14, the smoothing domain corresponding to an inner edge k , and the smoothing domain for a boundary edge m are illustrated.

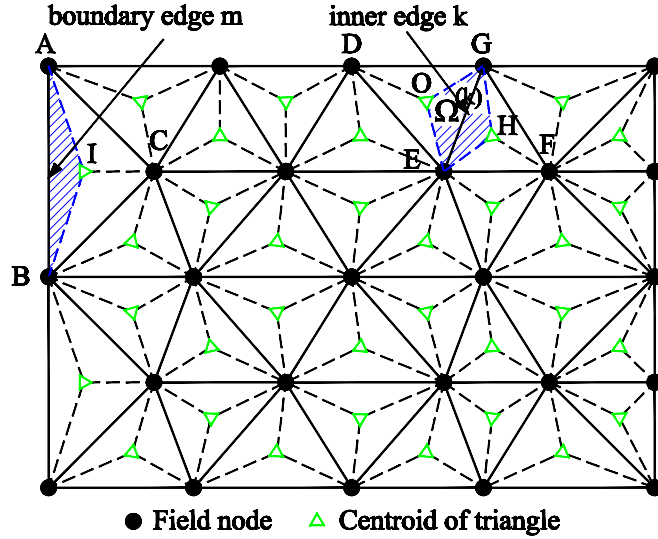


Figure 2.14: Construction of edge-based strain smoothing domains.

Introducing the edge-based smoothing operation, the compatible strain $\epsilon = \nabla_s \mathbf{u}_k^h$

2.5 Design of experiments (DOE)

is smoothed over cell $\Omega^{(k)}$ associated with edge k as follows:

$$\bar{\epsilon}_k = \int_{\Omega^{(k)}} \epsilon(\mathbf{x}) \Phi_k(\mathbf{x}) \, d\Omega = \int_{\Omega^{(k)}} \nabla_s \mathbf{u}^h(\mathbf{x}) \Phi_k(\mathbf{x}) \, d\Omega \quad (2.54)$$

where Φ_k is a given normalized smoothing function that satisfies

$$\int_{\Omega^{(k)}} \Phi_k(\mathbf{x}) \, d\Omega = 1 \quad (2.55)$$

Using the following constant smoothing function

$$\Phi = \begin{cases} 1/A^{(k)} & \mathbf{x} \in \Omega^{(k)} \\ 0 & \mathbf{x} \notin \Omega^{(k)} \end{cases} \quad (2.56)$$

$$\bar{\epsilon}_k = \frac{1}{A^{(k)}} \int_{\Omega^{(k)}} \nabla_s \mathbf{u}^h(\mathbf{x}) \, d\Omega = \frac{1}{A^{(k)}} \int_{\Gamma^{(k)}} \mathbf{L}_n \mathbf{u}^h(\mathbf{x}) \, d\Gamma \quad (2.57)$$

where $A^{(k)} = \int_{\Omega^{(k)}} d\Omega$ is the area of the smoothing domain $\Omega^{(k)}$, $\Gamma^{(k)}$ is the boundary of the smoothing domain $\Omega^{(k)}$, and \mathbf{L}_n is the outward unit normal matrix which can be expressed as:

$$\mathbf{L}_n = \begin{bmatrix} n_x & 0 \\ 0 & n_y \\ n_y & n_x \end{bmatrix}. \quad (2.58)$$

2.5 Design of experiments (DOE)

2.5.1 Monte Carlo sampling (MCS)

Monte Carlo (MC) is the most commonly used random-number despite the least sophisticated of sampling methods which is used to generate random input parameters from prescribed probability distributions. A realization of the random parameter is sampled using random or pseudo-random numbers generator from a probability density function (PDF). Monte Carlo sampling method is entirely random, hence any sampled realization may fall anywhere within the input's design space. The randomly generated realizations are more likely lie in domains of the input distribution which have higher frequencies of occurrence. From the cumulative curve, a value between 0 and 1 is randomly selected as an MC sample. With enough iterations, a random vector of the parameter is sampled through MC sampling.

2.5 Design of experiments (DOE)

2.5.2 Latin hypercube sampling (LHS)

Latin Hypercube Sampling (LHS) (MCB79, IC82) is an improved sampling strategy that enables a reliable approximation of the stochastic properties even for a small number of samples N . LHS is used to provide the design points which are spread throughout the design space. The LHS can be summarized as:

- Divide the cumulative curve into N equal intervals on the cumulative distribution of each parameter;
- A probability value is then randomly selected from each interval of the parameter distribution

$$Prob_i = (1/N)r_u + (i - 1)/N, \quad (2.59)$$

in the i th interval, where r_u is uniformly distributed random number varying over the range $[0, 1]$, see (WJ98);

- Use the inverse cumulative distribution function (CDF) to map the probability value $Prob_i$ into the design space as:

$$x = F^{-1}(Prob); \quad (2.60)$$

where F^{-1} denotes the inverse CDF.

By using LHS, computer effort can be saved due to the dense stratification across the range of each sampled variable (HD03).

2.5.3 Sobol' quasi-random sequences

The algorithm for LP_τ quasi-random (QR) sequences (STLS92), employed to generate the samples X_1, X_2, \dots, X_k as uniformly as possible over the unit hypercube Ω , has been implemented in FORTRAN77. All LP_τ sequences suggested by Sobol' satisfy the following three main requirements:

1. The uniformity of the distribution are asymptotically optimal when the length of the sequence is large.
2. Good distribution for fairly small initial sets (the number of sampled points is small).
3. A very fast computational algorithm.

Figure 2.15 shows the samples generated by Monte Carlo sampling (MCS), Latin Hypercube sampling (LHS) and Sobol' quasi-random sequences sampling strategy. It is shown that the samples obtained by Sobol' quasi-random sequences and LHS are better distributed compared to those obtained by MCS.

2.5 Design of experiments (DOE)

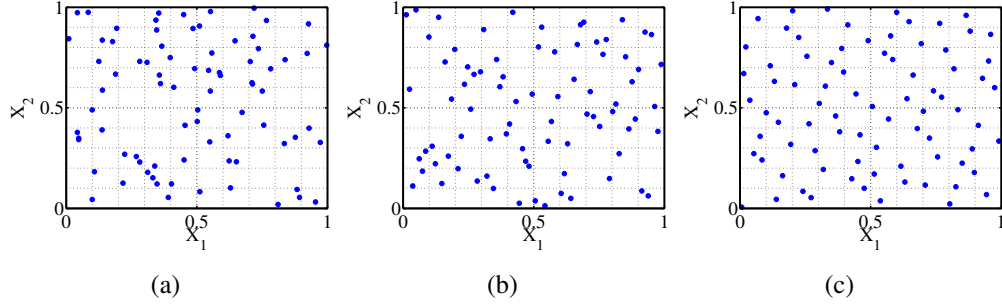


Figure 2.15: (a) Monte Carlo, (b) Latin Hypercube and (c) Sobol' sampling.

2.5.4 Inducing correlation in Latin hypercube sampling

Iman and Conover (IC82) proposed a method that aims to rearrange the input parameters so that the Spearman rank correlation matrix is approximately equal to the target rank correlation matrix, while unchanging certain important properties of the sampling scheme used to generate them. The method is based on the Cholesky decomposition of the correlation matrix. Suppose matrix \mathbf{X} has rank correlation matrix \mathbf{I} , as its parameters (i.e., columns) were generated independently. Let \mathbf{C} the desired correlation matrix of some transformation of \mathbf{X} . If $\mathbf{P}\mathbf{P}'$ is the Cholesky decomposition of matrix \mathbf{C} , then \mathbf{P} is the lower triangular matrix and $\mathbf{C} = \mathbf{P}\mathbf{P}'$. Multiplication by \mathbf{P}' , $\mathbf{X}\mathbf{P}'$ results in random parameters with correlation matrix \mathbf{C} . The method is summarized as follows:

- Use Latin hypercube sampling (LHS) to generate matrix \mathbf{R} of k parameters at sample size ns .
- Compute \mathbf{T} , the correlation matrix of \mathbf{R} .
- The Cholesky decomposition is used to obtain the \mathbf{P} lower triangular matrix of the desired correlation matrix \mathbf{C} such that $\mathbf{C} = \mathbf{P}\mathbf{P}'$. Similarly, \mathbf{Q} the lower triangular matrix of \mathbf{T} is also obtained.

$$\mathbf{T} = \mathbf{Q}\mathbf{Q}'; \quad (2.61)$$

- Compute matrix \mathbf{S} from $\mathbf{S} = \mathbf{P}\mathbf{Q}^{-1}$.
- Compute target correlation matrix $\mathbf{R}^* = \mathbf{R}\mathbf{S}'$, which has a correlation matrix close to \mathbf{C} .
- The values of each parameter in \mathbf{R} are reordered so that they have the same rank as the corresponding parameter in target matrix \mathbf{R}^* .

2.6 Scatter plots

A preliminary step in SA is to visualise the relationship of the input parameters and the output using scatter plots. We use the model as described in the following chapters and a set of data generated by the LHS method. The advantage of this approach is that we can get a first graphical understanding under acceptable efforts the effect of the input on the output value. A scatter plot can draw the correlation between Y and X_i , or even by estimating variance-based measures by nonlinear regression (PSS12).

2.7 Sensitivity analysis

The purpose of quantitative uncertainty analysis is to use currently available information in order to quantify the degree of confidence in the existing simulations containing a set of assumptions and conceived models that are used to predict the mechanical behavior of the material.

According to (SRA⁺08), SA in general is the study of how much model output values are affected by changes in model input values. In the following, a general description of SA methods is given, which is usually exploited to rank the model's input parameters and their contribution to the model output.

We have conducted SA with the aim of

- realizing the most influential parameters on model response, and additional research upon those parameters need to be studied to reduce model response uncertainty,
- eliminating the parameters which insignificantly influence on the model response,
- taking the interaction among input parameters into account,
- determining the optimum region within the design space which is used for a subsequent model calibration.

SA performance consist of

- defining input parameters and model response associated with the computational model,
- determining PDFs which characterize input parameter distributions,
- generating a sample accordingly with the parameter PDFs using an adequate sampling strategy. Subsequently, we evaluate the model responses at each design point,
- quantifying the effects of input parameters on the model responses.

2.7 Sensitivity analysis

2.7.1 The ANOVA-representation

Let $Y = f(\mathbf{X})$ be computational model defined in \mathbb{R}^k with $\mathbf{X} = \{X_1, X_2, \dots, X_k\}$ being a set of random parameters, then $f(\mathbf{X})$ can always be described in terms of functional decomposition scheme:

$$f(\mathbf{X}) = f_0 + \sum_{i=1}^k f_i(X_i) + \sum_{i=1}^k f_{ij}(X_i, X_j) \dots + f_{1\dots k}(X_1, \dots, X_k) \quad (2.62)$$

where $f_0 = E[f(\mathbf{X})]$; $f_0 + f_i(X_i) = E[f(\mathbf{X}|X_i)]$; $f_0 + f_i(X_i) + f_{ij}(X_i, x_j) = E[f(\mathbf{X}|X_i, X_j)]$ and so on for higher order terms.

Equation (2.62) is deduced as shown in (MT12)

$$V = \sum_{i=1}^k V_i + \sum_{j>i}^k V_{ij} + \dots + V_{1\dots k} \quad (2.63)$$

where V is the total variance of $f(\mathbf{X})$, V_i is the partial variance of f due to X_i and $V_{i_1\dots i_s}$ is the partial variance of f due to the interactions among $\{x_{i_1}, \dots, x_{i_s}\}$. Dividing both sides of Equation (2.63) by V , we obtain

$$\sum_{i=1}^k S_i + \sum_{j>i}^k S_{ij} + \dots + S_{1\dots k} = 1 \quad (2.64)$$

where S_i is the first-order effect which measures the part of variance of model response due to X_i .

2.7.2 The variance-based sensitivity indices

Variance-based sensitivity indices are derived from Equation (2.63) as:

$$S_i = \frac{V[E[f(\mathbf{X})|X_i]]}{V[f(\mathbf{X})]}; \quad (2.65)$$

and the second-order sensitivity index S_{ij} , the total-effect index S_{T_i} defined as the sum of all the sensitivity indices consisting of the parameter X_i are respectively given by

$$S_{ij} = \frac{V[E[f(\mathbf{X})|X_i, X_j]]}{V[f(\mathbf{X})]}; \quad (2.66)$$

$$S_{T_i} = S_i + \sum_{j \neq i}^k S_{ij} + \dots + S_{1\dots i\dots n}. \quad (2.67)$$

2.8 Sensitivity analysis of model response with uncorrelated input parameters

The total-effect index can be rewritten as

$$S_{T_i} = \frac{E[V[f(\mathbf{X})|X_{\sim i}]]}{V[f(\mathbf{X})]}. \quad (2.68)$$

In practice, the computation of S_i and S_{T_i} require a high number of samples. The costs of applying these measures is of $\mathcal{O}(N(k+2))$, where N is the number of samples. Thus, a surrogate model $\hat{\mathbf{Y}}$ is used to estimate the real response that will be presented in section 2.13.

2.8 Sensitivity analysis of model response with uncorrelated input parameters

2.8.1 Best practices for computing S_i and S_{T_i}

In this section, we briefly present a Monte Carlo estimation of the Sobol' indices, the so-called matrix combination method. A further improvement proposed by Saltelli *et al.* (SAA⁺10) and alternative forms for the sensitivity estimators offered by Jansen (Jan99) are also described briefly.

For the Monte Carlo estimation of the Sobol' indices, two independent sampling matrices \mathbf{A} and \mathbf{B} with corresponding entries a_{ji} and b_{ji} , both of dimension $(N \times k)$ for the input parameters \mathbf{X} are generated. We then define a matrix $\mathbf{A}_B^{(i)}$ ($\mathbf{B}_A^{(i)}$) with entries from \mathbf{A} (\mathbf{B}) except the i th column, which is taken from \mathbf{B} (\mathbf{A}). S_i can be computed from \mathbf{A} , $\mathbf{B}_A^{(i)}$ or \mathbf{B} , $\mathbf{A}_B^{(i)}$ (Sob93):

$$V_{X_i}(E_{\mathbf{X}_{\sim i}}(\mathbf{Y}|X_i)) = \frac{1}{N} \sum_{j=1}^N f(\mathbf{A})_j f(\mathbf{B}_A^{(i)})_j - f_0^2 \quad (2.69)$$

where $(\mathbf{B})_j$ denotes the j -th row of matrix \mathbf{B} , and

$$f_0^2 = \left(\frac{1}{N} \sum_{j=1}^N f(\mathbf{A})_j \right)^2 \quad (2.70)$$

With $V_{\mathbf{X}_{\sim i}}(E_{X_i}(\mathbf{Y}|\mathbf{X}_{\sim i}))$ the, S_{T_i} in Equation (2.68) is rewritten as follows:

$$V_{\mathbf{X}_{\sim i}}(E_{X_i}(\mathbf{Y}|\mathbf{X}_{\sim i})) = \frac{1}{N} \sum_{j=1}^N f(\mathbf{A})_j f(\mathbf{A}_B^{(i)})_j - f_0^2. \quad (2.71)$$

2.8 Sensitivity analysis of model response with uncorrelated input parameters

Similarly, the estimation of S_i from Equation (2.69) can be derived (Sal02, STG+07)

$$V_{X_i}(E_{\mathbf{X}_{\sim i}}(\mathbf{Y}|X_i)) = \frac{1}{N} \sum_{j=1}^N f(\mathbf{A})_j \left(f(\mathbf{B}_{\mathbf{A}}^{(i)})_j - f(\mathbf{B})_j \right). \quad (2.72)$$

An improvement of the variance-based method is suggested by Saltelli *et al.* (SAA+10) where the triplet \mathbf{A} , \mathbf{B} and $\mathbf{A}_{\mathbf{B}}^{(i)}$ were used instead of the triplet \mathbf{B} , \mathbf{A} and $\mathbf{B}_{\mathbf{A}}^{(i)}$ in Equation (2.72). The modified method is based on the use of quasi-Monte Carlo samples as will be discussed in section 2.5.3.

The estimator for S_{T_i} in Equation (2.71) has been improved by Sobol' (Soban):

$$V_{\mathbf{X}_{\sim i}}(E_{X_i}(\mathbf{Y}|\mathbf{X}_{\sim i})) = V(\mathbf{Y}) - \frac{1}{N} \sum_{j=1}^N f(\mathbf{A})_j \left(f(\mathbf{A})_j - f(\mathbf{A}_{\mathbf{B}}^{(i)})_j \right). \quad (2.73)$$

Jansen (Jan99) proposed alternative formulas for the estimators of S_i and S_{T_i} where $V_{X_i}(E_{\mathbf{X}_{\sim i}}(\mathbf{Y}|X_i))$ is obtained from:

$$V_{X_i}(E_{\mathbf{X}_{\sim i}}(\mathbf{Y}|X_i)) = V(\mathbf{Y}) - \frac{1}{2N} \sum_{j=1}^N \left(f(\mathbf{B})_j - f(\mathbf{A}_{\mathbf{B}}^{(i)})_j \right)^2. \quad (2.74)$$

Using $E_{\mathbf{X}_{\sim i}}(V_{X_i}(\mathbf{Y}|\mathbf{X}_{\sim i}))$ in Equation (2.68), an alternative formula for S_{T_i} is given by

$$V_{\mathbf{X}_{\sim i}}(E_{X_i}(\mathbf{Y}|\mathbf{X}_{\sim i})) = \frac{1}{2N} \sum_{j=1}^N \left(f(\mathbf{A})_j - f(\mathbf{A}_{\mathbf{B}}^{(i)})_j \right)^2. \quad (2.75)$$

The formulas (2.69) - (2.75) were used to compute S_i and S_{T_i} as summarized in Table 2.2 Saltelli suggested that \mathbf{A} , $\mathbf{A}_{\mathbf{B}}^{(i)}$ should be sampled by using the quasi-random numbers to compute S_{T_i} estimates.

Total effects of pairs of factors are estimated through a straightforward generalization of Jansen's estimator. The following Equation (2.76) introduces total effects of couples of parameters. These estimates are not independent from those of the total effect for single parameters, as all are proceeded in the same simulations.

$$E_{\mathbf{X}_{\sim ij}}(V_{X_i X_j}(\mathbf{Y}|\mathbf{X}_{\sim ij})) = \frac{1}{2N} \sum_{w=1}^N \left(f(\mathbf{A}_{\mathbf{B}}^{(i)})_w - f(\mathbf{A}_{\mathbf{B}}^{(j)})_w \right)^2. \quad (2.76)$$

Note that $E_{\mathbf{X}_{\sim ij}}(V_{X_i X_j}(\mathbf{Y}|\mathbf{X}_{\sim ij}))$ refers to the estimation of the total effects of couples of parameters – not to be confused with that of the second-order sensitivity index for the couple of parameters i , and $j(\neq i)$ S_{ij} .

2.8 Sensitivity analysis of model response with uncorrelated input parameters

Table 2.2: Formulas to compute S_i and S_{T_i} .

$V_{X_i}(E_{\mathbf{X}_{\sim i}}(\mathbf{Y} X_i))$ for S_i	Reference
(a) $\frac{1}{N} \sum_{j=1}^N f(\mathbf{A})_j f(\mathbf{B}_{\mathbf{A}}^{(i)})_j - f_0^2$	(Sob93)
(b) $\frac{1}{N} \sum_{j=1}^N f(\mathbf{B})_j \left(f(\mathbf{A}_{\mathbf{B}}^{(i)})_j - f(\mathbf{A})_j \right)$	(SAA+10)
(c) $V(\mathbf{Y}) - \frac{1}{2N} \sum_{j=1}^N \left(f(\mathbf{B})_j - f(\mathbf{A}_{\mathbf{B}}^{(i)})_j \right)^2$	(Jan99)
$E_{\mathbf{X}_{\sim i}}(V_{X_i}(\mathbf{Y} \mathbf{X}_{\sim i}))$ for S_{T_i}	
(d) $V(\mathbf{Y}) - \frac{1}{N} \sum_{j=1}^N f(\mathbf{A})_j f(\mathbf{A}_{\mathbf{B}}^{(i)})_j + f_0^2$	(HS96)
(e) $\frac{1}{N} \sum_{j=1}^N f(\mathbf{A})_j \left(f(\mathbf{A})_j - f(\mathbf{A}_{\mathbf{B}}^{(i)})_j \right)$	(Soban)
(f) $\frac{1}{2N} \sum_{j=1}^N \left(f(\mathbf{A})_j - f(\mathbf{A}_{\mathbf{B}}^{(i)})_j \right)^2$	(Jan99, SAA+10)

2.8.2 Computational scheme for S_{T_i}

As presented in (SAA+10), different methods may be used to construct the design matrices \mathbf{A} and $\mathbf{A}_{\mathbf{B}}^{(i)}$. Two different designs are adopted in this work: (1) the 'radial design' (Sal02) and (2) the 'winding design' (Jan99). The two designs with the first block of size $q = k + 1$ model evaluations are illustrated in Table 2.3.

Table 2.3: Radial (left-hand) and Winding stairs (right-hand) designs.

Radial sampling	Step	Winding stairs
$a_{11}, a_{12}, a_{13}, \dots, a_{1k}$		$a_{11}, a_{12}, a_{13}, \dots, a_{1k}$
$b_{11}, a_{12}, a_{13}, \dots, a_{1k}$	X_1	$b_{11}, a_{12}, a_{13}, \dots, a_{1k}$
$a_{11}, b_{12}, a_{13}, \dots, a_{1k}$	X_2	$b_{11}, b_{12}, a_{13}, \dots, a_{1k}$
$a_{11}, a_{12}, b_{13}, \dots, a_{1k}$	X_3	$b_{11}, b_{12}, b_{13}, \dots, a_{1k}$
$\dots \dots \dots \dots \dots$	\dots	$\dots \dots \dots \dots \dots$
$a_{11}, a_{12}, a_{13}, \dots, b_{1k}$	X_k	$b_{11}, b_{12}, b_{13}, \dots, b_{1k}$

The sampling scheme of two different designs and the computational issues for the above-mentioned estimators in Table 2.2 can be found in (SAA+10, Jan99, Sal02, CST00).

A quasi-random sequence of size $(N \times 2k)$ is sampled and separated into matrices \mathbf{A} (left half) and \mathbf{B} (right half) of size $(N \times k)$.

2.8 Sensitivity analysis of model response with uncorrelated input parameters

The triplet \mathbf{A} , $\mathbf{A}_B^{(i)}$ and \mathbf{B} is preferred to the triplet \mathbf{A} , $\mathbf{B}_A^{(i)}$ and \mathbf{B} for computation of S_i and S_{T_i} because the former contains a higher number of better points.

2.8.3 The method of slices

The main idea of the method of slices (MOS) is to cut each scatterplot into slices according to the parameter distribution. The expected value of \mathbf{Y} within each slice is then quantified as it varies over the slices. If the number of slices is large (the slice is very thin) the variation over the slices of the expected value of \mathbf{Y} within each slice is identical to keeping each parameter fixed while averaging over the others. Application of the MOS involves

- The X_i axis is cut into M slices of equal probability according to the statistical distribution of the i th parameter,
- compute the expected value and the variance of \mathbf{Y} for points included in each slice,
- evaluate the variation over the slices $V_{X_i}[E_{\mathbf{X} \sim i}(\mathbf{Y}|X_i)]$ of the expected value of \mathbf{Y} within each slice,
- evaluate the variance $V(\mathbf{Y})$ of \mathbf{Y} ,
- measure the first-order indices S_i with $i = 1, \dots, k$ by Equation (2.65),
- iterate the described steps above for all parameters.

More details of this method can be found in (ML13).

2.8.4 Fourier amplitude sensitivity test (FAST)

From the probability distribution of $\mathbf{Y} = f(X_1, X_2, \dots, X_k)$, the expected value can be computed from the r -th moment given by

$$\langle Y^{(r)} \rangle = \int_{\mathbb{R}^k} f^r(X_1, X_2, \dots, X_k) P(X_1, X_2, \dots, X_k) dx, \quad (2.77)$$

where P is the k -dimensional probability density for \mathbf{X} , $P(\mathbf{X}) = P(X_1, X_2, \dots, X_k)$.

The main idea of the FAST is to transform the k -dimensional integral into a one-dimensional integral by using a set of parametric equations. We employ the following transformation function (XG07)

$$X_i = F_i^{-1} \left(\frac{1}{2} + \frac{1}{\pi} \arcsin(\sin \omega_i s) \right), \quad (2.78)$$

2.8 Sensitivity analysis of model response with uncorrelated input parameters

where F_i^{-1} is the inverse cumulative distribution function (CDF) for X_i and $s \in [-\pi, \pi]$ is the parametric variable. Through the derived transformation function, $f(X_1(s), X_2(s), \dots, X_k(s))$ is transformed to a periodic function $f(s)$. If ω_i , $i = 1, \dots, 6$ are positive integers, then the period is 2π . Thus, $f(s)$ can be expanded in a Fourier series:

$$\mathbf{Y} = f(X_1, X_2, \dots, X_k) = f(s) = \sum_{n=1}^{+\infty} \{A_n \cos(ns) + B_n \sin(ns)\}, \quad (2.79)$$

where A_n and B_n are the Fourier coefficients determined by

$$\begin{aligned} A_n &= \frac{1}{2\pi} \int_{-\pi}^{\pi} f(s) \cos ns ds, \\ B_n &= \frac{1}{2\pi} \int_{-\pi}^{\pi} f(s) \sin ns ds \end{aligned} \quad (2.80)$$

For the physical problem n is limited to finite integers, $n = 1, \dots, (N-1)/2$ where N is the size of the sample (N is odd) and $(N-1)/2$ is determined by the Nyquist critical frequency, see (STC99).

Let $S = \{s_1, s_2, \dots, s_j, \dots, s_N\}$ denote the parametric variable with $s_j = -\pi + \pi/N + (2\pi/N)(j-1)$, $j = 1, 2, \dots, N$. The sample values for each parameter are obtained using the transformation function given in Equation (2.78)

$$\mathfrak{X}_i = \{x_{1i}, x_{2i}, \dots, x_{ji}, \dots, x_{Ni}\}, \quad (2.81)$$

Subsequently, the model is evaluated N times on the transformed sample values

$$f(s_j) = f(X_1(s_j), X_2(s_j), \dots, X_k(s_j)). \quad (2.82)$$

The Fourier coefficients A_n and B_n in terms of discretized expressions are

$$\begin{aligned} A_n &= \frac{1}{N} \sum_{j=1}^N f(s_j) \cos ns_j, \\ B_n &= \frac{1}{N} \sum_{j=1}^N f(s_j) \sin ns_j \end{aligned} \quad (2.83)$$

The variance of the model output is approximated by summing the spectrum of the Fourier series expansion.

$$V(\mathbf{Y}) = 2 \sum_{n=1}^{(N-1)/2} (A_n^2 + B_n^2), \quad (2.84)$$

2.8 Sensitivity analysis of model response with uncorrelated input parameters

Evaluating the spectrum A_n and B_n for the fundamental integer frequency ω_i and its higher harmonics $p\omega_i$, the partial variance contributed by X_i can be estimated by

$$V_i(\mathbf{Y}) = 2 \sum_{p=1}^M (A_{p\omega_i}^2 + B_{p\omega_i}^2), \quad (2.85)$$

with M being the inference factor. The minimum sample size is selected as

$$N = 2M\omega_{max} + 1, \quad (2.86)$$

where ω_{max} is the largest frequency among the set of ω_i frequencies. The selection of the frequency set for all parameters in order to avoid inference effect is discussed in detail in (CLS78).

At last, the normalized sensitivity measure $S_i^{FAST} = V_i/V$ is the main effect of X_i on \mathbf{Y} .

2.8.5 Extended Fourier amplitude sensitivity test (EFAST)

Saltelli *et al.* (STC99) proposed an extended FAST method (EFAST) to estimate the total-effect sensitivity index for parameter X_i , $i = 1, 2, \dots, k$ in Equation (2.67).

The total-effect S_{T_i} is obtained by assigning a certain frequency ω_i for the i th parameter and a different frequency $\omega_{\sim i}$ for the complementary set of the i th parameter including all the remaining parameters. Hence, we can estimate the partial variance $V_{\sim i}(\mathbf{Y})$ by evaluating the spectrum at the frequency $\omega_{\sim i}$ and its higher harmonics $p\omega_{\sim i}$. Similarly, the partial variance $V_i(\mathbf{Y})$ and total variance $V(\mathbf{Y})$ are obtained by Equations (2.85) and (2.84), respectively. The total-effect S_{T_i} is then obtained from Equation (2.67).

The maximum allowable frequency for the complementary set is given by $\max\{\omega_{\sim i}\} = (1/M)(\omega_i/2)$.

For the EFAST method, a transformation, G_i , has been adopted (CST97):

$$X_i = F_i^{-1} \left(\frac{1}{2} + \frac{1}{\pi} \arcsin(\sin(\omega_i s + \varphi_i)) \right) \quad (2.87)$$

where φ_i is a random phase-shift chosen uniformly in $[0, 2\pi)$. Figure 2.16 illustrates the difference between the transformations in Equations (2.78) and (2.87).

In the resampling scheme, the sample size given in Equation (2.86) must be redefined as

$$N_s = (2M\omega_{max} + 1)N_r \quad (2.88)$$

where N_r denotes the number of used curves and $\omega_{max} = \max\{\omega_i, \omega_{\sim i}\}$.

2.8 Sensitivity analysis of model response with uncorrelated input parameters

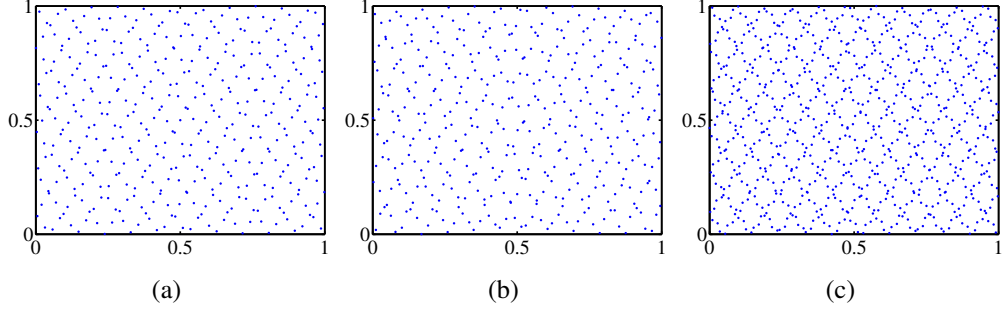


Figure 2.16: Scatter plots of sampling points in a two-parameters case obtained from the transformation given by: (a) Equation (2.78), (b) Equation (2.87), $N_r = 1$, (c) Equation (2.87), $N_r = 2$.

2.8.6 Random balance design method

In the random balance design (RBD) method (TGM06) N design points are selected over a curve in the input space of the same frequency ω , which is arbitrary integer, usually equal to 1 for simplicity. An independent variable s is sampled over $(-\pi, \pi)$ using N points. Transform s_i into X_i by using a set of parametric equations similar to Equation (2.78):

$$X_i(s_{ji}) = F_i^{-1} \left(\frac{1}{2} + \frac{1}{\pi} \arcsin(\sin \omega_i s_{ji}) \right), \quad i = 1, 2, \dots, k; j = 1, 2, \dots, N. \quad (2.89)$$

where F_i^{-1} is the inverse CDF for X_i , $\{s_{1i}, s_{2i}, \dots, s_{Ni}\}$ denotes the i th random permutation of the N points.

We evaluate the model output at each of N design points

$$Y(s_j) = f(X_1(s_{j1}), X_2(s_{j2}), \dots, X_k(s_{jk})). \quad (2.90)$$

Subsequently, we reorder $Y(s_j)$ so that $X_i(s_{ji})$ is in increasing order. The Fourier spectrum of the re-ordered $Y(s_j)$, denoted by $Y^R(s_j)$, is evaluated at low frequencies $\{\omega, 2\omega, \dots, M\omega\}$ where M is the inference factor (usually 4 or higher)

$$F(\omega) = \frac{1}{\pi} \sum_{j=1}^N Y^R(s_j) \exp(-i \text{Im} k \omega s_j) \quad (2.91)$$

evaluated at $\omega = 1$ and its higher harmonics (in our case $\omega = 2, \omega = 3, \dots$) up to order $M = 6$.

2.8 Sensitivity analysis of model response with uncorrelated input parameters

In the discrete case,

$$\hat{V}_i = V[E(\mathbf{Y}|X_i)] = \sum_{l=1}^M F(\omega)|_{w=l} = \sum_{l=1}^M F(l). \quad (2.92)$$

The first-order sensitivity index S_i is determined via the estimator V_i known as the nominator of the main effect for the i th parameter.

2.8.7 Effective algorithm for sensitivity indices

2.8.7.1 First-order sensitivity indices

According to Plischke (Pli10) the EASI algorithm can be considered as an inverse of the RBD method in section 2.8.6, as a random permutation of coordinates of given design points is taken directly. A sorting-and-shuffling strategy over such points was used to approximate the transformation in Equation (2.89).

Based on the computational model $\mathbf{Y} = f(X_1, X_2, \dots, X_k)$, we assume that x is the i th column (X_i) of the input matrix \mathbf{X} , $\mathbf{X} = (x_{ji})_{j=1, \dots, N, i=1, \dots, k}$. The sorting-and-shuffling strategy is summarized as follows

- Order vector $x = (x_j)$ to obtain an ordered vector $(x_{(j)})$ whose entries are in increasing order, $x_{(1)} \leq x_{(2)} \leq \dots \leq x_{(N)}$,
- reorder the vector $(x_{(j)})$ such that the entries $x_{[j]}$ with the odd indices are increasing followed by those with the decreasing even indices,

$$x_{[j]} = \begin{cases} x_{(2j-1)}, & j \leq \frac{N+1}{2}, \\ x_{(2(N+1-j))}, & j > \frac{N+1}{2}, \end{cases} \quad j = 1, 2, \dots, N, \quad (2.93)$$

for which the entries follow the zig-zag relation

$$x_{[j]} \leq x_{[j+1]} \quad \text{if} \quad j \leq \frac{N+1}{2}, \quad x_{[j]} \geq x_{[j+1]} \quad \text{if} \quad j > \frac{N+1}{2}. \quad (2.94)$$

The k -parametric model (scalar output) $y = f(x_1, x_2, \dots, x_i, \dots, x_k)$ is then evaluated at each design point. Subsequently, the model output \mathbf{Y} is reordered such that the design points satisfy the zig-zag relation, so-called triangular-shaped vector, shown in Equation (2.93). Figure 2.17 illustrates the reordering process for 50 uniformly distributed sample points.

If we denote the permutation forming the triangular-shaped vector $(x_{[j]})$ from (x_j) by $\pi((x_j)) = (x_{[j]})$, the Fourier spectrum is then evaluated at the frequency $\omega =$

2.8 Sensitivity analysis of model response with uncorrelated input parameters

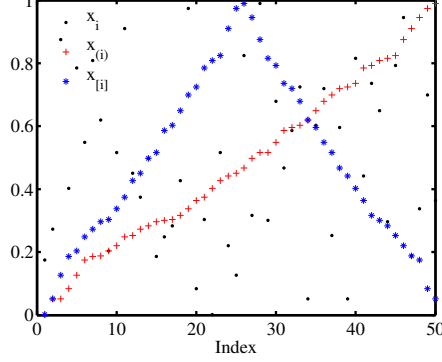


Figure 2.17: Sorting-and-shuffling strategy.

1 and its higher harmonics of the permuted output $\pi(y)$ yields the estimate of the sensitivity index of parameter X_i . If $c_m = \sum_{\kappa=1}^N (\pi(y)) \kappa \eta_N^{(\kappa-1)}$, $\eta_N = e^{-2\pi j/N}$, $m = 0, \pm 1, \pm 2, \dots, \pm[N/2]$ are the complex coefficients of the discrete Fourier transform of $\pi(y)$, the first order sensitivity index is estimated by

$$\hat{S}_i = \frac{\sum_{m=1}^M |c_m|^2 + |c_{-m}|^2}{\sum_{m \neq 0} |c_m|^2} = 2 \frac{\sum_{m=1}^M |c_m|^2}{\sum_{m \neq 0} |c_m|^2}, \quad (2.95)$$

where the maximum harmonic M is usually 4 or 6.

2.8.7.2 Higher order effects

Let us split the input matrix \mathbf{X} into $\mathbf{X}' = (x_{ji})_{j=1, \dots, N, i \in I}$ and $\bar{\mathbf{X}} = (x_{ji})_{j=1, \dots, N, i \notin I}$ where group I of dimensionality l ($l \leq k$), includes the random vector $(X_{i_1}, \dots, X_{i_l})$ with $i_j \in I$ and an $k - l$ dimensional random vector of the remaining parameters X_j , $i_j \in I$ is included in group \hat{I} .

The sensitivity index S_I of an index group I for the model $y = f(x^I, x^{\hat{I}})$ can be estimated based on the index-assignment strategy (Pli10) that is summarized as follows:

- Construct an index table for l -dimensional row of matrix \mathbf{X}' via the plough-track curve.
- Reshape the matrix \mathbf{X}' w.r.t. the index table constructed above to obtain the matrix $(\mathbf{X}'_{(j)})$
- Transform the matrix $(\mathbf{X}'_{(j)})$ to the matrix $(\mathbf{X}'_{[j]})$ such that its entries satisfy the triangle-shaped form (zig-zag relation).

2.9 Sensitivity analysis of model response with correlated input parameters

- If the permutation of coordinates of $(\mathbf{X}'_{[j]})$ denoted by $\pi(\mathbf{X}') = (\mathbf{X}'_{(j)})$, evaluate the Fourier spectrum of the reshaped $\pi(\mathbf{Y})$ at the fundamental and its higher frequencies.

The frequencies contributing to the sensitivity index S_I are listed as

$$\Omega_I = \{\pm m_1\omega_1 \pm m_2\omega_2 \dots \pm m_l\omega_l, m_i \in \{1, 2, \dots, M\}\}. \quad (2.96)$$

The first order of group I , S_I , using the complex coefficients c_m of a discrete Fourier transform of the reshaped output vector $\pi(\mathbf{Y})$ is evaluated by

$$\hat{S}_I = \frac{\sum_{m \in \Omega_I} |c_m|^2}{\sum_{m \neq 0} |c_m|^2}. \quad (2.97)$$

The estimate of the total effects (the accumulated effect of all indexed parameters in group I), based on the the frequency set Ω_I which is augmented by frequency components from the subsets of I , $\Omega_{TI} = \cup_{J \subset I} \Omega_J$, is given by

$$S_{TI} = \sum_{i \in I} S_i + \sum_{i, j \in I, i < j} S_{ij} + \sum_{i, j, k \in I, i < j < k} S_{ijk} + \dots \quad (2.98)$$

The set Ω_{TI} contains all frequencies from 1 up to $M(P^l - 1)/(P - 1)$ if the basic frequency P is equal to $2M + 1$. Therefore, the total effects is evaluated by summing over the first few Fourier coefficients of $\pi(\mathbf{Y})$.

2.9 Sensitivity analysis of model response with correlated input parameters

2.9.1 Correlated input parameters

In probabilistic models, the most common measure of correlation in statistics is the Pearson correlation, which shows the linear relationship between two input parameters. For two random inputs, X_i and X_j , the correlation coefficient, ρ_{ij} , is calculated by:

$$\rho_{ij} = \frac{Cov(X_i, X_j)}{\sigma_{X_i} \sigma_{X_j}} \quad (2.99)$$

The covariance $Cov(X_i, X_j)$ between X_i, X_j is derived by:

$$Cov(X_i, X_j) = E[(X_i - \bar{X}_i)(X_j - \bar{X}_j)] \quad (2.100)$$

2.9 Sensitivity analysis of model response with correlated input parameters

where \bar{X}_i , \bar{X}_j and σ_{X_i} , σ_{X_j} are means and standard deviations of X_i and X_j , respectively. The covariance matrix $C_{\mathbf{X}\mathbf{X}}$ for a set of random input parameters \mathbf{X} is given by:

$$C_{\mathbf{X}\mathbf{X}} = E[(\mathbf{X} - \bar{\mathbf{X}})(\mathbf{X} - \bar{\mathbf{X}})^T], \quad (2.101)$$

with $\bar{\mathbf{X}}$ being the mean of \mathbf{X} and $E(\cdot)$ is the expectation of (\cdot) . By assuming the input parameters are linearly correlated, the correlated part of an input parameter X_i can be represented in term of a linear combination of the remaining input parameters of $\mathbf{X}_{\sim i}$. The details will be discussed in the following section.

2.9.2 Improvements of Fourier amplitude sensitivity test to models with correlated parameters (IFAST)

For models with correlated parameters, the variance of the model output due to a parameter of interest results not only from variations of the parameter itself but also from the variations of other parameters. Xu and Gertner (XG07) proposed an extension of FAST to models with correlated parameters. The characteristic frequency of a parameter is exploited to capture both the uncertainties of the parameter itself and the dependent variations of other parameters. FAST for models with correlated parameters can be implemented as follows:

- Generate a sample for a parametric variable s , $S = \{s_1, s_2, \dots, s_j, \dots, s_N\}$; s_j was derived in section 2.8.4 and N is the minimum sample size introduced by Equation (2.86).
- Define a set of different frequencies ω_i associated with each parameter. The sample values of each parameter (\aleph_i) are obtained by applying the search curve specified by Equation (2.78) on sample S .
- Employ the Iman and Conover's method (IC82) to induce the desired correlation among input parameters by reordering the independent sample values \aleph_i ($i = 1, \dots, k$).
- The model output is then evaluated at each sample value.
- Subsequently, the model output is reordered w.r.t. the original sample order (i.e., the order before reordering the independent sample values) of the parameter of interest. In this way, the characteristic frequency for the parameter is restored.
- Based on the reordered output we apply Equations (2.84) and (2.85) to evaluate the partial variances (V_i) and the total variance V , respectively. The sensitivity indices S_i^{IFAST} for each parameter is estimated by V_i/V .

2.9 Sensitivity analysis of model response with correlated input parameters

Figure 2.18 shows the search curves for linear two-dimensional model $Y = 2X_1 + 3X_2$, where X_1 and X_2 are standard normally distributed with a positive correlation ($\rho_{12} = 0.7$). Fundamental frequency of 5 and 23 are assigned to X_1 and X_2 , respectively.

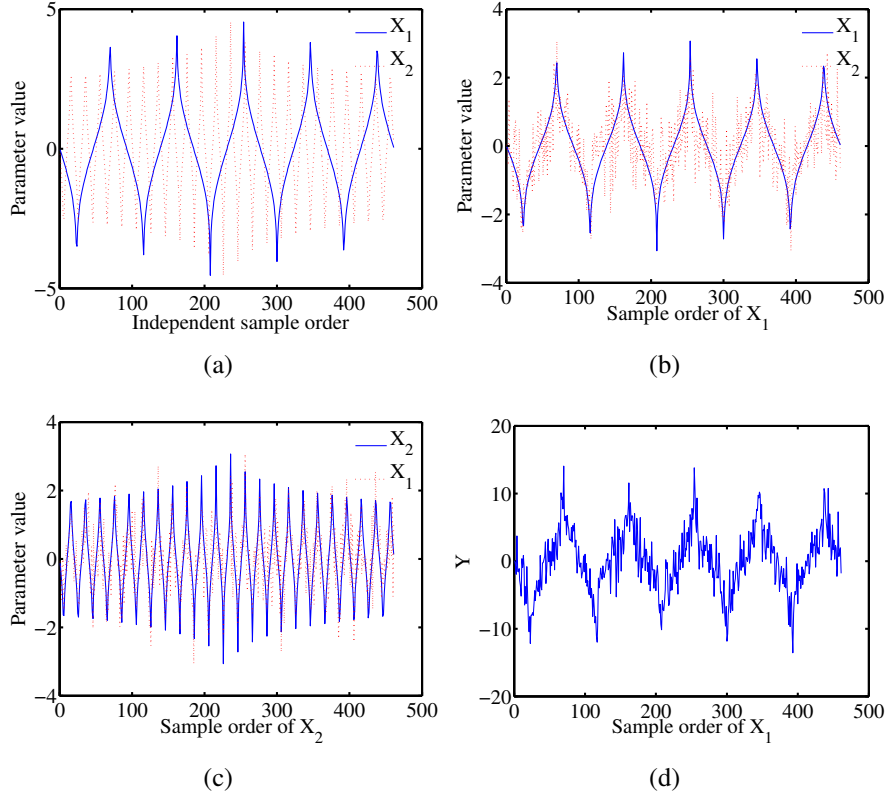


Figure 2.18: (a) Conventional independent FAST sample; (b) reordered sample values based on X_1 's original sample order; (c) reordered sample values based on X_2 's original sample order; and (d) response values from the reordered sample (based on X_1 's original sample order).

2.9.3 Variance decomposition by regression with correlated input

Xu and Gertner (XG08) proposed a method by decomposing the variance V_i into two components: the partial variance V_i^U due to uncorrelated variations and the partial variance V_i^C due to correlated variations of the i th input parameter.

$$V_i = V_i^U + V_i^C. \quad (2.102)$$

2.9 Sensitivity analysis of model response with correlated input parameters

The partial variance V_i is derived by regressing the model Y only on X_i

$$Y = \theta_0 + \theta_i X_i + e, \quad (2.103)$$

where θ_0 and θ_i are regression coefficients of the linear regression model and e represents the error. The partial variance V_i can be estimated as follows:

$$\hat{V}_i = \frac{1}{N-1} \sum_{j=1}^N \left(\hat{Y}_j^{(i)} - \bar{Y} \right)^2, \quad (2.104)$$

where $\hat{Y}_j^{(i)}$ is the value of the response surface \hat{Y} of sample j .

To determine the uncorrelated partial variance V_i^U , the input parameter is decomposed into a correlated part \hat{X}_i and an uncorrelated part \hat{Z}_i . A regression model w.r.t. \hat{Z}_i is derived by

$$Y = r_0 + r_i \hat{Z}_i + e, \quad (2.105)$$

where r_0 and r_i are regression coefficients and \hat{Z}_i is the estimated residual from the regression of X_i over all other parameters X_{j_s} ($j_s \neq i$)

$$\hat{Z}_i = X_i - \hat{X}_i = \left(\hat{\eta}_0 + \sum_{j_s \neq i} \hat{\eta}_{j_s} X_{j_s} \right), \quad (2.106)$$

$\hat{\eta}_0$ and $\hat{\eta}_{j_s}$ being the least-square estimation as discussed in (XG08).

The uncorrelated partial variance can be obtained by

$$\hat{V}_i^U = \frac{1}{N-1} \sum_{j=1}^N \left(\hat{Y}_j^{(-i)} - \bar{Y} \right)^2, \quad (2.107)$$

with $\hat{Y}_j^{(-i)} = \hat{\eta}_0 + \hat{\eta}_i \hat{Z}_{ij}$. The factors $\hat{\eta}_0$ and $\hat{\eta}_i$ are least-square estimates of r_0 and r_i in the regression of Equation (2.105).

Based on Equation (2.102), the correlated partial variance is estimated by the following equation:

$$\hat{V}_i^C = \hat{V}_i - \hat{V}_i^U. \quad (2.108)$$

The sensitivity indices can easily be determined by:

$$\hat{S}_i = \frac{\hat{V}_i}{\hat{V}}, \quad \hat{S}_i^U = \frac{\hat{V}_i^U}{\hat{V}}, \quad \hat{S}_i^C = \frac{\hat{V}_i^C}{\hat{V}} \quad (2.109)$$

with \hat{V} as total uncertainty of the model output.

2.9 Sensitivity analysis of model response with correlated input parameters

2.9.4 Sampling from the conditional distribution (reordering)

In order to extend the original approach for the correlated input parameters, the parameters of $X_{\sim i}$ are resampled while keeping X_i fixed for the estimation of $V_{X_i}(E_{\mathbf{X}_{\sim i}}(\mathbf{Y}|X_i))$. The sampling of parameters of $\mathbf{X}_{\sim i}$ should be done w.r.t. the joint probability distribution of \mathbf{X} together with the fixed samples of X_i . Hence, the sampling of $\mathbf{X}_{\sim i}$ conditioning over X_i is required.

It can be shown that if X_i is the first variable in the random vector \mathbf{X} , only the samples in the uncorrelated space have to be modified and transformed to the original space. From this beneficial relation, the matrix approach is performed by (MSR10) according to the following algorithm:

1. Reorder the random vector \mathbf{X} so that a specific random variable X_i is the first random variable in the reordered $\tilde{\mathbf{X}}$,
2. A vector of standard normally distributed random variables $\tilde{\mathbf{Z}} = [\tilde{Z}_1, \tilde{Z}_2, \dots, \tilde{Z}_k]^T$ is obtained by the marginal transformation of the original random vector $\tilde{\mathbf{X}}$ as

$$\tilde{Z}_i = \Phi^{-1} \left[F_{\tilde{X}_i}(\tilde{X}_i) \right], \quad i = 1, \dots, k; \quad (2.110)$$

where $\Phi^{-1}(\cdot)$ is the inverse cumulative distribution function (CDF) of a standard normal random variable and $F_{\tilde{X}_i}(\cdot)$ is the CDF of \tilde{X}_i .

3. Perform the Cholesky decomposition with modified order $\mathbf{C}_{\tilde{\mathbf{Z}}\tilde{\mathbf{Z}}} = \mathbf{L}_{\tilde{\mathbf{Z}}\tilde{\mathbf{Z}}}\mathbf{L}_{\tilde{\mathbf{Z}}\tilde{\mathbf{Z}}}^T$ to transform the sampling matrices \mathbf{A} and \mathbf{B} to the reordered uncorrelated $\mathbf{A}_{\tilde{\mathbf{U}}}$ and $\mathbf{B}_{\tilde{\mathbf{U}}}$ in standard normal space $\tilde{\mathbf{U}}$;
4. A modified $\mathbf{C}_{\tilde{\mathbf{U}}_1}$ is assembled and transformed back to $\tilde{\mathbf{C}}_1$ in the original space;
5. Finally the first-order indices can be computed by Equations (2.69) and (2.71).

More details of this method can be found in (MSR10).

2.9.5 Extension of the matrix combination approach

In order to calculate the correlated first-order and total-effect indices, the samples of X_i and all correlated parts of all input parameters but X_i , $\mathbf{X}_{\sim i}$, have to be modified w.r.t. X_i . Both matrices \mathbf{A} and \mathbf{B} are transformed to the correlated standard normal space by the marginal transformations under the assumption the model is a linear correlation in the standard normal space as shown by (Mos12)

$$\mathcal{A}_{ml} = \Phi^{-1} [F_{X_i}(A_{ml})], \quad \mathcal{B}_{ml} = \Phi^{-1} [F_{X_i}(B_{ml})] \quad (2.111)$$

2.9 Sensitivity analysis of model response with correlated input parameters

where $F_{X_l}(\cdot)$ is the CDF of X_l .

By individually mapping all random variables X_l to standard normal space, we obtain a set of discrete samples \mathbf{Z} in which Z_l , $l = 1, \dots, k$ are standard normally distributed random variables. Assuming \mathbf{Z} are arranged in matrix \mathbf{A} and \mathbf{B} , a decomposition is performed in standard normal space to obtain the columns of the correlated and uncorrelated sampling matrices as:

$$\begin{aligned} \mathcal{A}_{(j)}^{C,Z_i} &= \rho(Z_i, Z_j) \mathcal{A}_{(i)}, & \mathcal{A}_{(j)}^{U,Z_i} &= \mathcal{A}_{(j)} - \mathcal{A}_{(j)}^{C,Z_i}, & i, j &= 1, \dots, k \\ \mathcal{B}_{(j)}^{C,Z_i} &= \rho(Z_i, Z_j) \mathcal{B}_{(i)}, & \mathcal{B}_{(j)}^{U,Z_i} &= \mathcal{B}_{(j)} - \mathcal{B}_{(j)}^{C,Z_i}, & i, j &= 1, \dots, k. \end{aligned} \quad (2.112)$$

Now a modified matrix $\tilde{\mathcal{C}}_i^C$ combining the uncorrelated part of \mathcal{B} w.r.t. Z_i with the correlated part of \mathcal{A} can be obtained.

$$\tilde{\mathcal{C}}_i^C = \mathbf{c}_i^{C,Z_i} = \mathcal{B}^{U,Z_i} + \mathcal{A}^{C,Z_i} \quad (2.113)$$

The matrix $\tilde{\mathcal{C}}_i^C$ is transformed into the original space by means of the inverse CDF

$$\tilde{\mathcal{C}}_{i,ml}^C = F_{X_l}^{-1} \left[\Phi(\tilde{\mathcal{C}}_{i,ml}^C) \right]. \quad (2.114)$$

Note that $\tilde{\mathcal{C}}_i^C$ follows the original joint probability distribution of \mathbf{X} .

In order to obtain the uncorrelated first-order and total-effect indices, we decompose the matrices \mathcal{A} and \mathcal{B} w.r.t. $\mathbf{X}_{\sim i}$ as

$$\begin{aligned} \mathcal{A}_{(j)}^{U,Z_{\sim i}} &= \mathcal{A} - \mathcal{A}^{C,Z_{\sim i}}, & \mathcal{A}_{(j=i)}^{C,Z_{\sim i}} &= \sum_{m=1, m \neq i}^k \beta_{Z_i, m} \mathcal{A}_{(m)}, & \mathcal{A}_{(j \neq i)}^{C,Z_{\sim i}} &= \mathcal{A}_{(j)}, \\ \mathcal{B}_{(j)}^{U,Z_{\sim i}} &= \mathcal{B} - \mathcal{B}^{C,Z_{\sim i}}, & \mathcal{B}_{(j=i)}^{C,Z_{\sim i}} &= \sum_{m=1, m \neq i}^k \beta_{Z_i, m} \mathcal{B}_{(m)}, & \mathcal{B}_{(j \neq i)}^{C,Z_{\sim i}} &= \mathcal{B}_{(j)}, \end{aligned} \quad (2.115)$$

$$\tilde{\mathcal{C}}_i^U = \mathbf{c}_i^{U,Z_{\sim i}} = \mathcal{A}^{U,Z_{\sim i}} + \mathcal{B}^{C,Z_{\sim i}}. \quad (2.116)$$

The resulting $\tilde{\mathcal{C}}_i^U$ contains the uncorrelated part w.r.t. Z_i of matrix \mathcal{A} and the correlated part w.r.t. $\mathbf{Z}_{\sim i}$ of matrix \mathcal{B}

$\tilde{\mathcal{C}}_i^U$ is transformed back similarly with the correlated part using the Equation (2.114) in order to obtain $\tilde{\mathcal{C}}_i^U$ in original space.

The first-order and total-effect indices of the correlated and uncorrelated parts can be calculated using Equations (2.69) and (2.71).

2.9 Sensitivity analysis of model response with correlated input parameters

2.9.6 Extension for regression based indices

As presented in (Mos12), the first-order index of a single parameter including all correlated parts of other parameters can be estimated by using the one-dimensional coefficient of determination (COD). The first-order indices are estimated in the standard normal space by using a matrix \mathcal{Z} containing the training points of the regression as follows:

$$\hat{S}_i^{R,C} = R_{\mathcal{Z},Z_i}^2, \quad i = 1, \dots, k. \quad (2.117)$$

The estimate for the total-effect indices quantifies the partial variance contributed by uncorrelated variations Z_i^U of parameter Z_i

$$\hat{S}_{T_i}^{R,U} = R_{\mathcal{Z},\mathcal{Z}}^2 - R_{\mathcal{Z},Z_i}^2. \quad (2.118)$$

Employing Equation (2.112), we decompose the sampling matrix \mathcal{Z} into the correlated and uncorrelated part w.r.t. Z_i . Then, the correlated total-effect indices contribution of parameter Z_i can be estimated based on the reduced model containing the uncorrelated part of the samples Z^{U,Z_i}

$$\hat{S}^{R,U} T_i = R_{\mathcal{Z},\mathcal{Z}}^2 - R_{\mathcal{Z}^{U,Z_i},Z_i}^2. \quad (2.119)$$

In order to estimate the uncorrelated first-order indices of the parameter Z_i w.r.t. all other parameters, Equation (2.115) is used to calculate the uncorrelated part of the i th column of the sample matrix \mathcal{Z}

$$\hat{S}_i^{R,U} = R_{\mathcal{Z}^{U,Z_i},Z_i}^2. \quad (2.120)$$

2.9.7 Extension of Sobol' approach for models with correlated inputs (ESACIs)

Let us consider a k -parametric computational model $f(X_1, X_2, \dots, X_k)$, with an input vector $\mathbf{X} = (X_1, \dots, X_k)$. If we split the input vector \mathbf{X} into a group of interest $y = (X_{i_1}, \dots, X_{i_s})$, $1 \leq i_s < k$ and a complementary group $z = (X_{i_s+1}, \dots, X_k)$, then the total variance of $f(X_1, X_2, \dots, X_k)$ can be expressed as

$$V = V_y[E_z f(y, \bar{z})] + E_y[V_z(f(y, \bar{z}))]. \quad (2.121)$$

The associated first-order and total-effect indices of the group y are

$$S_y = \frac{V_y[E_z(f(y, \bar{z}))]}{V} \quad (2.122)$$

2.9 Sensitivity analysis of model response with correlated input parameters

$$S_{Ty} = \frac{E_y[V_z(f(\bar{y}, z))]}{V} \quad (2.123)$$

where z and \bar{z} are random vectors generated from a joint PDF $p(y, z)$ and from a conditional probability distribution $p(y, \bar{z}|y)$, respectively. According to Kucherenko *et al.* (KTA12), the first-order index is given by:

$$S_y = \frac{1}{V} \left[\int_{\mathbb{R}^s} p(y) dy \left[\int_{\mathbb{R}^{k-s}} f(y, \bar{z}) p(y, \bar{z}|y) d\bar{z} \right]^2 - f_0^2 \right]. \quad (2.124)$$

with $p(y)$ being a marginal distribution; f_0^2 is computed by Equation (2.70) and Equation (2.124) can be written as

$$S_y = \frac{1}{V} \left[\int_{\mathbb{R}^s} p(y) dy \left[\int_{\mathbb{R}^{k-s}} f(y, \bar{z}) p(y, \bar{z}|y) d\bar{z} \int_{\mathbb{R}^{k-s}} f(y, \bar{z}') p(y, \bar{z}'|y) d\bar{z}' \right] - f_0^2 \right], \quad (2.125)$$

with (y, z) and (y', z') being two different random vectors generated from the joint PDF $p(y, z)$. In order to apply Equation (2.125), it is required to generate (1) a random vector (y, z) from the joint PDF $p(y, z)$ and (2) a random vector (y, \bar{z}') from the conditional probability distribution $p(y, \bar{z}'|y)$. Equation (2.125) can be deduced as follows:

$$S_y = \frac{1}{V} \left[\int_{\mathbb{R}^s} f(y, z) p(y, z) dy dz \left[\int_{\mathbb{R}^{k-s}} f(y, \bar{z}') p(y, \bar{z}'|y) d\bar{z}' \int_{\mathbb{R}^{k-s}} f(y', z') p(y', z') dy' dz' \right] \right]. \quad (2.126)$$

Equation (2.124) w.r.t. y' can be expressed as

$$S_y = \frac{1}{V} \left[\int_{\mathbb{R}^s} p(y') dy' \left[\int_{\mathbb{R}^{k-s}} f(y', \hat{z}) p(y, \bar{z}|y) d\bar{z} \int_{\mathbb{R}^{k-s}} f(y, \bar{z}') p(y, \bar{z}'|y) d\bar{z}' \right] - f_0^2 \right]. \quad (2.127)$$

By combining

$$S_{Ty} = V - V_z[E_y(f(\bar{y}, z))], \quad (2.128)$$

with Equation (2.125), we finally obtain the explicit formula for S_{Ty}

$$S_{Ty} = \frac{1}{2V} \int_{\mathbb{R}^{k+s}} [f(y, z) - f(\bar{y}', z)]^2 p(y, z) p(\bar{y}', z|z) dy d\bar{y}' dz. \quad (2.129)$$

For practical applications, an MC algorithm has been used to estimate S_y and S_{Ty} numerically.

2.9 Sensitivity analysis of model response with correlated input parameters

2.9.8 Variance-based sensitivity indices for models with correlated inputs (VBCIs)

In this subsection, we apply a variance-based sensitivity indices for models with correlated parameters as suggested by Mara *et al.* (MT12). The sensitivity indices are computed based on the new set of independent parameters after decorrelating the input parameters.

2.9.8.1 Dependences among random inputs

Let us recall the following relationship for three dependent inputs:

$$p(X_1, X_2, X_3) = p(X_1)p(X_2|X_1)p(X_3|X_1, X_2). \quad (2.130)$$

where $p(X_1, X_2, X_3)$ is the joint PDF; $p(X_1)$, $p(X_2|X_1)$ and $p(X_3|X_1, X_2)$ denote the marginal PDF of X_1 , the marginal PDF of X_2 conditioned on X_1 and the marginal PDF of X_3 conditioned on $\{X_1, X_2\}$, respectively.

If we set

$$X_{2-1} = X_2 - E[X_2|X_1], \quad X_{3-12} = X_3 - E[X_3|X_1, X_2], \quad (2.131)$$

then, we can write

$$p(X_1, X_2, X_3) = p(X_1)p(X_{2-1})p(X_{3-12}). \quad (2.132)$$

Alternatively, $\{X_1, X_{2-1}, X_{3-12}\}$ is a set of independent random inputs.

2.9.8.2 Orthogonalization of the correlated inputs

Let us consider a set of standardized correlated random parameters \mathbf{X} . A set of orthogonal parameters is derived by

$$\bar{X}_1 = X_1, \quad (2.133a)$$

$$\bar{X}_i = X_i - E[X_i|X_1, \dots, X_{i-1}], \quad \forall i = 2, \dots, k. \quad (2.133b)$$

Subsequently, we use the ANOVA decomposition (Sob93) to estimate the sensitivity indices of the new input parameters such as the first-order index \bar{S}_i due to \bar{X}_i , the second-order index \bar{S}_{ij} due to the pairs of parameters \bar{X}_i and \bar{X}_j , etc.

2.10 Sensitivity analysis based on coefficients of determination

2.9.8.3 Interpretation of the sensitivity indices

For the ease of notation, we note $\bar{X}_1 = X_1$, $\bar{X}_i = X_i|X_1, \dots, X_{i-1}$, $1 < i \leq k$. Since $\bar{X}_1 = X_1$, the sensitivity indices of \bar{X}_1 are equal to those of X_1 : $\bar{S}_1 = S_1$ and $\bar{S}_{T_1} = S_{T_1}$ are the full sensitivity indices. When $\bar{X}_2 = X_2|X_1$, the sensitivity indices of \bar{X}_2 are those of X_2 without its mutual correlated contribution with X_1 : $\bar{S}_2 = S_{2-1}$ and $\bar{S}_{T_2} = S_{T_2-1}$. For $\bar{X}_k = X_k|X_{\sim k}$, the sensitivity indices of \bar{X}_k are those of X_k without its mutual correlated contribution with $X_{\sim k}$: $\bar{S}_k = S_k^U$ and $\bar{S}_{T_k} = S_{T_k}^U$ are the uncorrelated contribution of X_k to the variance $V[f(\mathbf{X})]$. It is worth noting that

$$S_i = \frac{V[E[f(\mathbf{X})|\bar{X}_i]]}{V[f(\mathbf{X})]}, \quad S_{T_i}^U = 1 - \frac{V[E[f(\mathbf{X})|\bar{X}_{\sim i}]]}{V[f(\mathbf{X})]} \quad (2.134)$$

2.9.8.4 Computational issues

The computation of the new sensitivity indices is done in 5 steps:

1. Employ Iman and Conover's method (IC82) to generate a sample set of correlated inputs \mathbf{X} ;
2. Evaluate the model \mathbf{Y} at each sample value;
3. Decorrelate the original dependent sample using Equations (2.133a) and (2.133b) to obtain a set of independent samples;
4. Compute the new sensitivity indices of interest based on the generated independent random parameters;
5. Perform a circular permutation of the parameters and go to step 3 until the $k - th$ iteration.

2.10 Sensitivity analysis based on coefficients of determination

The COD R^2 for the full model is compared to the value $R_{p_i}^2$, which is evaluated when we remove the parameter p_i from the full regression basis. This removal will result in a measurable drop

$$\begin{aligned} \Delta R_{p_i}^2 &= R^2 - R_{p_i}^2 \\ &= R^2 ([1 \ X_1 \ X_2 \ \dots \ p_{i-1} \ p_i \ p_{i+1} \ \dots \ X_1^2 \ X_2^2 \ \dots]) \\ &\quad - R_{p_i}^2 ([1 \ X_1 \ X_2 \ \dots \ p_{i-1} \ p_{i+1} \ \dots \ X_1^2 \ X_2^2 \ \dots]) \end{aligned} \quad (2.135)$$

2.11 Partial derivatives

The values of $\Delta R_{p_i}^2$ show which parameter p_i is important. The larger the value of $\Delta R_{p_i}^2$, the more important the variable is and vice versa. We normalize the value of $\Delta R_{p_i}^2$ with the purpose of limiting the maximum value by 1. This defines a coefficient of importance

$$I_{p_i} = \frac{\Delta R_{p_i}^2}{R^2} = 1 - \frac{R_{p_i}^2}{R^2}. \quad (2.136)$$

2.11 Partial derivatives

Assume that the model output \mathbf{Y} is a scalar function of a vector $\mathbf{X} = (X_1, X_2, \dots, X_k)$ of k input parameters. Partial derivatives can be seen as a mathematical definition of the sensitivity of the model output \mathbf{Y} versus the input parameters X_i , i.e., the partial derivatives will be shown for two following cases

1) If we fix the other parameters, the partial derivatives are written by (SRA+08)

$$\begin{aligned} S_{X_i}^{pd} &= \frac{1}{N} \sum_{j=1}^N \frac{\partial \mathbf{Y}_j}{\partial X_i} \\ &= \frac{1}{N} \sum_{j=1}^N \left(\lim_{\Delta X_i \rightarrow 0} \frac{\mathbf{Y}(x_{ji} + \Delta X_i) - \mathbf{Y}(x_{ji})}{\Delta X_i} \right); \quad i = 1, \dots, k. \end{aligned} \quad (2.137)$$

2) If we vary other parameters, the partial derivatives are written as follows

$$\begin{aligned} S_{X_i}^{pda} &= \frac{1}{N^k} \sum_{j_1=1}^N \dots \sum_{j_k=1}^N \frac{\partial \mathbf{Y}_{j_i}}{\partial X_i} \\ &= \frac{1}{N^k} \sum_{j_1=1}^N \dots \sum_{j_k=1}^N \left(\lim_{\Delta X_i \rightarrow 0} \frac{[\mathbf{Y}(X_1, \dots, x_{j_i i} + \Delta X_i, \dots, X_k) - \mathbf{Y}(X_1, \dots, x_{j_i i}, \dots, X_k)]}{\Delta X_i} \right); \\ & \quad i = 1, \dots, k, \quad j_i = 1, \dots, N. \end{aligned} \quad (2.138)$$

where N is the number of samples.

Computing the partial derivatives at one point \mathbf{x}_j , $j = 1, \dots, N$ is clearly a local measure of the parameter's sensitivity. Averaging different partial derivatives gives an approximation of global sensitivity measures under the assumption of no change in the sign of the derivatives at the different points.

Saltelli *et al.* (SRA+08) suggested computing these partial derivatives at a set of different points in the design space of input parameters so that an average response of

2.11 Partial derivatives

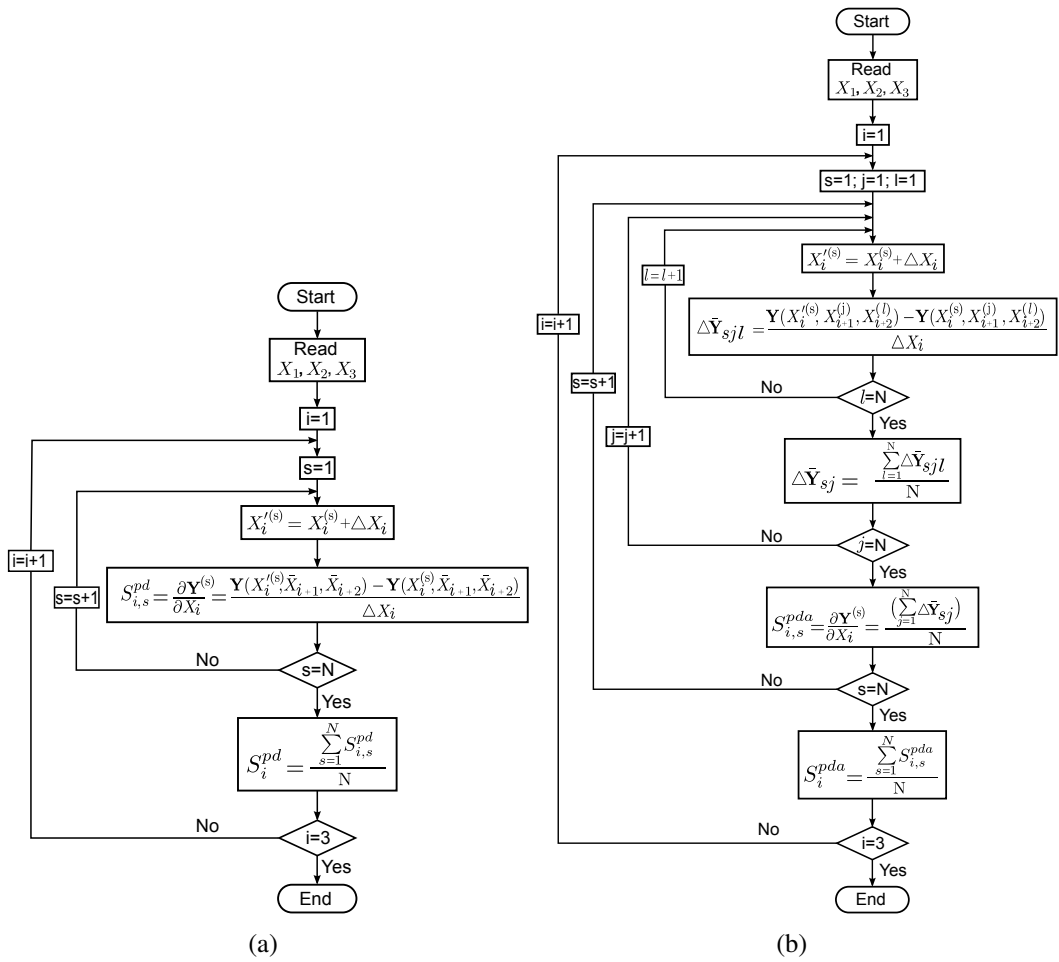


Figure 2.19: Flowchart of partial derivatives of the surrogate model output w.r.t X_i (a) when we fix the others and (b) when we vary the others.

2.12 Elementary effects

Y_j can be obtained when moving a factor X_i of a step ΔX_i at different points. Using this concept, the elementary effects method was developed where now the choice of the parameter increment follows another strategy.

2.12 Elementary effects

Consider a vector \mathbf{X} of input parameters with k components $\mathbf{X} = (X_1, X_2, \dots, X_k)$, each X_i varies in the unit across p selected levels as presented in (CB99). For a given value of \mathbf{X} in the p -level grid Ω , the elementary effects for the i -th input parameter are defined as in (SRA⁺08)

$$EE_i = \frac{[\mathbf{Y}(X_1, X_2, \dots, X_i + \Delta, \dots, X_k) - \mathbf{Y}(X_1, X_2, \dots, X_i, \dots, X_k)]}{\Delta} \quad (2.139)$$

where p is the number of levels, Δ is a preselected value in $\{1/(p-1), \dots, 1-1/(p-1)\}$ so that the transformed point $\mathbf{X} + \mathbf{e}_i \Delta$ is still in Ω for each index $i = 1, \dots, k$ and \mathbf{e}_i vector of zeros but with a unit as its i -th component.

In its simplest form, the computation of the i -th elementary effect requires the evaluation of the output \mathbf{Y} at two points \mathbf{X} and $(\mathbf{X} + \mathbf{e}_i \Delta)$. The total computation requires $n = 2rk$ model executions, where r is a number of elementary effects that shall be calculated. A more efficient sampling scheme has been suggested by Morris (Mor91) that constructs r trajectories of $(k+1)$ points in the input space $n = r(k+1)$ model executions. The performance of this method was presented in (SRA⁺08, CB99).

1. A base value \mathbf{x}^* is randomly chosen in Ω
2. We use \mathbf{x}^* to generate all trajectory points including the points $\mathbf{x}^{(g)}$, $g = 1, \dots, k+1$ (note that \mathbf{x}^* is not part of the trajectory). The first trajectory point, $\mathbf{x}^{(g)}$, is obtained by increasing one or more components of \mathbf{x}^* . The trajectory points $\mathbf{x}^{(g)}$ then is generated by $\mathbf{x}^{(g+1)} = \mathbf{x}^{(g)} + \mathbf{e}_i \Delta$ or $\mathbf{x}^{(g+1)} = \mathbf{x}^{(g)} - \mathbf{e}_i \Delta$ in such a way that $\mathbf{x}^{(g+1)}$ and $\mathbf{x}^{(g)}$ differ only in the i -th component. A detailed sampling scheme will be presented in section 2.12.1.
3. Each trajectory allows computing an elementary effect $EE_i(\mathbf{x}^{(g)})$ and the computation of the elementary effect for i -th input parameter will be presented in section 2.12.2.
4. Different base values \mathbf{x}^* can be used to generate r different trajectories. It means that the sample size of each of elementary effect is r .

2.13 Surrogate models

2.12.1 The sampling strategy for elementary effects

According to (Mor91) in the first step a $(k + 1) \times k$ sampling matrix \mathbf{B} is selected as follows:

$$\mathbf{B} = \begin{bmatrix} 0 & 0 & 0 & \dots & 0 \\ 1 & 0 & 0 & \dots & 0 \\ 1 & 1 & 0 & \dots & 0 \\ \dots & \dots & \dots & \dots & \dots \\ 1 & 1 & 1 & \dots & 1 \end{bmatrix} \quad (2.140)$$

A version of the sampling matrix is then randomly given by

$$\mathbf{B}^* = (\mathbf{J}_{k+1,k} \mathbf{x}^* + (\Delta/2))[(2\mathbf{B} - \mathbf{J}_{k+1,k})\mathbf{D}^* + \mathbf{J}_{k+1,k}] \mathbf{P}^* \quad (2.141)$$

where $\mathbf{J}_{k+1,k}$ is a $(k + 1) \times k$ of 1's; \mathbf{x}^* is a randomly selected base value of \mathbf{X} ; \mathbf{D}^* is a k -dimensional diagonal matrix in which each element laying on the main diagonal is either +1 or -1 with equal probability; \mathbf{P}^* is a $k \times k$ matrix in which columns of the identity matrix are permuted randomly, all others are 0, and no two columns have 1's in the same position. \mathbf{B}^* is called random orientation that provides one elementary effect per input.

2.12.2 The computation of the sensitivity measures

Supposing that, $\mathbf{x}^{(g)}$ and $\mathbf{x}^{(g+1)}$, with g in the set $1, \dots, k$, the elementary for i -th input parameter can be estimated along the j -th trajectory via two above sampling points as presented in (SRA⁺08)

$$EE_i^j(\mathbf{x}^{(g)}) = \frac{[\mathbf{Y}(\mathbf{x}^{(g+1)}) - \mathbf{Y}(\mathbf{x}^{(g)})]}{\Delta} \quad (2.142)$$

if the i -th component of $\mathbf{x}^{(g)}$ is increased by Δ , and

$$EE_i^j(\mathbf{x}^{(g)}) = \frac{[\mathbf{Y}(\mathbf{x}^{(g)}) - \mathbf{Y}(\mathbf{x}^{(g+1)})]}{\Delta} \quad (2.143)$$

if the i -th component of $\mathbf{x}^{(g)}$ is decreased by Δ .

2.13 Surrogate models

A surrogate model (MM02) is an approximate mechanical model, used to predict the response at a new point based on a limited amount of observed data. By employing the surrogate model, we aim to construct a continuous k -dimensional function \hat{f} of k

2.13 Surrogate models

random parameters \mathbf{x} . Both global regression (polynomial regression) and local regression using polynomials (moving least squares, etc.) or kernel functions approaches, to name a few, can be used to construct the surrogate model.

2.13.1 Polynomial regression model

Based on linear polynomial basis, $\hat{\mathbf{Y}}$ has been chosen to approximate the response of the mechanical model \mathbf{Y} of N observed data points $\mathbf{x}_j = [x_{j1}, \dots, x_{jk}]$, $j = 1, \dots, N$.

$$\hat{\mathbf{Y}} = \beta_0 + \sum_{i=1}^k \beta_i X_i + \mathbf{e}. \quad (2.144)$$

where k is the number of polynomial base functions, β are the unknown regression coefficients, e is the error term that is the difference between the approximation $\hat{\mathbf{Y}}$ and the mechanical model \mathbf{Y} . The mean square difference (residual) RSS is defined as

$$RSS = \sum_{j=1}^N (Y_j - \hat{Y}_j)^2. \quad (2.145)$$

The parameter vector $\hat{\beta}$ is determined by minimizing the mean square difference S between the value of surrogate surface $\hat{\mathbf{Y}}$ and the observed response \mathbf{Y} as presented in (Buc09)

$$\frac{\partial(RSS)}{\partial\beta_i} = 0; \quad i = 1, \dots, k \quad (2.146)$$

which, together with Equation (2.145) results in

$$\sum_{j=1}^N \left\{ X_i \left[Y_j - \sum_{i=1}^k \beta_i x_{ji} \right] \right\} = 0; \quad i = 1, \dots, k. \quad (2.147)$$

The parameter vector $\hat{\beta}$ is obtained by solving the system of linear equations

$$\mathbf{Q}\beta = \mathbf{q} \quad (2.148)$$

in which the matrix \mathbf{Q} and vector \mathbf{q} are

$$Q_{il} = \sum_{j=1}^N x_{ji} x_{jl}; \quad q_l = \sum_{j=1}^N Y_j x_{jl}; \quad i, l = 1, \dots, k \quad (2.149)$$

2.13 Surrogate models

The coefficient of determination (COD) R^2 allows an estimation of the quality of the approximation,

$$R^2 = 1 - \frac{RSS}{RSS_{tot}}, \quad 0 \leq R^2 \leq 1 \quad (2.150)$$

where the total variation S_{tot} is defined as

$$RSS_{tot} = V(\mathbf{Y}) = (\mathbf{Y} - \bar{\mathbf{Y}})^T (\mathbf{Y} - \bar{\mathbf{Y}}) \quad (2.151)$$

$\bar{\mathbf{Y}}$ is being the mean value of all Y_j ;

$$\bar{\mathbf{Y}} = \frac{1}{N} \sum_{j=1}^N (Y_j). \quad (2.152)$$

The COD can be rewritten as:

$$R^2 = 1 - \frac{\sum_{j=1}^N (Y_j - \hat{Y}_j)}{\sum_{j=1}^N (Y_j - \bar{Y})}. \quad (2.153)$$

A COD of $R^2 = 1$ means that the regression model can reproduce the response of the mechanical model exactly. To construct surrogate model connecting an alternate input-output relation R^2 should be at least larger equal 0.8.

An alternative to R^2 is the adjusted COD R_{adj}^2 . This measure additionally takes into account the number of supporting points N as well as the number of regression coefficients k_R . If N is large compared to k_R the R^2 and R_{adj}^2 provide in the limit case the same results.

$$R_{adj}^2 = 1 - \frac{RSS/(N - k_R)}{RSS_{tot}/(N - 1)} = 1 - \frac{N - 1}{N - k_R} (1 - R^2). \quad (2.154)$$

Besides the regression based on linear polynomials, higher order approaches considering quadratic terms can be applied

$$\hat{\mathbf{Y}} = \beta_0 + \beta_1 X_1 + \beta_2 X_2 + \dots + \beta_{kN} X_{kN} + \beta_{11} X_1^2 + \beta_{22} X_2^2 + \dots + \beta_{kk} X_k^2 + \mathbf{e}. \quad (2.155)$$

as well as quadratic and mixed terms

$$\begin{aligned} \hat{\mathbf{Y}} = & \beta_0 + \beta_1 X_1 + \beta_2 X_2 + \dots + \beta_k X_k + \beta_{11} X_1^2 + \beta_{22} X_2^2 + \dots \\ & + \beta_{kk} X_k^2 + \beta_{12} X_1 X_2 + \dots + \beta_{k-1k} X_{k-1} X_k + \mathbf{e} \end{aligned} \quad (2.156)$$

can be used.

2.13 Surrogate models

2.13.2 Moving least squares (MLS)

The idea of MLS is to account for a set of unorganized point samples by introducing local weighting functions $w(d)$ (LS86). At a point \mathbf{x}_m , the interpolated value $\hat{\mathbf{Y}}_{MLS}$ is written as follows

$$\hat{\mathbf{Y}}_{MLS}(\mathbf{x}_m) = \mathbf{p}^T(\mathbf{x}_m)\boldsymbol{\beta}_W. \quad (2.157)$$

where $\mathbf{p}(\mathbf{x}_m)$ is base vector evaluated at the point \mathbf{x}_m

$$\mathbf{p}^T(\mathbf{x}_m) = [1 \quad x_{m1} \quad x_{m2} \quad \dots \quad x_{m1}^2 \quad x_{m2}^2 \quad \dots \quad x_{m1}x_{m2} \quad \dots]. \quad (2.158)$$

and $\boldsymbol{\beta}_W$ contains the coefficient of the polynomial.

The coefficients are determined by a weighted least squares method minimizing the L^2 -norm error \mathbf{L}_W

$$\mathbf{L}_W = (\mathbf{Y} - \mathbf{p}^T(\mathbf{x}_m)\boldsymbol{\beta}_W)^T \mathbf{W}(\mathbf{x}_m) (\mathbf{Y} - \mathbf{p}^T(\mathbf{x}_m)\boldsymbol{\beta}_W) \quad (2.159)$$

w.r.t the unknown coefficients $\boldsymbol{\beta}_W$ yielding

$$\frac{\partial \mathbf{L}_W}{\partial \boldsymbol{\beta}_W} = 0 \rightarrow \hat{\boldsymbol{\beta}}_W = (\mathbf{X}^T \mathbf{W}(\mathbf{x}) \mathbf{X})^{-1} \mathbf{X}^T \mathbf{W}(\mathbf{x}) \mathbf{Y} \quad (2.160)$$

where $\boldsymbol{\beta}_W$ are the moving coefficients, and $\mathbf{W}(\mathbf{x})$ is the diagonal matrix

$$\mathbf{W}(\mathbf{x}_m) = \begin{bmatrix} w(\mathbf{x}_m - \mathbf{x}_1) & 0 & \dots & 0 \\ 0 & w(\mathbf{x}_m - \mathbf{x}_2) & \dots & 0 \\ \dots & \dots & \dots & \dots \\ 0 & 0 & \dots & w(\mathbf{x}_m - \mathbf{x}_N) \end{bmatrix}. \quad (2.161)$$

We use the cubic polynomial weighting function (MB05)

$$w(d) = \begin{cases} 1 - 3d^2 + 2d^3 & d \leq 1 \\ 0 & d > 1 \end{cases} \quad (2.162)$$

where $d_j = \|\mathbf{x}_m - \mathbf{x}_j\| / D$ is the normalized distance between the interpolation point and the supporting point; D is an influence radius which is constant or dependent on position \mathbf{x} ; in our examples, D is fixed.

Substituting Equation (2.160) into Equation (2.157) yields the MLS approximation

$$\hat{\mathbf{Y}}_{MLS} = \mathbf{p}^T(\mathbf{x}_m) [\mathbf{X}^T \mathbf{W}(\mathbf{x}_m) \mathbf{X}]^{-1} \mathbf{X}^T \mathbf{W}(\mathbf{x}_m) \mathbf{Y}. \quad (2.163)$$

2.13 Surrogate models

2.13.3 Hybrid algorithm

A hybrid (quadratic polynomial regression/MLS regression) model is presented in this section with the purpose of capturing the localities of global output without overfitting. This approximation model used the MLS in the dimension where the polynomial regression fails to account for. It can be written as:

$$\begin{aligned}\hat{\mathbf{Y}}_{hybrid} &= \hat{\mathbf{Y}} + \hat{\mathbf{Y}}_{MLS}(\mathbf{R}) \\ \mathbf{R} &= \left[Y_1 - \hat{Y}_1, \dots, Y_j - \hat{Y}_j, \dots, Y_N - \hat{Y}_N \right]\end{aligned}\quad (2.164)$$

It is worth mentioning that the higher order of polynomial regression model results in a more accurate approximation of the input output relationship. However, the higher order the polynomial regression model, the more flexible is the regression model. It can lead to overfitting the output of the mechanical model, see (Kar11).

2.13.4 Kriging regression

2.13.4.1 Maximum likelihood estimation

Maximum likelihood estimation (MLE) is a general technique of estimating the parameters of a statistical model. Maximum likelihood estimators provide estimates for the model parameters when applied to a data set and given a statistical model.

Let \mathbf{Y} denote the vector of observed responses under a probability density function (PDF) $P_{\mathbf{Y}}(\mathbf{Y}; \boldsymbol{\theta})$; $\boldsymbol{\theta}$ is a vector of parameters requiring estimation. The likelihood is expressed in terms of the sample data as

$$L = \frac{1}{(2\pi\sigma^2)^{N/2}\sqrt{\det(\boldsymbol{\Psi})}} \exp \left[-\frac{(\mathbf{Y} - \mathbf{1}\mu)^T \boldsymbol{\Psi}^{-1} (\mathbf{Y} - \mathbf{1}\mu)}{2\sigma^2} \right] \quad (2.165)$$

The logarithmic likelihood (ln-likelihood) function $\ln(L)$ is given by

$$\ln(L) = -\frac{N}{2} \ln(2\pi) - \frac{N}{2} \ln(\sigma^2) - \frac{1}{2} \ln|\boldsymbol{\Psi}| - \frac{(\mathbf{Y} - \mathbf{1}\mu)^T \boldsymbol{\Psi}^{-1} (\mathbf{Y} - \mathbf{1}\mu)}{2\sigma^2} \quad (2.166)$$

Taking derivatives of the ln-likelihood in Equation (2.166) w.r.t. the parameter vector and setting the resulting gradient vector to zero, we obtain the maximum likelihood estimates (MLEs) of μ and σ^2

$$\hat{\mu} = \frac{\mathbf{1}^T \boldsymbol{\Psi}^{-1} \mathbf{Y}}{\mathbf{1}^T \boldsymbol{\Psi}^{-1} \mathbf{1}}, \quad \hat{\sigma}^2 = \frac{(\mathbf{Y} - \mathbf{1}\hat{\mu})^T \boldsymbol{\Psi}^{-1} (\mathbf{Y} - \mathbf{1}\hat{\mu})}{N}, \quad (2.167)$$

2.13 Surrogate models

Substituting these MLEs back into Equation (2.166) yields the concentrated ln-likelihood function:

$$\ln(L) \approx -\frac{N}{2}\ln(\sigma^2) - \frac{1}{2}\ln|\Psi|. \quad (2.168)$$

In order to search the kriging regression model, the regression constant $\lambda > 0$ is added to the diagonal of Ψ . Therefore, μ , σ^2 and $\ln(L)$ become

$$\hat{\mu} = \frac{\mathbf{1}^T(\Psi + \lambda\mathbf{I})^{-1}\mathbf{Y}}{\mathbf{1}^T(\Psi + \lambda\mathbf{I})^{-1}\mathbf{1}}, \quad \hat{\sigma}^2 = \frac{(\mathbf{Y} - \mathbf{1}\hat{\mu})^T(\Psi + \lambda\mathbf{I})^{-1}(\mathbf{Y} - \mathbf{1}\hat{\mu})}{N}, \quad (2.169)$$

$$\ln(L) \approx -\frac{N}{2}\ln(\sigma^2) - \frac{1}{2}\ln|\Psi + \lambda\mathbf{I}| \quad (2.170)$$

The value of $\ln(L)$ depends on the unknown parameters θ_i and λ .

2.13.4.2 Kriging prediction

Given a set of sample data, $\mathbf{X} = \{\mathbf{x}_1, \mathbf{x}_2, \dots, \mathbf{x}_N\}^T$, with observed responses, $\mathbf{Y} = \{Y_1, Y_2, \dots, Y_N\}^T$, we want to find a regression model, which can filter the noise from stochastic simulations, to predict the value at a new point \mathbf{x} . The observed responses are expressed in terms of the set of random vectors as $\mathbf{Y} = \{Y(\mathbf{x}_1), Y(\mathbf{x}_2), \dots, Y(\mathbf{x}_N)\}^T$.

The correlation between elements of the vector \mathbf{Y} is described by the anisotropic exponential correlation functions:

$$\text{cor}(Y(\mathbf{x}_j), Y(\mathbf{x}_l)) = \sigma^2 \exp\left(-\sum_{i=1}^k \theta_i (x_{ji} - x_{li})^2\right), \quad j, l = 1, \dots, N. \quad (2.171)$$

where σ^2 is the variance of the response at sampled design points, and θ_i is a parameter measuring the degree of correlation among the data along the i th direction.

The correlation matrix of all the design points is constructed from Equation (2.171)

$$\Psi = \begin{pmatrix} \text{cor}(Y(\mathbf{x}_1), Y(\mathbf{x}_1)) & \cdots & \text{cor}(Y(\mathbf{x}_1), Y(\mathbf{x}_N)) \\ \vdots & \ddots & \vdots \\ \text{cor}(Y(\mathbf{x}_N), Y(\mathbf{x}_1)) & \cdots & \text{cor}(Y(\mathbf{x}_N), Y(\mathbf{x}_N)) \end{pmatrix}. \quad (2.172)$$

The parameters μ , σ^2 , $\boldsymbol{\theta}$, and λ are estimated such that the ln-likelihood given by Equation (2.170) is maximized. A global search method such as a genetic algorithm (GA) usually is employed to produce the best values for these parameters (FSK 1).

2.13 Surrogate models

Once the model parameters have been estimated, the value at a new point is evaluated by first defining a vector of correlations between the observed data and our new prediction

$$\boldsymbol{\psi} = \begin{pmatrix} \text{cor}(Y(\mathbf{x}_1), Y(\mathbf{x})) \\ \vdots \\ \text{cor}(Y(\mathbf{x}_N), Y(\mathbf{x})) \end{pmatrix} = \begin{pmatrix} \psi_1 \\ \vdots \\ \psi_N \end{pmatrix}. \quad (2.173)$$

and then employing the derived Kriging regression to predict the new values

$$\hat{Y}(\mathbf{x}) = \hat{\mu} + \boldsymbol{\psi}^T (\boldsymbol{\Psi}^{-1} + \lambda \mathbf{I})^{-1} (\mathbf{Y} - \mathbf{1}\hat{\mu}). \quad (2.174)$$

2.13.5 Nonparametric regression model

2.13.5.1 Cross-Validation

As presented by Ruppert *et al.* (RWC62), the residual sum of squares is one of the most common measures for the "good-ness of fit" of a regression curve to a scatterplot

$$RSS = \sum_{j=1}^N (Y_j - \hat{Y}_j)^2 = \|\mathbf{Y} - \hat{\mathbf{Y}}\|^2. \quad (2.175)$$

Let $\hat{f}(x; \alpha)$ denote the nonparametric regression estimator at a point x with smoothing parameter α . Then, we can rewrite the RSS in Equation (2.175) as

$$RSS(\alpha) = \sum_{j=1}^N \{Y_j - \hat{f}_{-j}(x_j; \alpha)\}^2. \quad (2.176)$$

The CV criterion is derived as

$$CV(\alpha) = \sum_{j=1}^N \{Y_j - \hat{f}_{-j}(x_j; \alpha)\}^2, \quad (2.177)$$

where \hat{f}_{-j} denotes the nonparametric regression estimator applied to the data with (x_j, Y_j) omitted. Cross-validation (CV) is used to find the optimum smoothing parameter of kernel regression; $\hat{\alpha}_{CV}$ being a CV choice of α that minimizes $CV(\alpha)$ for $\alpha \geq 0$.

For computational efficiency, we have employed the generalized cross-validation (GCV) (HdH85).

$$GCV(\alpha) = \frac{RSS(\alpha)}{\{1 - df_{fit}(\alpha)/N\}^2}. \quad (2.178)$$

The smoothing parameter $\hat{\alpha}_{GCV}$ is obtained by minimizing Equation (2.178).

2.13 Surrogate models

2.13.5.2 Penalized spline regression

Let us consider a general spline model with K knots. We use the truncated power basis of degree \wp , $[1, x, \dots, x^\wp, (x - \kappa_1)_+^\wp, \dots, (x - \kappa_K)_+^\wp]$ with knots at $\kappa_1, \dots, \kappa_K$. The spline model is defined as

$$f(x) = \beta_0 + \beta_1 x + \dots + \beta_\wp x^\wp + \sum_{n=1}^K \beta_{\wp n} (x - \kappa_n)_+^\wp, \quad \text{for } \wp = 1, 2, \dots \quad (2.179)$$

Fitting is performed by minimizing $\|\mathbf{Y} - \mathbf{X}_C \boldsymbol{\beta}\|^2 + \alpha \boldsymbol{\beta}^T \mathbf{D} \boldsymbol{\beta}$ w.r.t. $\boldsymbol{\beta}$ yielding to the fitted values of the penalized spline regression

$$\hat{\mathbf{Y}} = \mathbf{X}_C (\mathbf{X}_C^T \mathbf{X}_C + \alpha \mathbf{D})^{-1} \mathbf{X}_C^T \mathbf{Y} \quad (2.180)$$

where the \mathbf{X}_C -matrix is

$$\mathbf{X}_C = \begin{bmatrix} 1 & x_1 & \dots & x_1^\wp & (x_1 - \kappa_1)_+^\wp & \dots & (x_1 - \kappa_K)_+^\wp \\ \vdots & \vdots & \ddots & \vdots & \vdots & \ddots & \vdots \\ 1 & x_N & \dots & x_N^\wp & (x_N - \kappa_1)_+^\wp & \dots & (x_N - \kappa_K)_+^\wp \end{bmatrix}, \quad (2.181)$$

and $\mathbf{D} = \text{diag}(\mathbf{0}_{\wp+1}, \mathbf{1}_K)$.

A fast computation of the penalized spline regression involves the following steps:

1. Obtain the Cholesky decomposition of $\mathbf{X}_C^T \mathbf{X}_C$:

$$\mathbf{X}_C^T \mathbf{X}_C = \mathbf{R}^T \mathbf{R}, \quad (2.182)$$

where \mathbf{R} is square and invertible.

2. Form the symmetric matrix $\mathbf{R}^{-T} \mathbf{D} \mathbf{R}^{-1}$ and obtain its singular value decomposition:

$$\mathbf{R}^{-T} \mathbf{D} \mathbf{R}^{-1} = \mathbf{U} \text{diag}(\mathbf{s}) \mathbf{U}^T. \quad (2.183)$$

3. Compute the matrix and vector,

$$\mathbf{A} \equiv \mathbf{X}_C \mathbf{R}^{-1} \mathbf{U} \quad \mathbf{b} \equiv \mathbf{A}^T \mathbf{Y}. \quad (2.184)$$

2.13 Surrogate models

4. The fitted values are

$$\hat{\mathbf{f}}_\alpha = \mathbf{A} \left(\frac{\mathbf{b}}{\mathbf{1} + \alpha \mathbf{s}} \right) \quad (2.185)$$

with corresponding degrees of freedom (DOFs)

$$df_{fit}(\alpha) = \mathbf{1}^T \left(\frac{\mathbf{1}}{\mathbf{1} + \alpha \mathbf{s}} \right). \quad (2.186)$$

Once the matrix \mathbf{A} and vectors \mathbf{b} and \mathbf{s} have been computed, $f(\alpha)$ and $df_{fit}(\alpha)$ can be computed for different values of α . Automatic smoothing parameter selection is then performed to search for the smoothing parameter α that minimizes $GCV(\alpha)$ in Equation (2.178) with obtained $df_{fit}(\alpha)$ and

$$RSS(\alpha) = \|\mathbf{Y} - \hat{\mathbf{f}}_\alpha\|^2. \quad (2.187)$$

In order to give an indication of the uncertainty of the fitted spline that measures how much the relationship between the conditional expected value $E(\mathbf{Y}|X_i)$ and the i th parameter X_i change, the confidence intervals (CIs) are examined. In addition, the prediction intervals (PIs) for \mathbf{Y} are also shown.

We assume that $\hat{\mathbf{Y}}$ is distributed as a t -distribution with df_{res} DOFs where $df_{res}(\alpha)$ is computed by

$$df_{res}(\alpha) = N - 2\mathbf{1}^T \left(\frac{\mathbf{1}}{\mathbf{1} + \alpha \mathbf{s}} \right) + \left\| \frac{\mathbf{1}}{\mathbf{1} + \alpha \mathbf{s}} \right\|. \quad (2.188)$$

The CIs for the penalized spline were given by Ruppert *et al.* (RWC62)

$$\sigma_{(\hat{\mathbf{f}}-\mathbf{f})} = \sigma_\epsilon \sqrt{\text{diag} \left\{ \mathbf{A} \text{diag} \left(\frac{\mathbf{1}}{\mathbf{1} + \alpha \mathbf{s}} \right) \mathbf{A}^T \right\}}, \quad (2.189)$$

where σ_ϵ is estimated by

$$\hat{\sigma}_\epsilon^2 = \frac{RSS(\alpha)}{df_{res}(\alpha)}, \quad (2.190)$$

Therefore, an approximate $100(1 - \gamma)\%$ confidence interval for $f(x)$ is

$$\hat{f}(x) \pm t \left(1 - \frac{\gamma}{2}; df_{res} \right) \sigma_{(\hat{\mathbf{f}}-\mathbf{f})}. \quad (2.191)$$

The PIs for the penalized spline are

$$\hat{f}(x) \pm t \left(1 - \frac{\gamma}{2}; df_{res} \right) \sigma_\epsilon \sqrt{1 + \text{diag} \left\{ \mathbf{A} \text{diag} \left(\frac{\mathbf{1}}{\mathbf{1} + \alpha \mathbf{s}} \right) \mathbf{A}^T \right\}}, \quad (2.192)$$

2.14 Normalization of the input

where $\mathbf{1}$ is an $((\varphi + 1 + K) \times 1)$ column vector of ones, $t(1 - \frac{\gamma}{2}; df_{res})$ denotes the $100(1 - \frac{\gamma}{2}) - th$ percentile of the t distribution with df_{res} DOFs.

2.14 Normalization of the input

Since the input parameters in our simulation are at different scales, they need to be normalized before building the surrogate models. The sth realization of the ith input factor X_i is normalized as follows:

$$x_{ji}^{norm} = \frac{x_{ji} - \min(X_i)}{\max(X_i) - \min(X_i)} \quad (2.193)$$

where $\min(X_i)$ and $\max(X_i)$ are the minimum and maximum of the samples of the ith input.

Chapter 3

Stochastic predictions of bulk properties of amorphous polyethylene based on molecular dynamics simulations

3.1 Introduction

Glassy amorphous polyethylene (PE) has been widely studied by many researchers due to its important physical, chemical and mechanical properties. Great effort has been made for many decades to predict the mechanical properties such as Young's modulus, yield strength, etc. Recent developments of molecular dynamics simulation have opened the door for understanding and predicting the mechanical and physical properties of various polymeric materials. Boyce *et al.* (CBR02) noticed that the Young's modulus and yield stress depends on the rate of deformation. Recently, Zhao *et al.* (ZNZ10) have found that the chain length, temperature and strain rate have a significant effect on the mechanical properties of amorphous PE under uniaxial deformation. The thermo-mechanical properties of PE were studied by coarse-grained MD simulations. Boyce *et al.* (BA00) stated when more than 100 atoms (units) are used in a chain, the chain will take on a randomly kinked shape and the polymer chains are arranged in a random orientation. Hossain *et al.* (HTW⁺10) showed the higher the chain length, the more entanglement the structure and hence the structure has a higher stiffness and yield stress. They also reported that the influence of the chain length on the stress-strain curve is more significant than the number of chains. Hoy and Robbins (RM91) observed strain softening for specific chain lengths. The influence of certain parameters on the mechanical behavior of glassy amorphous polymers has been obtained qualitatively (HTW⁺10, RM91, CBR04). However, quantitative results in the

3.2 Molecular dynamics method

context of stochastic analysis are missing.

This chapter aims to quantify the influence of the chain length, temperature and strain rate on the yield stress and Young's modulus. Therefore, we compute first-order, total-effect sensitivity indices in the context of global sensitivity analysis (SA). Moreover, we perform a local SA where we calculate partial derivatives and elementary effects. The probability distribution of the Young's modulus is characterized by using a probability plot method and the residual sum of squares (RSS) is employed to determine the best fitted distribution of the sample output data.

This chapter is outlined as follows. In section 3.2, we briefly describe the MD model for PE. The results of the MD model will be shown in section 3.3. In section 3.4, the coefficients of determination and the sensitivity indices will be presented before we discuss the numerical results. Finally, we end the manuscript with concluding remarks.

3.2 Molecular dynamics method

The united atom model using the dreiding potential was used to describe the molecular structure of PE. The functional form and parameters of the force field are summarized in Table 2.1.

The initial chain structures were created by implementing a Monte Carlo random walk growth algorithm with rigid bond length (Bin95). The simulation cell had a face centered cubic (FCC) lattice each site representing a possible monomer location. Similar methods have successfully been generated in (HTW⁺10, She06). Subsequently, the equilibration and deformation processes described in subsection 2.1.3 were performed to study stress-strain response in dependence of different chain lengths, temperatures and strain rates. Figure 3.1 illustrates the undeformed (left) and deformed (right) representative volume elements. Simulations were performed by a parallel molecular dynamics code LAMMPS (Pli95).

To verify the glass transition temperature of various thermodynamics quantities, two consecutive equilibration steps were implemented (HTW⁺10). Firstly, the model (20,000 atoms) was equilibrated at 500 K. Then, the system was cooled down to 100 K at a rate of 0.8 K/ps over 500 ps by a series of NPT runs. The glass transition temperature was identified as the location of the discontinuity in the slope of the specific volume versus temperature curve are shown in Figure 3.2.

3.3 Molecular dynamics simulation results

In this section, the influence of the chain length, temperature and strain rate on the mechanical properties of PE is obtained by UA-MD simulations.

Gaussian, Schulz-Flory, log normal and the Poisson distribution are often used

3.3 Molecular dynamics simulation results

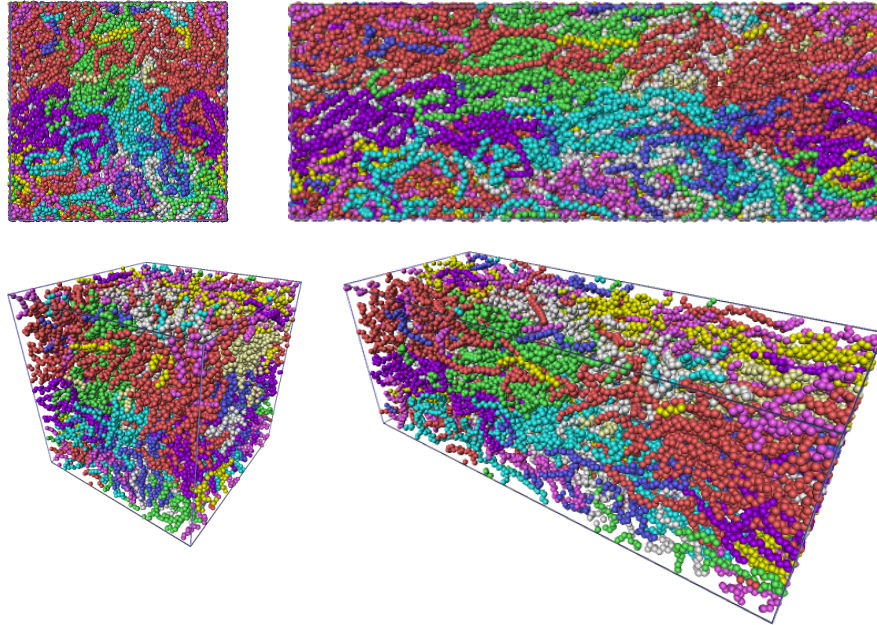


Figure 3.1: Undeformed (left) and deformed (right) (100% strain) representative volume elements built for PE

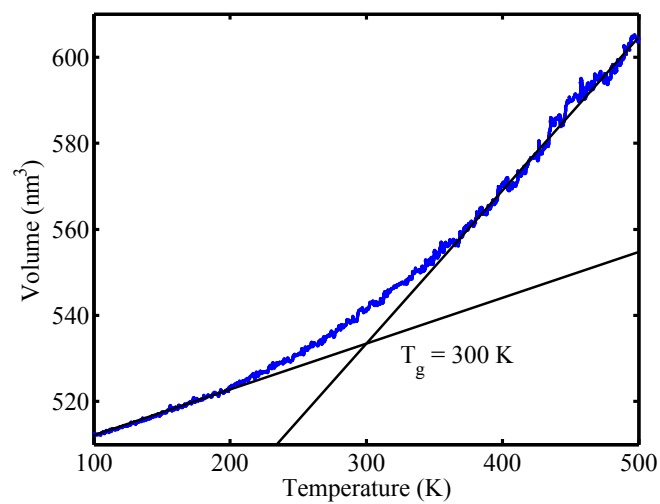


Figure 3.2: Plot of the relationship between volume evolution and temperature during cooling process.

3.3 Molecular dynamics simulation results

(Bow01) to approximate the chain length distribution. A small number of monomers (N_e) does not increase the strength because short chains slip too easily (Qia). The strength increases with the chain length (N_e), but so does viscosity (hard to mold) if N_e is larger than 2000 units. The experimental studies of Ungar *et al.* (USK⁺85) and Lee and Wegner (LW85) on the linear long-chain showed that polymer chains kink only for chain lengths larger than 100 CH_2 units, the so-called entanglement length (SK95). In our simulations, 100 to 2000 units are chosen as lower and upper bounds of a truncated Gaussian distribution

For glassy PE, the temperature should be lower than the glass transition temperature T_g ($T_g = 300$ K, see Figure 3.2). However, the temperature has to be high enough to observe strain-rate effects for the thermal equilibrium (CBR04). Brown and Clarke (BC91) pointed out that the Young's modulus decreases significantly when the temperature increases above 100 K. Therefore, we modify the temperature from 100 K to 300 K assuming uniform distribution.

The Young's modulus and the yield stress decrease with decreasing strain rate. As only a few pico -or nano seconds can be modeled in MD simulations, strain rates below 10^9 1/s cannot be captured though they are unrealistic in practical applications. Constant true strain rates ranging from 5×10^9 to 5×10^{10} 1/s are used in our MD simulations (CBR04). We assume a uniform distribution.

The stress-strain response for glassy amorphous PE system with 10 chains, 1000-units deformed in uniaxial tension at temperature of 250 K and strain rate of 1×10^{-5} 1/fs is shown in Figure 2.2. Stress-strain curves with different chain lengths, temperatures and strain rates are illustrated from Figure 3.3 to Figure 3.5.

Three initial chain structures were randomly generated with initial densities $\rho_0 = 0.5$ g/cm³, 0.4 g/cm³, 0.2 g/cm³, respectively. After the equilibration sequence, the densities for the amorphous equilibrated now are almost the same ($\rho_1 = 0.885$ g/cm³, $\rho_2 = 0.890$ g/cm³, $\rho_3 = 0.883$ g/cm³, respectively). Figure 3.6 shows for a strain rate of 10^{-5} 1/fs and temperature of 250 K the stress-strain curve is independent of the initial structures.

Figure 3.7 illustrates stress-strain curves for quasi-static and dynamic MD-simulations with different strain rates exemplary for two temperatures. The strain-rate dependence is obvious. So far, there is no contribution that quantitatively determines the influence of temperature and strain-rate on the bulk properties of PE.

The random input variables are listed in Table 3.1.

Table 3.1: Model uncertainties

Input parameters	Type of distribution	Mean value	Standard deviation	Source
Chain length (units)	Gaussian (truncated)	800	300	(Qia)
Temperature (K)	Uniform	200	$200/\sqrt{12}$	assumed
Strain rate (1/fs)	Uniform	2.75×10^{-5}	$4.5 \times 10^{-5}/\sqrt{12}$	assumed

3.3 Molecular dynamics simulation results

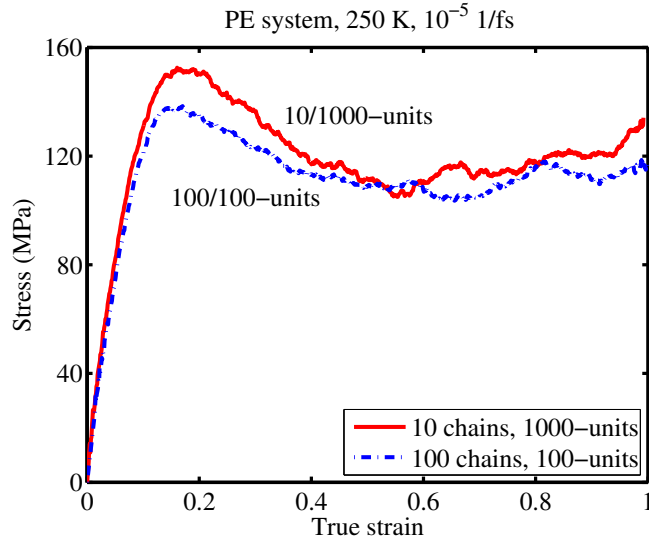


Figure 3.3: Stress-strain curves for a glassy PE system (10 chains, 1000 units) and (100 chains, 100 units), respectively, deformed in uniaxial tension at a temperature of 250 K and strain rate of 10^{-5} 1/fs.

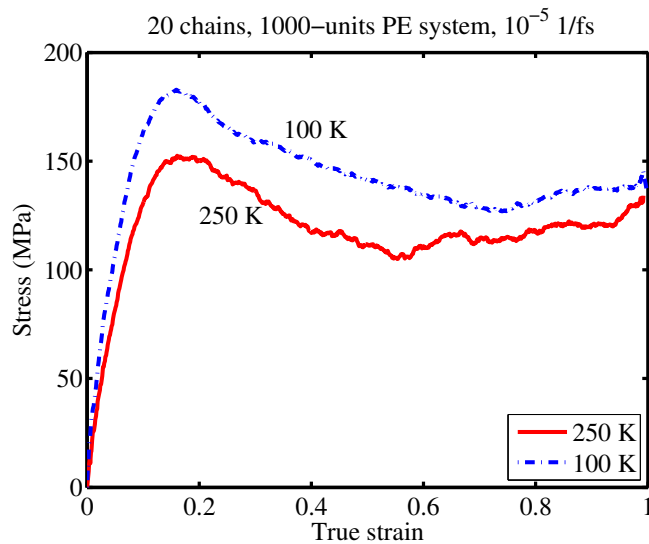


Figure 3.4: Stress-strain curves for a glassy PE system (10 chains, 1000-units) deformed in uniaxial tension at a strain rate of 10^{-5} 1/fs and temperature of 250 K and 100 K, respectively.

3.3 Molecular dynamics simulation results

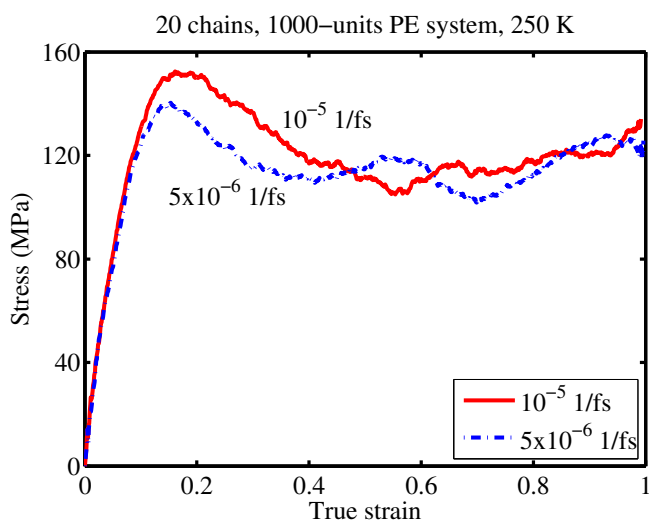


Figure 3.5: Stress-strain curves for a glassy PE system (10 chains, 1000 units) deformed in uniaxial tension at temperature of 250 K, strain rates of 10^{-5} 1/fs and 5×10^{-6} 1/fs, respectively.

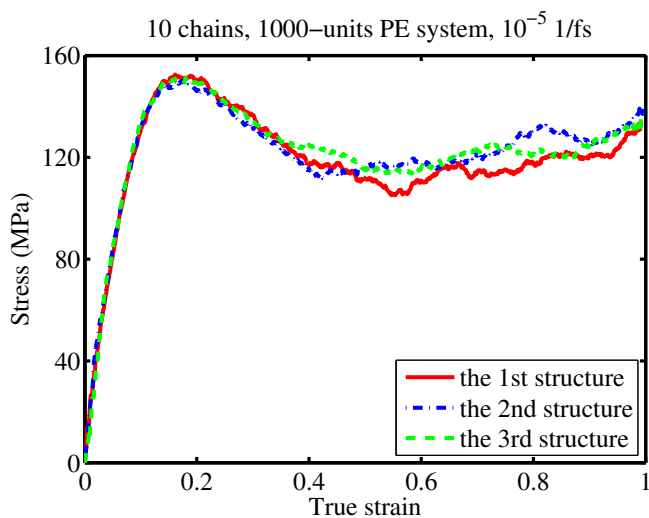
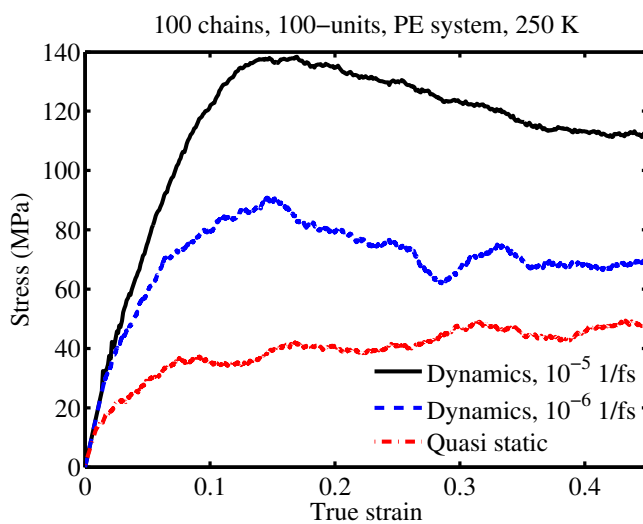
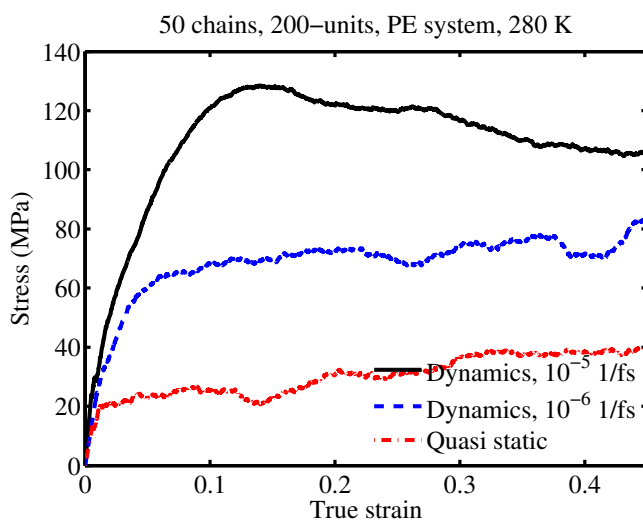


Figure 3.6: Stress-strain curves for glassy PE systems (10 chains, 1000 units) at a strain rate of 10^{-5} 1/fs and temperature of 250 K.

3.3 Molecular dynamics simulation results



(a)



(b)

Figure 3.7: Stress-strain curves at (a) 250 K and (b) 280 K for quasi-static and dynamics techniques

3.4 Numerical results

The schematic diagram of all sensitivity assessment methods are provided in Figure 3.8.

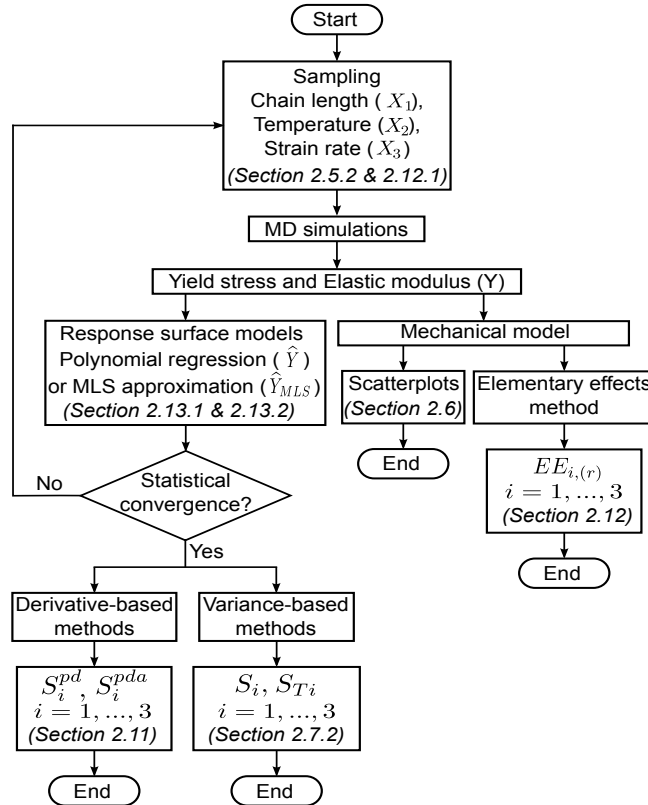


Figure 3.8: Schematic diagram of all sensitivity assessment methods presented in this paper.

In the sequel the model output (\mathbf{Y}) is either the computed yield stress or the Young's modulus. The three model input parameters are chain length (X_1), temperature (X_2) and strain rate (X_3).

3.4.1 Scatter plots

Scatter plots in Figures 3.9 and 3.10 show the influence of the chain length, temperature and strain rate on the yield stress and Young's modulus, respectively. The highest influence seems to be the temperature. To quantify the effect of the input parameters, the sensitivity indices were studied using the surrogate model.

3.4 Numerical results

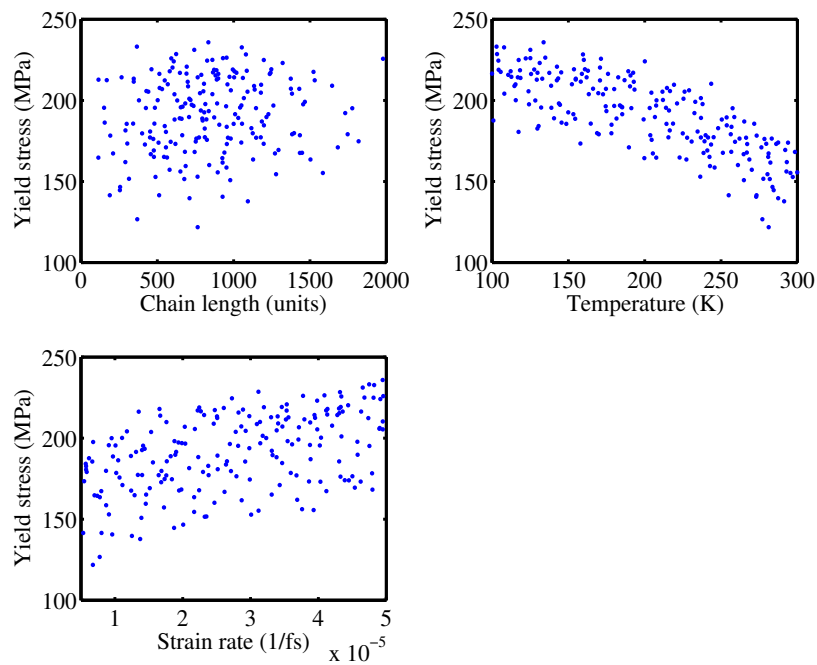


Figure 3.9: Scatter plots of the yield stress (Y) versus the chain length (X_1), temperature (X_2) and strain rate (X_3), respectively.

3.4 Numerical results

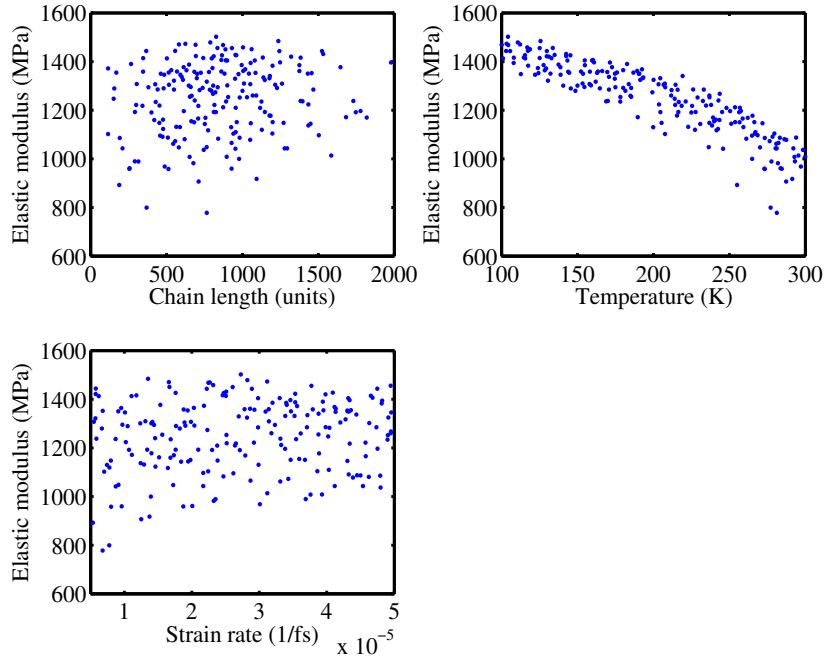


Figure 3.10: Scatter plots of the Young's modulus versus (Y) the chain length (X_1), temperature (X_2) and strain rate (X_3), respectively.

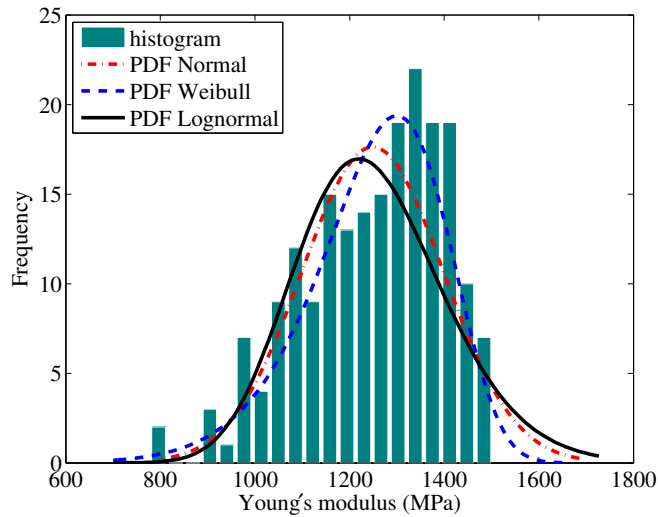


Figure 3.11: Histogram of the Young's modulus and assumed probability density functions (PDFs) for different distribution types.

3.4 Numerical results

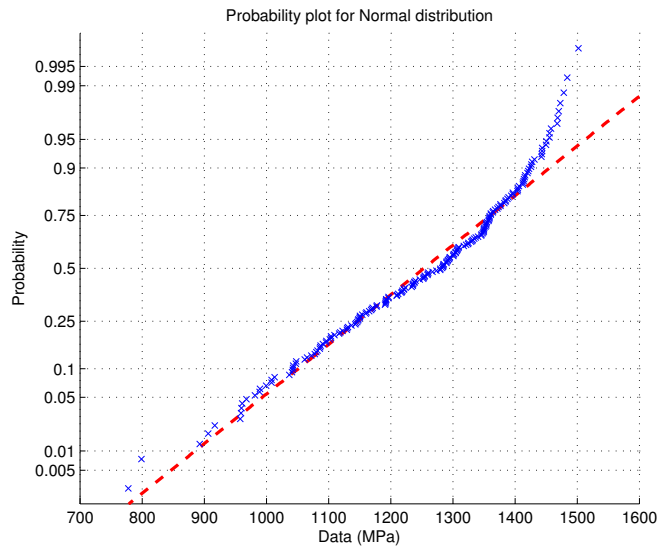


Figure 3.12: Normal probability plot for the distribution of the Young's modulus.

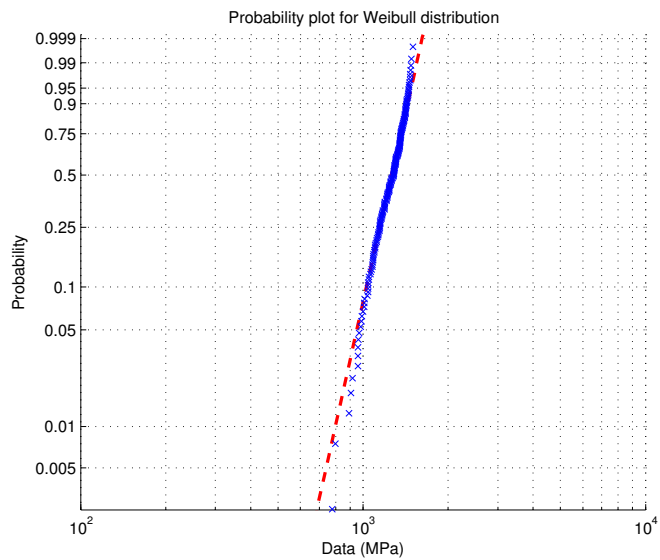


Figure 3.13: Weibull probability plot for the distribution of the Young's modulus.

3.4 Numerical results

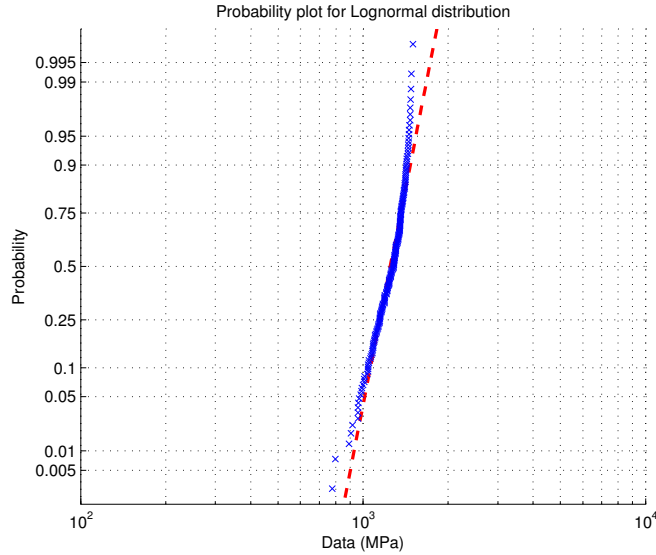


Figure 3.14: Log-normal probability plot for the distribution of the Young’s modulus.

The Young’s modulus uncertainty of the investigated mechanical model can be described by a probability distribution function. Judging from the shape of the histogram shown in Figure 3.11, either normal or Weibull, Log-normal distributions are proper candidates that can be used to account for the mechanical output uncertainty.

The purpose of probability plot is to graphically assess if the Young’s modulus’ data can be characterized by a given distribution. If the probability plot produces the least deviations from a linear line, the exploited theoretical distribution is chosen as a goodness-of-fit of the data (GK90). The Normal, Weibull and Log-normal probability plots are illustrated in Figures 3.12, 3.13 and 3.14, respectively.

The difference between mean (4.30×10^{-4}) and mode value (4.02×10^{-4}) reveals that the output is skewed, see Figure 3.11 and Table 3.2. Hence, the Normal distribution is not a good candidate to characterize the mechanical output. It is more reasonable to describe the skewed data by a Weibull distribution or a Log-normal distribution. In order to quantitatively assess the best fits to the data, the sum of the squares of the estimated residuals (RSS) are computed in Equation (2.145) in which cross blue points of the probability plots are considered as Y_j and the regression values (linear red lines) play the same role as \hat{Y}_j . Obviously, the Weibull probability plot provides the best fit to characterize the Young’s modulus’ histogram due to the smallest RSS given in Table 3.3. Note that the RSS values are estimated within 95% confidence intervals.

3.4 Numerical results

Table 3.2: Statistical results for the ISS

Output	Mode value (MPa)	Mean value (MPa)	Std. dev.
Young's modulus	778.05	1248.72	149.00

Table 3.3: Uncertainties of mechanical output using various distributions

Type of assumed PDF	Parameter 1	Parameter 2	Error
Normal PDF	Mean value (MPa)	Std. dev.	RSS
	1248.72	149.38	0.2312
Weibull PDF	Scale parameter (A)	Shape parameter (B)	RSS
	1312.30	10.42	0.1040
Log-normal PDF	Mean value (MPa)	Std. dev.	RSS
	7.12	0.13	0.3409

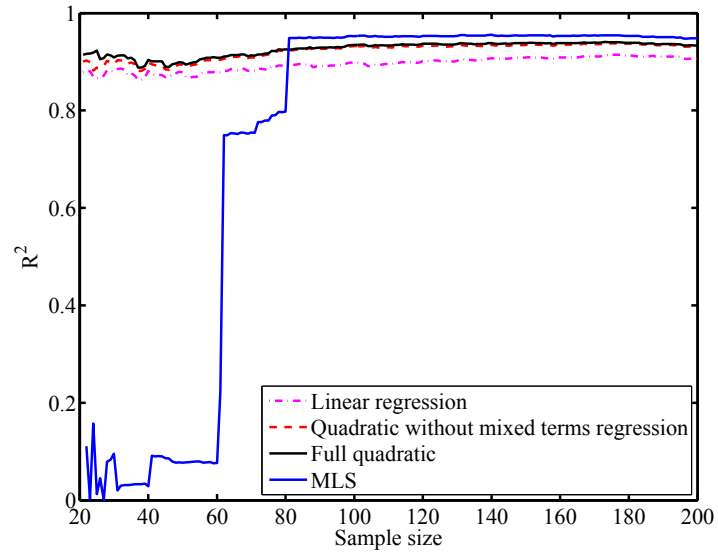
3.4.2 Surrogate model

Figure 3.15 shows that statistical convergence can be achieved with only 20 samples for the polynomial regression model and 80 samples for the MLS-model. There are barely any differences between the linear and the higher order regression models.

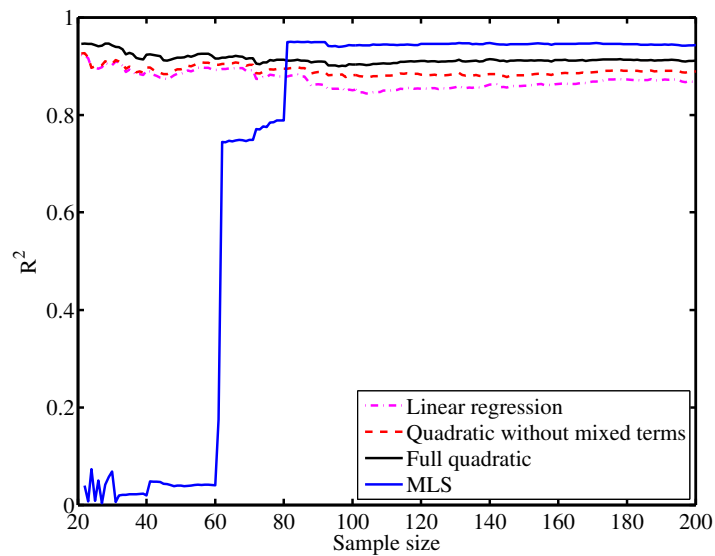
Subsequently, we compute the regression coefficient sets of samples, COD R^2 and adjusted COD R_{adj}^2 for 200 samples.

The surrogate model is used to approximate the output of the mechanical model. The regression coefficient β_k , Equation (2.148) is listed in Table 3.4 (for the yield stress) and Table 3.5 (for the Young's modulus). Table 3.4 and Table 3.5 also show the COD R^2 and adjusted coefficient R_{adj}^2 w.r.t. linear, quadratic without mixed terms and the full quadratic polynomial regression. The higher the order of the polynomial basis function, the larger these values. The MLS approximation with appropriate chosen radius (radius of 500) leads to the best surrogate model (highest value for R^2 and R_{adj}^2). A three-dimensional scatter plot and the associated surrogate model is shown in dependence of the temperature and strain rate in Figure 3.16 (for the yield stress) and Figure 3.17 (for the Young's modulus). The highest gradients (in either temperature or strain-rate direction) occur in the temperature direction, indicating the temperature is the key parameter for the yield-stress and the Young's modulus. Figure 3.17 shows that for a fixed temperature of 100 K, there is barely a change in the Young's modulus. The strain-rate effect on the Young's modulus is increased with increasing temperature. The strain-rate effect influences the yield stress even for low temperatures around 100 K, see the gradient for fixed temperature in strain-rate direction in Figure 3.16. With increasing temperature, this gradient slightly increases.

3.4 Numerical results



(a)



(b)

Figure 3.15: The plot of R^2 versus the number of samples when polynomial regression and MLS are used in both cases: the output model are yield stress (a) and Young's modulus (b).

3.4 Numerical results

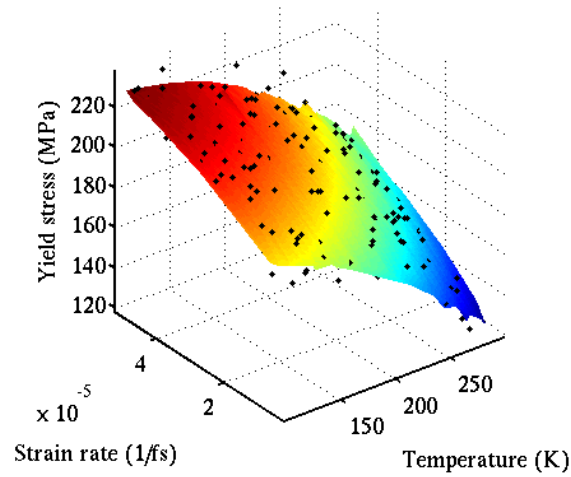
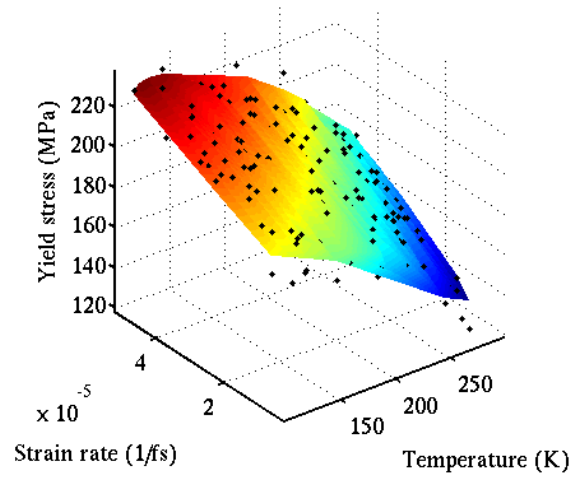


Figure 3.16: Scatter points got from MD simulations (black points) and projection surface of RS model which express the yield stress versus the temperature and strain rate. In this figure, the full quadratic regression (a) and MLS (b) are used.

3.4 Numerical results

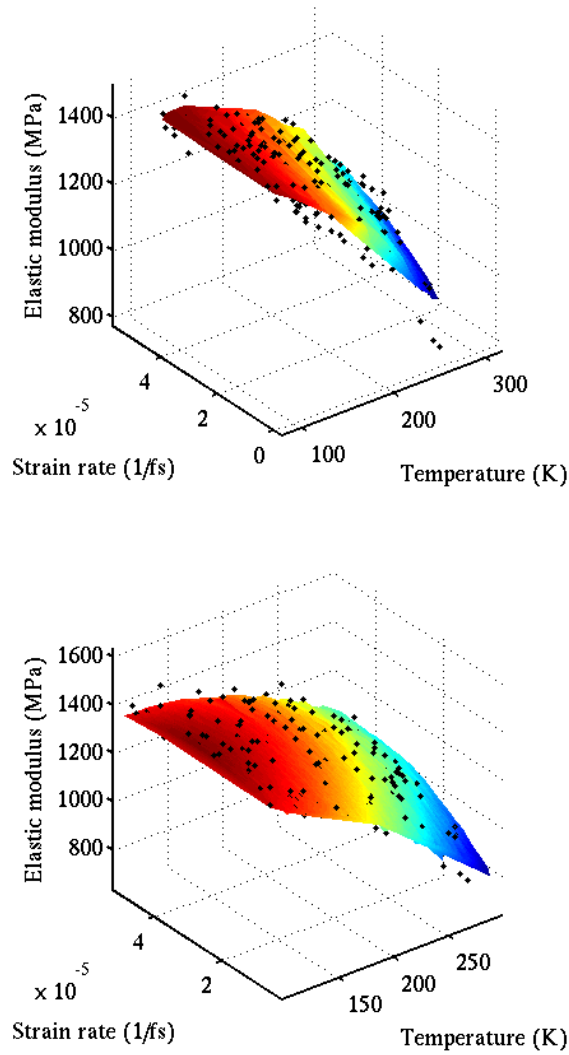


Figure 3.17: Scatter points got from MD simulations (black points) and projection surface of surrogate model which express the Young's modulus versus the temperature and strain rate. In this figure, the full quadratic regression (a) and MLS (b) are used.

3.4 Numerical results

Table 3.4: Regression coefficient, COD R^2 and adjusted COD R_{adj}^2 in case the output is yield stress

Response surface methods	Regression coefficient
Linear regression $R^2 = 0.90$ $R_{adj}^2 = 0.90$	$\beta_0 = 226.19$ $\beta_1 = 4.4e-3$ $\beta_2 = -0.33$ $\beta_3 = 1.01e+6$
Quadratic without mixed terms $R^2 = 0.93$ $R_{adj}^2 = 0.93$	$\beta_0 = 176.75$ $\beta_1 = 0.01$ $\beta_2 = 0.18$ $\beta_3 = 1.02e+6$ $\beta_{11} = -3.36e-6$ $\beta_{22} = -1.2e-3$ $\beta_{33} = 0$
Full quadratic $R^2 = 0.93$ $R_{adj}^2 = 0.93$	$\beta_0 = 185.33$ $\beta_1 = 0.0061$ $\beta_2 = 0.15$ $\beta_3 = 7.7e+5$ $\beta_{11} = -3.23e-6$ $\beta_{22} = -1.3e-3$ $\beta_{33} = 0$ $\beta_{12} = 1.78e-5$ $\beta_{13} = 2.25$ $\beta_{23} = 1277.82$
Moving least squares $R^2 = 0.95$ $R_{adj}^2 = 0.95$	

The coefficients of determination listed in Table 3.4 and Table 3.5 demonstrate that the surrogate model obviously reflects almost exactly the response of the mechanical model because the COD are 0.93 for the yield stress and 0.91 for the Young's modulus. In other words, 93 % of the yield stress and 91 % of the Young's modulus variation are represented by the regression model. The obtained R^2 , R_{adj}^2 when using the linear, quadratic without mixed terms, full quadratic regression and MLS are similar. In this paper, we have used the full regression model as the computational cost increases only insignificantly compared to the linear model.

3.4.3 Partial derivatives

Long MD simulations are generating cumulative errors in the numerical integration that can be minimized with proper selection of algorithms and parameters, but not eliminated entirely. Therefore, the approximation of partial derivatives with finite different schemes is critical in particular when ΔX_i approaches to 0. This is the rea-

3.4 Numerical results

Table 3.5: Regression coefficient, COD R^2 and adjusted COD R_{adj}^2 in case the output is Young's modulus

Response surface methods	Regression coefficient
Linear regression $R^2 = 0.87$ $R_{adj}^2 = 0.87$	$\beta_0 = 1615.78$ $\beta_1 = 0.03$ $\beta_2 = -2.35$ $\beta_3 = 2.79e+6$
Quadratic without mixed terms $R^2 = 0.89$ $R_{adj}^2 = 0.89$	$\beta_0 = 1336.02$ $\beta_1 = 0.08$ $\beta_2 = 0.48$ $\beta_3 = 2.83e+6$ $\beta_{11} = -2.73e-5$ $\beta_{22} = -7.0e-3$ $\beta_{33} = 0$
Full quadratic $R^2 = 0.91$ $R_{adj}^2 = 0.91$	$\beta_0 = 1512.74$ $\beta_1 = 3.8e-3$ $\beta_2 = -0.13$ $\beta_3 = -2.92e+6$ $\beta_{11} = -2.50e-5$ $\beta_{22} = -8.1e-3$ $\beta_{33} = 0$ $\beta_{12} = 3.11e-4$ $\beta_{13} = 272.47$ $\beta_{23} = 28091.99$
Moving least squares $R^2 = 0.94$ $R_{adj}^2 = 0.94$	

son why we apply the partial derivative approach solely on the generated response surfaces, which, by construction, are sufficiently smooth for approximating derivatives numerically. The full quadratic surrogate model is used. Each X_i will be discretized into 10 values in the interval $[0,1]$, and the input space represents a scaling of a 3D unit cube and discretization of 10-level grid Ω . Then applying the inverse cumulative function we obtain a 10-level grid for three input parameters (chain length (X_1), temperature (X_2) and strain rate (X_3)) in the real interval. We evaluate $\mathbf{Y} = (\text{Yield stress, Elastic modulus})$ twice, first at the selected values and second after increasing X_i by the quantity $\Delta = 0.01\%$. The partial derivatives are computed from Equations (2.137) and (2.138) for two cases: (1) keeping the other parameters fixed; (2) considering variation of other parameters, respectively. Flowcharts of these processes are provided in Figure 2.19. To quantify the relative importance of the influence of each input parameter, the partial derivatives need to be normalized w.r.t. an input parameter, e.g., \bar{X}_2 in this example named $S_{X_i}^{\bar{X}_2}, i = 1, 3$ as follows

3.4 Numerical results

$$S_{X_1}^{\bar{X}_2,(pd)} = \left(\frac{1}{N} \sum_{s=1}^N \frac{\partial \mathbf{Y}^{(s)}}{\partial X_1} \right) \frac{X_1}{\bar{X}_2} \quad (3.1a)$$

$$S_{X_1}^{\bar{X}_2,(pda)} = \left(\frac{1}{N^3} \sum_{s=1}^N \sum_{j=1}^N \sum_{l=1}^N \frac{\partial \mathbf{Y}^{(s)}}{\partial X_1} \right) \frac{X_1}{\bar{X}_2} \quad (3.1b)$$

$$S_{X_2}^{\bar{X}_2,(pd)} = \left(\frac{1}{N} \sum_{s=1}^N \frac{\partial \mathbf{Y}^{(s)}}{\partial X_2} \right) \quad (3.2a)$$

$$S_{X_2}^{\bar{X}_2,(pda)} = \left(\frac{1}{N^3} \sum_{j=1}^N \sum_{s=1}^N \sum_{l=1}^N \frac{\partial \mathbf{Y}^{(j)}}{\partial X_2} \right) \quad (3.2b)$$

$$S_{X_3}^{\bar{X}_2,(pd)} = \left(\frac{1}{N} \sum_{s=1}^N \frac{\partial \mathbf{Y}^{(s)}}{\partial X_3} \right) \frac{X_3}{\bar{X}_2} \quad (3.3a)$$

$$S_{X_3}^{\bar{X}_2,(pda)} = \left(\frac{1}{N^3} \sum_{l=1}^N \sum_{s=1}^N \sum_{j=1}^N \frac{\partial \mathbf{Y}^{(l)}}{\partial X_3} \right) \frac{X_3}{\bar{X}_2} \quad (3.3b)$$

These normalized partial derivatives (NPD) $\hat{S}_{X_i}^{\bar{X}_2}, i = 1, 3$ are reduced by the COD R^2

$$\hat{S}_{X_1}^{\bar{X}_2,(pd)} = R^2 S_{X_1}^{\bar{X}_2,(pd)} \quad (3.4a)$$

$$\hat{S}_{X_1}^{\bar{X}_2,(pda)} = R^2 S_{X_1}^{\bar{X}_2,(pda)} \quad (3.4b)$$

$$\hat{S}_{X_2}^{\bar{X}_2,(pd)} = R^2 S_{X_2}^{\bar{X}_2,(pd)} \quad (3.5a)$$

$$\hat{S}_{X_2}^{\bar{X}_2,(pda)} = R^2 S_{X_2}^{\bar{X}_2,(pda)} \quad (3.5b)$$

$$\hat{S}_{X_3}^{\bar{X}_2,(pd)} = R^2 S_{X_3}^{\bar{X}_2,(pd)} \quad (3.6a)$$

$$\hat{S}_{X_3}^{\bar{X}_2,(pda)} = R^2 S_{X_3}^{\bar{X}_2,(pda)} \quad (3.6b)$$

Table 3.6 shows the average of the reduced normalized partial derivatives (ARNPD) for the yield stress and the Young's modulus, respectively. The partial derivatives

3.4 Numerical results

$\hat{S}_{X_i}^{\bar{X}_2,(pd)}$ are almost identical to the partial derivatives $\hat{S}_{X_i}^{\bar{X}_2,(pda)}$, $i = 1...3$ meaning that the input parameters are all independent. The chain length has almost no influence on the Young's modulus and the yield stress. The key input parameter is the temperature followed by the strain rate. While the strain rate has an effect on the yield stress – the ARNPD of the strain rate is around 40% of the ARNPD of the temperature, the strain rate does barely affect the Young's modulus. The ratio $\hat{S}_{X_3}^{\bar{X}_2,(pda),(mod)} / \hat{S}_{X_2}^{\bar{X}_2,(pda),(mod)}$ is only 0.17; Table 3.7.

Table 3.6: Average of reduced NPD for the yield stress

ARNPD calculated by Eqs. (3.4a), (3.5a) and (3.6a)	ARNPD calculated by Eqs. (3.4b), (3.5b) and (3.6b)
$\bar{S}_{X_1}^{\bar{X}_2,(pd),(yield)} = 0.01$	$\bar{S}_{X_1}^{\bar{X}_2,(pda),(yield)} = 0.01$
$\bar{S}_{X_2}^{\bar{X}_2,(pd),(yield)} = 0.31$	$\bar{S}_{X_2}^{\bar{X}_2,(pda),(yield)} = 0.31$
$\bar{S}_{X_3}^{\bar{X}_2,(pd),(yield)} = 0.13$	$\bar{S}_{X_3}^{\bar{X}_2,(pda),(yield)} = 0.13$

Table 3.7: Average of reduced NPD for the Young's modulus

ARNPD calculated by Eqs. (3.4a), (3.5a) and (3.6a)	ARNPD calculated by Eqs. (3.4b), (3.5b) and (3.6b)
$\bar{S}_{X_1}^{\bar{X}_2,(pd),(mod)} = 0.07$	$\bar{S}_{X_1}^{\bar{X}_2,(pda),(mod)} = 0.07$
$\bar{S}_{X_2}^{\bar{X}_2,(pd),(mod)} = 2.09$	$\bar{S}_{X_2}^{\bar{X}_2,(pda),(mod)} = 2.14$
$\bar{S}_{X_3}^{\bar{X}_2,(pd),(mod)} = 0.37$	$\bar{S}_{X_3}^{\bar{X}_2,(pda),(mod)} = 0.37$

3.4.4 Elementary effects

To measure elementary effects of the mechanical model with 3 input parameters, we have randomly built $r = 8$ trajectories for $p = 10$ and assumed $\Delta = 3/9$. Suppose that the randomly generated \mathbf{x}^* , \mathbf{D}^* and \mathbf{P}^* are

$$\mathbf{x}^* = \begin{bmatrix} 2/9 & 5/9 & 1/9 \\ 3/9 & 6/9 & 2/9 \\ 1/9 & 4/9 & 4/9 \\ 4/9 & 3/9 & 3/9 \\ 6/9 & 2/9 & 3/9 \\ 5/9 & 0 & 2/9 \\ 1/7 & 2/7 & 1/5 \\ 0 & 1/7 & 2/5 \end{bmatrix}; \mathbf{D}^* = \begin{bmatrix} 1 & 0 & 0 \\ 0 & -1 & 0 \\ 0 & 0 & 1 \end{bmatrix}; \mathbf{P}^* = \begin{bmatrix} 1 & 0 & 0 \\ 0 & 1 & 0 \\ 0 & 0 & 1 \end{bmatrix}. \quad (3.7)$$

3.4 Numerical results

Using the Equation (2.141) to generate 8 trajectories of quantiles for 3 variables and applying the inverse cumulative function, we obtain corresponding values for three input parameters: chain length (X_1), temperature (X_2) and strain rate (X_3).

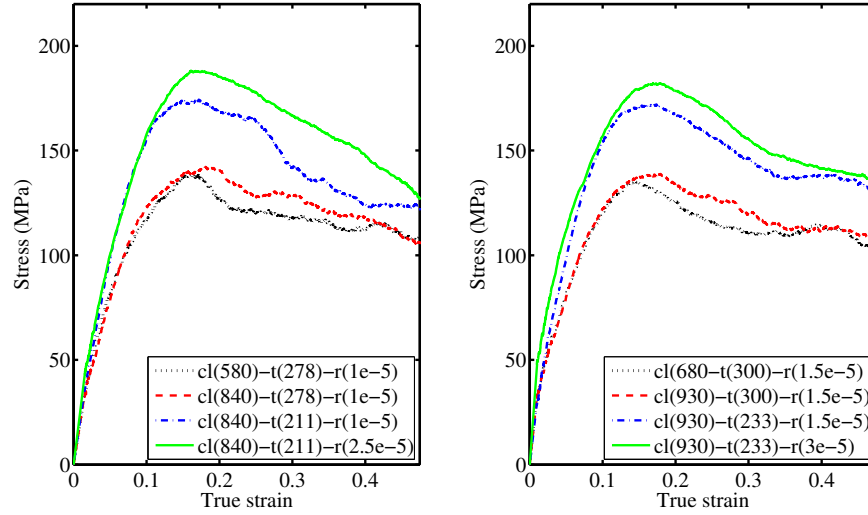


Figure 3.18: Stress-strain curves of two trajectories (left) trajectory 1 and (right) trajectory 2

Figure 3.18 to Figure 3.21 illustrate the stress-strain curves corresponding to 4 points on each trajectory from 1st to 8th, respectively. Note that the legend cl(580) - t(278) - r(1e-5) e.g., in the Figure 3.18 expresses $X_1 = 580$ -units, $X_2 = 278$ K, and $X_3 = 1 \times 10^{-5}$ 1/fs.

The elementary effects relative to each input parameter is estimated by Equation (2.142) or Equation (2.143).

Tables 3.8 and 3.9 show the elementary effects of the input parameters on the Young's modulus and the yield stress, respectively. The key input parameter is the temperature followed by the strain rate as predicted in the previous subsection. Also the elementary effects method predicts no influence of the chain length. Comparing the ratios $\overline{EE}_3^{(yield)} / \overline{EE}_2^{(yield)}$ and $\overline{EE}_3^{(mod)} / \overline{EE}_2^{(mod)}$, we obtain almost identical results as in the previous section 3.4.3. Note that the elementary effects are computed based on the *mechanical model* for only 8(trajectories) \times 4 = 32 samples.

3.4.5 Global sensitivity analysis

Based on the determined surrogate models, we generated the desired number of samples (10,000) by using the LHS method. The first-order sensitivity indices \hat{S}_i , total-effect sensitivity indices \hat{S}_{T_i} , $i = 1, \dots, 3$ of the input parameters ($X_1 =$ chain length;

3.4 Numerical results

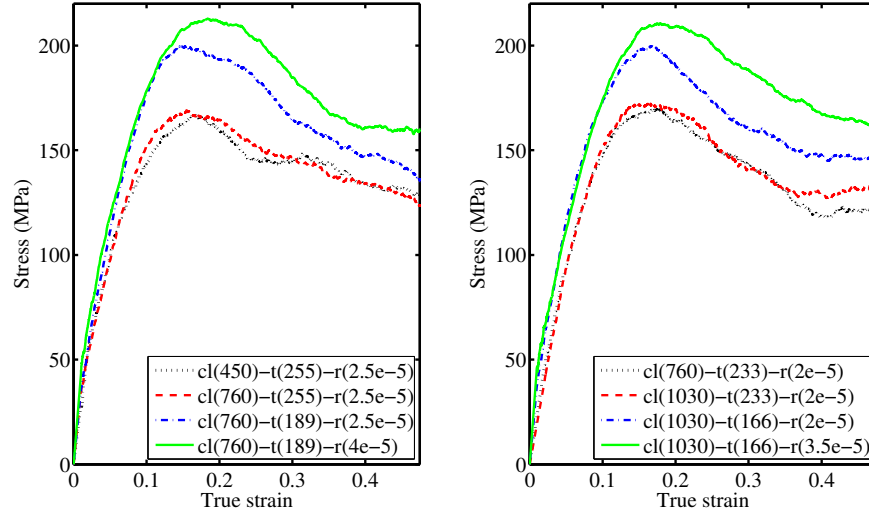


Figure 3.19: Stress-strain curves of two trajectories (left) trajectory 3 and (right) trajectory 4

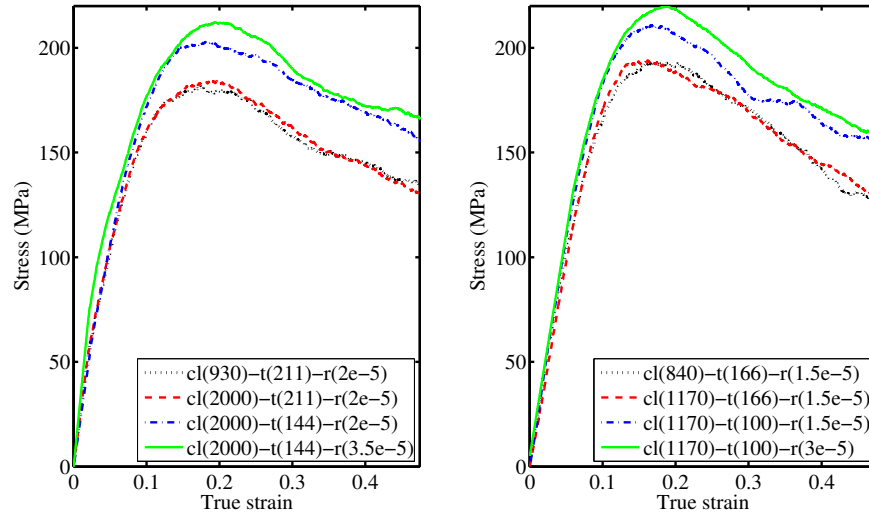


Figure 3.20: Stress-strain curves of two trajectories (left) trajectory 5 and (right) trajectory 6

3.4 Numerical results

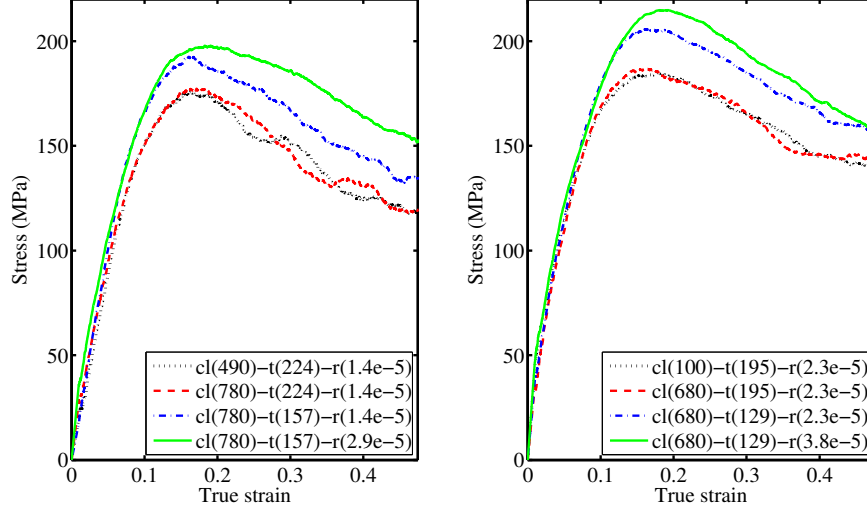


Figure 3.21: Stress-strain curves of two trajectories (left) trajectory 7 and (right) trajectory 8

Table 3.8: Elementary effects for the yield stress

Trajectory \ Elementary effects	$EE_{1,(r)}^{(yield)}$	$EE_{2,(r)}^{(yield)}$	$EE_{3,(r)}^{(yield)}$
Trajectory 1	12.12	96.39	41.52
Trajectory 2	8.46	99.87	27.00
Trajectory 3	6.48	92.91	38.37
Trajectory 4	5.91	81.63	32.64
Trajectory 5	8.56	55.67	28.34
Trajectory 6	4.07	48.82	24.04
Trajectory 7	4.29	46.26	15.46
Trajectory 8	6.36	56.28	27.05
Average elementary effects	$\overline{EE}_1^{(yield)} = 7.03$	$\overline{EE}_2^{(yield)} = 72.23$	$\overline{EE}_3^{(yield)} = 29.68$
<small>Note: $EE_{1,(r)}^{(yield)}$, $EE_{2,(r)}^{(yield)}$, $EE_{3,(r)}^{(yield)}$ indicate the elementary effects of the yield stress relative to the chain length, temperature, strain rate computed along trajectory r, respectively.</small>			

$X_2 = \text{temperature}$; $X_3 = \text{strain rate}$) are computed based on the polynomial regression and the MLS approximation and are presented in Tables 3.10 (for the yield stress) and 3.11 (for the Young's modulus). The computational cost (CPU time on 1 processor of the DELL PC Intel[®] Core[™] i5 CPU 750 @ 2.67 GHz \times 4) that is required for each method is also presented.

The sensitivity indices \hat{S}_i and \hat{S}_{T_i} , Equations (2.65) and (2.68), are reduced by the COD as

$$\hat{S}_i = R^2 S_i \quad (3.8)$$

3.4 Numerical results

Table 3.9: Elementary effects for the Young's modulus

Trajectory \ Elementary effects	$EE_{1,(r)}^{(mod)}$	$EE_{2,(r)}^{(mod)}$	$EE_{3,(r)}^{(mod)}$
Trajectory 1	80.40	820.20	166.50
Trajectory 2	21.30	769.20	125.70
Trajectory 3	78.00	728.70	124.20
Trajectory 4	47.10	569.40	107.70
Trajectory 5	32.70	424.80	85.20
Trajectory 6	32.70	325.50	93.60
Trajectory 7	11.10	364.20	53.70
Trajectory 8	38.40	392.10	74.40
Average elementary effects	$\overline{EE}_1^{(mod)} = 42.71$	$\overline{EE}_2^{(mod)} = 549.26$	$\overline{EE}_3^{(mod)} = 106.65$

Note: $EE_{1,(r)}^{(mod)}$, $EE_{2,(r)}^{(mod)}$, $EE_{3,(r)}^{(mod)}$ indicate the elementary effects of the Young's modulus relative to the chain length, temperature and strain rate computed along trajectory r , respectively.

$$\hat{S}_{T_i} = R^2 S_{T_i} \quad (3.9)$$

\hat{S}_i and \hat{S}_{T_i} are the first-order and total-effect sensitivity indices on the surrogate model. They infer that only $R^2\%$ of response can be explained with the surrogate model.

Table 3.10: First-order and total-effect sensitivity indices computed on the surrogate model of the input parameters contributing to the yield stress

Linear regression model	Quadratic without mixed terms	Full quadratic	MLS
First-order indices $\hat{S}_i^{(yield)}$ $\hat{S}_1^{(yield)} = 0.00$ $\hat{S}_2^{(yield)} = 0.61$ $\hat{S}_3^{(yield)} = 0.28$ $\sum_{i=1}^3 \hat{S}_i^{(yield)} = 0.89$	First-order indices $\hat{S}_i^{(yield)}$ $\hat{S}_1^{(yield)} = 0.00$ $\hat{S}_2^{(yield)} = 0.64$ $\hat{S}_3^{(yield)} = 0.29$ $\sum_{i=1}^3 \hat{S}_i^{(yield)} = 0.93$	First-order indices $\hat{S}_i^{(yield)}$ $\hat{S}_1^{(yield)} = 0.00$ $\hat{S}_2^{(yield)} = 0.63$ $\hat{S}_3^{(yield)} = 0.29$ $\sum_{i=1}^3 \hat{S}_i^{(yield)} = 0.92$	First-order indices $\hat{S}_i^{(yield)}$ $\hat{S}_1^{(yield)} = 0.00$ $\hat{S}_2^{(yield)} = 0.64$ $\hat{S}_3^{(yield)} = 0.31$ $\sum_{i=1}^3 \hat{S}_i^{(yield)} = 0.95$
Total-effect indices $\hat{S}_{T_i}^{(yield)}$ $\hat{S}_{T_1}^{(yield)} = 0.00$ $\hat{S}_{T_2}^{(yield)} = 0.62$ $\hat{S}_{T_3}^{(yield)} = 0.29$ $\sum_{i=1}^3 \hat{S}_{T_i}^{(yield)} = 0.91$	Total-effect indices $\hat{S}_{T_i}^{(yield)}$ $\hat{S}_{T_1}^{(yield)} = 0.01$ $\hat{S}_{T_2}^{(yield)} = 0.64$ $\hat{S}_{T_3}^{(yield)} = 0.29$ $\sum_{i=1}^3 \hat{S}_{T_i}^{(yield)} = 0.94$	Total-effect indices $\hat{S}_{T_i}^{(yield)}$ $\hat{S}_{T_1}^{(yield)} = 0.01$ $\hat{S}_{T_2}^{(yield)} = 0.64$ $\hat{S}_{T_3}^{(yield)} = 0.30$ $\sum_{i=1}^3 \hat{S}_{T_i}^{(yield)} = 0.95$	Total-effect indices \hat{S}_{T_i} $\hat{S}_{T_1}^{(yield)} = 0.01$ $\hat{S}_{T_2}^{(yield)} = 0.64$ $\hat{S}_{T_3}^{(yield)} = 0.31$ $\sum_{i=1}^3 \hat{S}_{T_i}^{(yield)} = 0.96$
CC = 216 (hours)	CC = 216 (hours)	CC = 216 (hours)	CC = 863 (hours)

Note: $\hat{S}_1^{(yield)}$ and $\hat{S}_{T_1}^{(yield)}$ are the reduced first-order and total-effect indices of the yield stress due to the chain length, respectively.
 $\hat{S}_2^{(yield)}$ and $\hat{S}_{T_2}^{(yield)}$ are the reduced first-order and total-effect indices of the yield stress due to the temperature, respectively.
 $\hat{S}_3^{(yield)}$ and $\hat{S}_{T_3}^{(yield)}$ are the reduced first-order and total-effect indices of the yield stress due to the strain rate, respectively.

The results of the variance-based methods are summarized in Tables 3.10 and 3.11. We notice:

3.4 Numerical results

Table 3.11: First-order and total-effect sensitivity indices computed on the surrogate model of the input parameters contributing to the Young's modulus

Linear regression model	Quadratic without mixed terms	Full quadratic	MLS
First-order indices $\hat{S}_i^{(mod)}$ $\hat{S}_1^{(mod)} = 0.00$ $\hat{S}_2^{(mod)} = 0.81$ $\hat{S}_3^{(mod)} = 0.06$ $\sum_{i=1}^3 \hat{S}_i^{(mod)} = 0.87$	First-order indices $\hat{S}_i^{(mod)}$ $\hat{S}_1^{(mod)} = 0.00$ $\hat{S}_2^{(mod)} = 0.82$ $\hat{S}_3^{(mod)} = 0.04$ $\sum_{i=1}^3 \hat{S}_i^{(mod)} = 0.86$	First-order indices $\hat{S}_i^{(mod)}$ $\hat{S}_1^{(mod)} = 0.00$ $\hat{S}_2^{(mod)} = 0.82$ $\hat{S}_3^{(mod)} = 0.06$ $\sum_{i=1}^3 \hat{S}_i^{(mod)} = 0.89$	First-order indices $\hat{S}_i^{(mod)}$ $\hat{S}_1^{(mod)} = 0.00$ $\hat{S}_2^{(mod)} = 0.84$ $\hat{S}_3^{(mod)} = 0.08$ $\sum_{i=1}^3 \hat{S}_i^{(mod)} = 0.92$
Total-effect indices $\hat{S}_{T_i}^{(mod)}$ $\hat{S}_{T_1}^{(mod)} = 0.01$ $\hat{S}_{T_2}^{(mod)} = 0.81$ $\hat{S}_{T_3}^{(mod)} = 0.06$ $\sum_{i=1}^3 \hat{S}_{T_i}^{(mod)} = 0.88$	Total-effect indices $\hat{S}_{T_i}^{(mod)}$ $\hat{S}_{T_1}^{(mod)} = 0.01$ $\hat{S}_{T_2}^{(mod)} = 0.84$ $\hat{S}_{T_3}^{(mod)} = 0.06$ $\sum_{i=1}^3 \hat{S}_{T_i}^{(mod)} = 0.91$	Total-effect indices $\hat{S}_{T_i}^{(mod)}$ $\hat{S}_{T_1}^{(mod)} = 0.00$ $\hat{S}_{T_2}^{(mod)} = 0.85$ $\hat{S}_{T_3}^{(mod)} = 0.07$ $\sum_{i=1}^3 \hat{S}_{T_i}^{(mod)} = 0.92$	Total-effect indices $\hat{S}_{T_i}^{(mod)}$ $\hat{S}_{T_1}^{(mod)} = 0.00$ $\hat{S}_{T_2}^{(mod)} = 0.83$ $\hat{S}_{T_3}^{(mod)} = 0.10$ $\sum_{i=1}^3 \hat{S}_{T_i}^{(mod)} = 0.93$
CC = 216 (hours)	CC = 216 (hours)	CC = 216 (hours)	CC = 863 (hours)
<small>Note: \hat{S}_1^{mod} and $\hat{S}_{T_1}^{mod}$ are the reduced first-order and total-effect indices of the Young's modulus due to the chain length, respectively. \hat{S}_2^{mod} and $\hat{S}_{T_2}^{mod}$ are the reduced first-order and total-effect indices of the Young's modulus due to the temperature, respectively. \hat{S}_3^{mod} and $\hat{S}_{T_3}^{mod}$ are the reduced first-order and total-effect indices of the Young's modulus due to the strain rate, respectively.</small>			

1. The first-order indices \hat{S}_i and total-effect indices \hat{S}_{T_i} are nearly identical indicating the independence of the input-parameters. These results agree with results based on the partial derivatives approach.
2. All surrogate models are suitable to study SA. The highest COD is obtained by the MLS-approach (0.95 for yield stress and 0.94 for Young's modulus) followed by the quadratic (with and without mixed terms) regression model (0.93 for the yield stress and 0.91 for Young's modulus) and the linear regression model (0.9 for the yield stress and 0.87 for the Young's modulus); Table (3.4 + 3.5). In other words, the MLS response surface model approximates best the mechanical results.
3. The temperature is the most influential parameter, the strain rate has smaller influence and the chain length has a negligible effect on the yield stress and Young's modulus, see Tables 3.10 and 3.11. The ratio $\hat{S}_{T_3}^{(yield)} / \hat{S}_{T_2}^{(yield)}$ is with a value of 0.45 slightly higher compared to the value of the other methods (0.41) indicating a higher influence of the strain rate on the yield stress. On the other hand, the ratio $\hat{S}_{T_3}^{(mod)} / \hat{S}_{T_2}^{(mod)} = 0.09$ for the Young's modulus is only half the values predicted by the elementary-effect method and the partial derivatives. The insignificant influence of the strain rate on the Young's modulus from experimental and theoretical studies is well known (CBR02, ABJ95). Therefore, it seems that the variance-based methods give the best results.

3.5 Conclusions

The mechanical properties of PE have been obtained by using UA-MD simulations. The Young's modulus is best characterized by the Weibull distribution. Based on the mechanical and surrogate model, we studied the influence of the chain length, temperature and strain rate on the yield stress and Young's modulus in the context of both local and global SA.

All sensitivity assessment methods predict the same tendencies, i.e.:

1. The most influential parameter on the yield stress and the Young's modulus is the temperature, followed by the strain rate.
2. The chain length used in our MD simulations has almost no influence on the yield stress and the Young's modulus.
3. While the strain rate affects the yield stress, it barely influences the Young's modulus. The latter effect is best predicted by the variance-based methods while the partial derivatives and the elementary-effects method slightly overpredict this influence.

Comments on the method:

1. It is difficult to predict the effectiveness of the methods beforehand. For the examples studied, it seems that the elementary-effects method requires less samples than the other methods. However, it fails to assess the mutual interaction of the input parameters. The variance-based method is a global SA method that can be used for such purpose. Therefore, the variance-based method is recommended due to its global SA property.
2. The most samples for statistical convergence are required by the MLS-approach and the number of samples dominate the overall efficiency.
3. The most robust methods are the regression models as they require the least number of input parameters.
4. The MLS-approach gives the highest COD and therefore seems to be the best surrogate model w.r.t. the predicted output. However, the adjustment of the dilation parameter D remains an open issue.
5. The computational most costly surrogate model is the MLS-approach. However, it is still negligible compared to the simulation time of the mechanical model. If the mechanical model's response is linear or quadratic, the linear or quadratic regression should be used. For complex mechanical models which the linear and quadratic regression fail to approximate ($R^2 < 0.8$), the MLS-approach should be used.

Chapter 4

Stochastic predictions of interfacial characteristic of polymeric nanocomposites

4.1 Introduction

The Carbon nanotubes (CNTs) are considered as an ideal reinforcement for polymer composites due to their exceptional mechanical and electrical properties (Dai02, SDR02, LGH06) and low density (SGA98, ASGR00, SW99). By adding CNTs into polymer, the properties of the resulting nanocomposite material such as strength, modulus, etc. are enhanced. However, the enhanced properties of these composites are strongly affected by the mechanics that govern the interface between CNT and polymer matrix (DH11). The mechanical properties of composite materials greatly depend on the load transfer mechanism through the interface between the polymer matrix and CNTs and the strength of the interface. Therefore, the interface plays a significant role in the load transfer and the consequent improvements in modulus and strength. For conventional fiber-reinforced polymer composites, the single fiber pull-out test (Fig95) is typically used to evaluate the interfacial shear strength. Great experimental efforts have been carried out in order to investigate interfacial properties. For instance, the direct CNT pull-out experiments were made in transmission electron microscopy (TEM) (QDAR00, Den11) or by atomic force microscopy (AFM) (BCKW03, BCKW04), Raman spectroscopy (SGA98), scanning probe microscope (SPM) (CRL+02a, CRL+02b). Experiments in (SGA98, ASGR00, QDAR00) demonstrated that since making atomic bonding between CNTs and polymer matrix is difficult, CNTs often interact mainly with the polymer matrix through van der Waals (vdW) forces. In the absence of atomic bonding (cross-links) between the CNT and the polymer matrix, the vdW forces especially govern the load transfer capability of

4.1 Introduction

the CNT/polymer interface. Due to difficulty of nanomanipulation in experiments, as mentioned by (RRP⁺13), numerical simulation is employed as a powerful alternative approach to study the CNT/polymer interface. Many molecular simulations have been carried out in order to investigate the CNT/polymer interfacial characteristics. In (LL01, FH03, GMW⁺04, CO07, ZXX⁺09), the research presented molecular mechanics (MM) and molecular dynamics (MD) simulations, in which the authors examined the interfacial shear stress (ISS) during the entire pull-out process of CNT from polymer matrix.

Wei *et. al.* (WSC02) used MD simulations to study the thermal expansion and diffusion characteristics of the single-walled carbon nanotube (SWCNT)/ polyethylene (PE) composite. He found that insertion of SWCNT into a polymer matrix increases the glass transition temperature T_g . For SWCNT/PE composites with long chained polymer molecules, the glass transition temperature T_g is around 400 K. He also studied the temperature dependent adhesion behavior of CNT/PE composites using MD simulations for tensile deformation of CNT/PE composites and reported that the interfacial shear stress between SWCNT and PE matrix decreases with the increase of temperature (Wei06). Frankland *et.al.* (FH03) developed an interfacial friction model depending on the pull-out force, an effective viscosity and strain rate. Based on this model, a linear force-sliding velocity relation is used to estimate the average interfacial interaction. Zhang *et.al.* (ZWX⁺11) studied the rate-dependent interfacial behavior between SWCNT and PE in the absence of cross-links by using MD simulations. They indicated that the ISS increases with an increase in the sliding velocity of CNT. They also investigated the effects of the SWCNT radius on the ISS and reported that the ISS decreases when the SWCNT radius increases. Li *et. al.* also showed that SWCNT radius have effect on the ISS, but the SWCNT length is independent of the ISS (LLP⁺11). They have studied the interfacial properties between SWCNT and polymer matrix. However, the pull-out simulations based on MM simulations were carried out without considering the deformation of the polymer matrix during the pull-out process by fixing the matrix.

While the influence of certain parameters on the ISS of CNT/polymer composite has been obtained qualitatively in most of literatures, quantitative results in the context of stochastic analysis has not yet been investigated.

In this chapter, a SA is performed in order to quantify the influence of the SWCNT radius, temperature and pulling velocity on the ISS. Therefore, we compute first-order, total-effect sensitivity indices and SA based on coefficients of determination (COD) in the context of a global SA. Moreover, we approximate global SA by performing a series of local SA where we calculate partial derivatives, elementary effects and average the results. It should be noted that SA is implemented on the average ISS as presented in (LL01, GMW⁺04, CO07). The variation in the distributions of ISS along the SWCNT length is not within the scope of this study.

The chapter is outlined as follows. In the next section, we briefly describe the

4.2 Molecular dynamics model

MD model for SWCNT/polymer composites. The results of the MD model will be shown in section 4.3. In section 4.4, the numerical regression models, the COD and the sensitivity indices will be presented before we discuss the numerical results. Finally, we close the manuscript with concluding remarks.

4.2 Molecular dynamics model

4.2.1 Potential functions and parameters

The adaptive intermolecular reactive empirical bond order (AIREBO) potential in (BSH⁺02, Pli95) is adopted to consider the intra-carbon nanotube interactions.

In this work, PE is chosen as a model matrix. A united-atom model is used in which each CH_2 group is lumped into a single site to represent the molecular structure of PE. The functional form and the parameters of the intra-polymer potential are outlined in Table 2.1.

A non-bonded vdW force of the truncated Lennard-Jones (LJ) 6-12 with $\epsilon = 0.1102$ kcal/mol and $\sigma = 3.65$ Å is used to describe the interaction between the SWCNT and the PE matrix, see (WSC02).

For the bulk PE, samples consist of 20 polymer chains with 500-units (united atoms) in each chain. The SWCNT/polymer composite samples with periodic boundary condition in x, y directions are composed of a non-covalent SWCNT and an amorphous PE matrix (10,000 units of CH_2) that was created by implementing a Monte Carlo random walk growth algorithm (She06). LAMMPS (Pli95) was used to perform the equilibration process as shown in subsection 2.1.4. The simulation box after the equilibration process is a cubic space as shown in Figure 4.1. Subsequently, SMD simulations described in subsection 2.1.4 were employed to simulate the pull-out of the SWCNT from the PE matrix.

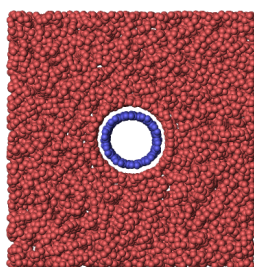


Figure 4.1: Cross section of SWCNT/PE composite

4.2 Molecular dynamics model

4.2.2 Pull-out simulations

Figure 4.2 illustrates snap-shots of the pull-out process. The PMF (pull-out energy) is computed and recorded during the pulling process. The total potential energy of SWCNT/PE system and pull-out energy are shown in Figure 2.4. The ISS can be calculated from the pull-out energy by (LL01, GMW⁺04):

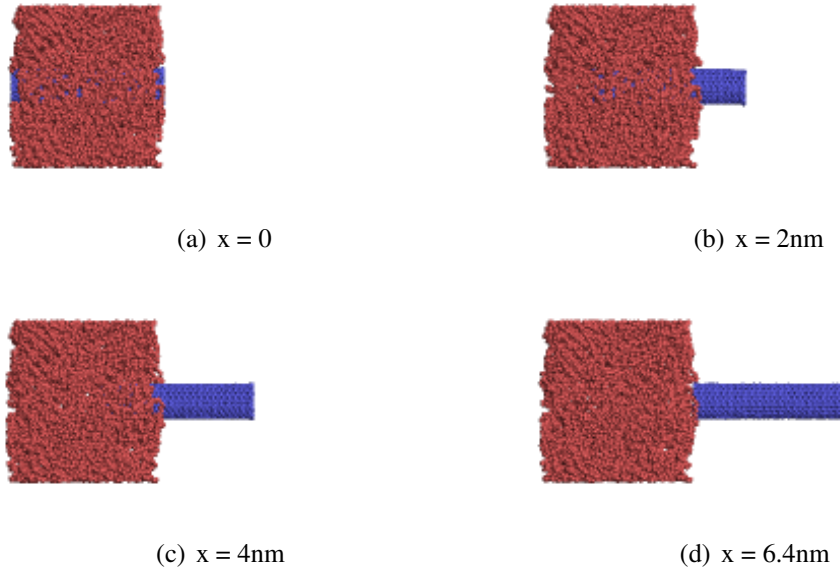


Figure 4.2: Snap shots of CNT pull-out from SWCNT/PE composite

$$E_{pullout} = \int_0^L 2\pi r(L-x)\tau_i dx = \pi r\tau_i L^2 \quad (4.1)$$

$$\tau_i = \frac{E_{pullout}}{\pi r L^2} \quad (4.2)$$

where r and L are the radius and embedded length of the SWCNT, respectively; x is the displacement of the SWCNT and τ_i is the ISS. Note that this formula gives average ISS.

The pull-out energy of SWCNT from the polymer matrix with different radii, temperatures and pulling velocities are illustrated in Figure 4.3, Figure 4.4 and Figure 4.5, respectively. Figure 4.6 shows that the ISS is independent of the simulation box size and fix-edge effect.

When the chain length ranges from 100-units to 1000-units, the density of polymer matrix is $0.87 - 0.91\text{g}/\text{cm}^3$ (VBLK⁺14, HTW⁺10). Figure 4.7 shows that the chain

4.2 Molecular dynamics model

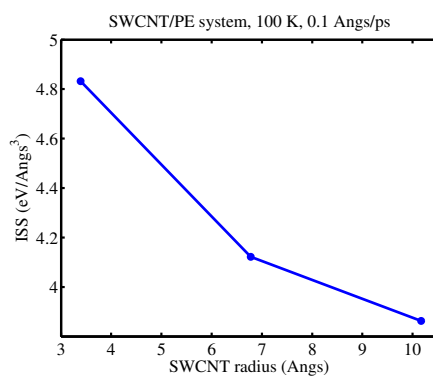


Figure 4.3: The ISS for SWCNT(5,5), SWCNT(10,10) and SWCNT(15,15) at 100 K and a pulling velocity of 0.1 Å/ps.

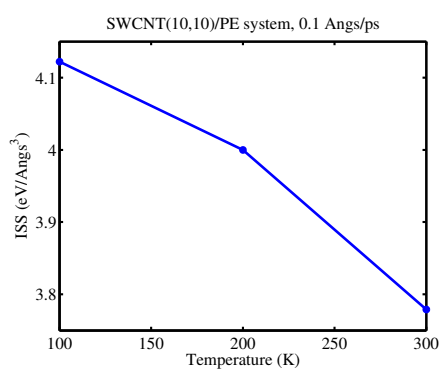


Figure 4.4: The ISS at a pulling velocity of 0.1 Å/ps for the temperature of 100K, 200K and 300K.

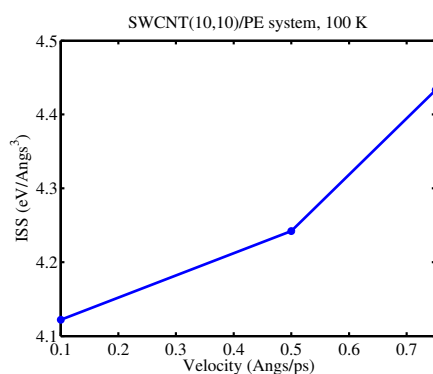


Figure 4.5: The ISS at 100 K for the pulling velocity of 0.1, 0.5 and 0.75 (Å/ps).

4.2 Molecular dynamics model

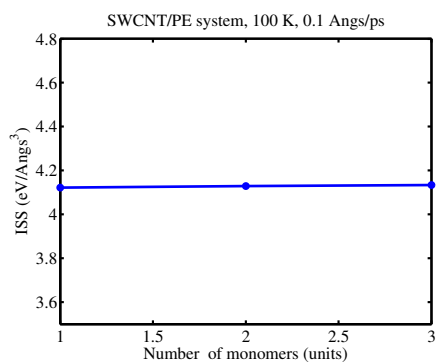


Figure 4.6: The ISS at 100 K for the simulation boxes with 10^4 , 1.5×10^4 and 2×10^4 monomeric units.

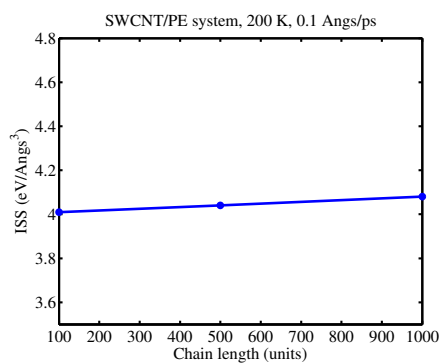


Figure 4.7: The ISS at 200 K for the chain length of 100 – *units*, 500 – *units* and 1000 – *units*.

4.3 Molecular dynamics simulation results

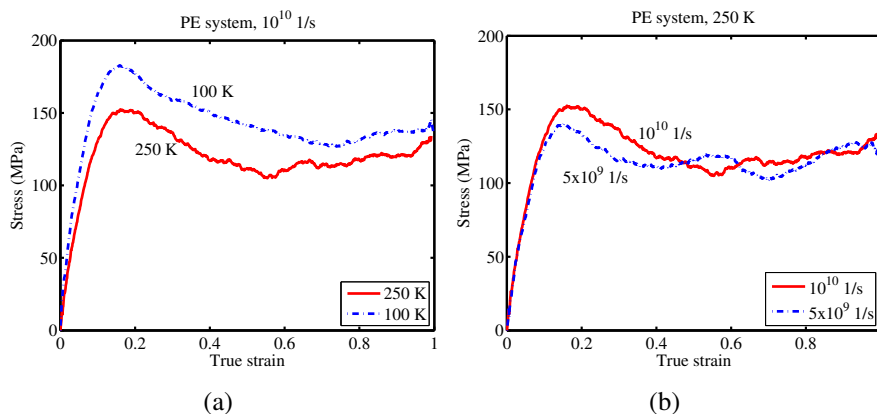


Figure 4.8: Stress–strain response at (a) different temperatures (b) different strain rates of pure PE system.

length is independent of the ISS. In our simulations, the chain length of 500-units is used.

Figure 4.8 illustrates the stress–strain response for glassy amorphous PE system for different temperatures and different strain rates. For the sake of comparison, we have simulated the PE system with 10 chains/1000-units. The results are in good agree with those in (VBLK⁺14, HTW⁺10).

4.3 Molecular dynamics simulation results

Normal distribution is typically assumed to approximate the CNT’s radius distribution (TJP⁺10). A mean diameter of 1.42 nm, and approximately 78% of the nanotubes ranging from 1.0 to 1.8 nm in diameter. As shown in Figure 4.9, an increase in the SWCNT radius results in a decrease in the PE region of the interaction with a carbon atom on the SWCNT (ZWX⁺11). Therefore, the ISS decreases with increasing SWCNT radius. The interaction between a large SWCNT radius with PE matrix can be considered the interaction of graphite sheet with PE so that the SWCNT (16,16) (radius = 10.848 Å) is chosen as upper bound and the SWCNT (4,4) (radius = 2.712 Å) as lower bound of truncated normal distribution in our MD simulations. For the sake of estimating SA, the armchair and zigzag SWCNT are chosen to ensure the SWCNT length to be nearly the same for all of samples.

The density of both the bulk PE and the composite is a function of temperature, see Wei *et. al.* (WSC02). A decrease in these densities with an increase in the temperature indicate the thermal expansions of the materials. The ISS decreases with increasing temperature, as expected. The composite behaves as a glass solid at low temperatures

4.4 Numerical results

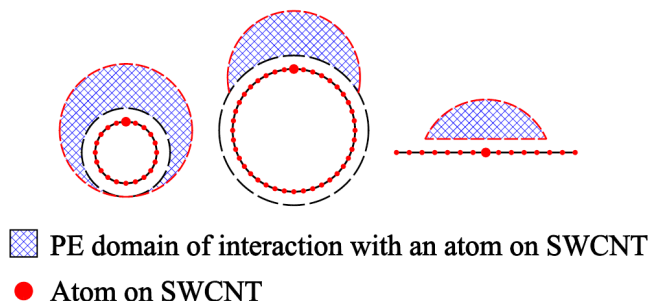


Figure 4.9: The schematic of PE region of interaction with an a carbon atom on the SWCNT (ZWX⁺11).

$T_g < 400K$ for long-chained PE, and its mechanical response is much weakened at high temperatures. Therefore, the temperature should be sufficient below the glass transition temperature and approximate the glass transition T_g . Therefore, the temperature from 100 K to 400 K assuming uniform distribution is used in our study.

Izrailevs *et. al.* (ISI⁺98) indicated that the motion of the SWCNT proceeds in the strong friction with surrounding matrix. The average applied force measures the local slope of the binding potential plus a frictional contribution that depends linearly on the pulling velocity. Therefore, the pull-out energy and the ISS depend on the pulling velocity as the average applied force depends on the pulling velocity. More details can be found in (ISI⁺98). An interfacial friction model developed by Frankland *et.al.* (FH03) shows that the average SWCNT velocity is linearly related to the average applied force. Hence, the pulling velocity influences on the ISS. The constant pull-out velocities ranging from $0.1 \text{ ps}/\text{\AA}$ to $1.0 \text{ ps}/\text{\AA}$ are examined in our MD simulations to reduce the computational cost in pull-out simulations as well as avoid the influence of molecular thermal vibration as mentioned in (FH03, ZWX⁺11). We assume a uniform distribution. The random input variables are listed in Table 4.1.

4.4 Numerical results

The schematic diagram of all sensitivity assessment methods are provided in Figure 4.10.

Scatter plots in Figure 4.11 show the influence of the SWCNT radius, temperature and pulling velocity on the ISS, respectively. The highest influence seems to be the SWCNT radius. To quantify the affect of the input parameters, the sensitivity indices were studied using the surrogate model.

Figure 4.12 shows that statistical convergence is achieved with 200 samples for all surrogate models the polynomial regression, MLS and hybrid models with appropriate

4.4 Numerical results

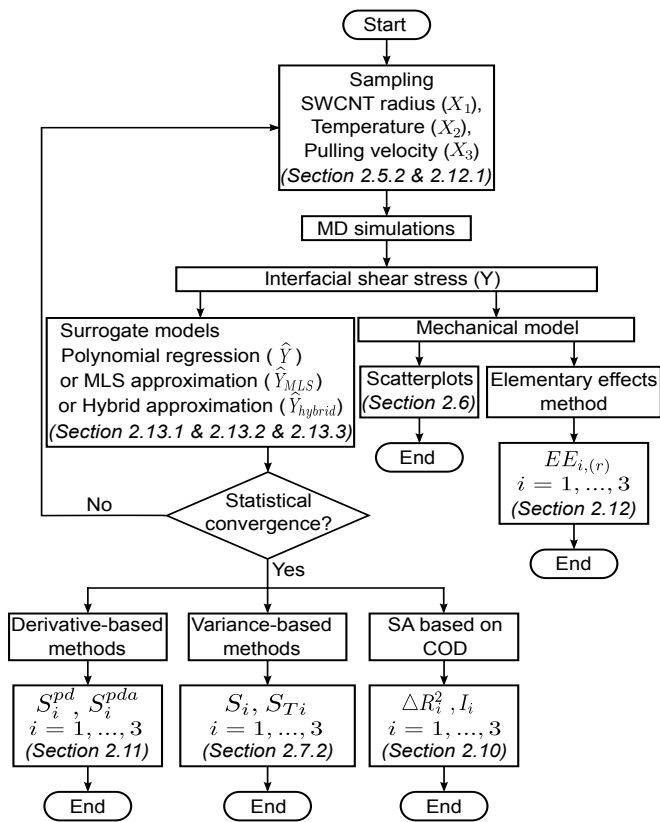


Figure 4.10: Schematic diagram of all sensitivity assessment methods presented in this paper.

4.4 Numerical results

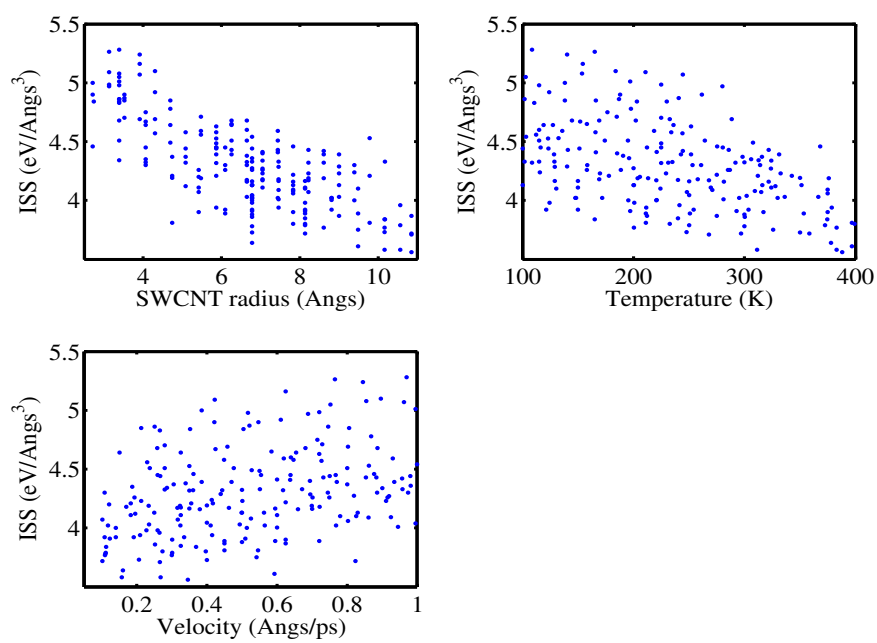
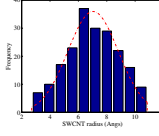
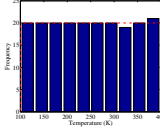
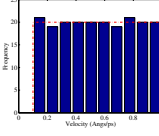


Figure 4.11: Scatter plots of the ISS (Y) versus the SWCNT radius (X_1), temperature (X_2) and pulling velocity (X_3), respectively.

4.4 Numerical results

Table 4.1: Model uncertainties

Input parameters	SWCNT radius	Temperature	Pulling velocity
Type of distribution			
Mean value	7.1	250	0.55
Standard deviation	2	$300/\sqrt{12}$	$0.9/\sqrt{12}$
Source	(TJP+10)	assumed	assumed

chosen radius (normalized radius of 0.6).

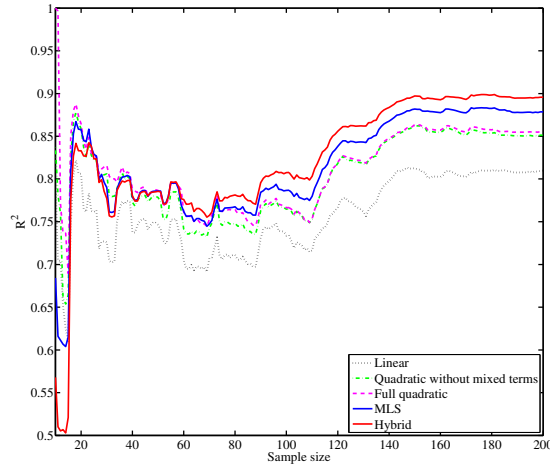


Figure 4.12: The plot of R^2 versus the number of samples when polynomial regression, MLS and hybrid models are used

In the following, the surrogate models are built to approximate the output of the mechanical model (200 samples). The COD R^2 and adjusted COD R_{adj}^2 in accordance with the linear, quadratic (with and without mixed terms), MLS and hybrid regression models are calculated and it is demonstrated that the predicted response using the surrogate models are good approximations of the response of the mechanical model, see Table 4.2.

As listed in Table 4.2, the COD is 0.90 for hybrid method, 0.88 for MLS with appropriate chosen radius (normalized radius of 0.6) and 0.86 (0.85) for quadratic (full and without mixed terms) regression, indicating that the surrogate model reflects al-

4.4 Numerical results

most exactly the response of the mechanical model. In other words, 90 %, 88 %, 86 (85)% of the ISS variation are represented by the hybrid the MLS and quadratic (with and without mixed terms) regression models, respectively. The obtained R^2 , R_{adj}^2 by using linear regression is 0.82 which is slightly lower than by the other methods. We have used the full quadratic regression model in this paper for further comparison.

Three-dimensional scatter plots and the associated surrogate models are shown in dependence of the SWCNT radius and temperature, pulling velocity in Figures 4.13 (full quadratic), 4.14 (MLS) and 4.15 (hybrid). The steepest gradient in the SWCNT radius direction indicates the SWCNT radius is a key parameter for the ISS.

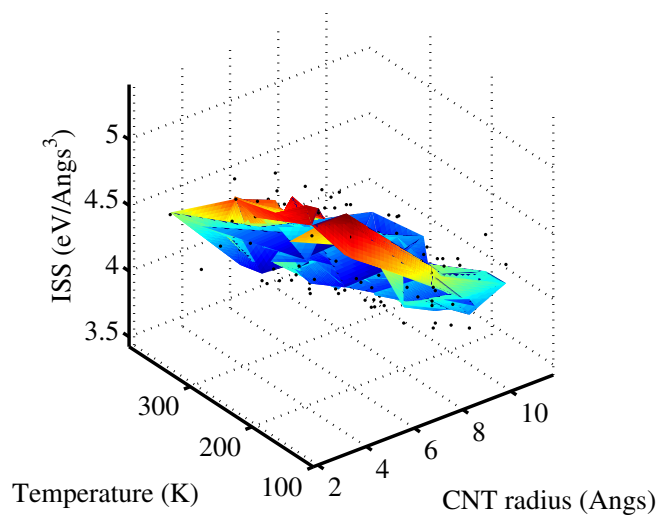
Table 4.2: Regression coefficient, COD R^2 and adjusted COD R_{adj}^2

Response surface methods	Regression coefficient
Linear regression $R^2 = 0.81$ $R_{adj}^2 = 0.81$	$\beta_0 = 5.27e-4$ $\beta_1 = -1.21e-5$ $\beta_2 = -1.80e-7$ $\beta_3 = 4.76e-5$
Quadratic without mixed terms $R^2 = 0.85$ $R_{adj}^2 = 0.85$	$\beta_0 = 5.66e-4$ $\beta_1 = -3.34e-5$ $\beta_2 = -3.19e-8$ $\beta_3 = 8.59e-5$ $\beta_{11} = 1.64e-6$ $\beta_{22} = -3.14e-10$ $\beta_{33} = -3.24e-5$
Full quadratic $R^2 = 0.86$ $R_{adj}^2 = 0.86$	$\beta_0 = 5.76e-4$ $\beta_1 = -3.39e-5$ $\beta_2 = -1.07e-7$ $\beta_3 = 8.93e-5$ $\beta_{11} = 1.48e-6$ $\beta_{22} = -3.81e-10$ $\beta_{33} = -3.47e-5$ $\beta_{12} = 1.35e-8$ $\beta_{13} = -1.25e-6$ $\beta_{23} = 2.90e-8$
Moving least squares $R^2 = 0.88$ $R_{adj}^2 = 0.88$	
Hybrid model of polynomial regression and MLS $R^2 = 0.90$ $R_{adj}^2 = 0.90$	

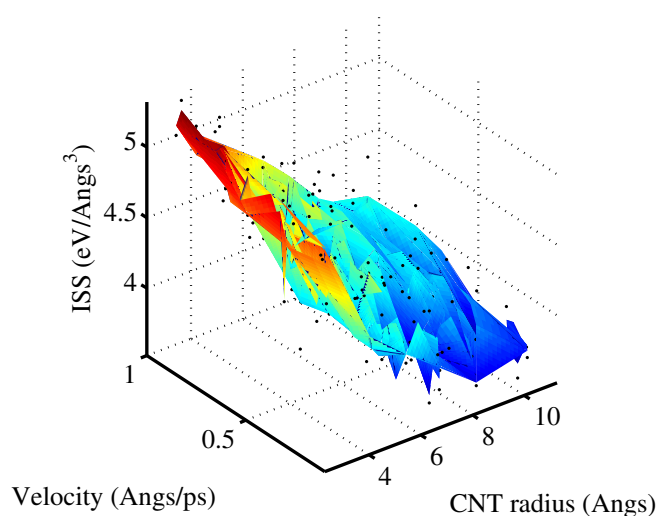
4.4.1 Derivative-based approach

The full quadratic surrogate model is used for this method. The interval [0,1] is split into 9 equal sized sub-intervals and placing X_i at each points. By applying the inverse

4.4 Numerical results



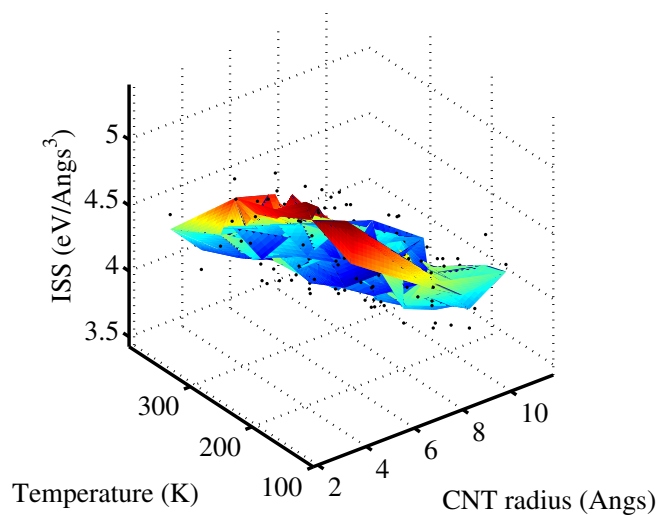
(a)



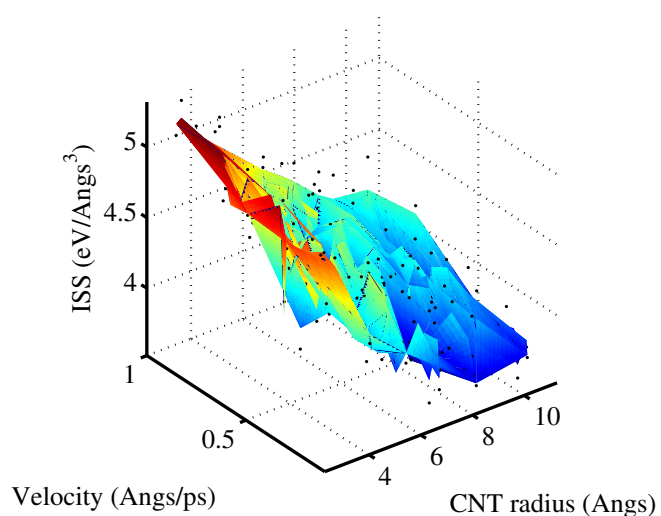
(b)

Figure 4.13: Scatter points got from MD simulations (black points) and projection surface of surrogate model which express the ISS versus the SWCNT radius and temperature (a) and the ISS versus the SWCNT radius and pulling velocity (b). In this figure, the full quadratic regression is used.

4.4 Numerical results



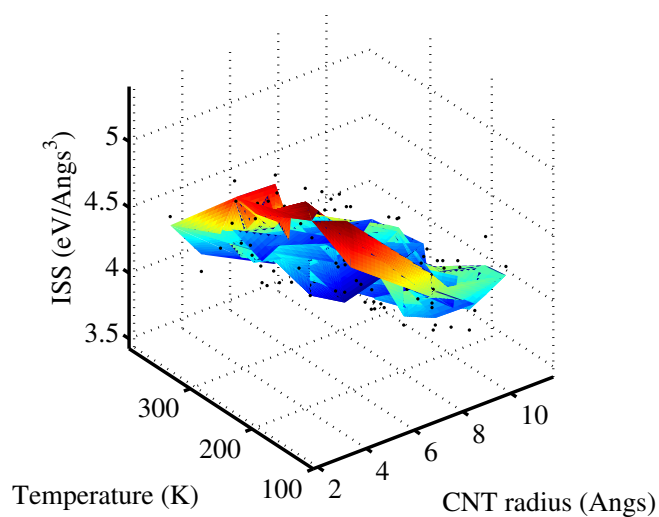
(a)



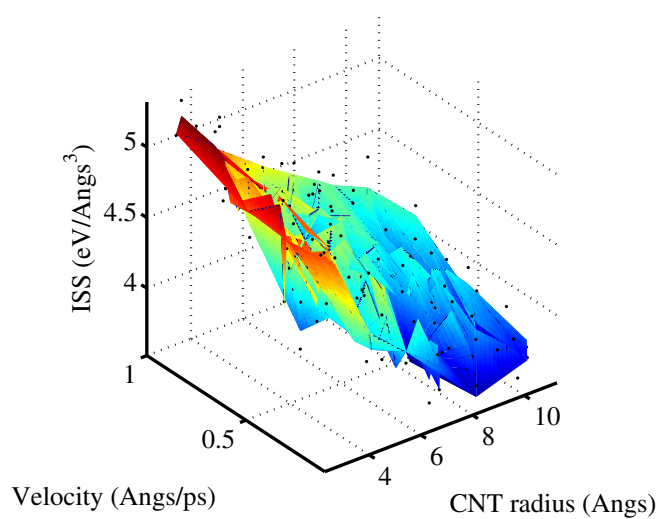
(b)

Figure 4.14: Scatter points got from MD simulations (black points) and projection surface of surrogate model which express the ISS versus the SWCNT radius and temperature (a) and the ISS versus the SWCNT radius and pulling velocity (b). In this figure, the MLS is used.

4.4 Numerical results



(a)



(b)

Figure 4.15: Scatter points got from MD simulations (black points) and projection surface of surrogate model which express the ISS versus the SWCNT radius and temperature (a) and the ISS versus the SWCNT radius and pulling velocity (b). In this figure, the hybrid model is used

4.4 Numerical results

cumulative function we obtain a 10-level grid for three input parameters (SWCNT radius (X_1), temperature (X_2) and pulling velocity (X_3)) in the interval. We evaluate \mathbf{Y} twice: first at X_i and second at $X_i + \Delta X_i$ with $\Delta X_i = 10^{-4}$. The partial derivatives are computed by Equations (2.137) and (2.138) for two cases: (1) keeping the other parameters fixed; (2) considering the variation of other parameters, respectively. Flowcharts of these processes are provided in Figure 2.19. Then, the partial derivatives are normalized w.r.t an input factor, e.g., \bar{X}_1 in this example named $S_{X_i}^{\bar{X}_1}$, $i = 1, 2, 3$ as follows

$$S_{X_1}^{\bar{X}_1,(pd)} = \left(\frac{1}{N} \sum_{s=1}^N \frac{\partial \mathbf{Y}_s}{\partial X_1} \right) \quad (4.3a)$$

$$S_{X_1}^{\bar{X}_1,(pda)} = \left(\frac{1}{N^3} \sum_{s=1}^N \sum_{j=1}^N \sum_{l=1}^N \frac{\partial \mathbf{Y}_s}{\partial X_1} \right) \quad (4.3b)$$

$$S_{X_2}^{\bar{X}_1,(pd)} = \left(\frac{1}{N} \sum_{s=1}^N \frac{\partial \mathbf{Y}_s}{\partial X_2} \right) \frac{X_2}{\bar{X}_1} \quad (4.4a)$$

$$S_{X_2}^{\bar{X}_1,(pda)} = \left(\frac{1}{N^3} \sum_{j=1}^N \sum_{s=1}^N \sum_{l=1}^N \frac{\partial \mathbf{Y}_j}{\partial X_2} \right) \frac{X_2}{\bar{X}_1} \quad (4.4b)$$

$$S_{X_3}^{\bar{X}_1,(pd)} = \left(\frac{1}{N} \sum_{s=1}^N \frac{\partial \mathbf{Y}_s}{\partial X_3} \right) \frac{X_3}{\bar{X}_1} \quad (4.5a)$$

$$S_{X_3}^{\bar{X}_1,(pda)} = \left(\frac{1}{N^3} \sum_{l=1}^N \sum_{s=1}^N \sum_{j=1}^N \frac{\partial \mathbf{Y}_l}{\partial X_3} \right) \frac{X_3}{\bar{X}_1} \quad (4.5b)$$

These normalized partial derivatives (NPD) $\hat{S}_{X_i}^{\bar{X}_1}$, $i = 1, 2, 3$ are reduced by the COD R^2

$$\hat{S}_{X_1}^{\bar{X}_1,(pd)} = R^2 S_{X_1}^{\bar{X}_1,(pd)} \quad (4.6a)$$

$$\hat{S}_{X_1}^{\bar{X}_1,(pda)} = R^2 S_{X_1}^{\bar{X}_1,(pda)} \quad (4.6b)$$

$$\hat{S}_{X_2}^{\bar{X}_1,(pd)} = R^2 S_{X_2}^{\bar{X}_1,(pd)} \quad (4.7a)$$

$$\hat{S}_{X_2}^{\bar{X}_1,(pda)} = R^2 S_{X_2}^{\bar{X}_1,(pda)} \quad (4.7b)$$

4.4 Numerical results

$$\hat{S}_{X_3}^{\bar{X}_1,(pd)} = R^2 S_{X_3}^{\bar{X}_1,(pd)} \quad (4.8a)$$

$$\hat{S}_{X_3}^{\bar{X}_1,(pda)} = R^2 S_{X_3}^{\bar{X}_1,(pda)} \quad (4.8b)$$

Table 4.3 shows the average of the reduced normalized partial derivatives (ARNPD) of the ISS versus the input parameters. Since the partial derivatives $\hat{S}_{X_i}^{\bar{X}_1,(pd)}$ are the same as the partial derivatives $\hat{S}_{X_i}^{\bar{X}_1,(pda)}$, $i = 1, 2, 3$, there is no interaction between the input parameters. The key input factor is the SWCNT radius ($\overline{\hat{N}S}_{X_1}^{\bar{X}_1,(pd)} = 0.50$) followed by the temperature ($\overline{\hat{N}S}_{X_2}^{\bar{X}_1,(pd)} = 0.35$). The pulling velocity has smaller influence on the ISS ($\overline{\hat{N}S}_{X_3}^{\bar{X}_1,(pd)} = 0.15$).

Table 4.3: Normalized average of reduced NPD for the ISS

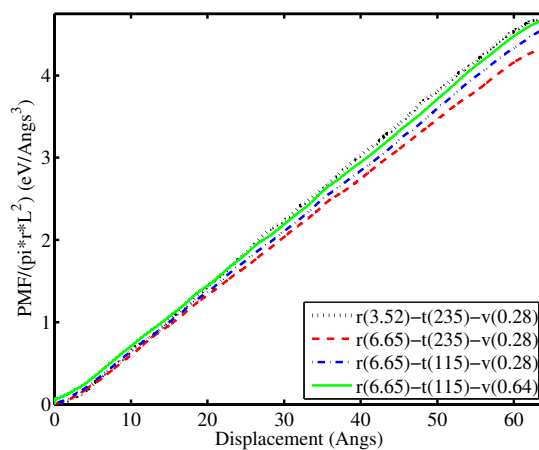
Normalized value of ARNPD calculated by Eqs. (4.6a), (4.7a), (4.8a)	Normalized value of ARNPD calculated by Eqs. (4.6b), (4.7b), (4.8b)
$\overline{\hat{N}S}_{X_i}^{\bar{X}_1,(pd)} = \frac{\overline{\hat{S}_{X_i}^{\bar{X}_1,(pd)}}}{\sum_{i=1}^3 \overline{\hat{S}_{X_i}^{\bar{X}_1,(pd)}}}$	$\overline{\hat{N}S}_{X_i}^{\bar{X}_1,(pda)} = \frac{\overline{\hat{S}_{X_i}^{\bar{X}_1,(pda)}}}{\sum_{i=1}^3 \overline{\hat{S}_{X_i}^{\bar{X}_1,(pda)}}}$
$\overline{\hat{N}S}_{X_1}^{\bar{X}_1,(pd)} = 0.50$	$\overline{\hat{N}S}_{X_1}^{\bar{X}_1,(pda)} = 0.51$
$\overline{\hat{N}S}_{X_2}^{\bar{X}_1,(pd)} = 0.35$	$\overline{\hat{N}S}_{X_2}^{\bar{X}_1,(pda)} = 0.34$
$\overline{\hat{N}S}_{X_3}^{\bar{X}_1,(pd)} = 0.15$	$\overline{\hat{N}S}_{X_3}^{\bar{X}_1,(pda)} = 0.15$

4.4.2 Elementary effects

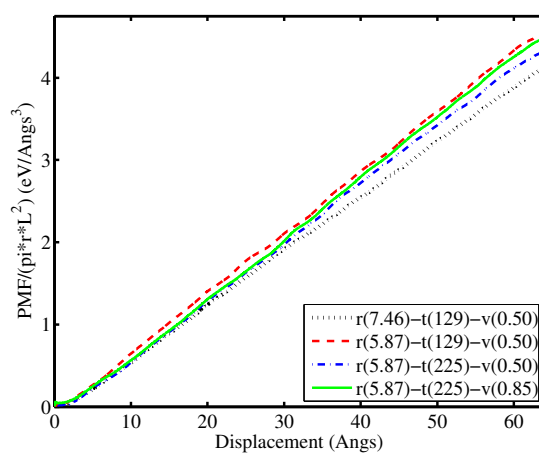
The elementary effects are calculated based on the mechanical model for 9 trajectories and 4 samples in each trajectory. So it is totally 36 samples tested. For the sake of comparison, the pull-out energy is reduced by $\pi r L^2$ as shown from Figure 4.16 to 4.18. Each of these figures corresponds to 4 points of a trajectory. Note that the legend rad(3.52) - temp(235) - vel(0.28) e.g., in the Figure 4.16 expresses the SWCNT radius (X_1) = 3.52 Å, temperature (X_2) = 235 K and pulling velocity (X_3) = 0.28 Å/ps.

Table 4.4 shows the elementary effects relative to parameter i , $i = 1, 2, 3$ computed along trajectory r , $r = 1, \dots, 9$, the average \overline{EE}_i and the normalized value of the average \overline{NEE}_i . The SWCNT radius is observed as the key factor ($\overline{NEE}_1 = 0.476$) on the ISS followed by the temperature ($\overline{NEE}_2 = 0.329$). The influence of the pulling velocity on the ISS is small ($\overline{NEE}_3 = 0.195$).

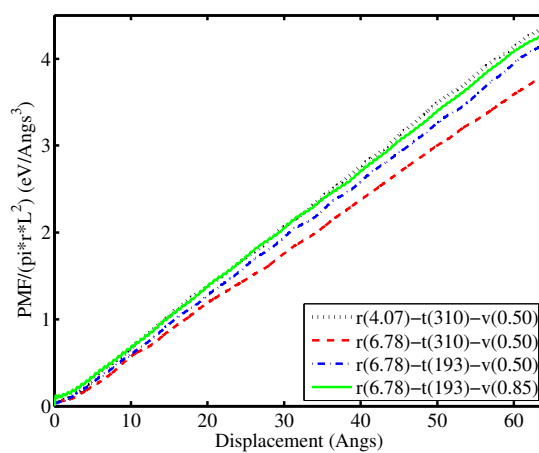
4.4 Numerical results



(a)



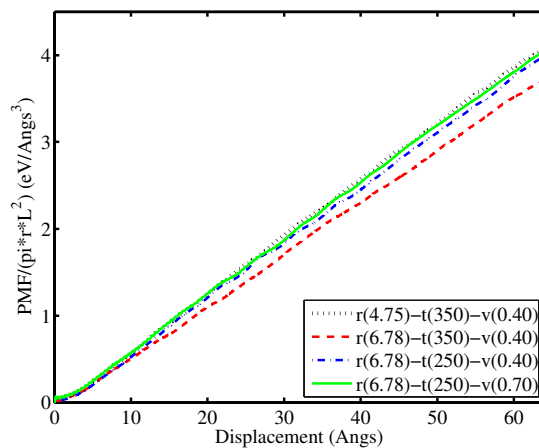
(b)



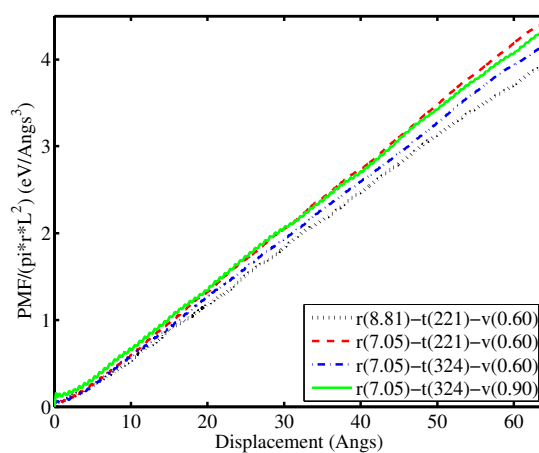
(c)

Figure 4.16: Reduced pull-out energy of three trajectories (a) trajectory 1, (b) trajectory 2 and (c) trajectory 3

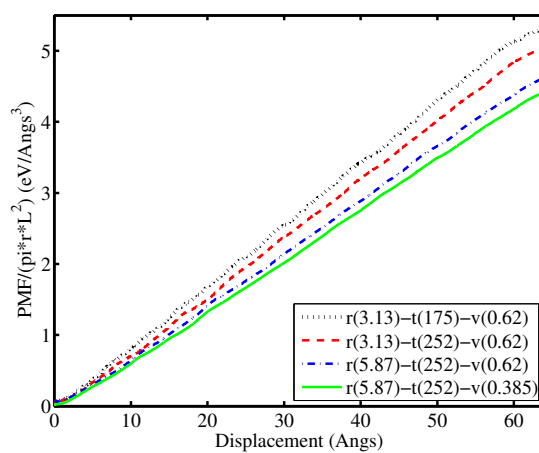
4.4 Numerical results



(a)



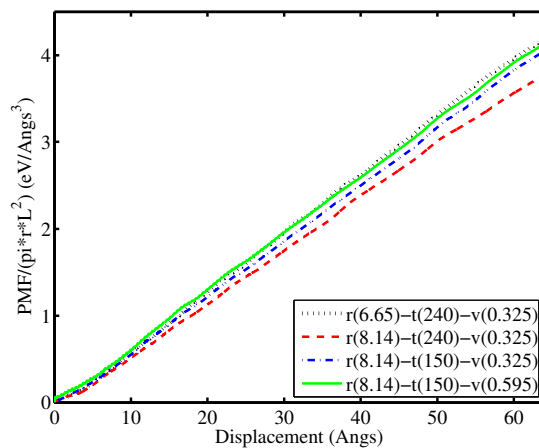
(b)



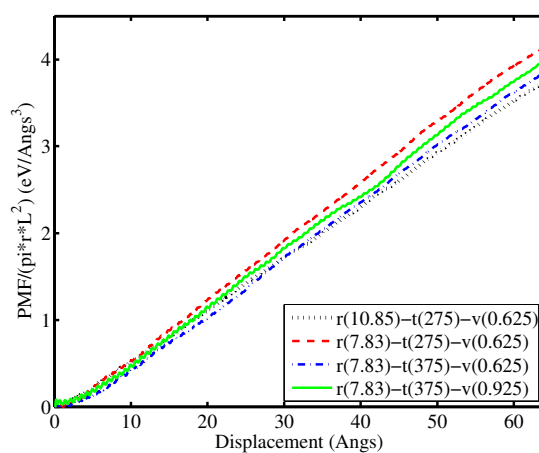
(c)

Figure 4.17: Reduced pull-out energy of three trajectories (a) trajectory 4, (b) trajectory 5 and (c) trajectory 6

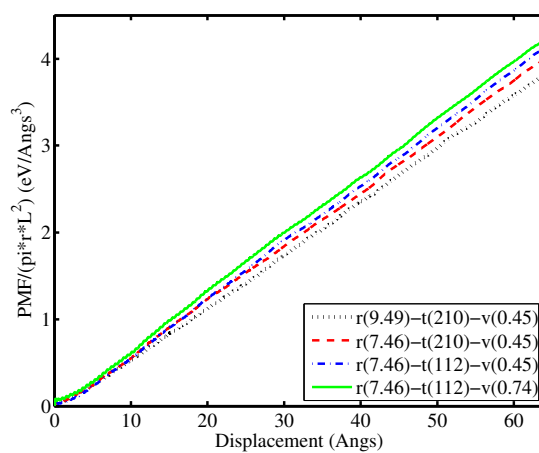
4.4 Numerical results



(a)



(b)



(c)

Figure 4.18: Reduced pull-out energy of three trajectories (a) trajectory 7, (b) trajectory 8 and (c) trajectory 9

4.4 Numerical results

Table 4.4: Elementary effects for the ISS

Trajectory \ Elementary effects	$EE_{1,(r)} \times 10^{-3}$	$EE_{2,(r)} \times 10^{-3}$	$EE_{3,(r)} \times 10^{-3}$
Trajectory 1	0.08	0.05	0.03
Trajectory 2	0.11	0.07	0.05
Trajectory 3	0.12	0.08	0.04
Trajectory 4	0.11	0.09	0.03
Trajectory 5	0.13	0.09	0.07
Trajectory 6	0.16	0.11	0.08
Trajectory 7	0.13	0.08	0.04
Trajectory 8	0.13	0.10	0.06
Trajectory 9	0.05	0.04	0.03
Average elementary effects	$\overline{EE}_1 = 0.110$	$\overline{EE}_2 = 0.076$	$\overline{EE}_3 = 0.045$
Normalized $\frac{NEE_i}{\sum_{i=1}^3 \overline{EE}_i}$	$\overline{NEE}_1 = 0.476$	$\overline{NEE}_2 = 0.329$	$\overline{NEE}_3 = 0.195$
Note: $EE_{1,(r)}$, $EE_{2,(r)}$, $EE_{3,(r)}$ indicate the elementary effects of the ISS relative to the SWCNT radius (X_1), temperature (X_2) and pulling velocity (X_3) computed along trajectory r , respectively.			

4.4.3 Sensitivity analysis based on coefficients of determination

In order to evaluate the importance of variables, we use the SA based coefficients of determination approach by leaving out terms containing X_1 , X_2 and X_3 from the full quadratic regression basis and compute the corresponding CODs, drop values ΔR_i^2 , $i = 1, 2, 3$ of reduced models, Equations (2.135) and (2.136). For example, carrying out a regression on the reduced full quadratic model containing X_2 , X_3 , the reduced quadratic model is given by

$$\hat{Y} = \beta_0 + \beta_2 X_2 + \beta_3 X_3 + \beta_{22} X_2^2 + \beta_{33} X_3^2 + \beta_{23} X_2 X_3, \quad (4.9)$$

The above model results in a COD (R_1^2) and an adjusted COD (R_{adj1}^2). The reduced MLS and hybrid regression models are constructed in the same fashion. The corresponding CODs, adjusted CODs, drop values ΔR_i^2 and normalized values I_i of ΔR_i^2 are listed in Table 4.5.

As shown in Table 4.5, the big drop in the value of R^2 and R_{adj}^2 when removing terms X_1 , X_1^2 , $X_1 X_2$, $X_1 X_3$ from the regression shows the relative importance of the SWCNT radius (X_1) compared to the others. The insignificant decrease in R^2 and R_{adj}^2 when removing terms associated either the variable X_2 or the variable X_3 indicates that the temperature has less influence on the ISS compared to the SWCNT radius. The influence of the pulling velocity on the ISS is smallest.

4.4 Numerical results

Table 4.5: The COD, adjusted COD, drop value of COD, and the coefficient of importance of the reduced quadratic polynomial, the reduced MLS and the reduced hybrid models

The reduced model containing X_2, X_3	The reduced model containing X_1, X_3	The reduced model containing X_1, X_2
The reduced quadratic polynomial model		
$R_1^2 = 0.39$ $R_{adj1}^2 = 0.39$ $\Delta R_1^2 = 0.47$ $I_1 = 0.54$	$R_2^2 = 0.70$ $R_{adj2}^2 = 0.70$ $\Delta R_2^2 = 0.16$ $I_2 = 0.18$	$R_3^2 = 0.74$ $R_{adj3}^2 = 0.74$ $\Delta R_3^2 = 0.12$ $I_3 = 0.13$
The reduced MLS model		
$R_1^2 = 0.41$ $R_{adj1}^2 = 0.39$ $\Delta R_1^2 = 0.46$ $I_1 = 0.53$	$R_2^2 = 0.70$ $R_{adj2}^2 = 0.69$ $\Delta R_2^2 = 0.16$ $I_2 = 0.19$	$R_3^2 = 0.76$ $R_{adj3}^2 = 0.75$ $\Delta R_3^2 = 0.10$ $I_3 = 0.12$
The reduced hybrid model		
$R_1^2 = 0.41$ $R_{adj1}^2 = 0.39$ $\Delta R_1^2 = 0.46$ $I_1 = 0.53$	COD $R_2^2 = 0.70$ $R_{adj2}^2 = 0.69$ $\Delta R_2^2 = 0.16$ $I_2 = 0.19$	$R_3^2 = 0.76$ $R_{adj3}^2 = 0.75$ $\Delta R_3^2 = 0.10$ $I_3 = 0.12$
Note: $R_1^2, R_{adj1}^2, \Delta R_1^2$ and I_1 are the COD, the adjusted COD, the drop value of COD and the coefficient of importance when the SWCNT radius (X_1) is removed from the regression model, respectively. $R_2^2, R_{adj2}^2, \Delta R_2^2$ and I_2 are the COD, the adjusted COD, the drop value of COD and the coefficient of importance when the temperature (X_2) is removed from the regression model, respectively. $R_3^2, R_{adj3}^2, \Delta R_3^2$ and I_3 are the COD, the adjusted COD, the drop value of COD and the coefficient of importance when the pulling velocity (X_3) is removed from the regression model, respectively.		

4.4.4 Global sensitivity analysis

Based on the determined surrogate models, we generated 50000 Latin hypercube samples. The regression based sensitivity indices by using those samples as approximation points are given in Table 4.6. The sensitivity indices S_i and S_{T_i} , $i = 1, 2, 3$, Equations (2.65) and (2.68), are calculated in accordance with the polynomial regression, the MLS and the hybrid approximation. These values are reduced by the COD inferring that only $R^2\%$ of response can be explained with surrogate model. The reduced sensitivity indices \hat{S}_i and \hat{S}_{T_i} are given by

$$\hat{S}_i = R^2 S_i \quad (4.10a)$$

$$\hat{S}_{T_i} = R^2 S_{T_i} \quad (4.10b)$$

The results of the variance-based methods are summarized in Table 4.6 and illustrated in Figure 4.19. They show:

4.5 Conclusions

Table 4.6: First-order and total effects sensitivity indices computed on the surrogate model of the input parameters contributing to the ISS

Linear regression model	Quadratic without mixed terms	Full quadratic	MLS	Hybrid
First-order indices \hat{S}_i $\hat{S}_1 = 0.44$ $\hat{S}_2 = 0.23$ $\hat{S}_3 = 0.14$ $\sum_{i=1}^3 \hat{S}_i = 0.81$	First-order indices \hat{S}_i $\hat{S}_1 = 0.41$ $\hat{S}_2 = 0.26$ $\hat{S}_3 = 0.17$ $\sum_{i=1}^3 \hat{S}_i = 0.84$	First-order indices \hat{S}_i $\hat{S}_1 = 0.41$ $\hat{S}_2 = 0.27$ $\hat{S}_3 = 0.17$ $\sum_{i=1}^3 \hat{S}_i = 0.85$	First-order indices \hat{S}_i $\hat{S}_1 = 0.41$ $\hat{S}_2 = 0.30$ $\hat{S}_3 = 0.15$ $\sum_{i=1}^3 \hat{S}_i = 0.86$	First-order indices \hat{S}_i $\hat{S}_1 = 0.40$ $\hat{S}_2 = 0.30$ $\hat{S}_3 = 0.16$ $\sum_{i=1}^3 \hat{S}_i = 0.86$
Total-effect indices \hat{S}_{Ti} $\hat{S}_{T1} = 0.44$ $\hat{S}_{T2} = 0.23$ $\hat{S}_{T3} = 0.15$ $\sum_{i=1}^3 \hat{S}_{Ti} = 0.82$	Total-effect indices \hat{S}_{Ti} $\hat{S}_{T1} = 0.41$ $\hat{S}_{T2} = 0.27$ $\hat{S}_{T3} = 0.17$ $\sum_{i=1}^3 \hat{S}_{Ti} = 0.85$	Total-effect indices \hat{S}_{Ti} $\hat{S}_{T1} = 0.42$ $\hat{S}_{T2} = 0.27$ $\hat{S}_{T3} = 0.17$ $\sum_{i=1}^3 \hat{S}_{Ti} = 0.87$	Total-effect indices \hat{S}_{Ti} $\hat{S}_{T1} = 0.41$ $\hat{S}_{T2} = 0.29$ $\hat{S}_{T3} = 0.17$ $\sum_{i=1}^3 \hat{S}_{Ti} = 0.88$	Total-effect indices \hat{S}_{Ti} $\hat{S}_{T1} = 0.44$ $\hat{S}_{T2} = 0.31$ $\hat{S}_{T3} = 0.17$ $\sum_{i=1}^3 \hat{S}_{Ti} = 0.92$
<small>Note: \hat{S}_1 and \hat{S}_{T1} are the reduced first-order and total-effect indices of the ISS (\mathbf{Y}) due to the SWCNT radius (X_1), respectively. \hat{S}_2 and \hat{S}_{T2} are the reduced first-order and total-effect indices of the ISS (\mathbf{Y}) due to the temperature (X_2), respectively. \hat{S}_3 and \hat{S}_{T3} are the reduced first-order and total-effect indices of the ISS (\mathbf{Y}) due to the pulling velocity (X_3), respectively.</small>				

1. The reduced first-order indices \hat{S}_i and reduced total-effect indices \hat{S}_{Ti} are nearly identical indicating the independence of the input-parameters. These results agree very well with results of the derivative-based approach.
2. All surrogate models are suitable to study SA. The highest COD is obtained by the hybrid model (0.90) followed by the MLS-approach (0.88), the quadratic (with and without mixed terms) regression model (0.86 and 0.85) and the linear regression model (0.82); Table 4.2.
3. The SWCNT radius is the most influential parameter followed by the temperature and pulling velocity, respectively. The ratio $\hat{S}_{T2}/\hat{S}_{T1}$ is with a value of 0.64 slightly lower compared to the value of the derivative-based approach and elementary effects (0.69). While the ratio $\hat{S}_{T3}/\hat{S}_{T1} = 0.4$ is identical to the ratio of the elementary effects, it is higher than the value of the derivative-based method (0.30), see Tables (4.6 + 4.4 + 4.3).

4.5 Conclusions

The mechanical properties of SWCNT/PE composites have been obtained by using MD simulations. The mechanical output (ISS) is best characterized by the Log-normal distribution. Based on the mechanical and surrogate models, the influence of the SWCNT radius, temperature and pulling velocity on the ISS in the context of both averaged local and global SA is quantitatively studied.

4.5 Conclusions

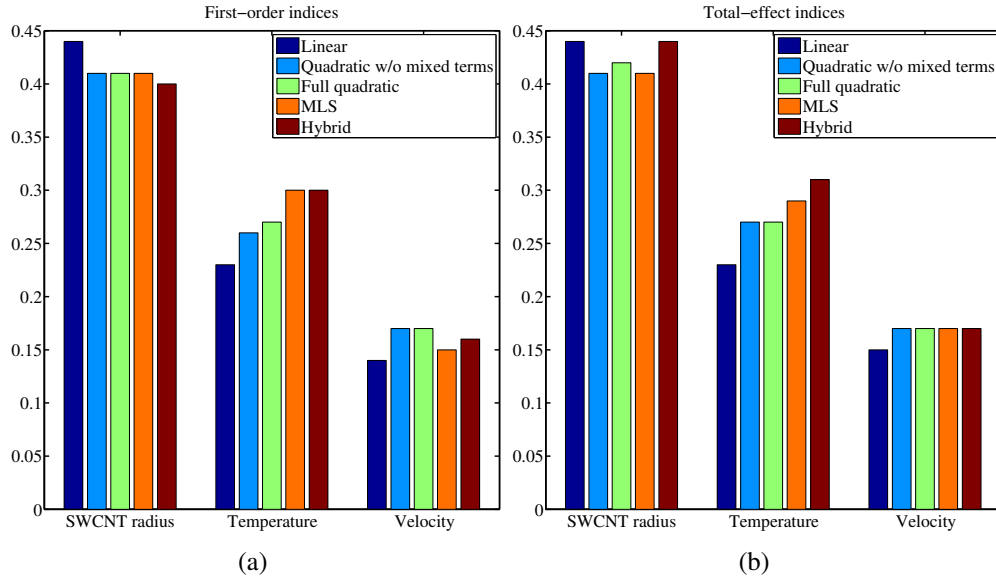


Figure 4.19: Sensitivity indices (a) First-order (b) Total effect

For the examples studied, the elementary-effects method requires less samples than the other methods. However, it fails to estimate the mutual interaction of the input parameters. The variance-based method is a global SA method that can be used for such purpose.

The regression methods are robust methods because they do not require a large number of samples number of input parameters.

The hybrid and MLS surrogate models are good approximations of the mechanical model. However, the adjustment of the influence radius D used in hybrid and MLS surrogate models remains an open issue.

All methods predict the same tendencies, i.e.:

1. The most influential parameter on the ISS is the SWCNT radius, followed by the temperature.
2. The pulling velocity has relatively small influence on the ISS.

Chapter 5

Uncertainty quantification for multiscale modeling of polymer nanocomposites with correlated parameters

5.1 Introduction

Carbon nanotubes (CNTs) are ideal reinforcement materials for polymeric composites due to their superior mechanical and electrical properties as well as their light weight (SW99, Dai02, LGH06). Substantial progress obtained from experiment studies were recently summarized by Thostenson *et al.* (TLC05). However, there remains a great challenge in the structural characterization and fabrication of polymer nanocomposites (PNCs) at nano-scales (ZYL08). Analytical and numerical simulations have been employed to assist the design of PNCs, and *a priori* prediction of their mechanical properties. Numerous micromechanical models have been developed to predict the mechanical properties of PNCs. As have been shown by Odegard and co-workers (OGW⁺03), the direct use of continuum micromechanical models might be inadequate to predict the mechanical properties of PNCs since the micromechanical models do not consider the lattice structure of the CNT but simplify it as a solid fiber. Furthermore, a continuum micromechanical model often assumes perfect bonding between the fibers and the matrix. Hence, it cannot capture the effect from the interphase between the CNT and the polymer matrix that is dominated by van der Waals (vdW) interactions (Gib07). In order to address these issues, Shokrieh and Rafiee (SR10b, SR10a) developed a transversely isotropic equivalent fiber (EF).

Due to the high aspect ratio and low bending stiffness of the CNTs, they normally exist in non-straight shape (LGSea04, GWFS). As shown by micrograph im-

5.1 Introduction

ages (FBB03), the embedded CNTs exhibit significant curvature. Several studies (FBB03, BFB03, AG06) have been carried out to investigate the influence of CNT curvature on the effective modulus of PNCs. Often a nanotube was substituted by a solid continuum fiber. Thus, the effect of the fiber waviness on their mechanical properties was studied instead of that of the CNT waviness. The results showed that the effective modulus of PNCs can be significantly degraded with an increasing fiber waviness. Most of previous researchers limited their studies to a sinusoidal waviness pattern that may improperly estimate the effects of the fiber waviness on the mechanical properties. This issue will be addressed in the numerical results and discussion section 5.4. Since the CNTs are concentrated in local regions due to van der Waals (vdW) interactions between CNTs and also due to the non-uniform dispersion of the CNTs during processing, local bundles of CNTs within the polymer matrix are formed. The PNCs were modeled as random heterogeneous media and homogenization models have been applied at the lower scale to determine their local material properties. Shi *et al.* (SFH⁺04) developed a two-parameter approach in combination with the Mori-Tanaka model to determine the influence of the agglomeration of CNTs on the mechanical properties of PNCs.

Several approaches have been developed to predict the mechanical properties of PNCs. However, the predicted mechanical properties were found significantly deviating from the measured values in experiments. The discrepancy was later discussed and explained by multiscale Monte-Carlo finite element simulations (SK08). The authors indicated that some induced uncertainties neglected by the deterministic approaches. However, in their stochastic multiscale model, only the volume fraction was considered as a random parameter whereas other parameters such as the CNT length, the orientation, the agglomeration, the waviness, and dispersion of CNTs were considered deterministic. A stochastic multiscale approach was also used by (SR10c) to predict mechanical properties of PNCs. This study allowed realizing the scale difference between micro and nano that was not modeled for PNCs on micro-level (FHO⁺03, VM07, HE07).

This chapter presents a comprehensive stochastic multiscale method to quantitatively determine the influence of many input parameters on the mechanical properties of PNCs. Sensitivity analysis (SA) methods are developed from the classical Sobol's estimator (Sob93) to quantify the influences of the correlated (dependent) input parameters on the Young's modulus and Poisson's ratio of PNCs. Six important parameters at the corresponding scales are selected: the single-walled carbon nanotube (SWNT) length (L_{SWNT}), the averaged longitudinal modulus (E_{LEF}) and transverse modulus of EF (E_{TEF}) being representative of the waviness parameters, the agglomeration parameters (ξ , ζ) and the volume fraction (V_f). To reduce computational cost, surrogate models are constructed to approximate the mechanical model and the SA was performed on the surrogate models.

The content of this chapter is outlined as follows. In the next section, we briefly

5.2 Multiscale model

describe the multiscale model. Section 5.3 presents the complete statistical distribution for each input parameter. The coefficients of surrogate model and sensitivity indices will be shown in section 5.4 before the discussion on the numerical results. Finally, we close the manuscript with concluding remarks.

5.2 Multiscale model

In this section, we briefly describe the bottom-up hierarchical multiscale method for PNCs connecting all scales of the nano-, micro-, meso- and macro-scale, see Figure 5.1. The stochastic multiscale approach is employed to consider effective parameters of different scales as uncertainties. In the nano-scale, material properties and the structure of the SWNT are considered. In the micro-scale, the SWNT embedded in the polymer matrix in the presence of the interphase is modeled and replaced by an EF. The SWNT waviness, the agglomeration and the SWNT orientation then are taken into account in the meso-scale. In the macro-scale, we consider the volume fraction as an uncertain variable.

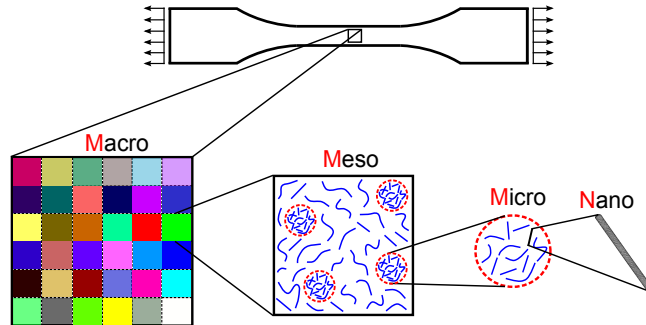


Figure 5.1: Multiscale modeling scheme

5.2.1 Nano-scale model

At nano-scale, a single-walled carbon nanotube (SWNT) is modeled as a space-frame structure. The $C - C$ covalent bonds in the frame-like structure are represented by 3D beam elements assuming a circular cross section with diameter d . Nodes representing carbon atoms are used to connect the beam elements to form the SWNT structure. The $C - C$ bond length L is selected as 0.1421 nm (SARA02, BZR⁺05). As suggested by (SR10c, LC03), the force constant values $k_r = 6.52 \times 10^{-7} \text{ N/nm}$, $k_\theta = 8.76 \times 10^{-10} \text{ N.nm/rad}^2$, $k_\phi = 2.78 \times 10^{-10} \text{ N.nm/rad}^2$ are adopted. Once the force constants k_r , k_θ , and k_ϕ are known, the sectional stiffness parameters EA ;

5.2 Multiscale model

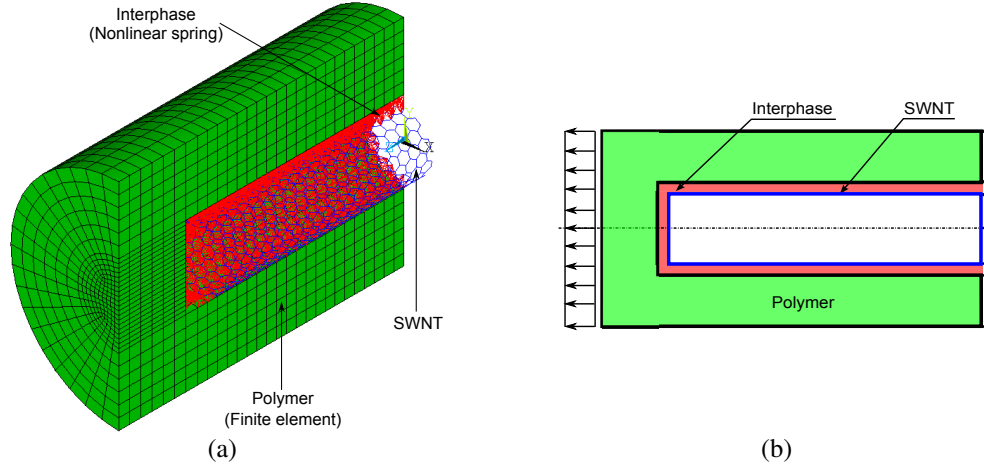


Figure 5.2: Finite element model of half of the RVE at micro-scale.

EI , and GJ can be obtained by Equation 2.13. A non-bonded vdW force formulated by Equation 2.14 with $\epsilon = 0.4492 \text{ kJ/mol}$, $\sigma = 0.3825 \text{ nm}$ and $r = 0.85 \text{ nm}$ (SR10a, KGR⁺10) is used to describe the interphase between the SWNT and the polymer matrix. The interphase thickness (0.17 nm) is chosen the same as half of thickness of SWNT (0.34 nm).

5.2.2 Micro-scale model

The micro-scale model considers a SWNT embedded in a polymer matrix modeled by a continuum mechanics approach (LC03). 20-node hexahedral elements with Young's modulus of 10 GPa and Poisson's ratio of 0.3 are used to model the surrounding polymer matrix (SR10a). 3-D nonlinear springs connecting the C atom on the SWNT and the nodes on the inner surface of the matrix are used to describe the interphase, see Figure 5.2(a).

We employed the adaptive vdW interaction (AVI) model (SR10b, SR10a, SR10c) to determine the mechanical properties of the EF as presented in subsection 2.3.1. The stress-strain curve is obtained from uniaxial tensile simulations by applying axial displacements to nodes at the left end and fix the nodes at the other end of the unit-cell, see Figure 5.2(b). The stress-strain curves in Figure 5.3 show agreement with those of (SR10a) in the linear state (strain < 3.0%). Since the simulations are too expensive, for SWNT with $L_{SWNT} > 800 \text{ nm}$ we used the results in (SR10a) and applied the least square method to construct the polynomial regression model. The regression model in Figure 5.4 represents the relationship between SWNT length (L_{SWNT}) and the corresponding longitudinal modulus of the straight EF. Note that the SWNT length does not affect the transverse modulus of the EF.

5.2 Multiscale model

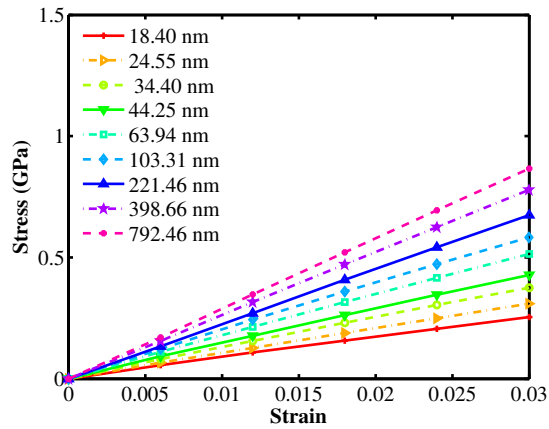


Figure 5.3: The tensile stress–strain curves versus the SWNT length.

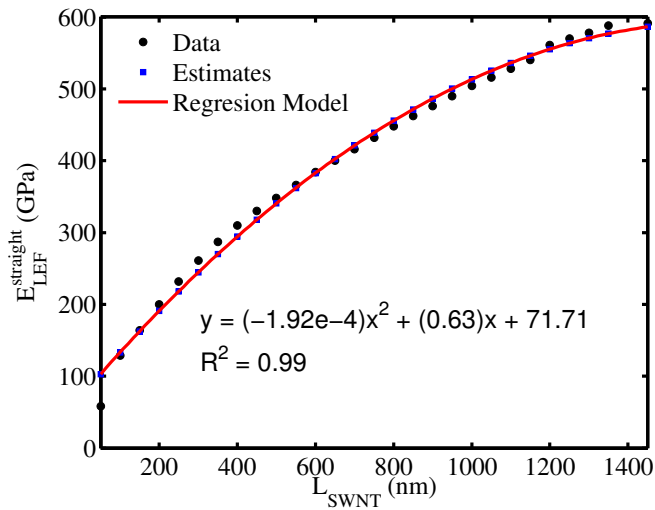


Figure 5.4: Regression model for $E_{LEF}^{straight}$ with respect to L_{SWNT} .

5.2 Multiscale model

As mentioned previously, the direct application of traditional micromechanical models to PNCs may lead to improper mechanical properties as the models are based on continuum mechanics formulation, while the SWNT and the interphase cannot be considered continuous at nano-scale. In order to overcome this deficiency, The inverse rule of mixture (IROM) described in subsection 2.3.2 was employed to convert the SWNT and its interphase to the equivalent fiber (EF), a solid cylinder with diameter of 2.374 nm. The properties of the EF are obtained by

$$\begin{aligned}
 E_{LEF}^{straight} &= \frac{E_{LC}}{V_{EF}} - \frac{E_M V_M}{V_{EF}} \\
 \frac{1}{E_{TEF}^{straight}} &= \frac{1}{E_{TC} V_{EF}} - \frac{V_M}{E_M V_{EF}} \\
 G_{EF}^{straight} &= \frac{1}{G_C V_{EF}} - \frac{V_M}{G_M V_{EF}} \\
 \nu_{EF}^{straight} &= \frac{\nu_C}{V_{EF}} - \frac{\nu_M V_M}{V_{EF}}
 \end{aligned} \tag{5.1}$$

where $E_{LEF}^{straight}$, $E_{TEF}^{straight}$, $G_{EF}^{straight}$, $\nu_{EF}^{straight}$ are the longitudinal modulus, the transverse modulus, the shear modulus and the Poisson's ratio of a straight EF, respectively; E_{LC} , E_{TC} , G_C , ν_C are the longitudinal modulus, the transverse modulus, the shear modulus and the Poisson's ratio of the composite, respectively; E_M , G_M , ν_M are the Young's modulus, the shear modulus and the Poisson's ratio of the matrix, respectively; V_{EF} , V_M are the volume fraction of the EF and the volume fraction of the matrix, respectively. The EF will be employed at the meso-scale where the micromechanics equations are applied. The effective properties of the developed EF are listed in Table 5.1.

Table 5.1: Effective properties of the EF (SR10b)

Mechanical property	Value
Longitudinal Young's modulus	From the regression model in Figure 5.4
Transverse Young's modulus	11.27 (GPa)
Longitudinal shear modulus	5.13 (GPa)
Poisson's ratio	0.284 (GPa)

5.2.3 Meso-scale model

In order to account for the effect of the SWNT waviness, Shokrieh and Rafiee (SR10c) suggested using the longitudinal ($E_{LEF}^{straight}$) and transverse modulus ($E_{TEF}^{straight}$) of the

5.2 Multiscale model

straight horizontal and vertical EF as upper and lower bound values. The stiffness of an RVE consisting of a non-straight EF is placed between these values. In other word, the effective stiffness (E_{LEF}^{wavy} and E_{TEF}^{wavy}) of the embedded non-straight EF within the polymer matrix are selected between the bounding values reflecting any arbitrary non-straight shape, see Figure 5.5.

$$E_{TEF}^{straight} \leq E_{LEF}^{wavy} \leq E_{LEF}^{straight} \quad (5.2a)$$

$$E_{TEF}^{straight} \leq E_{TEF}^{wavy} \leq E_{LEF}^{straight} \quad (5.2b)$$

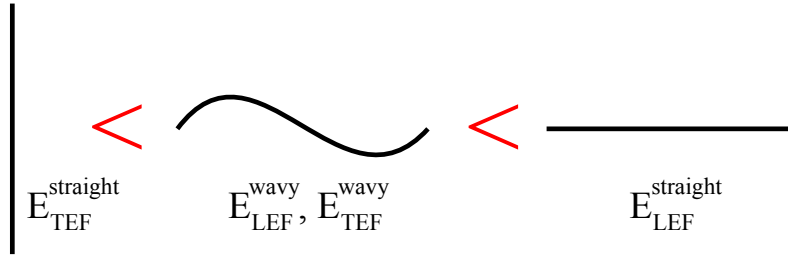


Figure 5.5: The effective stiffness of the wavy EFs in longitudinal and transverse directions is generated between two bounding values.

It is assumed that short SWNTs ($L_{SWNT} \leq 100nm$) are straight. The values of $E_{TEF}^{straight} = 11.27 GPa$ and $E_{LEF}^{straight}$ depending on the SWNT length are taken from the regression model as shown in Figure 5.4. The two-parameter model presented in subsection 2.2.3 is used to account for the agglomeration in the PNCs at meso-scale.

5.2.4 Macro-scale model

In order to simulate the spatial dispersion of SWNTs within the PNCs and quantify its effects on the mechanical properties, the volume fraction of SWNTs in PNC is considered as a random parameter. Particularly, the volume fraction in each RVE is randomly generated according to the overall volume fraction of the material region (MR).

Since the employed model relies on the Mori-Tanaka method that can only handle uniform inclusion properties and microstructures due to their deterministic nature, the effective mechanical property of MR cannot be computed directly; (Tsa10). To overcome this limitation, the MR is split into several independent blocks, the so-called unit elements as depicted in Figure 5.6.

5.3 Stochastic modeling

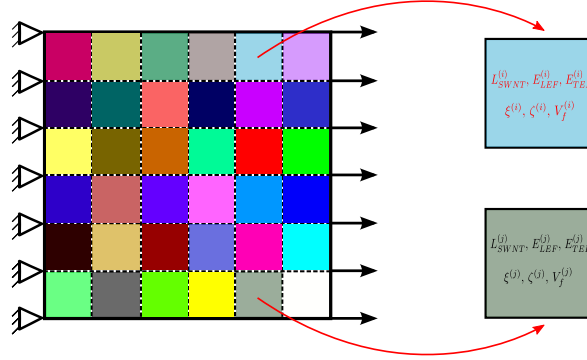


Figure 5.6: Finite element analysis of partitioned material region (MR)

5.3 Stochastic modeling

In this section we consider the randomness of all parameters in the model on the different scales. According to Wang *et al.* (WLWZ06), the distribution of the SWNT length is characterized by a Weibull distribution with scale parameter $A = 550 \text{ nm}$ and shape parameter $B = 2.1$. The SWNT length of 1400 nm is taken as an upper bound.

As mentioned in section 5.2.3, the longitudinal and transverse modulus of wavy EF are randomly generated by Equation (5.2). Then the averaged E_{LEF} and E_{TEF} are computed. The distribution of both averaged values are characterized by a truncated normal distribution with the mean and standard deviation listed in the Table 5.2.

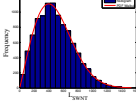
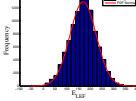
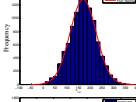
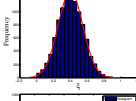
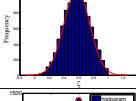
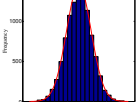
The two parameters ξ and ζ are generated in such a way that the dispersion index ζ is larger than the agglomeration index ξ . Therefore, the spatial distribution of SWNTs is heterogeneous. We randomly generate the two parameters ξ and ζ from 0 to 1 assuming normal distribution. The mean and standard deviation values are listed in the Table 5.2.

The truncated normal distribution is assumed to describe the dispersion of SWNTs within polymer matrix. The mean value of the distribution is set equal to the SWNT volume fraction of 5%. The standard deviation is selected so that the volume fraction cannot be negative. Thus, the standard deviation of 2% is adopted from (SR10c).

In the scope of this study, Monte-Carlo (MC) simulations are done to randomly generate samples from the corresponding distribution. The scatter plot matrix for input parameters is shown in Figure 5.7.

5.4 Numerical results

Table 5.2: Model uncertainties

Level	Inputs	mean	standard deviation	Type of distribution	Sources
Nano/Micro	$L_{SWNT} (X_1)$	488.34	249.18		(WLWZ06)
Meso	$E_{LEF} (X_2)$	169.18	55.85		[modeling]
	$E_{TEF} (X_3)$	169.18	55.85		[modeling]
	$\xi (X_4)$	0.4	0.15		[assumed]
	$\zeta (X_5)$	0.58	0.18		[assumed]
Macro	$V_f (X_6)$	5 %	2%		(SR10c)

5.4 Numerical results

The schematic diagram of all sensitivity assessment methods are provided in Figure 5.8.

The model outputs (\mathbf{Y}) are the macro-scale Young's modulus and Poisson's ratio, respectively. The six input parameters are the SWNT length $L_{SWNT} (X_1)$, the averaged longitudinal modulus $E_{LEF} (X_2)$ and the averaged transverse modulus $E_{TEF} (X_3)$ of the EF in the presence of waviness, the parameter $\xi (X_4)$ denotes the volume fraction of spherical inclusion w.r.t. the total volume of the RVE, the parameter $\zeta (X_5)$ denotes the volume ratio of SWNTs inside the spherical inclusion w.r.t. the total volume of the SWNTs, and the volume fraction $V_f (X_6)$ of SWNTs in the PNC.

The mean value of the Young's modulus and Poisson's ratio of 10000 samples are computed based on the Voigt method (Tsa10). The Young's modulus (12.88 GPa) and the Poisson ratio (0.292) are in agreement with those in (SR10c).

5.4.1 Scatter plots

Scatter plots in Figures 5.9 and 5.10 show the influence of the L_{SWNT} , E_{LEF} , E_{TEF} , ξ , ζ , and V_f on the Young's modulus and Poisson's ratio, respectively. It is observed

5.4 Numerical results

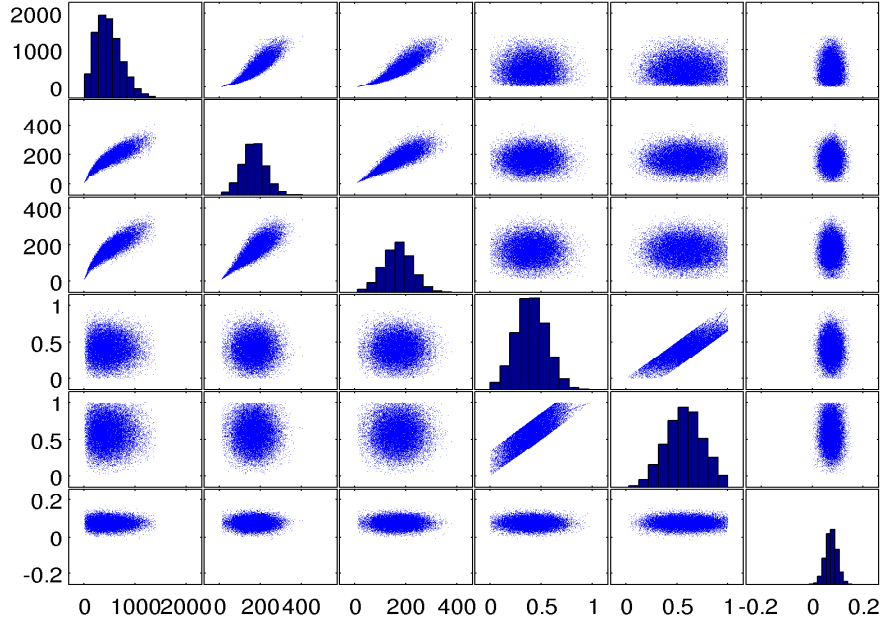


Figure 5.7: Scatter plot matrix for input parameters.

that the volume fraction V_f and the averaged longitudinal modulus of EF E_{LEF} have the most significant effect on the Young's modulus and the Poisson's ratio. On the other hand, the agglomeration parameters ξ and ζ seem to have an insignificant effect on the mechanical outputs.

In Figures 5.9 and 5.10 the volume fraction V_f values are distributed from 0 to 0.1. This may result in an insignificant influence of each agglomeration parameter on either the Young's modulus or the Poisson's ratio, see Shi *et al.* (SFH⁺04).

Based on the scatter plots, the subset averages were examined. First, the X_i parameter and the corresponding output \mathbf{Y} is sorted in ascending order. Then, the X_i axis is cut into slices (subset) containing equal samples and the expected value of \mathbf{Y} in each subset, which is equivalent to $E_{\mathbf{X} \sim i}(\mathbf{Y}|X_i)$, named conditional expectation of \mathbf{Y} given X_i , is calculated. $E_{\mathbf{X} \sim i}(\mathbf{Y}|X_i)$ varies across the subsets and its variance can be used to estimate the first-order sensitivity indices. However, it cannot be applied to measure the total-effect sensitivity indices (MSR10, Mos12).

To quantify the effect of the input parameters, the sensitivity indices were computed using the surrogate model.

5.4 Numerical results

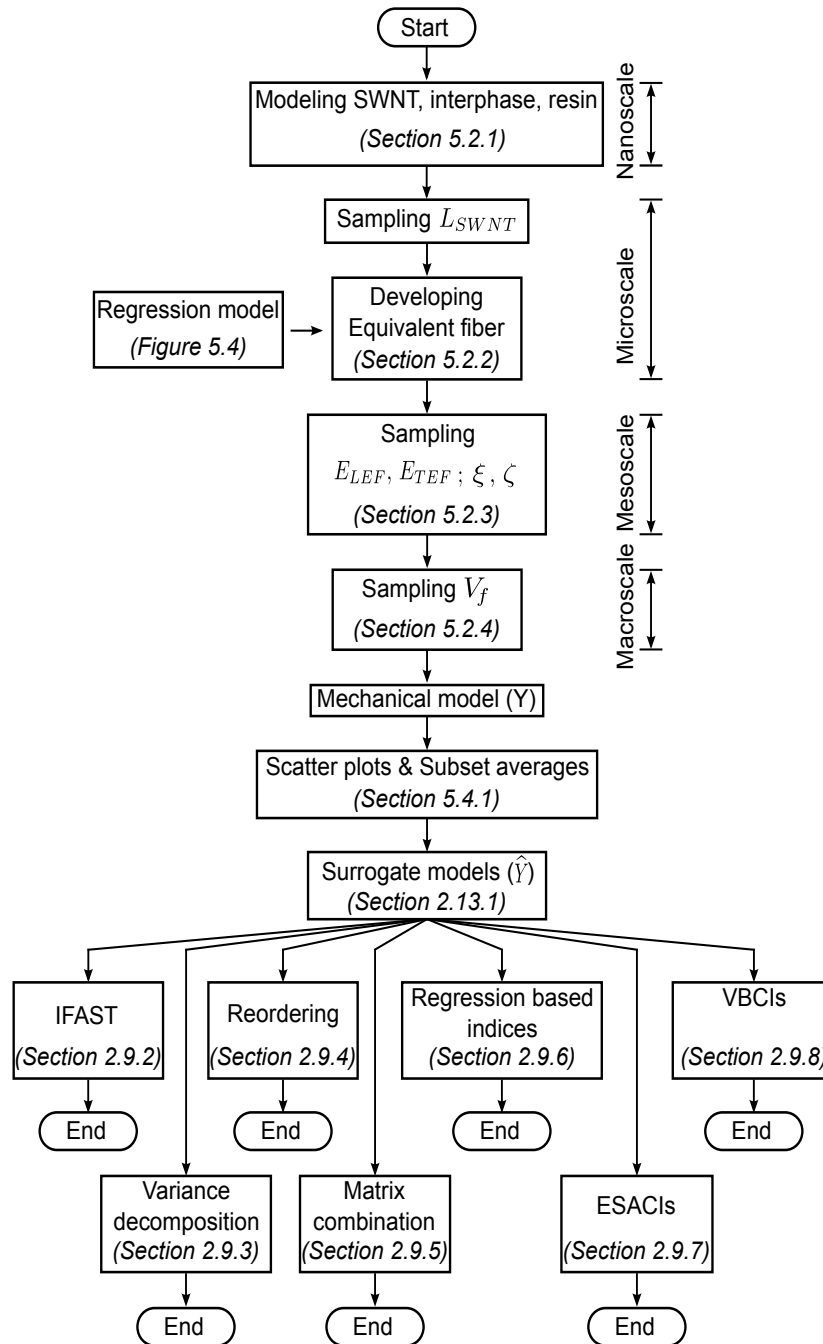


Figure 5.8: Schematic diagram of sensitivity assessment methods.

5.4 Numerical results

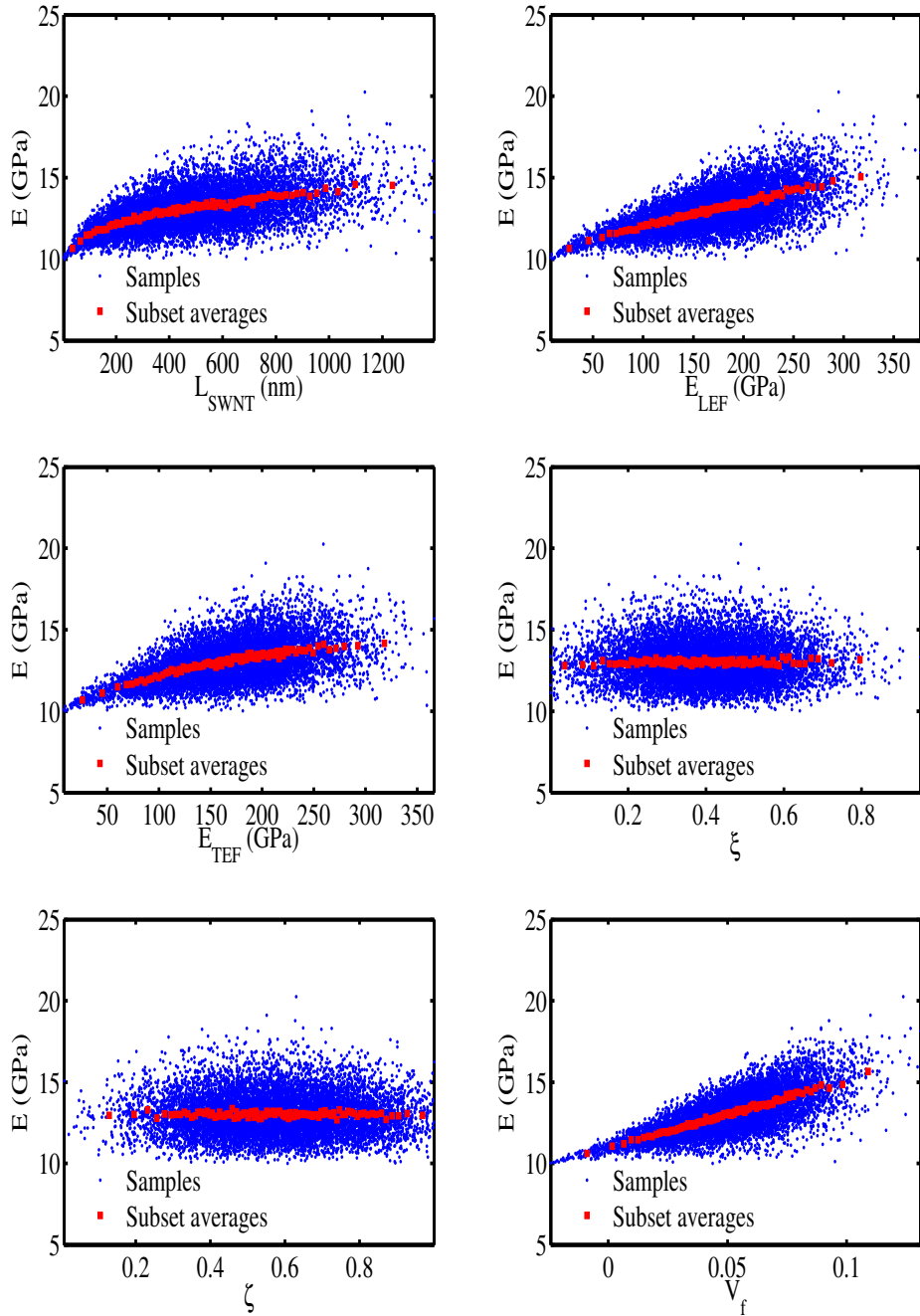


Figure 5.9: Scatter plots of input parameters with the Young's modulus including subset averages.

5.4 Numerical results

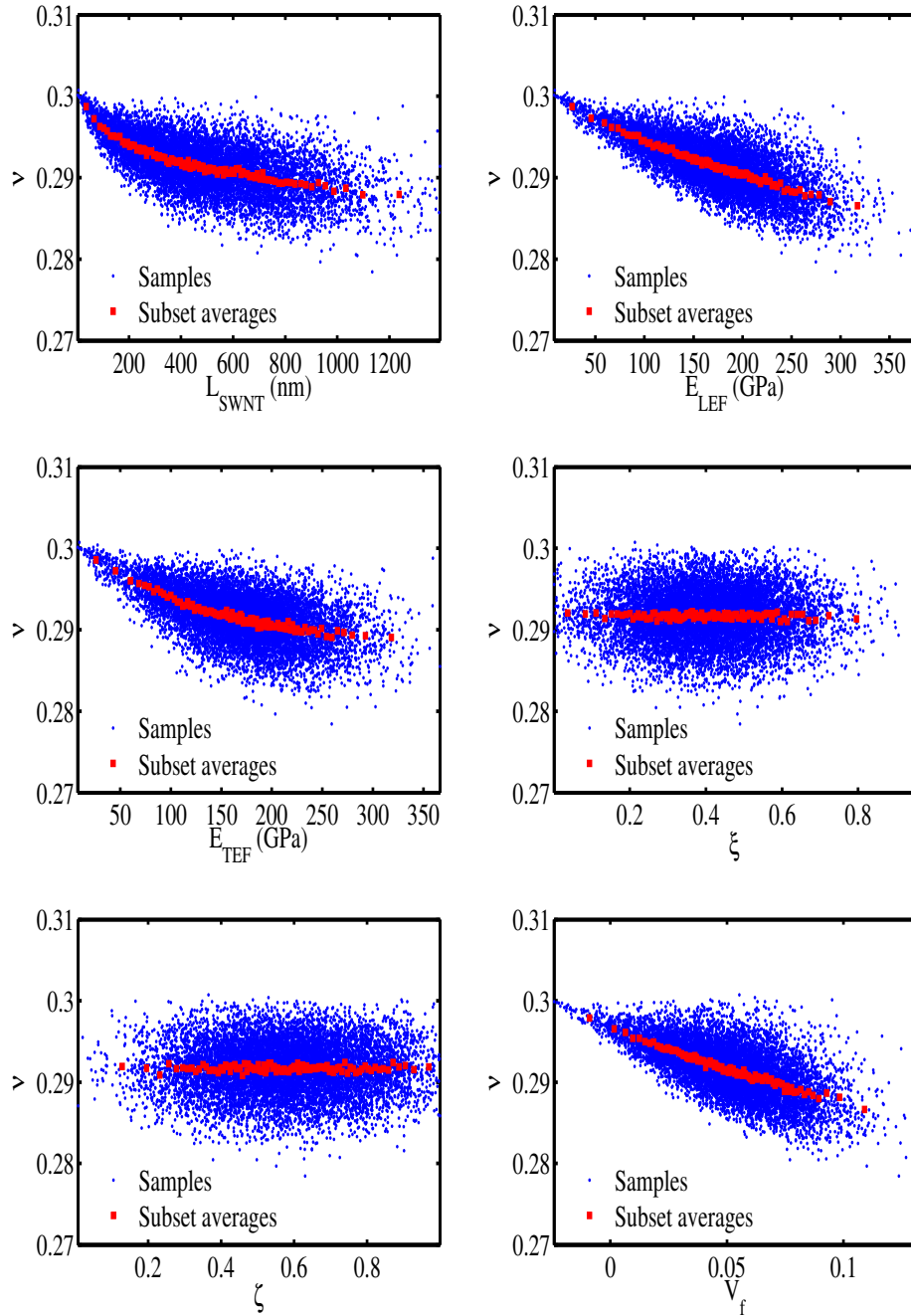


Figure 5.10: Scatter plots of input parameters with the Poisson's ratio including subset averages.

5.4 Numerical results

5.4.2 Covariance matrix

The covariance matrix $C_{\mathbf{X}\mathbf{X}}$ which displays the covariance relation between X_i and X_j , $i, j = 1, \dots, 6$ is calculated as section 2.9.1:

$$C_{\mathbf{X}\mathbf{X}} = \begin{bmatrix} \sigma_{X_1}^2 & 0.90\sigma_{X_1}\sigma_{X_2} & 0.90\sigma_{X_1}\sigma_{X_3} & 0 & 0 & 0 \\ 0.90\sigma_{X_2}\sigma_{X_1} & \sigma_{X_2}^2 & 0.85\sigma_{X_2}\sigma_{X_3} & 0 & 0 & 0 \\ 0.90\sigma_{X_3}\sigma_{X_1} & 0.85\sigma_{X_3}\sigma_{X_2} & \sigma_{X_3}^2 & 0 & 0 & 0 \\ 0 & 0 & 0 & \sigma_{X_4}^2 & 0.82\sigma_{X_4}\sigma_{X_5} & 0 \\ 0 & 0 & 0 & 0.82\sigma_{X_5}\sigma_{X_4} & \sigma_{X_5}^2 & 0 \\ 0 & 0 & 0 & 0 & 0 & \sigma_{X_6}^2 \end{bmatrix} \quad (5.3)$$

with $\sigma_{X_1}, \dots, \sigma_{X_6}$ being the standard deviations in Table 5.2.

5.4.3 Surrogate model

The linear and quadratic without mixed terms regression models were used to approximate the Young's modulus or Poisson's ratio from the mechanical model. Here we generated 10^4 training points by using MC sampling to construct the regression model and to compute the sensitivity indices. The estimated regression coefficients β and the COD's of the linear and the quadratic without mixed terms regression models are summarized in the Tables 5.3 and 5.4, respectively. The responses of the mechanical model (the Young's modulus and the Poisson's ratio) are 98 % exactly approximated by the surrogate models.

Table 5.3: Linear regression model result summary

	β_0	β_1	β_2	β_3	β_4	β_5	β_6	$R^2 = R_{adj}^2$
E	7.49	0.00	0.02	0.00	0.52	-0.48	41.62	0.98
ν	0.31	0.00	0.00	0.00	0.00	0.00	-0.09	0.98

Table 5.4: Quadratic polynomial without mixed terms regression model result summary

E	β_0	β_1	β_2	β_3	β_4	β_5	β_6
	7.25	0.00	0.02	0.00	0.99	-0.60	38.55
	β_{11}	β_{22}	β_{33}	β_{44}	β_{55}	β_{66}	$R^2 = R_{adj}^2$
	0.00	0.00	0.00	-0.57	0.10	20.57	0.98
ν	β_0	β_1	β_2	β_3	β_4	β_5	β_6
	0.31	0.00	0.00	0.00	0.00	0.00	-0.13
	β_{11}	β_{22}	β_{33}	β_{44}	β_{55}	β_{66}	$R^2 = R_{adj}^2$
	0.00	0.00	0.00	0.00	0.00	0.25	0.98

5.4 Numerical results

The first-order S_i and total-effect S_{T_i} , $i = 1, \dots, 6$ sensitivity indices of both correlated and uncorrelated inputs are computed based on the surrogate model. The \hat{S}_i and \hat{S}_{T_i} are reduced by the COD to infer that only R^2 of the mechanical response can be explained with the surrogate model.

$$\hat{S}_i = R^2 S_i \quad (5.4a)$$

$$\hat{S}_{T_i} = R^2 S_{T_i} \quad (5.4b)$$

5.4.4 FAST and IFAST methods

The sensitivity analysis has been performed for both uncorrelated and correlated input parameters. The classical FAST method is used to estimate the main effect of the uncorrelated parameters on the Young's modulus and Poisson's ratio. In order to investigate the sensitivities for highly correlated parameters, the IFAST method is employed. For both methods we have selected $M = 6$ and the vector $\{\omega_i\} = \{1, 21, 31, 37, 45, 49\}$.

The first noticeable result is that the effects of L_{SWNT} and E_{TEF} on the mechanical properties are approximately equal to zero when considering the input parameters as independent variables; Tables 5.5 and 5.6. If the correlation among the parameters is induced, the influences of L_{SWNT} and E_{TEF} on the mechanical properties are significant and the first-order indices for E_{LEF} are decreased, see results in Tables 5.7 and 5.8 and Figures 5.11 and 5.12. We know that the longer the SWNT, the more efficient the load transfer between the SWNT and the polymer matrix and hence the PNCs are strengthened and consequently stiffer. The results obtained from the IFAST method are more reasonable compared to those obtained from the FAST method. Therefore, if we considered the inputs as independent parameters or limited the non-straight SWNT to sinusoidal wavy form (the SWNT waviness is deterministic) as suggested by (FBB03, BFB03), the L_{SWNT} , E_{LEF} and E_{TEF} would be barely correlated to each other. By doing so, the effect of each parameter on the mechanical properties may not be estimated accurately.

Table 5.5: Sensitivity indices computed on the linear regression model with *uncorrelated parameters* of the Young's modulus contributed by the input parameter X_i .

FAST for the model with uncorrelated parameters							
	L_{SWNT} (X_1)	E_{LEF} (X_2)	E_{TEF} (X_3)	ξ (X_4)	ζ (X_5)	V_f (X_6)	Σ
\hat{S}_i^{FAST}	0.01	0.50	0.02	0.01	0.01	0.42	0.97

5.4 Numerical results

Table 5.6: Sensitivity indices computed on the linear regression model with *uncorrelated parameters* of the Poisson's ratio contributed by the *uncorrelated* input parameter X_i .

FAST for the model with uncorrelated parameters							
	L_{SWNT} (X_1)	E_{LEF} (X_2)	E_{TEF} (X_3)	ξ (X_4)	ζ (X_5)	V_f (X_6)	Σ
\hat{S}_i^{FAST}	0.00	0.63	0.06	0.01	0.00	0.28	0.98

Table 5.7: Sensitivity indices computed on the linear regression model of the Young's modulus contributed by the input parameter X_i .

Improvements of FAST							
	L_{SWNT} (X_1)	E_{LEF} (X_2)	E_{TEF} (X_3)	ξ (X_4)	ζ (X_5)	V_f (X_6)	Σ
\hat{S}_i^{IFAST}	0.34	0.43	0.26	0.00	0.01	0.54	1.58

Table 5.8: Sensitivity indices computed on the linear regression model of the Poisson's ratio contributed by the input parameter X_i .

Improvements of FAST							
	L_{SWNT} (X_1)	E_{LEF} (X_2)	E_{TEF} (X_3)	ξ (X_4)	ζ (X_5)	V_f (X_6)	Σ
\hat{S}_i^{IFAST}	0.40	0.53	0.29	0.00	0.01	0.42	1.65

5.4.5 Variance decomposition by regression with correlated input

According to Xu and Gertner (XG08), the variance decomposition approach relies on the assumption that the output linearly relates to the input parameters and the linear regression-based method is a valid approximation. Therefore, the linear regression model was employed to construct the surrogate model for this method whereas the quadratic without mixed terms is employed to construct the surrogate model for the others.

The reduced sensitivity indices for the Young's modulus and Poisson's ratio w.r.t. the total (\hat{S}_i^{VD}), correlated ($\hat{S}_i^{VD,C}$) and uncorrelated part ($\hat{S}_i^{VD,U}$), $i = 1, \dots, 6$ of the input parameters using the variance decomposition approach, are shown in Tables 5.9 and 5.10, respectively.

Large values of \hat{S}_1^{VD} , \hat{S}_2^{VD} and \hat{S}_3^{VD} with small values of $\hat{S}_1^{VD,U}$, $\hat{S}_2^{VD,U}$ and $\hat{S}_3^{VD,U}$ indicate that the effects of L_{SWNT} , E_{LEF} and E_{TEF} on both Young's modulus and Poisson's ratio come from their mutual correlation rather than from themselves.

5.4 Numerical results

Table 5.9: Sensitivity indices computed on the linear regression model of the Young's modulus contributed by the input parameter X_i , the correlated part and uncorrelated part of the input parameter X_i .

Variance decomposition by regression with correlated input							
	L_{SWNT} (X_1)	E_{LEF} (X_2)	E_{TEF} (X_3)	ξ (X_4)	ζ (X_5)	V_f (X_6)	Σ
\hat{S}_i^{VD}	0.32	0.43	0.26	0.00	0.00	0.54	1.55
$\hat{S}_i^{VD,C}$	0.32	0.31	0.26	0.00	0.00	0.00	0.89
$\hat{S}_i^{VD,U}$	0.00	0.12	0.00	0.00	0.00	0.54	0.56

Table 5.10: Sensitivity indices computed on the linear regression model of the Poisson's ratio contributed by the input parameter X_i , the correlated part and uncorrelated part of the input parameter X_i .

Variance decomposition by regression with correlated input							
	L_{SWNT} (X_1)	E_{LEF} (X_2)	E_{TEF} (X_3)	ξ (X_4)	ζ (X_5)	V_f (X_6)	Σ
\hat{S}_i^{VD}	0.37	0.53	0.28	0.00	0.00	0.42	1.60
$\hat{S}_i^{VD,C}$	0.37	0.34	0.27	0.00	0.00	0.00	0.98
$\hat{S}_i^{VD,U}$	0.00	0.19	0.01	0.00	0.00	0.42	0.62

5.4.6 Sampling from the conditional distribution (reordering)

Tables 5.11 and 5.12 respectively show the reduced main-effect indices for the Young's modulus and Poisson's ratio w.r.t. the correlated (\hat{S}_i^S) $i = 1, \dots, 6$ parts of the input parameters.

Table 5.11: Main-effect indices computed on the quadratic without mixed terms regression model of the Young's modulus with correlated input parameters.

Sampling from the conditional distribution							
	Length (X_1)	E_{LEF} (X_2)	E_{TEF} (X_3)	ξ (X_4)	ζ (X_5)	V_f (X_6)	Σ
\hat{S}_i^S	0.31	0.42	0.26	0.00	0.00	0.54	1.53

Table 5.12: Main-effect indices computed on the quadratic without mixed terms regression model of the Poisson's ratio with correlated input parameters.

Sampling from the conditional distribution							
	Length (X_1)	E_{LEF} (X_2)	E_{TEF} (X_3)	ξ (X_4)	ζ (X_5)	V_f (X_6)	Σ
\hat{S}_i^S	0.35	0.53	0.28	0.00	0.00	0.42	1.58

5.4 Numerical results

5.4.7 Extension of the matrix combination approach

The reduced first-order and total-effect sensitivity indices $\hat{S}_i^{M,C}$ and $\hat{S}_{T_i}^{M,U}$, $i = 1, \dots, 6$ of the input parameters, respectively, are given in Tables 5.13 and Figure 5.11 (for the Young's modulus) and 5.14 and Figure 5.12 (for the Poisson's ratio).

Table 5.13: First-order and total-effect sensitivity indices computed on the quadratic without mixed terms regression model of the Young's modulus with correlated input parameters.

Extension of the matrix combination approach							
	L_{SWNT} (X_1)	E_{LEF} (X_2)	E_{TEF} (X_3)	ξ (X_4)	ζ (X_5)	V_f (X_6)	Σ
$\hat{S}_i^{M,C}$	0.34	0.45	0.28	0.01	0.01	0.55	1.64
$\hat{S}_{T_i}^{M,U}$	0.01	0.10	0.00	0.00	0.00	0.55	0.66

Table 5.14: First-order and total-effect sensitivity indices computed on the quadratic without mixed terms regression model of the Poisson's ratio with correlated input parameters.

Extension of the matrix combination approach							
	L_{SWNT} (X_1)	E_{LEF} (X_2)	E_{TEF} (X_3)	ξ (X_4)	ζ (X_5)	V_f (X_6)	Σ
$\hat{S}_i^{M,C}$	0.41	0.50	0.26	0.01	0.01	0.41	1.60
$\hat{S}_{T_i}^{M,U}$	0.08	0.07	0.04	0.00	0.00	0.42	0.61

5.4.8 Extension for regression based indices

The results for the regression based indices method are summarized in Table 5.15 and illustrated in Figure 5.11 (for the Young's modulus) and Table 5.16 and Figure 5.12 (for the Poisson's ratio).

Table 5.15: First-order and total-effect sensitivity indices computed on the quadratic without mixed terms regression model of the Young's modulus with correlated input parameters.

Extension for regression based indices							
	L_{SWNT} (X_1)	E_{LEF} (X_2)	E_{TEF} (X_3)	ξ (X_4)	ζ (X_5)	V_f (X_6)	Σ
$\hat{S}_i^{R,C}$	0.34	0.43	0.27	0.00	0.00	0.54	1.58
$\hat{S}_{T_i}^{R,U}$	0.03	0.10	0.04	0.00	0.00	0.54	0.71

5.4 Numerical results

Table 5.16: First-order and total-effect sensitivity indices computed on the quadratic without mixed terms regression model of the Poisson's ratio with correlated input parameters.

Extension for regression based indices							
	L_{SWNT} (X_1)	E_{LEF} (X_2)	E_{TEF} (X_3)	ξ (X_4)	ζ (X_5)	V_f (X_6)	Σ
$\hat{S}_i^{R,C}$	0.40	0.53	0.30	0.00	0.00	0.42	1.58
$\hat{S}_{T_i}^{R,U}$	0.00	0.15	0.02	0.00	0.00	0.42	0.59

5.4.9 Extension of Sobol' approach for models with correlated inputs (ESACIs)

The sensitivity indices of the ESACIs are computed using Equations (2.125), (2.126), (2.127) for the first-order indices and (2.129) for the total-effect indices. The results are reported in Tables 5.17 and 5.18 and shown in Figures 5.11 and 5.12.

Table 5.17: First-order and total-effect sensitivity indices computed on the quadratic without mixed terms regression model of the Young's modulus with correlated input parameters.

Extension of Sobol' approach for models with correlated parameters							
	L_{SWNT} (X_1)	E_{LEF} (X_2)	E_{TEF} (X_3)	ξ (X_4)	ζ (X_5)	V_f (X_6)	Σ
$\hat{S}_i^{K,a}$	0.33	0.43	0.26	0.00	0.00	0.54	1.56
$\hat{S}_i^{K,b}$	0.33	0.43	0.26	0.00	0.00	0.54	1.56
$\hat{S}_i^{K,c}$	0.33	0.43	0.26	0.00	0.00	0.54	1.56
$\hat{S}_{T_i}^K$	0.00	0.10	0.00	0.00	0.00	0.54	0.64

Table 5.18: First-order and total-effect sensitivity indices computed on the quadratic without mixed terms regression model of the Poisson's ratio with correlated input parameters.

Extension of Sobol' approach for models with correlated parameters							
	L_{SWNT} (X_1)	E_{LEF} (X_2)	E_{TEF} (X_3)	ξ (X_4)	ζ (X_5)	V_f (X_6)	Σ
$\hat{S}_i^{K,a}$	0.38	0.53	0.26	0.00	0.00	0.40	1.57
$\hat{S}_i^{K,b}$	0.38	0.53	0.26	0.00	0.00	0.41	1.58
$\hat{S}_i^{K,c}$	0.38	0.53	0.26	0.00	0.00	0.40	1.57
$\hat{S}_{T_i}^K$	0.00	0.17	0.02	0.00	0.00	0.40	0.59

5.4 Numerical results

5.4.10 Variance-based sensitivity indices for models with correlated inputs (VBCIs)

The sensitivity indices, computed by the VBCIs method are shown in Tables 5.19 and 5.20 and plotted in Figures 5.11 and 5.12.

Table 5.19: First-order and total-effect sensitivity indices computed on the quadratic without mixed terms regression model of the Young's modulus with correlated input parameters.

Variance-based sensitivity indices for models with correlated inputs							
	L_{SWNT} (X_1)	E_{LEF} (X_2)	E_{TEF} (X_3)	ξ (X_4)	ζ (X_5)	V_f (X_6)	Σ
\hat{S}_i^{MR}	0.33	0.42	0.25	0.00	0.00	0.53	1.53
$\hat{S}_{T_i}^{MR,U}$	0.00	0.10	0.00	0.00	0.00	0.53	0.63

Table 5.20: First-order and total-effect sensitivity indices computed on the quadratic without mixed terms regression model of the Poisson's ratio with correlated input parameters.

Variance-based sensitivity indices for models with correlated inputs							
	L_{SWNT} (X_1)	E_{LEF} (X_2)	E_{TEF} (X_3)	ξ (X_4)	ζ (X_5)	V_f (X_6)	Σ
\hat{S}_i^{MR}	0.38	0.52	0.28	0.00	0.00	0.41	1.59
$\hat{S}_{T_i}^{MR,U}$	0.01	0.15	0.01	0.00	0.00	0.41	0.58

5.4.11 Discussion

It is inferred from Figures 5.11 and 5.12 for both Young's modulus and Poisson's ratio that $\hat{S}_{T_6} \approx \hat{S}_6$ as the parameter X_6 (V_f) is not involved in correlation with other variables. $\hat{S}_{T_1} < \hat{S}_1$, $\hat{S}_{T_2} < \hat{S}_2$ and $\hat{S}_{T_3} < \hat{S}_3$ due to the dominant effect of mutual correlation among the parameters X_1 (L_{SWNT}), X_2 (E_{LEF}) and X_3 (E_{TEF}). Since the input parameters (L_{SWNT} , E_{LEF} and E_{TEF}) are strongly correlated with each other, the first order indices are higher than total-effect indices for L_{SWNT} , E_{LEF} and E_{TEF} and the total-effect indices tend to zero. In the uncorrelated case, the sum of sensitivity indices of an additive model is 1. This is not the case for the model containing correlated inputs since the correlation between the inputs indirectly introduces the coupling terms into the model such that the sum can be large than 1 as the presented model.

5.4 Numerical results

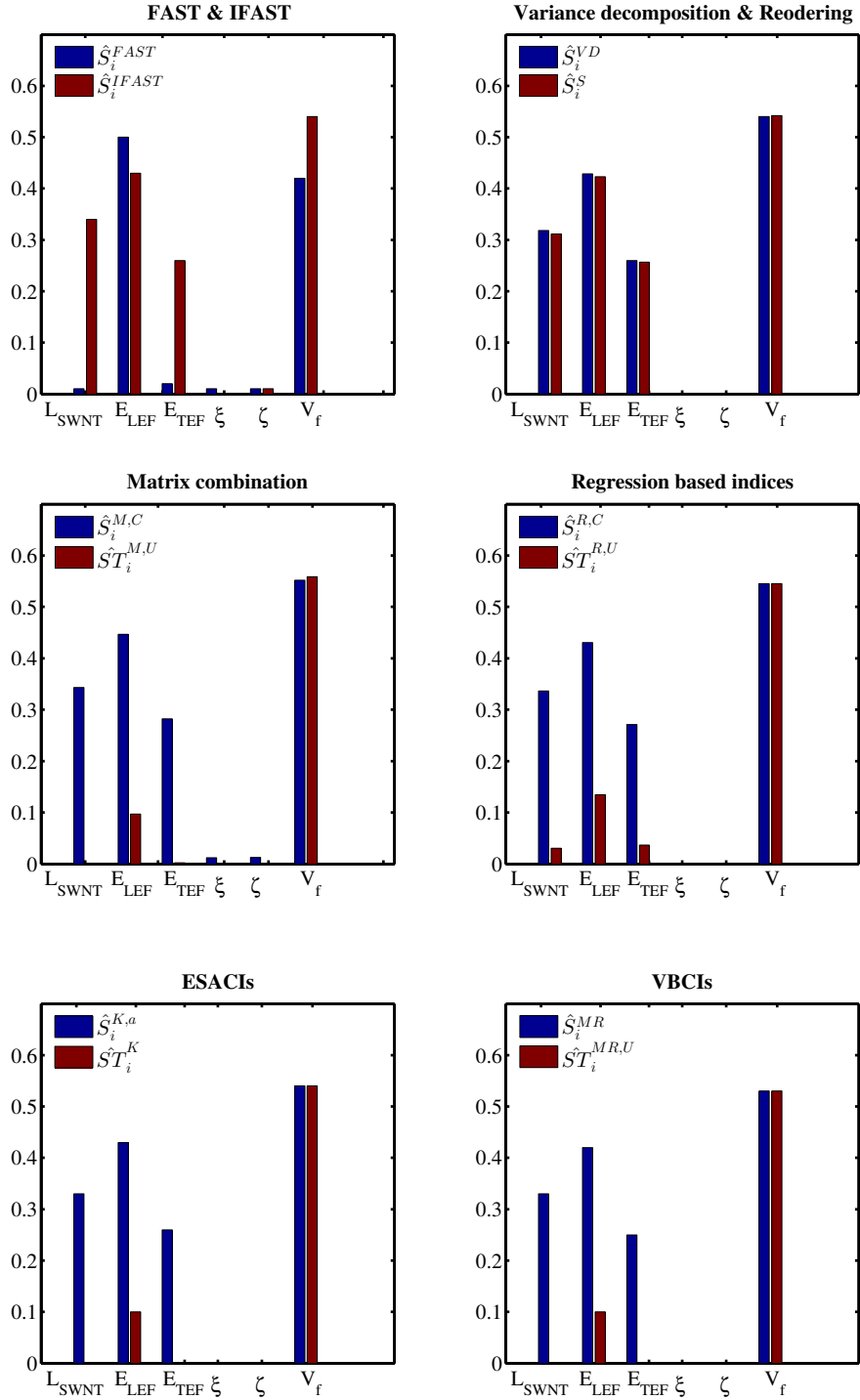


Figure 5.11: First-order and total-effect sensitivity indices for the Young's modulus of different methods.

5.4 Numerical results

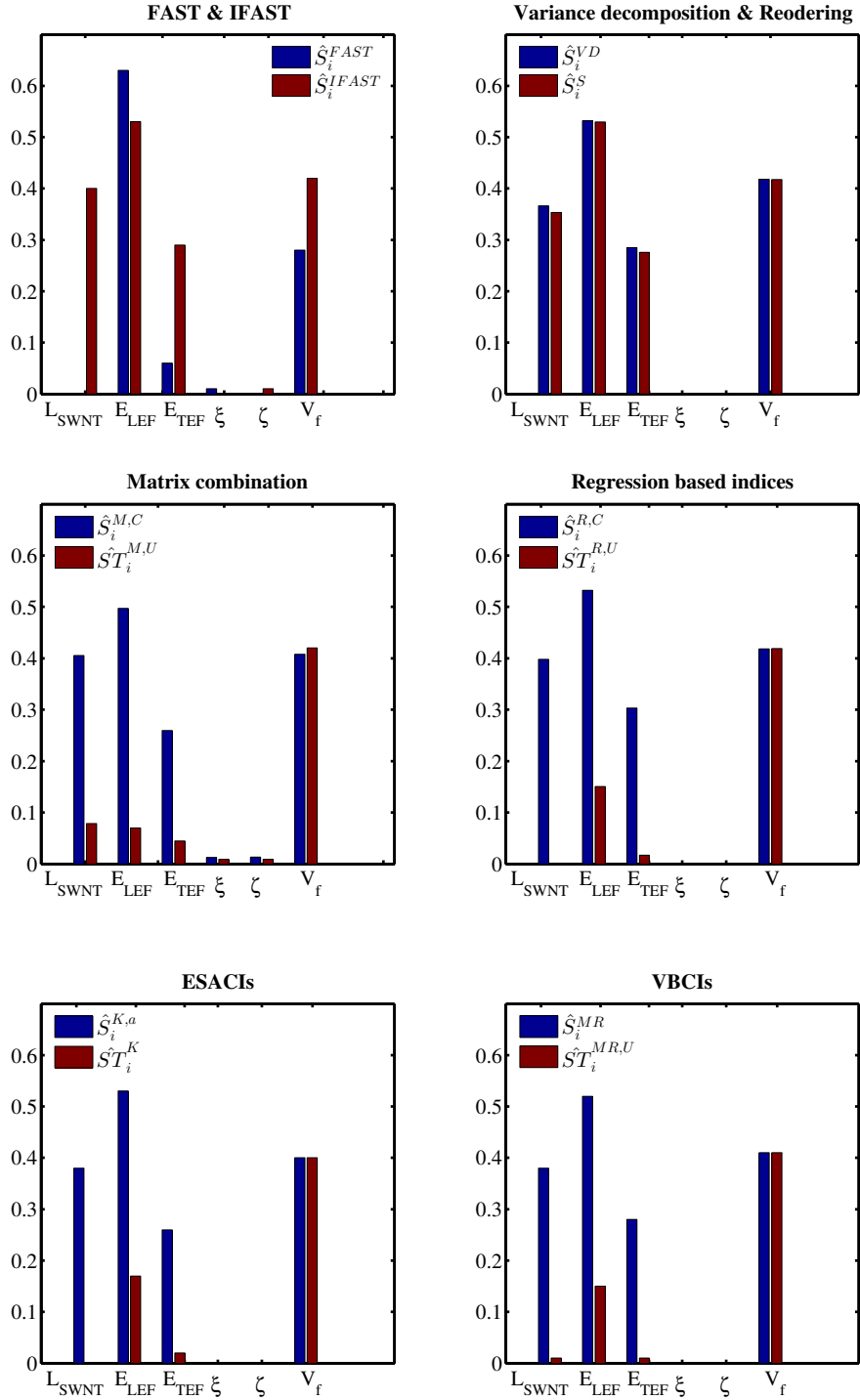


Figure 5.12: First-order and total-effect sensitivity indices for the Poisson's ratio of different methods.

5.5 Conclusions

A hierarchical multiscale model bridging four (nano, micro, meso and macro) scales was employed to study the effect of uncertain model inputs on the macroscopic Young's modulus and Poisson's ratio. The uncertain input parameters include the SWNT length, the averaged longitudinal and transverse modulus of EF with arbitrary waviness, the agglomeration and the volume fraction of randomly oriented SWNTs in PNCs at different scales. Different SA methods were employed to estimate the effect of these uncertain correlated (dependent) inputs on the Young's modulus and Poisson's ratio for the multiscale model in the context of a global SA. Estimates for correlated parameters are performed for both first-order and total sensitivity indices.

The stochastic prediction can be summarized as follows:

1. With regard to the Young's modulus, the most important parameter is the volume fraction followed by the averaged longitudinal modulus of EF (E_{LEF}) in the presence of the waviness, the SWNT length (L_{SWNT}) and the averaged transverse modulus of EF (E_{TEF}), respectively.
2. The averaged longitudinal modulus of EF is the most significant parameter for the Poisson's ratio followed by the volume fraction, SWNT length and averaged transverse modulus of EF, respectively.
3. The agglomeration parameters (ξ and ζ) do not have a significant effect on the Young's modulus and Poisson's ratio. This is mainly due to the assumed range of the volume fraction V_f . In other words, the model is not a function of the agglomeration parameters for a small portion of SWNTs. However, with the increasing volume fraction, the agglomeration might significantly affect the results.
4. Results show an interesting effect of correlation on the sensitivity indices, effects of the input parameters L_{SWNT} , E_{LEF} and E_{TEF} on the mechanical properties apparently depend on the level of correlation. For the examples studied, the waviness pattern of the SWNT were randomly generated such that the correlations between L_{SWNT} , E_{LEF} and E_{TEF} are considered. Remarkably, the SA enables the accurate quantification of the effect of the correlated parameters on the mechanical properties.

Chapter 6

A unified framework for stochastic predictions of mechanical properties of polymeric nanocomposites

6.1 Introduction

Polymer (epoxy) clay nanocomposites (PCNs) have been studied extensively as a new generation of polymeric materials and received wide interests in the research community of material sciences and engineering due to their exceptional thermal and mechanical properties. The clay particle structure is either exfoliated or intercalated. For enhanced functional properties of nanocomposites at the same clay concentration the former is preferred (HWC07). An exfoliated PCN was developed by the Toyota group by synthesizing a nylon 6/clay nanocomposite (UKK⁺93b, UKK⁺93a). They reported that the mechanical properties (tensile modulus and strength) of nylon 6/clay nanocomposites were significantly improved even at low clay concentrations. It is believed that the enhanced properties of PCNs strongly depend on the clay aspect ratio and the mechanical properties of the nano clay. After pioneering success in the nylon 6/clay system, the nanocomposite technology has been extended to other polymeric systems, including elastomers (WP98, BG00) and epoxies (TLP02, RMV⁺03). It was shown that enhancement of the thermal/mechanical properties in the polymeric nanocomposites is sensitive to the particular polymer chosen.

Analytical and numerical predictions of the overall composite stiffness have been extensively studied (VBLZ⁺14). A comprehensive review of micromechanical models fiber-reinforced polymers, such as Halpin–Tsai (Hal69) and Mori and Tanaka (MT73), was outlined by Tucker and Liang (TL99). Analytical studies (FP03, WP04) suggest that the high clay stiffness, high aspect ratio and volume fraction are the key parameters governing the stiffness of clay nanocomposite. Sheng *et al.* (SBP⁺04) proposed a

6.2 Model for PCN

multiscale finite element method (FEM), accounting for the hierarchical morphology of the PCNs, to predict the macroscopic properties of PCNs by using the so-called 'effective particles' in which the model parameters such as the particle volume fraction, particle aspect ratio and orientation and particle/matrix property ratios were taken into consideration. Scocchi *et al.* (SPD⁺07) developed a bottom-up approach to study the relative macroscopic properties of PCNs. Fermeglia *et al.* (FP07b) proposed a hierarchical procedure for bridging the atomistic and macroscopic results through mesoscopic simulations.

As the mechanical properties of a certain polymer clay nanocomposite system are affected by multiple uncertain parameters such as the clay volume fraction, clay aspect ratio, clay curvature, clay stiffness and epoxy stiffness, a comprehensive study of the effects of such above-mentioned parameters on the mechanical behavior of PCNs is required. So far, the stochastic effects of these parameters on the mechanical properties have not been quantified.

In this chapter, we conduct a comprehensive global sensitivity analysis (SA) based on a stochastic modeling of PCNs. The finite element (FE) analysis is used to predict the stiffness of the fully exfoliated PCNs within the framework of the stochastic modeling. Based on a micromechanical approach, a homogenized Young's modulus is computed at the meso-scale. Subsequently, different SA methods are employed to quantify the influence of the input parameters on the PCN Young's modulus. A bootstrap technique has been performed in order to assess the robustness of different SA methods.

The chapter is outlined as follows. In the next section, we briefly describe the FE model and homogenization techniques. Section 6.3 presents the complete statistical distribution for each input parameter. Different SA methods are described in section 6.4. The coefficients of surrogate model, sensitivity indices and bootstrap confidence intervals for the sensitivity indices will be detailed in section 6.5 before the chapter ends with a discussion on the numerical results and the concluding remarks.

6.2 Model for PCN

We focus on PCNs that are built using the slurry compounding process. The epoxy resin is diglycidyl ether of bisphenol A (D.E.R.TM 332) and the curing agent is diethyltoluenediamine (Ethacur 100-LC, Albemarle). The pristine clay is sodium montmorillonite (MMT) (WCW⁺05, WWW⁺05, WWC⁺06, SZRET12).

Models of various periodic representative volume elements (RVEs) of the epoxy matrix filled with exfoliated clay platelets (particles) that are randomly oriented and dispersed are constructed. Figure 6.1 shows a detailed view of the FE mesh inside the RVE of the PCN. The micromechanical FE model was implemented in ABAQUS as detailed in (STZR⁺13).

6.2 Model for PCN

In this work, we assume a simplified case of *perfectly bonded* particles in an isotropic matrix.

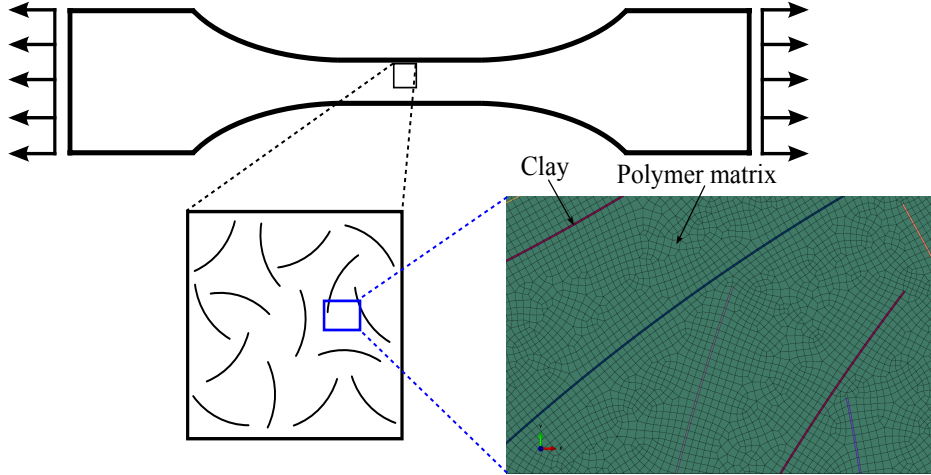


Figure 6.1: A detailed view of the mesh.

6.2.1 RVE definition

The RVE approach uses the solution of the homogenization for an original heterogeneous medium to obtain an equivalent homogeneous one that is able to substitute the heterogeneous (polymer/platelet) material. Hence, the RVE size should be defined so that the RVE contains enough information to reasonably simulate an infinite medium.

Since the RVE is randomly generated, the ensemble of many realizations (RVEs) needs to be generated to create a good statistical representation of the PCN. In other words, we replace a large RVE that reasonably simulates an infinite medium by a statistical ensemble of RVEs for sake of computational efficiency. The number of realizations is determined such that the entire ensemble contains the same amount of information as a large one. The ensemble average is given by Spencer and Sweeney (SS 9)

$$\langle R \rangle = \frac{1}{M} \sum_{k=1}^M R^{(k)} \quad (6.1)$$

where $R^{(k)}$ is a response measured in the k -th RVE ($k = 1, 2, \dots, M$); M is the number of RVE realizations in the ensemble. In order to estimate convergence of the

6.2 Model for PCN

statistical ensemble, the saturation criterion was used

$$\left| \frac{\langle R^{(k+1)} \rangle - \langle R^{(k)} \rangle}{\langle R^{(k)} \rangle} \right| < Tol = 1\%. \quad (6.2)$$

where $R^{(k)}$ denotes an expected value of k realisations, and $R^{(k+1)}$ is averaged over $k + 1$ realizations. Equation (6.2) allows to recognize whether the result reaches a reasonable accuracy.

6.2.2 Boundary conditions

Usually, three types of BCs can be applied to the RVE, namely linear displacement, uniform traction and mixed type BCs (which includes periodic BCs). For linear elasticity, there is an ordering relationship among the results which are obtained from those three kinds of BCs (HH94). This ordering relationship finally motivates the use of periodic BCs in case of periodic structures (Ant95, HK92).

In practical applications, periodic BCs are also used in case of non-periodic microstructures. It has been shown in numerous numerical studies that periodic BCs yield a fast convergence rate of the effective properties with respect to (w.r.t.) the size of the RVE (Hil67, Has83, CKG12). The periodic BCs are imposed on the RVE as shown in Figure 6.2 by applying a displacement on a rigid reference node that is kinematically coupled with the RVE edges in the axial direction so that the displacements of all boundary nodes are identical to those of the equivalent node on the opposite edge.

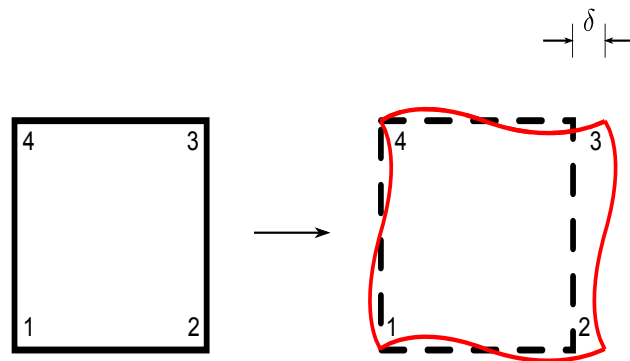


Figure 6.2: Boundary conditions imposed on the RVE: (left) an undeformed RVE and (right) a deformed RVE.

6.2 Model for PCN

6.2.3 RVE generation algorithm

The characteristics of the clay particles (their aspect ratio (length), curvature (radius) and stiffness) are randomly generated according to predefined sets of statistical distributions, (SS 9), e.g. all clay particles have the same aspect ratio, curvature radius, stiffness, and the clay particles are randomly dispersed in the epoxy matrix. The resulting clay particle configurations are ideal for estimating the influence of each particle-characteristic on the mechanical response. A scheme of the RVE generation algorithm is shown in Figure 6.3.

Firstly, the control parameters including the number of RVEs for each value of clay concentrations (volume fraction), the size of the RVE, the clay length, curvature and orientation distribution are set. According to the randomly generated volume fraction, the aspect ratio and the size of the RVE, we compute the number of clay particles (n) in the RVE. The particles are sequentially placed in the RVE based on the random sequential addition algorithm (RSA).

The clay corner position, the aspect ratio, the clay radius and the clay stiffness are randomly selected according to their probability density functions (PDFs). The clay particle is generated by randomly placing its corner to a trial position and assigning a random angle between the particle and the x axis. The uniform distribution is used to randomly place the clay particles inside the RVE.

Once a clay particle is generated, a condition for non-overlap and non-intersection with existing particles is checked. If the condition is violated a new particle is regenerated and the condition is checked again. Since the RVE is geometrically periodic, the clay particles crossing an edge of the RVE must reappear at the opposite edge. Therefore, we mesh the RVE and produce the set of equations for periodic BCs. After solving the boundary value problem (BVP), the homogenization over the RVE is performed and the results are saved for the stochastic analysis.

6.2.4 Output

The output of the proposed stochastic method is the effective Young's modulus that is computed based on the homogenization technique as presented in subsection 2.3.3. Since the clay particles are randomly distributed, the bulk material at the macro-scale can be considered as isotropic. Therefore, only two independent elastic constants (the bulk modulus K and shear modulus μ) exist. The elastic constants can be determined by applying the BC to the RVE as addressed in subsection 6.2.2. Predefining δ as horizontal strain, we have $\epsilon_{11} = \delta$ and $\sigma_{22} = 0$. After loading, the ϵ_{22} and σ_{11} can be computed by homogenization. This method was used to compute the effective Young's modulus E of the intact nanocomposite.

6.2 Model for PCN

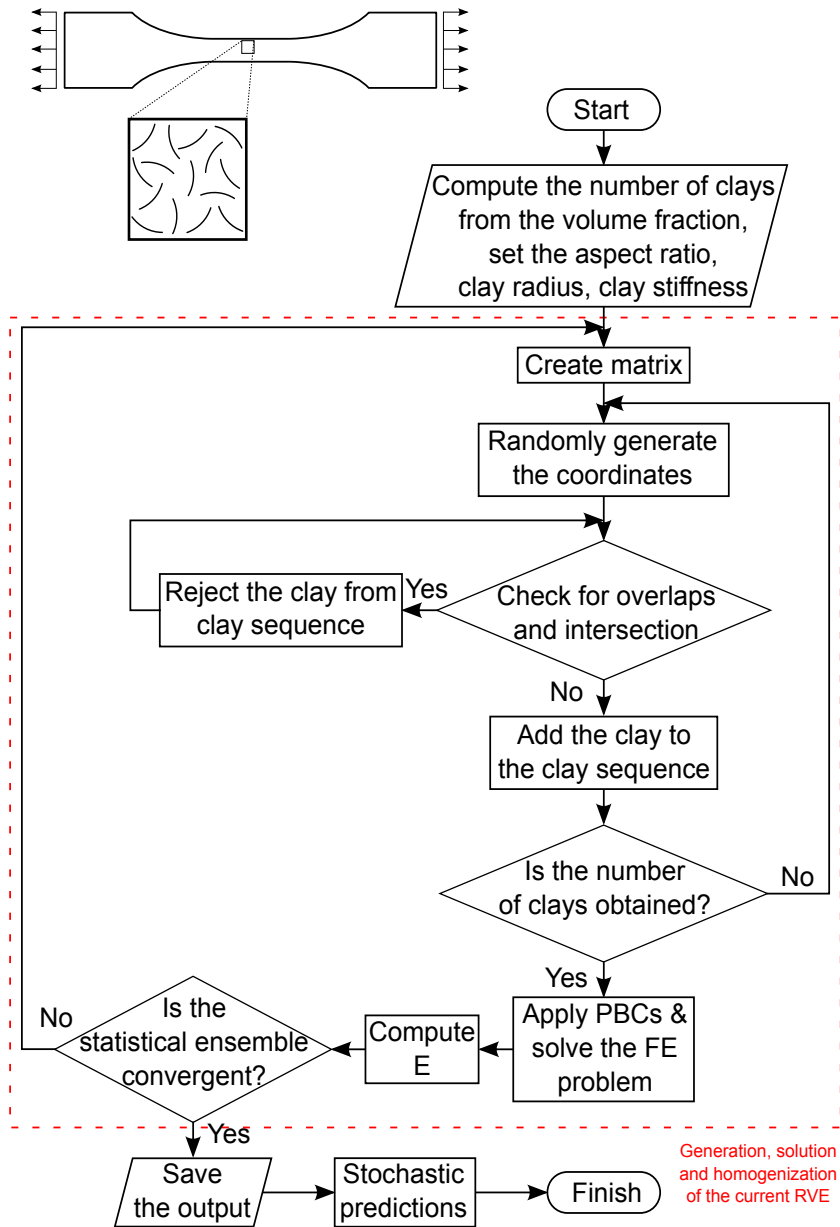


Figure 6.3: Flowchart of the proposed stochastic modeling.

6.3 Stochastic input parameters

Zunjarrao *et al.* (ZSS06) stated that the volume fraction of clay particles commonly ranges from 0.5% to 6%. In order to reduce the computational cost, we modify the clay volume fraction from 0.5% to 5% assuming a truncated Gaussian distribution. The mean and standard deviation are shown in Table 6.1.

Experimental observations (WCW⁺05, WWW⁺05) show that the aspect ratio of 1 nm thick sodium montmorillonite platelets ranges from 200 to 400 nm. The clay length distribution can be characterized by the truncated Gaussian distribution with the respective mean and variance value of 300 nm and 45 nm.

In order to reveal the MMT clay radius distribution, image processing techniques were used on the TEM image of PCNs (WCW⁺05, SZRET12). The quantified clay radii were extracted based on high resolution TEM images. A Log-normal distribution with the mean value of 5.72 nm and standard deviation of 0.91 nm is used, see Table 6.1.

According to Vanorio *et al.* (VPN03), it is difficult to measure the Young's modulus of mineral clays due to their small grain sizes. Chen and Evans (CE06) surveyed estimates of the Young's modulus of clay platelets and concluded that the Young's modulus of clay platelets is within the range of 178 GPa – 265 GPa. We assume a Gaussian distribution with the mean value of 221.5 GPa and the variance of 20 GPa for the Young's modulus of clays.

The Gaussian distribution is used to describe the Young's modulus of the epoxy (SZRET12). The mean value and the standard deviation are 1.96 GPa and 0.08 GPa, respectively.

The scatter plot matrix for the independent input parameters is also shown in Figure 6.4.

6.4 Global sensitivity analysis

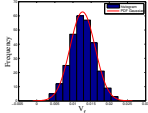
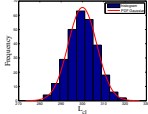
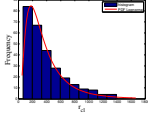
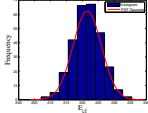
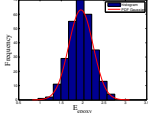
Global sensitivity analysis aims to relate output uncertainties to uncertainties in the input parameters. In this chapter, different global SA methods based on different surrogate models are employed to estimate how much the model response is affected by changes in the model parameters, taken one by one and in interaction with one another. The schematic diagram of all sensitivity assessment methods applied in this study are illustrated in Figure 6.5.

6.5 Numerical results

Uncertainty of the predicted response (E) of the mechanical model can be described by a probability distribution. Judging from the drawn histogram (sample size = 280)

6.5 Numerical results

Table 6.1: Statistical properties of model parameters

Inputs	mean	standard deviation	Type of distribution	Sources
$V_f (X_1)$	2.75%	0.75%		[assumed]
$L_{clay} (X_2)$	300 nm	$\sqrt{45}$ nm		(WCW+05, WWW+05)
$r_{clay} (X_3)$	5.72 nm	0.91 nm		(WCW+05, SZRET12)
$E_{clay} (X_4)$	221.5 GPa	$\sqrt{20}$ GPa		(CE06)
$E_{epoxy} (X_5)$	1.96 GPa	$\sqrt{0.08}$ GPa		(SZRET12)

in Figure 6.6, either Normal or Weibull, Log-normal distributions can be candidates to characterize for the mechanical response uncertainty.

The probability plots are used to graphically assess whether the predicted Young's modulus can be characterized by a given distribution. If the probability plot produces the least deviations from a straight line, the exploited theoretical distribution is chosen as a goodness-of-fit of the data (GK90). The respective Normal, Weibull and Log-normal probability plots are drawn in Figures 6.7, 6.8 and 6.9.

The difference between mean (2.43) and mode value (1.45) indicates that the output is skewed, see Figure 6.6 and Table 6.2. Hence, the normal distribution is not a good candidate to characterize the mechanical output. It is more reasonable to describe the skewed data by a Weibull or Log-normal distributions. In order to quantitatively assess the best fitted distribution of the sample data, the residual sum of squares (RSS) are computed in which cross blue points of the probability plots are considered as Y_j and the regression values (straight red lines) serve as \hat{Y}_j in Equation (2.145). Obviously, the Log-normal is the best fitted distribution to the Young's modulus' histogram due to the smallest RSS given in Table 6.3. Note that the RSS values are estimated within 95% CIs.

The mean value of the Young's modulus is shown in Table 6.2. Scatter plots in Figure 6.10 show that the obtained Young's modulus of the PCNs agrees well with the experimental results (WCW+05) and the numerical results (STZR+13), respectively.

6.5 Numerical results

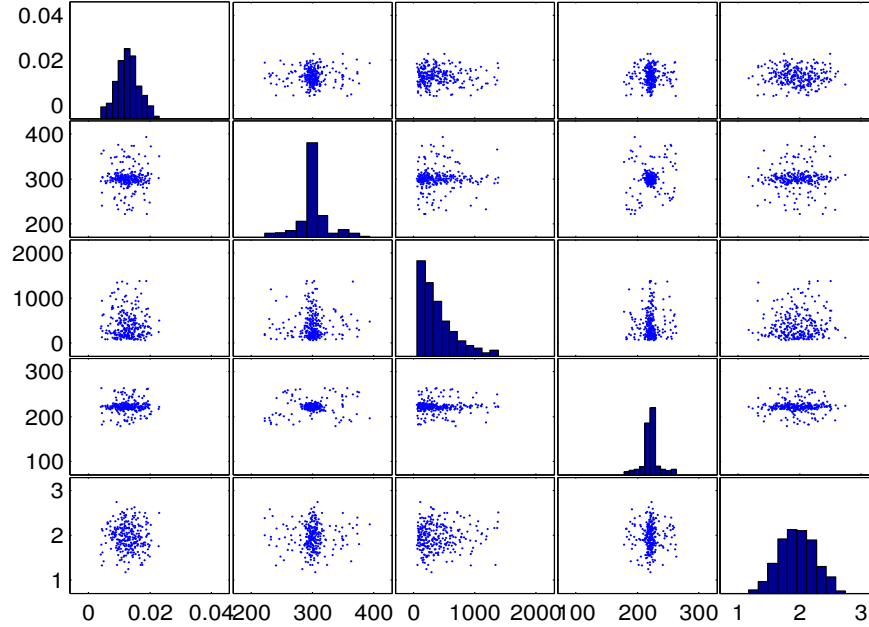


Figure 6.4: Scatter plot matrix for input parameters.

Table 6.2: Statistical results for the Young's modulus

Output	Mode value (MPa)	Mean value (MPa)	Standard deviation
Young's modulus	1.45	2.43	0.35

Table 6.3: Uncertainties of mechanical output using various distributions

Type of assumed PDF	Parameter 1	Parameter 2	Error
Normal PDF	Mean value (MPa)	Standard deviation	RSS
	2.43	0.35	0.0686
Weibull PDF	Scale parameter (A)	Shape parameter (B)	RSS
	2.58	7.53	0.1810
Log-normal PDF	Mean value (MPa)	Standard deviation	RSS
	0.88	0.15	0.0662

The highest influence seems to be the epoxy stiffness (E_{epoxy}). To quantify the affect of the input parameters, the sensitivity indices will be studied using different surrogate models.

We have used the penalized cubic spline ($\varphi = 3$) regression model for a single continuous predictor parameter in order to plot $E(Y|X_i)$. The first-order sensitivity indices have been estimated by Equation (2.65). The results are shown in Table 6.6

6.5 Numerical results

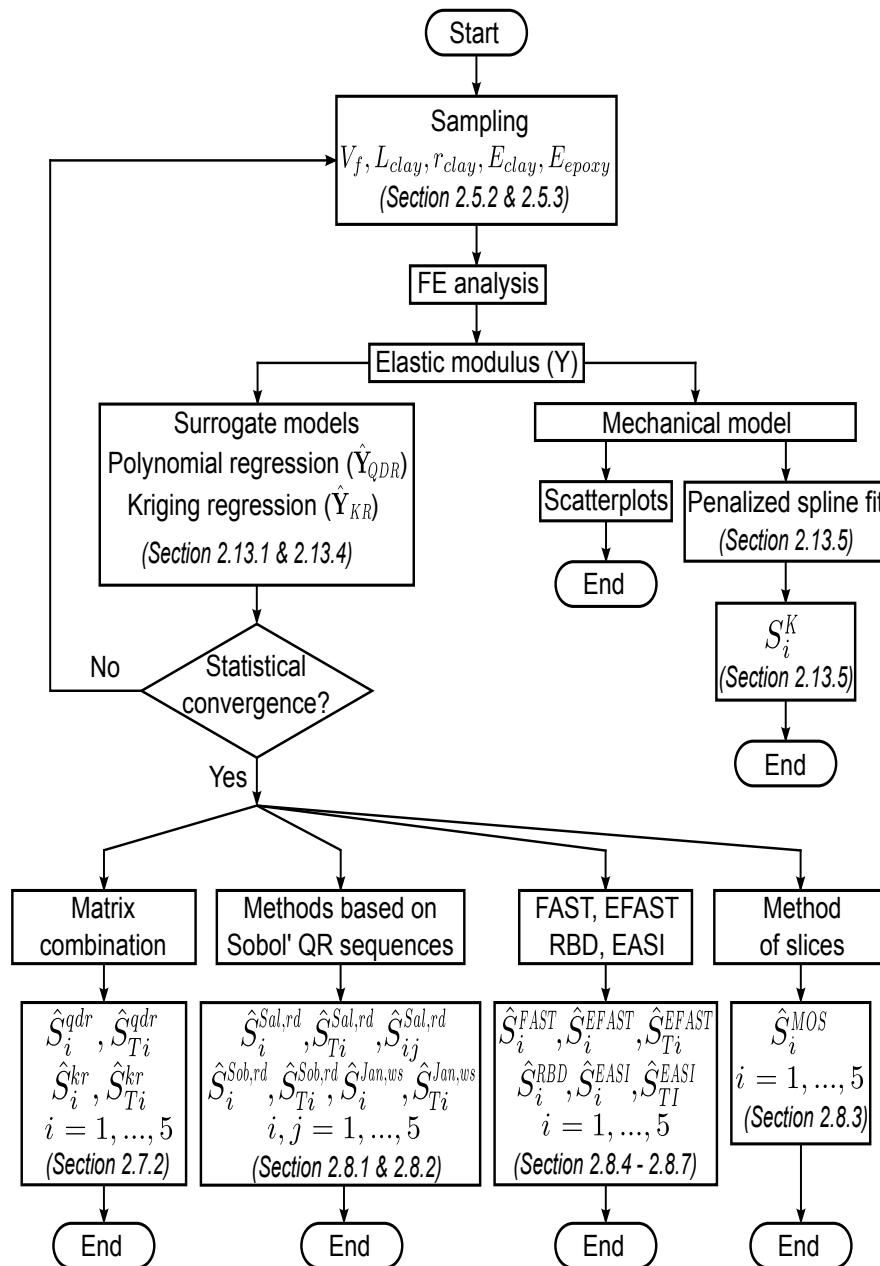


Figure 6.5: Schematic diagram of sensitivity assessment methods.

6.5 Numerical results

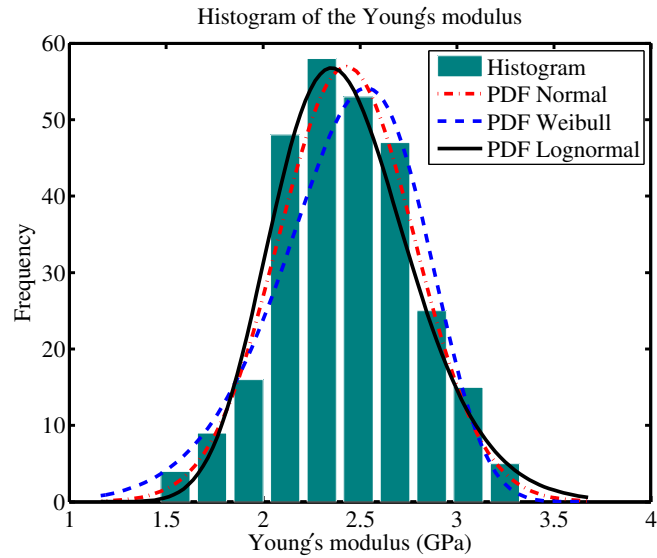


Figure 6.6: Histogram of the Young's modulus E of the PCNs and assumed probability density functions (PDFs) for different distribution types.

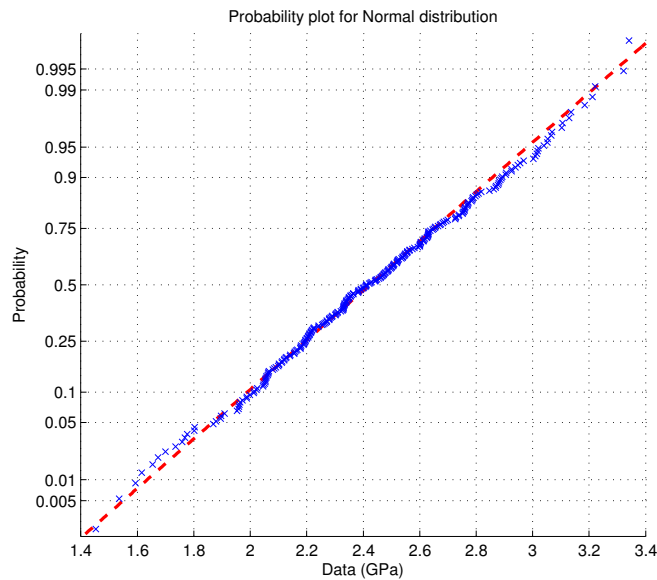


Figure 6.7: Normal probability plot for the distribution of the Young's modulus E .

6.5 Numerical results

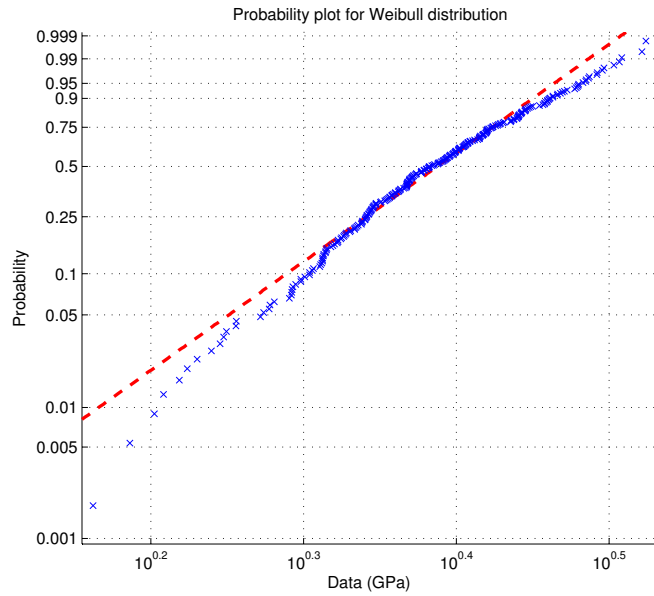


Figure 6.8: Weibull probability plot for the distribution of the Young's modulus E .

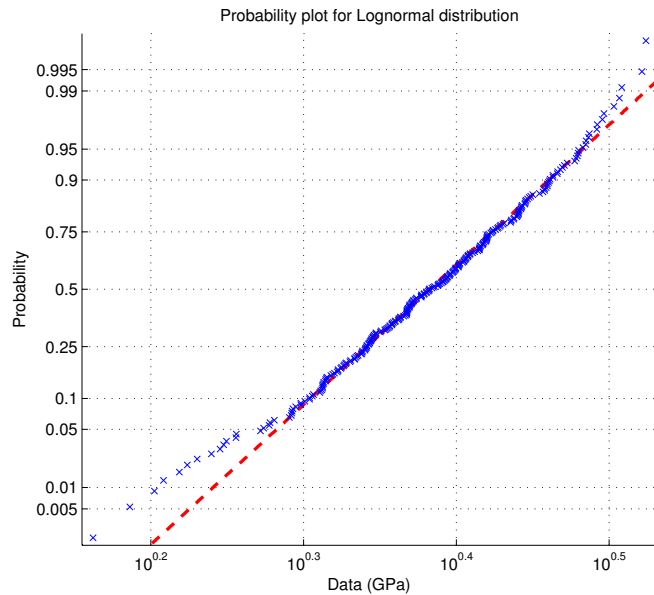


Figure 6.9: Log-normal probability plot for the distribution of the Young's modulus E .

6.5 Numerical results

and plotted in Figure 6.12.

Figure 6.10 also shows the 95% CIs and PIs. We can be 95% confident that the conditional expected value $E(\mathbf{Y}|X_i)$ given that X_i lies in the light grey region. The region between the values cut off by the magenta dashed lines, corresponds to 95% PIs in which any new predictions lie. The PIs are wider than the CIs as they are inference on \mathbf{Y} , rather than $E(\mathbf{Y}|X_i)$.

Since scatter points are randomly distributed according to the PDF, the CIs are narrower in the highly contributed training data region and wider in the scattered training data region. Furthermore, the CIs w.r.t. the epoxy stiffness E_{epoxy} are narrower than the others at 95%. The CIs infer that (1) the highest influence seems to be the epoxy stiffness (E_{epoxy}); and (2) the corresponding sensitivity index is more precise (and reliable) than the sensitivity indices due to other parameters.

Table 6.4: QDR model result summary

E	β_0	β_1	β_2	β_3	β_4	β_5
	-1.25	40.64	0.00	0.00	0.01	1.27
	β_{11}	β_{22}	β_{33}	β_{44}	β_{55}	$R^2 = R_{adj}^2$
	-299.20	0.00	0.00	0.00	-0.03	0.97

Table 6.5: KR model result summary

E	λ	θ_1	θ_2	θ_3	θ_4	θ_5	$R^2 = R_{adj}^2$
	0.01	0.01	0.00	0.10	0.00	0.02	0.98

Table 6.6: First-order sensitivity indices computed on the penalized cubic spline regression model of the Young's modulus E

First-order indices based penalized cubic spline regression						
	V_f (X_1)	L_{clay} (X_2)	r_{clay} (X_3)	E_{clay} (X_4)	E_{epoxy} (X_5)	Σ
S_i^K	0.11	0.00	0.04	0.00	0.84	0.99

The surrogate models, based on the quadratic regression without mixed terms (QDR) and the kriging regression (KR), are constructed to approximate the mechanical response. Figure 6.11 shows that stochastic convergence is achieved with 280 samples for both QDR and KR models. The corresponding COD R^2 and adjusted COD R_{adj}^2 are computed and shown in Tables 6.4 and 6.5. The COD R^2 of 0.97 for QDR and 0.98 for KR indicate that the predicted response using the surrogate models are good approximations of the mechanical response. Subsequently, we used only the QDR model to estimate the sensitivity indices by different SA methods.

6.5 Numerical results

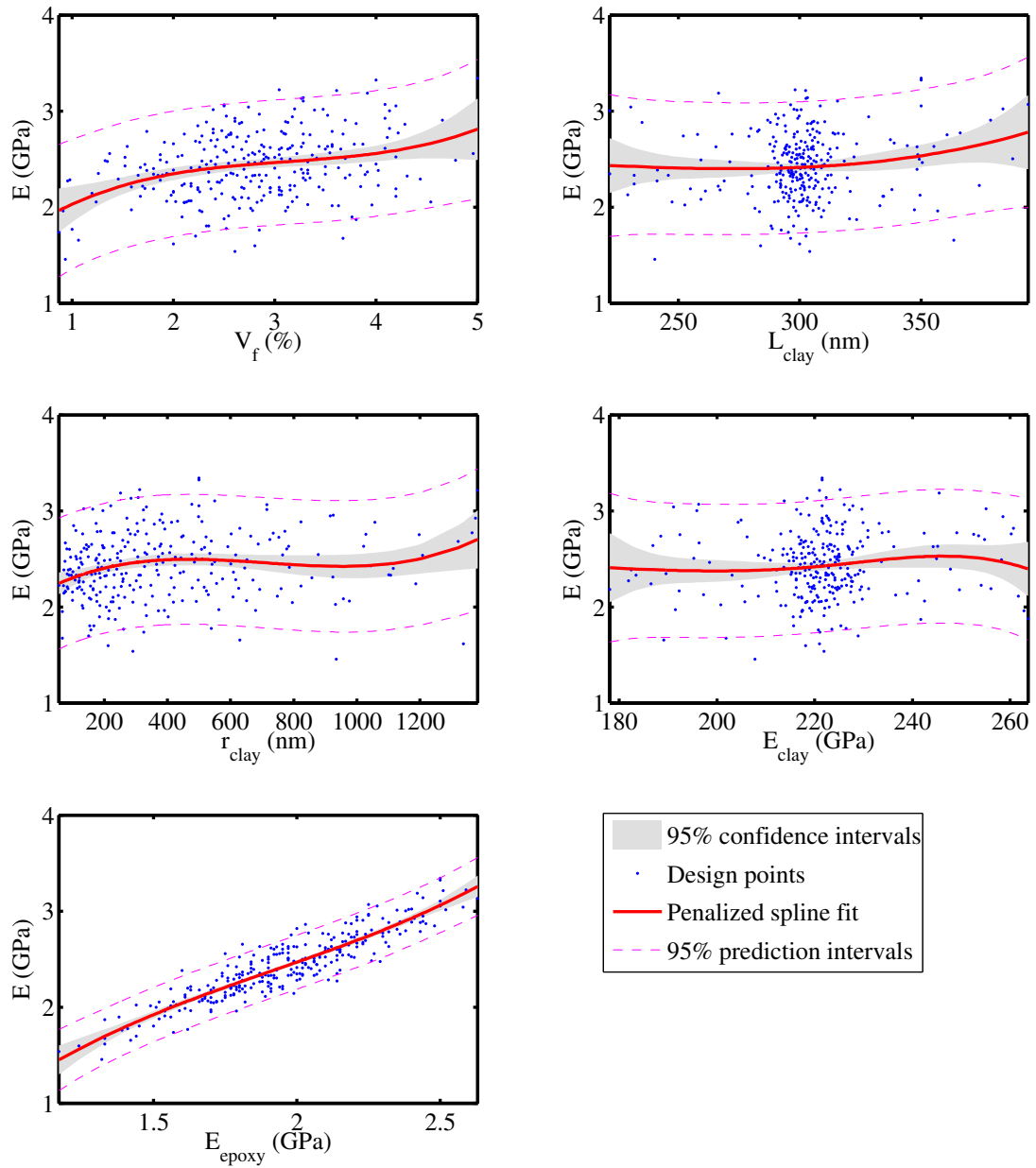


Figure 6.10: Scatter plots of input parameters versus the Young's modulus including the penalized spline regression.

6.5 Numerical results

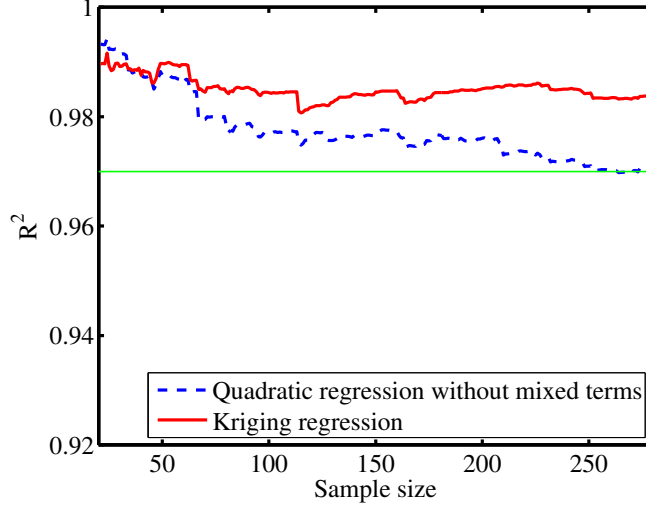


Figure 6.11: The plot of R^2 versus sample size when QDR and KR models are used

A sample containing 10,000 realizations of the k -dimensional model ($k = 5$) has been generated using the Latin hypercube sampling (LHS). The LP_τ QR sequences are generated (improved formulas in Table 2.2) by the Sobol's FORTRAN77 code LPTAU51 (STLS92). The reduced first-order indices (\hat{S}_i) and total-effect (\hat{S}_{Ti}) indices with $i = 1, \dots, 5$ for the Young's modulus of the PCNs are estimated by

$$\begin{aligned}\hat{S}_i &= R^2 S_i, \\ \hat{S}_{Ti} &= R^2 S_{Ti}.\end{aligned}\tag{6.3}$$

Employing the matrix combination method (Sal02), the reduced first-order (\hat{S}_i^{qdr}) and total-effect indices (\hat{S}_{Ti}^{qdr}) based on the QDR and \hat{S}_i^{kr} and \hat{S}_{Ti}^{kr} based on the KR are computed. The results are summarized in Tables 6.7 and 6.8 and illustrated in Figure 6.12. The results based on both regression models are nearly identical.

Table 6.7: First-order and total-effect sensitivity indices computed by the combination method based on the QDR model of the Young's modulus E

Matrix combination method based on the QDR model						
	V_f (X_1)	L_{clay} (X_2)	r_{clay} (X_3)	E_{clay} (X_4)	E_{epoxy} (X_5)	Σ
\hat{S}_i^{qdr}	0.10	0.00	0.02	0.00	0.85	0.97
\hat{S}_{Ti}^{qdr}	0.10	0.00	0.02	0.00	0.85	0.97

6.5 Numerical results

Table 6.8: First-order and total-effect sensitivity indices computed by the combination method based on the KR model of the Young's modulus E

Matrix combination method based on the KR model						
	V_f (X_1)	L_{clay} (X_2)	r_{clay} (X_3)	E_{clay} (X_4)	E_{epoxy} (X_5)	Σ
\hat{S}_i^{kr}	0.11	0.00	0.02	0.00	0.85	0.98
\hat{S}_{Ti}^{kr}	0.11	0.00	0.02	0.00	0.85	0.98

From Table 2.2, the respective Sobol' indices ($\hat{S}_i^{Sob,rd}$ and $\hat{S}_{Ti}^{Sob,rd}$) associated with formulas (a) and (d), and Saltelli/Sobol' indices ($\hat{S}_i^{Sal,rd}$ and $\hat{S}_{Ti}^{Sal,rd}$) associated with formulas (b) and (f) for single parameters are computed. Both methods are associated with the radial sampling scheme. In addition, $\hat{S}_i^{Jan,ws}$ and $\hat{S}_{Ti}^{Jan,ws}$ are estimated from Jansen's formulas (c) and (f) associated with the winding stairs sampling scheme. Those results are summarized in Table 6.9 and plotted in Figure 6.12. Furthermore, the total effects of pairs of parameters $\hat{S}_{ij}^{Sal,rd}$ with $i = 1, \dots, 5, j = i + 1$ is estimated by Equation (2.76) associated with the radial sampling scheme. The results are depicted in Table 6.10 and Figure 6.14.

Table 6.9: First-order and total-effect sensitivity indices computed by the improved formulas in section 2.8.1 based on the QDR model of the Young's modulus E

Sobol' indices (formulas (a), (d)) (radial sampling)						
	V_f (X_1)	L_{clay} (X_2)	r_{clay} (X_3)	E_{clay} (X_4)	E_{epoxy} (X_5)	Σ
$\hat{S}_i^{Sob,rd}$	0.11	0.00	0.01	0.00	0.84	0.97
$\hat{S}_{Ti}^{Sob,rd}$	0.12	0.00	0.01	0.00	0.85	0.98
Saltelli/Sobol' method (formulas (b), (f)) (radial sampling)						
	V_f (X_1)	L_{clay} (X_2)	r_{clay} (X_3)	E_{clay} (X_4)	E_{epoxy} (X_5)	Σ
$\hat{S}_i^{Sal,rd}$	0.10	0.00	0.02	0.00	0.85	0.97
$\hat{S}_{Ti}^{Sal,rd}$	0.10	0.00	0.02	0.00	0.85	0.97
Jansen's method (formulas (c), (f)) (winding stairs sampling)						
$\hat{S}_i^{Jan,ws}$	0.11	0.00	0.01	0.00	0.85	0.97
$\hat{S}_{Ti}^{Jan,ws}$	0.11	0.00	0.01	0.00	0.85	0.97

The first-order indices, computed by the MOS are shown in Table 6.11 and Figure 6.12. We have chosen the number of slices equal to 1/10 of the generated samples. The number of samples is fixed in each slice and the number of slices is increased with increasing number of samples.

6.5 Numerical results

Table 6.10: Total effects of pairs of parameters computed by the Saltelli/Sobol' method based on the QDR model of the Young's modulus E

Saltelli/Sobol' method (radial sampling)					
		L_{clay} ($j = 2$)	r_{clay} ($j = 3$)	E_{clay} ($j = 4$)	E_{epoxy} ($j = 5$)
$\hat{S}_{1j}^{Sal,rd}$	$V_f(X_1)$	0.10	0.12	0.10	0.95
$\hat{S}_{2j}^{Sal,rd}$	$L_{clay}(X_2)$		0.02	0.00	0.85
$\hat{S}_{3j}^{Sal,rd}$	$r_{clay}(X_3)$			0.02	0.87
$\hat{S}_{4j}^{Sal,rd}$	$E_{clay}(X_4)$				0.85

Table 6.11: First-order sensitivity indices computed by the MOS method based on the QDR model of the Young's modulus E

Method of slices (MOS)						
	V_f (X_1)	L_{clay} (X_2)	r_{clay} (X_3)	E_{clay} (X_4)	E_{epoxy} (X_5)	Σ
\hat{S}_i^{MOS}	0.10	0.00	0.01	0.00	0.86	0.97

For the FAST method we have selected $M = 4$ and $\{\omega_i\} = \{11, 21, 27, 35, 39\}$ as suggested by (STC99). The first-order indices are given in Table 6.12 and Figure 6.13. For the EFAST method; M is 4, $N_r = 1$ and the vector $\{\omega_i\} = 24$. As shown in section 2.8.5 we then obtain $\omega_{\sim i} = \{1, 2, 3, 1\}$ and $\max\{\omega_{\sim i}\} = (1/M)(\omega_i/2) = 3$. The computed first-order and total-effect indices are listed in Table 6.13 and Figure 6.13.

Table 6.12: First-order sensitivity indices computed by the FAST method based on the QDR model of the Young's modulus E

Fourier amplitude sensitivity test (FAST)						
	V_f (X_1)	L_{clay} (X_2)	r_{clay} (X_3)	E_{clay} (X_4)	E_{epoxy} (X_5)	Σ
\hat{S}_i^{FAST}	0.10	0.00	0.00	0.00	0.86	0.96

We have set $\omega_i = 1$, $M = 6$ for the RBD method. Table 6.14 and Figure 6.13 show the first-order indices.

The first-order indices of the EASI method with $M = 6$ are reported in Table 6.15 and Figure 6.13. Furthermore, let us consider the index group set $I = \{1, 2, 3, 4, 5\}$ including all $k = 5$ parameters. The estimated total effect $\hat{S}_{TI}^{EASI} = 0.97$ computed Equation (2.98) is identical to $\sum_{i=1}^5 S_{Ti}$ obtained by all other methods.

The FAST, EFAST, RBD, and EASI methods are the affine of Fourier based technique which are used to evaluate the global sensitivity indices. The computational

6.5 Numerical results

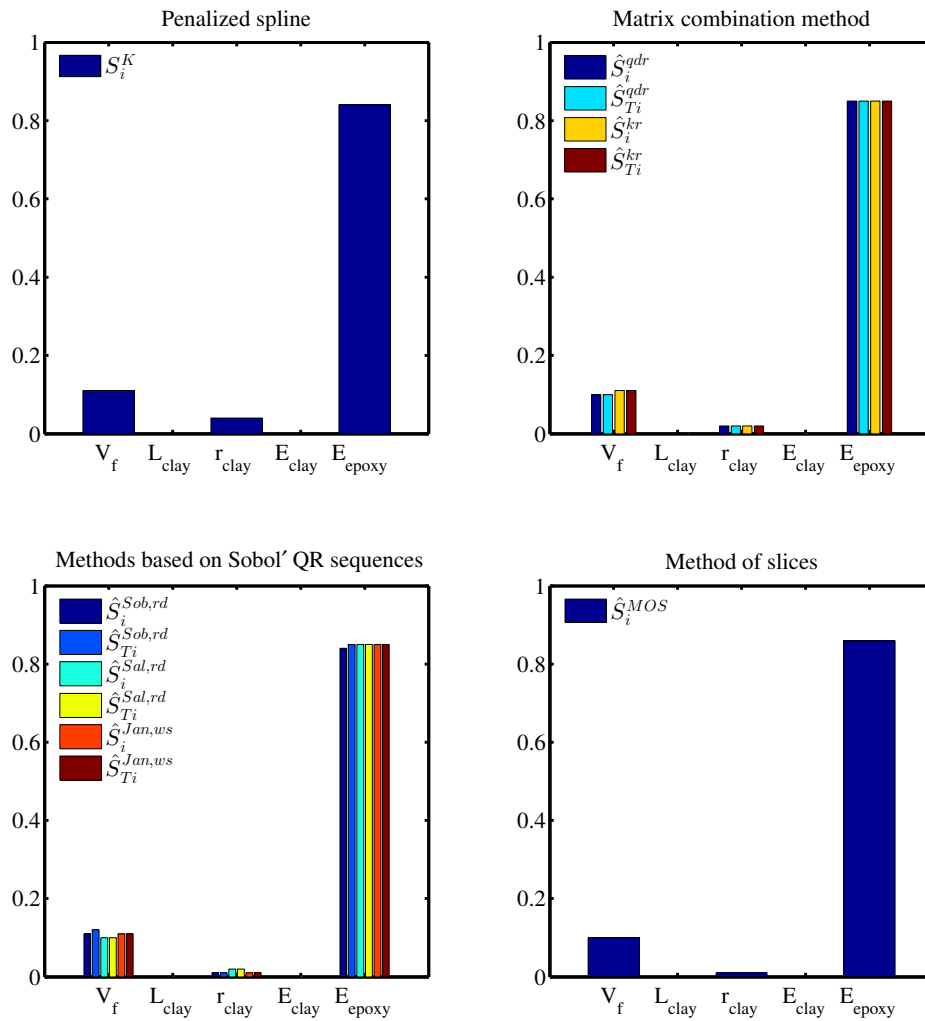


Figure 6.12: First-order and total-effect sensitivity indices w.r.t. the penalized spline regression, the matrix combination method, Saltelli/Sobol', Jansen's method and MOS.

6.5 Numerical results

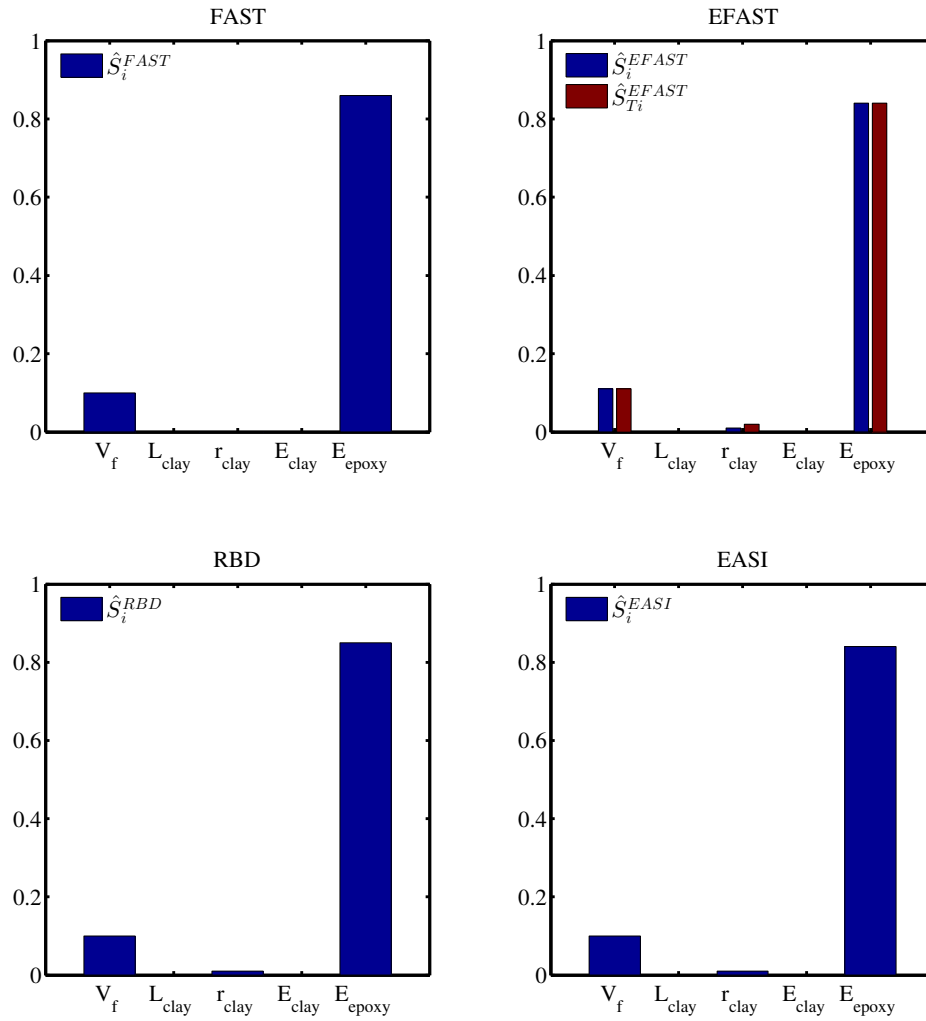


Figure 6.13: First-order and total-effect sensitivity indices w.r.t. FAST, EFAST, RBD and EASI.

6.5 Numerical results

Table 6.13: First-order and total-effect sensitivity indices computed by the EFAST method based on the QDR model of the Young's modulus E

Extended Fourier amplitude sensitivity test (EFAST)						
	V_f (X_1)	L_{clay} (X_2)	r_{clay} (X_3)	E_{clay} (X_4)	E_{epoxy} (X_5)	Σ
\hat{S}_i^{EFAST}	0.11	0.00	0.01	0.00	0.84	0.96
$\hat{S}_{T_i}^{EFAST}$	0.11	0.00	0.02	0.00	0.84	0.97

Table 6.14: First-order sensitivity indices computed by the RBD method based on the QDR model of the Young's modulus E

Random balance designs (RBD)						
	V_f (X_1)	L_{clay} (X_2)	r_{clay} (X_3)	E_{clay} (X_4)	E_{epoxy} (X_5)	Σ
\hat{S}_i^{RBD}	0.10	0.00	0.01	0.00	0.85	0.96

Table 6.15: First-order sensitivity indices computed by the EASI method based on the QDR model of the Young's modulus E

Effective algorithm for sensitivity indices (EASI)						
	V_f (X_1)	L_{clay} (X_2)	r_{clay} (X_3)	E_{clay} (X_4)	E_{epoxy} (X_5)	Σ
\hat{S}_i^{EASI}	0.10	0.00	0.01	0.00	0.84	0.95

expense (the value in the parentheses) of these methods is efficient and can be performed independently for each parameter. For example, the number of minimum simulations is $N_s = 313$ for the FAST method. With respect to EFAST method, as the total-effect indices are desired, a new set of model evaluations for estimating each S_{T_i} , $i = 1, \dots, 5$ is needed such that the total number of required simulations is increased k times; $N_s = 193 \times 5$.

In order to assess the robustness of Sobol' approaches and the improved formulas in section 2.8.1, we have performed bootstrapping the blocks to obtain CIs for the total-effect indices (**SAA+10**, **ASS97**). Note that $q = k + 1$ model evaluations are needed for bootstrapping one block. The total-effect estimators (formulas (d) and (f) in Table 2.2) of 95% CIs for the most important parameter (V_f (X_5)) are evaluated. With regards to the bootstrap CIs of the total-effect indices, Saltelli/Sobol' and Jansen's methods (formulas (b), (c) and (f)) associated with the radial and winding stairs sampling, respectively, are preferred to the Sobol' approach using formula (d) (with radial sampling) and the matrix combination method as the CIs of the former methods (0.04) are narrower than the latter's (0.34 and 0.38) at the same and even a larger

6.6 Conclusions

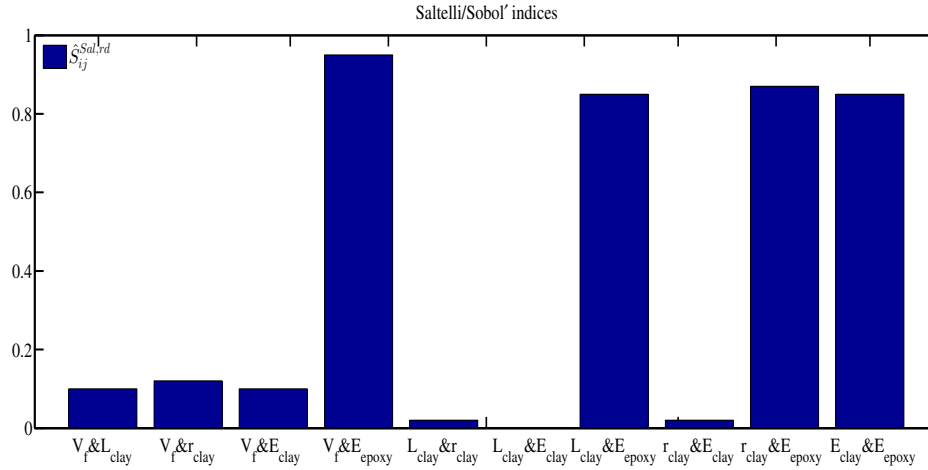


Figure 6.14: Total sensitivity indices estimated via Saltelli/Sobol' for all pairs of parameters X_i & X_j with $j \neq i$.

number of model evaluations, see Figure 6.5 and Table 6.16.

95% CIs for the first-order indices contributed by the volume fraction V_f (X_5) of the FAST, EFAST, RBD, EASI and MOS were also measured. Figures 6.16 and 6.17 and Table 6.16 show that the FAST and EFAST methods require less model evaluations than the others but obtain the higher confidence.

6.6 Conclusions

A stochastic numerical approach, considering uncertain input parameters - the volume fraction, the aspect ratio of clay, the clay radius, the clay stiffness, and the epoxy stiffness, was employed to evaluate the Young's modulus of the mechanical model. Subsequently, the framework of SA using different methods were performed to quantitatively estimate the influence of the input parameters on the Young's modulus. Global SA can provide robust predictions of the Young's modulus of PCNs. The results of all SA methods are nearly identical.

All sensitivity assessment methods predict the same tendencies, they are:

1. The Young's modulus of exfoliated PCNs is governed by the stiffness of the epoxy matrix.
2. The clay volume fraction has insignificant influence on the Young's modulus.
3. The clay length (aspect ratio), clay radius and clay stiffness have no influence on the Young's modulus of the PCNs.

6.6 Conclusions

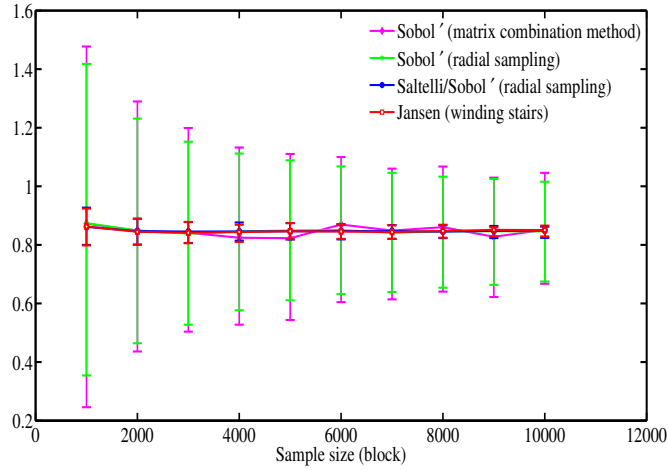


Figure 6.15: The total-effect indices and 95% CIs estimated for the parameter $V_f(X_5)$ via Monte Carlo method. The indices were evaluated using the matrix combination method and formulas (a), (b), (c), (d), and (f) in Table 2.2 with 1000 bootstrapping replicas.

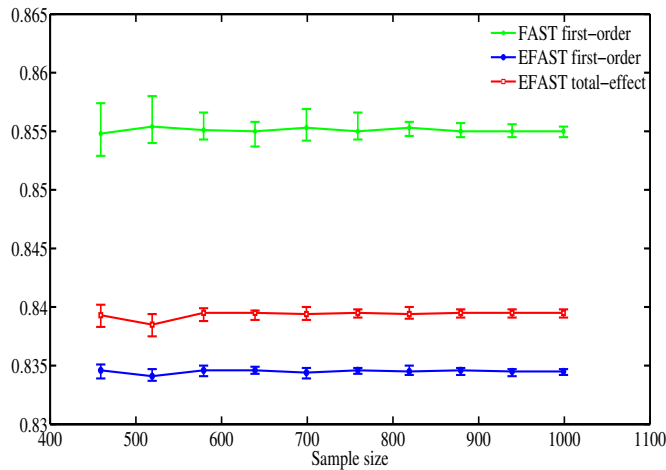


Figure 6.16: The sensitivity indices and 95% CIs estimated for the parameter $V_f(X_5)$ via Monte Carlo method. The indices were evaluated using FAST and EFAST methods with 1000 bootstrapping replicas.

6.6 Conclusions

Table 6.16: Comparison of SA methods in terms of bootstrap CIs versus the number of model evaluations.

Method	Number of evaluations of QDR model	CIs' band
Methods used to compute (S_i)		
FAST	999	1e-3
EFAST	999	1e-3
RBD	1000	0.03
EASI	1000	0.02
MOS	1000	0.03
Methods used to compute (S_{Ti})		
EFAST	999	1e-3
Sobol' (matrix combination)	10000×7	0.38
Sobol' (radial sampling)	10000×6	0.34
Saltelli/Sobol' (radial sampling)	10000×6	0.04
Jansen (winding stairs)	10000×6	0.04

Comments on the methods:

1. The penalized spline regression is used as a smooth function to plot $E(\mathbf{Y}|X_i)$ and compute the first-order indices S_i^K . The computation requires a small number of model evaluations such that the first-order indices can be straightforwardly estimated based on the mechanical model.
2. Although the KR model gives a little higher COD ($R^2 = 0.98$) than the QDR model's ($R^2 = 0.97$), the computation of sensitivity indices is computationally more expensive (420.21 s) than QDR model (0.16 s). However, it is still negligible compared to the simulation time of the mechanical model.
3. With respect to the matrix combination method and the improved formulas presented in section 2.8.1, a large number of model evaluations were required to compute the sensitivity indices as a price paid to capture the total-effect indices. However, the modification of the variance-based methods can be used for the models with dependent input parameters, see (KTA12, MT12).
4. The most robust methods are the FAST and EFAST. If both main effect and total effect of models with independent input parameters are desired, the EFAST is especially suited for this aim.

6.6 Conclusions

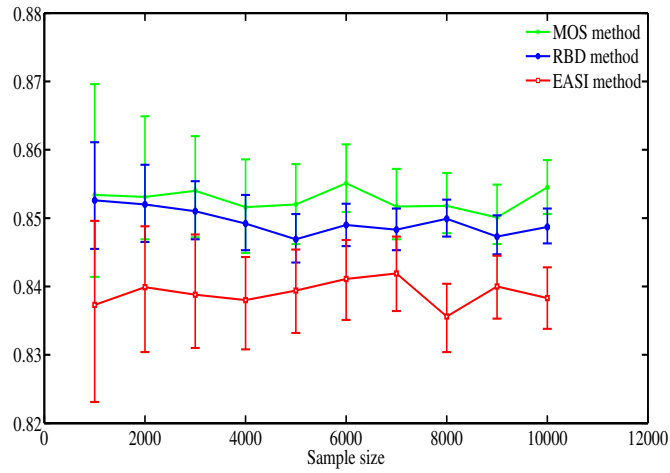


Figure 6.17: The first-order indices and 95% CIs estimated for the parameter $V_f (X_5)$ via Monte Carlo method. The indices were evaluated using MOS, RBD and EASI methods with 1000 bootstrapping replicas.

5. If the main effect is the quantity of interest, the FAST approach, which allows all first-order indices to be computed from the single curve, requires a small number of model evaluations such that the first-order indices can also be directly estimated on the mechanical model. This feature is an attractive robustness compared to the EFAST and other methods.

Chapter 7

A node-based smoothed extended finite element method (NS-XFEM) for fracture analysis

7.1 Introduction

The classical finite element method (FEM) is quite burdensome for modeling crack growths because it is required to remesh and align the new mesh to the crack's topology. Several finite element techniques such as GFEM (MB97, SBC00) and XFEM (BB99, MDB99) have been proposed to overcome those difficulties. More recently, the meshfree method has been successful in modeling static and dynamic fracture in 2-dimensions and 3-dimensions performed in (RB04, RA06, RE06, RB07b, RBZ07, RS08).

For the problems with complex geometries, triangular or tetrahedral elements, are usually preferred. However, FEM and XFEM based on such meshes suffer from some difficulties:

- The XFEM based on triangular elements is too stiff.
- The XFEM requires sub-triangulation for integration increasing complexity.
- The XFEM requires the derivatives of the shape function and requires many Gauss points for integrating the crack tip singularity.

We propose a new method to overcome those difficulties. The method is based on the node-based smoothed finite element method (NS-FEM). Smoothing was first used by (CWYY00) to stabilize nodal integration in meshfree method. By combining this strain smoothing technique with the finite element methods, Liu *et al.* have formulated a family of smoothed FEM models named SFEM (LNDL07, NRNB08), cell-based

7.1 Introduction

SFEM (CS-FEM) (LDN07, DLN7a, NBN08, BN10, CNA⁺10), node-based SFEM (NS-FEM) (LNNL09, NVRNX10, NRN⁺10), edge-based SFEM (ES-FEM) (LNL09), face-based SFEM (FS-FEM) (NLLZ09), alpha-FEM (NRNB09, NRNXB10). In all of these methods, smoothing strain operations are performed over smoothing domains to compute the system stiffness matrix.

In NS-FEM, the system stiffness matrix is calculated by using strain smoothing technique over the cells associated with nodes. As a result, line integration is used along the edges of the smoothing cells instead of volume integration. Moreover, no mapping is needed in the NS-FEM and only the shape functions themselves need to be computed, not their derivatives. It was also shown that the results are less sensitive for distorted elements.

In this paper, we propose a novel numerical method that exploits this special property of the line integration in the NS-XFEM. The system stiffness matrix is computed directly from the special basis shape functions along the boundaries of the smoothing domains. The combination of the NS-FEM and the XFEM can alleviate some of the following difficulties:

1. Simplify integration of discontinuous functions by transforming domain integration on Gauss points into boundary integration by using the divergence theorem. Consequently, there is no need to integrate the $1/\sqrt{r}$ term.
2. The functions to be integrated remain non-polynomial, and optimized one-dimensional integration techniques for these functions are promising routes to increase the accuracy of XFEM.
3. Insensibility to mesh distortion.
4. No subtriangulation is needed for integration reducing complexity.
5. Inherit robustness and accuracy of the triangular NS-FEM.

The paper is outlined as follows. In the next section, we briefly present the methodology for coupling NS-FEM and XFEM. Section 3 confirms the accuracy, efficiency and convergence properties of the present method by benchmark problems taken from linear elastic fracture mechanics. Finally, we end the manuscript with concluding remarks and future work.

7.2 Nodal-based smoothed extended finite element method (NS-XFEM)

7.2.1 Displacement and Strain Field

XFEM is based on a local partition of unity. For the case of linear elastic fracture mechanics (LEFM), two sets of enrichment functions are utilized: a Heaviside function to account for the jump across the crack faces and asymptotic branch (near-tip) functions (BB99, RW06):

$$\mathbf{u}^h(\mathbf{x}) = \underbrace{\sum_{I \in N^{ns-fem}} N_I(\mathbf{x}) \mathbf{d}_I}_{\mathbf{u}^{standard}} + \underbrace{\sum_{J \in N^{ns-c}} N_J(\mathbf{x}) H(\mathbf{x}) \mathbf{a}_J + \sum_{K \in N^{ns-f}} N_K(\mathbf{x}) \sum_{\alpha=1}^4 \Phi_\alpha(\mathbf{x}) \mathbf{b}_K}_{\mathbf{u}^{enr}} \quad (7.1)$$

where $N_I(\mathbf{x})$, $N_J(\mathbf{x})$ and $N_K(\mathbf{x})$ are finite element shape functions whose support domain is shown in Figure 2.13, while \mathbf{d}_I are nodal degrees of freedom associated with node I , \mathbf{a}_J and \mathbf{b}_K are additional nodal degrees of freedom corresponding to the Heaviside function $H(\mathbf{x})$ and the near-tip functions, $\{\Phi_\alpha\}_{1 \leq \alpha \leq 4}$, respectively.

Nodes in set N^{ns-c} are such that their support is split by the crack and nodes in set N^{ns-f} belong to the smoothing domains that contain a crack tip. These nodes are enriched with the Heaviside and asymptotic branch function fields depicted with squares and circles, respectively, in Figure 7.1. A set of nodes N^{ns-fem} whose support domain associated with a node of NS-FEM is illustrated in Figure 2.13.

Now we show how to create the support domain in NS-XFEM. Therefore, we determine the node-based smoothing domains in which at least one \mathbf{x} exists such that $N_I(\mathbf{x}) > 0$, where $N_I(\mathbf{x})$ is the shape function associated with node I . The smoothing domain corresponding to the inner node k , Ω_k^s , is combined from six sub-domains (sub-parts) of elements containing this node. Therefore, the domain Ω_k^s , can be considered to be the smoothing domain of seven nodes from six neighbouring elements: (1) one connectivity node of six neighbouring elements; (2) six remaining points of neighbouring elements. These seven nodes are called the associated nodes of smoothing domain Ω_k^s . The same procedure is applied for the smoothing domain associated with nodes located on the boundary of the domain. The shape of node-based smoothing domains is illustrated in Figure 2.13 in which FGHMN, ABCDE are associated nodes of smoothing domain Ω_k^s and Ω_m^s , respectively. The support domain of node I is shown by the hatched region in Figure 2.13.

In NS-XFEM, Heaviside enriched degrees of freedom are added to nodes in N^{ns-c} whose support domain is split by the crack and tip enriched degrees of freedom are added to nodes in set N^{ns-f} whose support domain contains the crack tip. These nodes

7.2 Nodal-based smoothed extended finite element method (NS-XFEM)

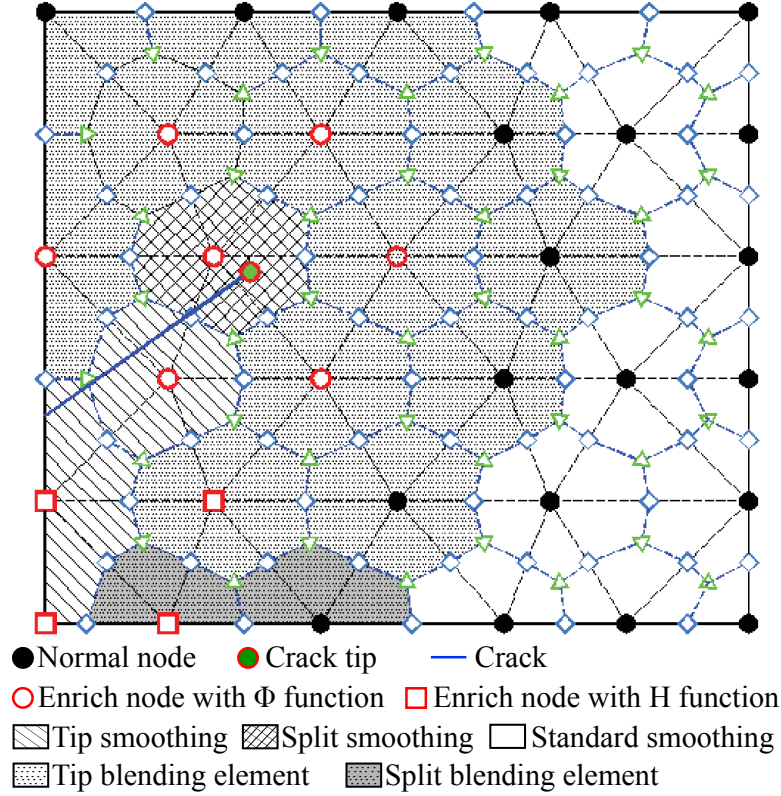


Figure 7.1: Illustration of node-based smoothing domain (sd) and node categories in NS-XFEM in terms of the support domain of nodal shape function.

are depicted by squares and circles, respectively, as shown in Figure 7.1. According to the chosen nodes, squared nodes are enriched by the step function whereas the circled nodes are enriched by the branch tip functions. In order to keep the convergence rate as high as possible, a so called geometric enrichment should be used that is independent from the discretization (LPRS05a).

In order to keep the enrichment domain narrow, we use a shifting

$$\begin{aligned}
 \mathbf{u}^h(\mathbf{x}) = & \sum_{I \in N^{ns-fem}} N_I(\mathbf{x}) \mathbf{d}_I + \sum_{J \in N^{ns-c}} N_J(\mathbf{x}) (H(\mathbf{x}) - H(\mathbf{x}_J)) \mathbf{a}_J \\
 & + \sum_{K \in N^{ns-f}} N_K(\mathbf{x}) \sum_{\alpha=1}^4 (\Phi_\alpha(\mathbf{x}) - \Phi_\alpha(\mathbf{x}_K)) \mathbf{b}_K^\alpha
 \end{aligned} \tag{7.2}$$

The shifting also circumvents problems due to blending for the Heaviside enrichment but not for the tip enrichment. Applying the node-based smoothing operation,

7.2 Nodal-based smoothed extended finite element method (NS-XFEM)

the smoothed strain associated with node k can be written as:

$$\begin{aligned} \bar{\boldsymbol{\epsilon}}_k = & \sum_{I \in N_k^s} \bar{\mathbf{B}}_I^u(\mathbf{x}_k) \bar{\mathbf{d}}_I + \sum_{J \in N^{ns-c}} \bar{\mathbf{B}}_J^a(\mathbf{x}_k) (H(\mathbf{x}) - H(\mathbf{x}_J)) \mathbf{a}_J \\ & + \sum_{k \in N^{ns-f}} \bar{\mathbf{B}}_K^b(\mathbf{x}_k) \sum_{\alpha=1}^4 (\Phi_\alpha(\mathbf{x}) - \Phi_\alpha(\mathbf{x}_K)) \mathbf{b}_K^\alpha \end{aligned} \quad (7.3)$$

where N_k^s is the set of nodes associated with the smoothing domain Ω_k^s , $\bar{\mathbf{B}}_I^u(\mathbf{x}_k)$ is the smoothed strain gradient matrix for the standard NS-FEM part, and $\bar{\mathbf{B}}_I^a(\mathbf{x}_k)$, $\bar{\mathbf{B}}_I^b(\mathbf{x}_k)$ correspond to the enriched parts of the smoothed strain gradient matrix associated with the Heaviside and branch functions, respectively. These matrixes operations can be written as follows:

$$\bar{\mathbf{B}}_I^r(\mathbf{x}_k) = \begin{bmatrix} \bar{b}_{Ix}^r(\mathbf{x}_k) & 0 \\ 0 & \bar{b}_{Iy}^r(\mathbf{x}_k) \\ \bar{b}_{Iy}^r(\mathbf{x}_k) & \bar{b}_{Ix}^r(\mathbf{x}_k) \end{bmatrix} \quad r = u, a, b \quad (7.4)$$

$$\bar{\mathbf{B}}_I^u = \int_{\Gamma_k^s} \frac{1}{A_k^s} \begin{bmatrix} n_x N_I & 0 \\ 0 & n_y N_I \\ n_y N_I & n_x N_I \end{bmatrix} d\Gamma$$

$$\bar{\mathbf{B}}_I^a = \int_{\Gamma_k^s} \frac{1}{A_k^s} \begin{bmatrix} n_x [N_I (H(\mathbf{x}) - H(\mathbf{x}_I))] & 0 \\ 0 & n_y [N_I (H(\mathbf{x}) - H(\mathbf{x}_I))] \\ n_y [N_I (H(\mathbf{x}) - H(\mathbf{x}_I))] & n_x [N_I (H(\mathbf{x}) - H(\mathbf{x}_I))] \end{bmatrix} d\Gamma$$

$$\bar{\mathbf{B}}_I^b = \int_{\Gamma_k^s} \frac{1}{A_k^s} \begin{bmatrix} n_x [N_I(\mathbf{x}_{m,n}) (\Phi_\alpha(x) - \Phi_\alpha(\mathbf{x}_I))] & 0 \\ 0 & n_y [N_I(\mathbf{x}_{m,n}) (\Phi_\alpha(\mathbf{x}) - \Phi_\alpha(\mathbf{x}_I))]_{,y} \\ n_y [N_I(\mathbf{x}_{m,n}) (\Phi_\alpha(\mathbf{x}) - \Phi_\alpha(\mathbf{x}_I))]_{,y} & n_x [N_I(\mathbf{x}_{m,n}) (\Phi_\alpha(\mathbf{x}) - \Phi_\alpha(\mathbf{x}_I))]_{,x} \end{bmatrix} d\Gamma \quad (\alpha = 1, 2, 3 \text{ and } 4) \quad (7.5)$$

7.2 Nodal-based smoothed extended finite element method (NS-XFEM)

Using Gauss-Legendre integration along Γ_k^s , we obtain:

$$\begin{aligned}
 \bar{\mathbf{B}}_I^u &= \frac{1}{A_k^s} \left[\begin{array}{cc} \sum_{m=1}^{N_{seg}} \left(\sum_{n=1}^{N_{gau}} n_x(\mathbf{x}_{m,n}) N_I(\mathbf{x}_{m,n}) w_{m,n} \right) & 0 \\ 0 & \sum_{m=1}^{N_{seg}} \left(\sum_{n=1}^{N_{gau}} n_y(\mathbf{x}_{m,n}) N_I(\mathbf{x}_{m,n}) w_{m,n} \right) \\ \sum_{m=1}^{N_{seg}} \left(\sum_{n=1}^{N_{gau}} n_y(\mathbf{x}_{m,n}) N_I(\mathbf{x}_{m,n}) w_{m,n} \right) & \sum_{m=1}^{N_{seg}} \left(\sum_{n=1}^{N_{gau}} n_x(\mathbf{x}_{m,n}) N_I(\mathbf{x}_{m,n}) w_{m,n} \right) \end{array} \right] \\
 \bar{\mathbf{B}}_I^a &= \frac{1}{A_k^s} \left[\begin{array}{cc} \sum_{m=1}^{N_{seg}} \left(\sum_{n=1}^{N_{gau}} n_x(\mathbf{x}_{m,n}) N_I(\mathbf{x}_{m,n}) \times \right. & 0 \\ \quad \left. \times (H(\mathbf{x}_{m,n}) - H(\mathbf{x}_I)) w_{m,n} \right) & \sum_{m=1}^{N_{seg}} \left(\sum_{n=1}^{N_{gau}} n_y(\mathbf{x}_{m,n}) N_I(\mathbf{x}_{m,n}) \times \right. \\ 0 & \quad \left. \times (H(\mathbf{x}_{m,n}) - H(\mathbf{x}_I)) w_{m,n} \right) \\ \sum_{m=1}^{N_{seg}} \left(\sum_{n=1}^{N_{gau}} n_y(\mathbf{x}_{m,n}) N_I(\mathbf{x}_{m,n}) \times \right. & \sum_{m=1}^{N_{seg}} \left(\sum_{n=1}^{N_{gau}} n_x(\mathbf{x}_{m,n}) N_I(\mathbf{x}_{m,n}) \times \right. \\ \quad \left. \times (H(\mathbf{x}_{m,n}) - H(\mathbf{x}_I)) w_{m,n} \right) & \quad \left. \times (H(\mathbf{x}_{m,n}) - H(\mathbf{x}_I)) w_{m,n} \right) \end{array} \right] \\
 \bar{\mathbf{B}}_I^b &= \frac{1}{A_k^s} \left[\begin{array}{cc} \sum_{m=1}^{N_{seg}} \left(\sum_{n=1}^{N_{gau}} n_x(\mathbf{x}_{m,n}) N_I(\mathbf{x}_{m,n}) \times \right. & 0 \\ \quad \left. \times (\Phi_\alpha(bfx_{m,n}) - \Phi_\alpha(\mathbf{x}_I)) w_{m,n} \right) & \sum_{m=1}^{N_{seg}} \left(\sum_{n=1}^{N_{gau}} n_y(\mathbf{x}_{m,n}) N_I(\mathbf{x}_{m,n}) \times \right. \\ 0 & \quad \left. \times (\Phi_\alpha(x) - \Phi_\alpha(\mathbf{x}_I)) w_{m,n} \right) \\ \sum_{m=1}^{N_{seg}} \left(\sum_{n=1}^{N_{gau}} n_y(\mathbf{x}_{m,n}) N_I(\mathbf{x}_{m,n}) \times \right. & \sum_{m=1}^{N_{seg}} \left(\sum_{n=1}^{N_{gau}} n_x(\mathbf{x}_{m,n}) N_I(\mathbf{x}_{m,n}) \times \right. \\ \quad \left. \times (\Phi_\alpha(\mathbf{x}_{m,n}) - \Phi_\alpha(\mathbf{x}_I)) w_{m,n} \right) & \quad \left. \times (\Phi_\alpha(\mathbf{x}_{m,n}) - \Phi_\alpha(\mathbf{x}_I)) w_{m,n} \right) \end{array} \right] \\
 & \quad (\alpha = 1, 2, 3 \text{ and } 4)
 \end{aligned} \tag{7.6}$$

where N_{seg} is the number of segments of the boundary Γ_k^s , N_{gau} is the number of Gauss points used in each segment, $w_{m,n}$ is the corresponding Gauss weights, n_x , n_y are the outward unit normal components to each segment on the smoothing domain boundary and $\mathbf{x}_{m,n}$ is the n -th Gaussian point on the m -th segment of the boundary Γ_k^s .

7.2.2 Weak form and discrete equation

Find $\mathbf{u}^h \in V$, $\forall \delta \mathbf{u}^h \in V_0$ such that

$$\int_{\Omega} \delta(\bar{\boldsymbol{\epsilon}}(\mathbf{u}^h))^T \mathbf{D}(\bar{\boldsymbol{\epsilon}}(\mathbf{u}^h)) d\Omega - \int_{\Omega} (\delta \mathbf{u}^h)^T \mathbf{b} d\Omega - \int_{\Gamma} (\delta \mathbf{u}^h)^T \mathbf{t}_{\Gamma} d\Gamma = 0 \tag{7.7}$$

7.2 Nodal-based smoothed extended finite element method (NS-XFEM)

with $V = \{\mathbf{u} \mid \mathbf{u} \in H^1(\Omega \setminus \Gamma_c), \mathbf{u} = \bar{\mathbf{u}} \text{ on } \Gamma_u, \mathbf{u} \text{ discontinuous on } \Gamma_c\}$
and $V_0 = \{\delta\mathbf{u} \mid \delta\mathbf{u} \in H^1(\Omega \setminus \Gamma_c), \delta\mathbf{u} = \mathbf{0} \text{ on } \Gamma_u, \delta\mathbf{u} \text{ discontinuous on } \Gamma_c\}$

Substituting the trial and test function into Equation (7.7), we finally obtain the well-known equation:

$$\bar{\mathbf{K}}\bar{\mathbf{d}} = \mathbf{f} \quad (7.8)$$

where \mathbf{f} is the nodal force vector that is identical to that in the standard XFEM. The smoothed enriched stiffness matrix $\bar{\mathbf{K}}$ for all sub-cells is computed by:

$$\bar{\mathbf{K}}_{IJ} = \sum_{k=1}^{N_s} \bar{\mathbf{K}}_{IJ,k}^s = \sum_{k=1}^{N_s} \begin{bmatrix} \int_{\Omega_k^s} (\bar{\mathbf{B}}_I^u)^T \mathbf{D} \bar{\mathbf{B}}_J^u d\Omega & \int_{\Omega_k^s} (\bar{\mathbf{B}}_I^u)^T \mathbf{D} \bar{\mathbf{B}}_J^a d\Omega & \int_{\Omega_k^s} (\bar{\mathbf{B}}_I^u)^T \mathbf{D} \bar{\mathbf{B}}_J^b d\Omega \\ \int_{\Omega_k^s} (\bar{\mathbf{B}}_I^a)^T \mathbf{D} \bar{\mathbf{B}}_J^u d\Omega & \int_{\Omega_k^s} (\bar{\mathbf{B}}_I^a)^T \mathbf{D} \bar{\mathbf{B}}_J^a d\Omega & \int_{\Omega_k^s} (\bar{\mathbf{B}}_I^a)^T \mathbf{D} \bar{\mathbf{B}}_J^b d\Omega \\ \int_{\Omega_k^s} (\bar{\mathbf{B}}_I^b)^T \mathbf{D} \bar{\mathbf{B}}_J^u d\Omega & \int_{\Omega_k^s} (\bar{\mathbf{B}}_I^b)^T \mathbf{D} \bar{\mathbf{B}}_J^a d\Omega & \int_{\Omega_k^s} (\bar{\mathbf{B}}_I^b)^T \mathbf{D} \bar{\mathbf{B}}_J^b d\Omega \end{bmatrix} \quad (7.9)$$

In NS-XFEM, the stiffness matrix in Equation (7.9) can therefore be rewritten as:

$$\bar{\mathbf{K}}_{IJ} = \sum_{k=1}^{N_s} \bar{\mathbf{K}}_{IJ,k}^s = \sum_{k=1}^{N_s} \begin{bmatrix} (\bar{\mathbf{B}}_I^u)^T \mathbf{D} \bar{\mathbf{B}}_J^u A_k^s & (\bar{\mathbf{B}}_I^u)^T \mathbf{D} \bar{\mathbf{B}}_J^a A_k^s & (\bar{\mathbf{B}}_I^u)^T \mathbf{D} \bar{\mathbf{B}}_J^b A_k^s \\ (\bar{\mathbf{B}}_I^a)^T \mathbf{D} \bar{\mathbf{B}}_J^u A_k^s & (\bar{\mathbf{B}}_I^a)^T \mathbf{D} \bar{\mathbf{B}}_J^a A_k^s & (\bar{\mathbf{B}}_I^a)^T \mathbf{D} \bar{\mathbf{B}}_J^b A_k^s \\ (\bar{\mathbf{B}}_I^b)^T \mathbf{D} \bar{\mathbf{B}}_J^u A_k^s & (\bar{\mathbf{B}}_I^b)^T \mathbf{D} \bar{\mathbf{B}}_J^a A_k^s & (\bar{\mathbf{B}}_I^b)^T \mathbf{D} \bar{\mathbf{B}}_J^b A_k^s \end{bmatrix} \quad (7.10)$$

7.2.3 Numerical integration

7.2.3.1 Numerical integration for the XFEM.

There are four types of elements used for numerical integration as mentioned in (BRN⁺08):

- *Tip elements* contain the crack tip. All nodes belonging to a tip element are enriched with the branch functions, Equation (2.39).
- *Split elements* are elements completely cut by the crack. Their nodes are enriched with the step function, Equation (2.38).
- *Tip-blending elements* are elements neighboring tip elements. Some of their nodes are enriched with branch functions, while others are not enriched at all.
- *Split-blending elements* are elements neighboring split elements. Some of their nodes are enriched with the Heaviside function, while others are not enriched.
- *Standard elements* are elements that are in neither of the above categories. None of their nodes are enriched.

7.2 Nodal-based smoothed extended finite element method (NS-XFEM)

Since the approximation differs from element to element, different integration parameters are used. For XFEM built on T3 elements, we chose the following Gauss quadrature rules as (BRN⁺08)

1. *Tip elements*: 7 Gauss points for each sub-element.
2. *Split elements*: 1 Gauss points for each sub-element.
3. *Tip-blending elements*: 7 Gauss points.
4. *Split-blending elements*: 1 Gauss point.
5. *Standard elements*: 1 Gauss point.

7.2.3.2 Numerical integration for the NS-XFEM.

There are five types of smoothing domains (sd) as shown in Figure 7.1:

- *Tip smoothing domains* contain a crack tip. All nodes are enriched with branch functions.
 - *Split smoothing domains* are completely cut by a crack surface, and their nodes are enriched with the Heaviside function.
 - In *Tip-blending smoothing domains*, one or more nodes are enriched with branch functions, and others are not enriched at all.
 - *Split-blending smoothing domains* contain step enriched nodes and not enriched nodes
 - *Standard smoothing domains* are smoothing domains that are in none of the above categories. None of their nodes are enriched.
- (i) *Split smoothing domains*: To perform Gauss integration for split smoothing domains, it is inevitable to divide them into several triangles and then use the familiar quadrature rules. However, the complex interior integration can be replaced by boundary integration which can be implemented on polygonal boundaries of sub-domains (BRN⁺08). One Gauss point on each boundary segment for split smoothing domains is sufficient. The scheme of partitioning the split smoothing domain is shown in Figure 7.2.
- (ii) *Split-blending smoothing domains*: Partitioning of smoothing domains is not necessary. One Gauss point on each boundary segment is sufficient.

7.3 Numerical results

- (iii) *Tip smoothing domains*: Special care has to be taken. Simply splitting the smoothing domains into sub-domains is not sufficient to guarantee accurate results (LPRS05a). A higher integration density should be used close to crack tip. We propose the following procedure: (1) Splitting the smoothing domain into triangles as shown in Figure 7.3; (2) Dividing triangle into n_{sc} sub-cells (also triangles) following the rules giving in Figure 7.4. Figure 7.3 shows the sub-cells after dividing sub-sd1 and sub-sd3 with $n_{sc} = 3$, e.g., sub-sd1 is split into sc1, sc2 and sc3; and sub-sd3 is split into sc4, sc5 and sc6; (3) The numerical integration is then performed on boundaries of triangular cells.

When we perform boundary integration along the crack face over sub-cells whose boundary segments coincide with the crack surface, so-called c-sub-cells are used as illustrated in Figure 7.3. For example two c-sub-cells that share a boundary segment along the crack surface are used (sc3 and sc6). Although the values of discontinuous function, $H(\mathbf{x})$, or branch functions, $\Phi_\alpha(\mathbf{x})$ for both c-sub-cells are the same, the displacement between two sides of crack has a jump and it is obviously not compatible with the above calculations. A remedy for this problem is proposed in which we calculate the values of the enrichment $H(\mathbf{x})$ and branch functions, $\Phi_\alpha(\mathbf{x})$ at the center instead of Gauss points on the side of this sub-cell.

Numerical experiments (CRL+10) suggest that eight smoothing cells in a smoothing domain ($n_{sc} = 8$), and five Gauss points on a segment of smoothing cells ($n_{sc} = 5$) are sufficient. This rule is also used in this paper.

- (iv) *Tip-blending smoothing domains*: no partition is required, and we also use eight smoothing cells in a smoothing domain with five Gauss points on each boundary segment.
- (v) *Standard smoothing domains* are computed as in NS-FEM.

7.2.4 Stress intensity factor

Fracture parameters such as mode I and mode II stress intensity factors (SIFs) are determined using the domain form (LSN85, MS87) of the interaction integral (YWC80). All the finite elements within a radius of $r_d = r_k h_e$ from the crack-tip are selected. Here, h_e is the crack-tip element size and r_k is a scalar.

7.3 Numerical results

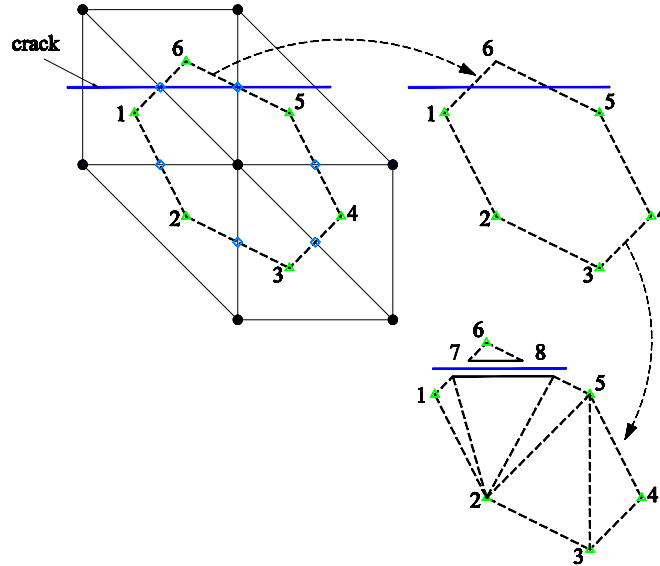


Figure 7.2: Partitioning split smoothing domain into triangular sub-domains (triangles).

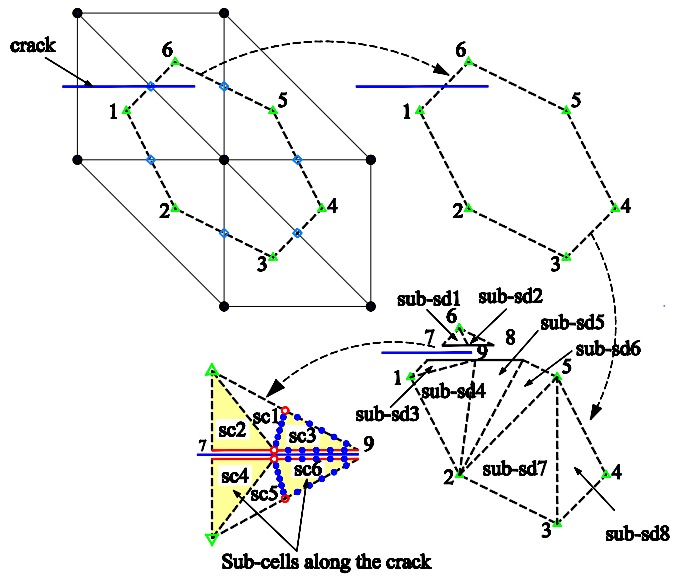


Figure 7.3: Partitioning tip smoothing domain into triangular sub-domains (triangles).

7.3 Numerical results

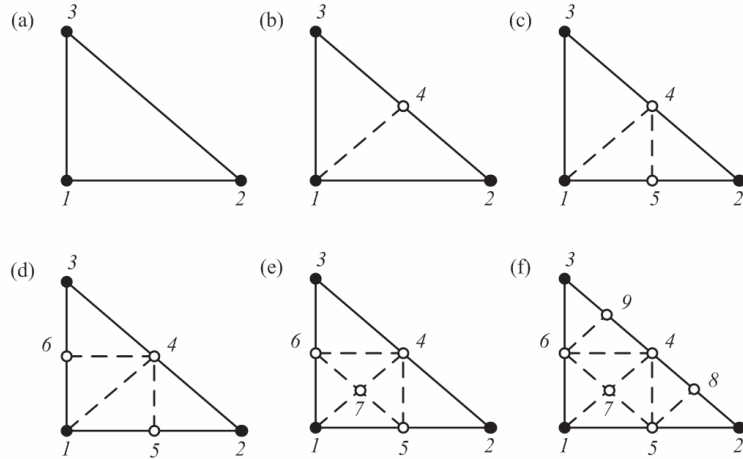


Figure 7.4: Division of a sub-smoothing domain into sub-smoothing cells (a) $n_{sc} = 1$; (b) $n_{sc} = 2$; (c) $n_{sc} = 3$; (d) $n_{sc} = 4$; (e) $n_{sc} = 6$; (f) $n_{sc} = 8$.

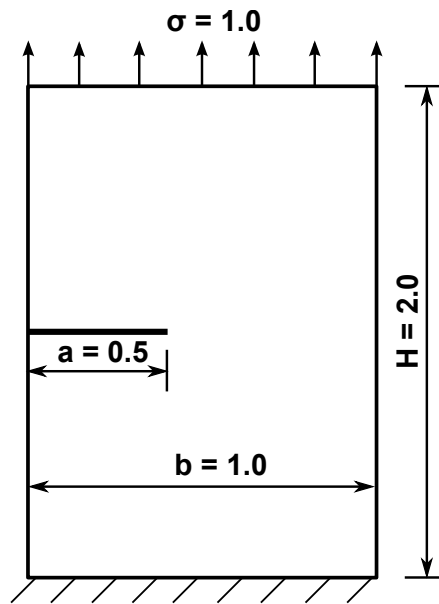


Figure 7.5: Plate with edge crack under tension.

7.3 Numerical results

7.3.1 Plate with edge-crack under tension

Consider a plate under uniaxial tension as shown in Figure 7.5. Plate's dimension is mm. The material parameters are Young's modulus $E = 3 \times 10^7 Pa$ and Poisson's

7.3 Numerical results

ratio $\nu = 0.3$; plane strain conditions are assumed. The reference mode I SIF is given by:

$$K_I^{exact} = F\left(\frac{a}{b}\right) \sigma \sqrt{a\pi} = 1.6118Pa\sqrt{mm} \quad (7.11)$$

where $a = 0.3$ is the crack length, b is the plate width and $F\left(\frac{a}{b}\right)$ is given by

$$F\left(\frac{a}{b}\right) = 1.12 - 0.231\left(\frac{a}{b}\right) + 10.55\left(\frac{a}{b}\right)^2 - 21.72\left(\frac{a}{b}\right)^3 + 30.39\left(\frac{a}{b}\right)^4 \quad (7.12)$$

The strain energy and the error in the energy norm are defined as:

$$E_{(\Omega)} = \frac{1}{2} \int_{\Omega} \boldsymbol{\epsilon}^T \mathbf{D} \boldsymbol{\epsilon} d\Omega \quad (7.13)$$

$$e_e = \left| \frac{E_{(\Omega)}^{num} - E_{(\Omega)}^{ref}}{E_{(\Omega)}^{ref}} \right|^{1/2} \quad (7.14)$$

$$e_k = \left| \frac{K_{sif}^{num} - K_{sif}^{ref}}{K_{sif}^{ref}} \right|^{1/2} \times 100\%, \quad sif = I, II \quad (7.15)$$

where the superscript "ref" denotes the exact or reference solution, and "num" denotes the numerical solution.

We subsequently consider the following NS-XFEM formulations:

- NS-XFEM(4t) with Heaviside enrichment and tip enrichment Φ , Eq. (2.39).
- NS-XFEM(1t) with Heaviside enrichment and branch enrichment $\Phi = \sqrt{r} \sin \frac{\theta}{2}$ (the last three terms in Equation (2.39) are omitted (RZ07)).
- NS-XFEM(0t) with only Heaviside enrichment but without branch tip enrichment.

The results of the NS-XFEM are compared with those of the ES-XFEM (LCN+10) and the XFEM-T3 (the "standard" XFEM formulation) with full tip enrichment. Both, ES-XFEM and XFEM-T3, employ the Heaviside enrichment and the full tip enrichment of Equation (2.39). Figure 7.6 shows that the strain energy of NS-XFEM(4t) and NS-XFEM(1t) models is closer to the reference value compared to the ES-XFEM. The NS-XFEM(0t) results in an upper-bound solution. We note that the tip enriched NS-XFEM formulations does not result in an upper bound solution. The convergence rates in terms of the strain energy norm and SIF K_I for different numerical methods are depicted in Figure 8.7 and Figure 8.9. The NS-XFEM (4t) achieves super-convergent results and is more accurate than both ES-XFEM and XFEM-T3. The NS-XFEM (1t) almost produces the same results as the ES-XFEM.

7.3 Numerical results

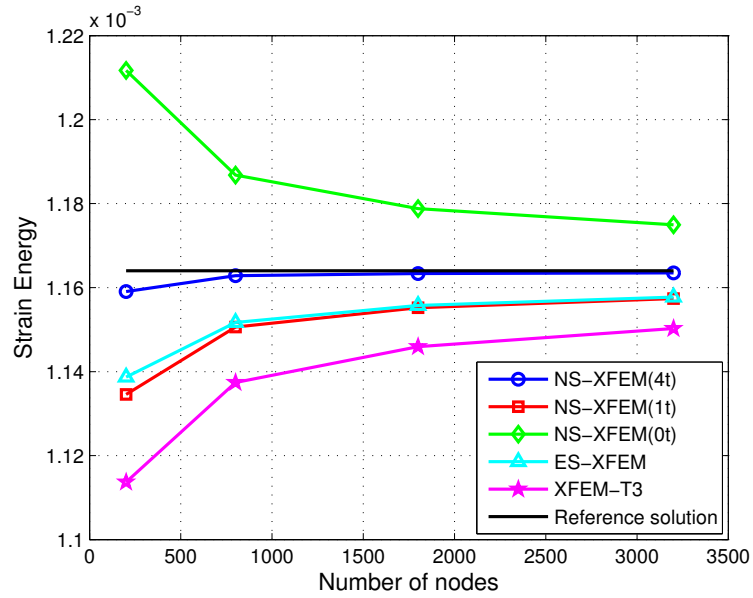


Figure 7.6: Strain energy for the plate with edge crack under tension.

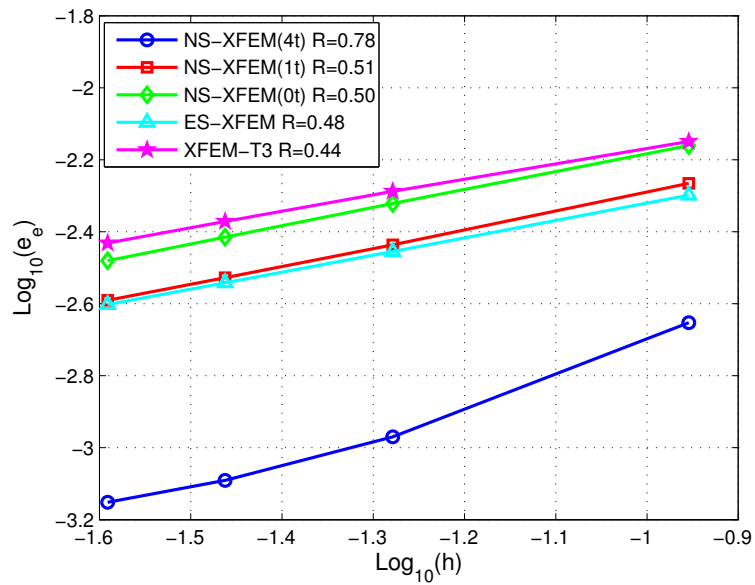


Figure 7.7: The convergence in the energy norm vs. h (mesh size) for the plate with edge crack under tension.

7.4 Conclusions

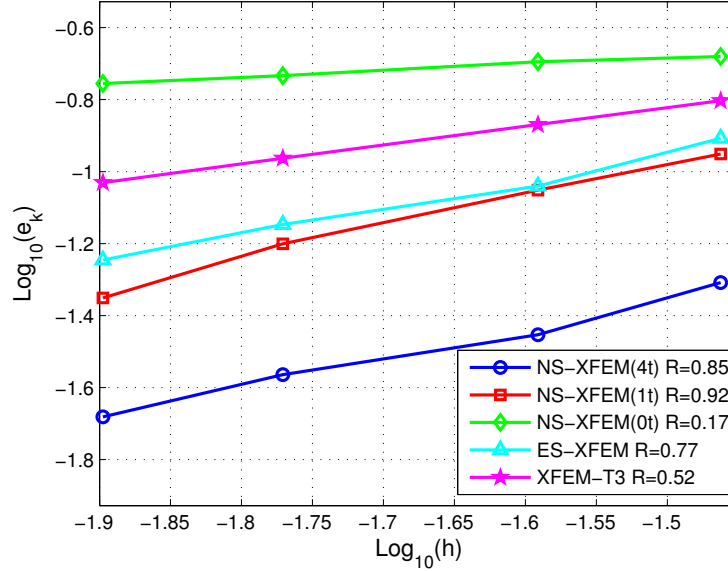


Figure 7.8: The convergence in the stress intensity factor K_I vs. h (mesh size) for the plate with edge crack under tension.

7.3.2 Plate with edge-crack under shear

In this example, we consider the edge crack geometry subjected to a shear load as shown in Figure 7.9. The material parameters are Young's modulus $E = 3 \times 10^7 Pa$ and Poisson's ratio $\nu = 0.25$. The exact stress intensity factors for this load case are given (YWC80) by

$$K_I = 34.0Pa\sqrt{mm}; K_{II} = 4.55Pa\sqrt{mm} \quad (7.16)$$

The results from Figure 7.10 to Figure 7.13 show that the NS-XFEM (1t) and NS-XFEM (4t) results are more accurate than those of ES-XFEM and XFEM-T3. NS-XFEM(4t) maintains superconvergent solutions and the NS-XFEM(0t) produces an upper bound solution in the strain energy.

7.4 Conclusions

We presented a novel numerical method called NS-XFEM that combines NS-FEM and XFEM for analysis of two-dimensional linear elastic fracture problems. Some benchmark examples were performed and we computed the convergence rate in terms of strain energy and stress intensity factor. The results of NS-XFEM were then compared

7.4 Conclusions

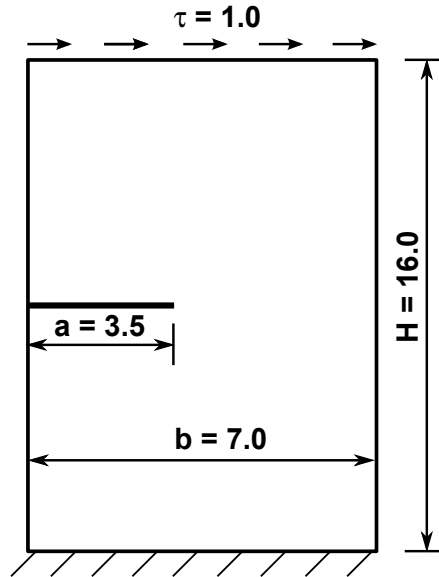


Figure 7.9: Plate with edge crack under shear.

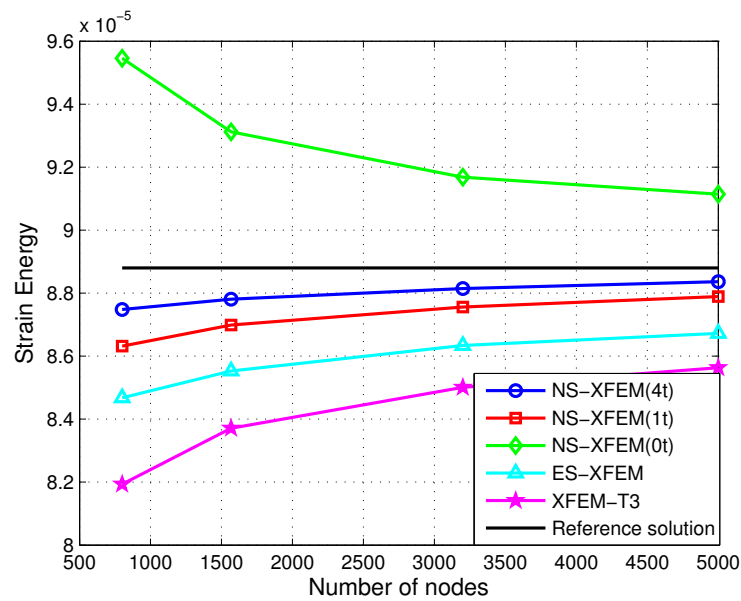


Figure 7.10: Strain energy for plate with edge crack under shear.

to those of ES-XFEM and the standard XFEM-T3. It was shown that the NS-XFEM can produce superconvergent solutions. The present method also simplifies the integra-

7.4 Conclusions

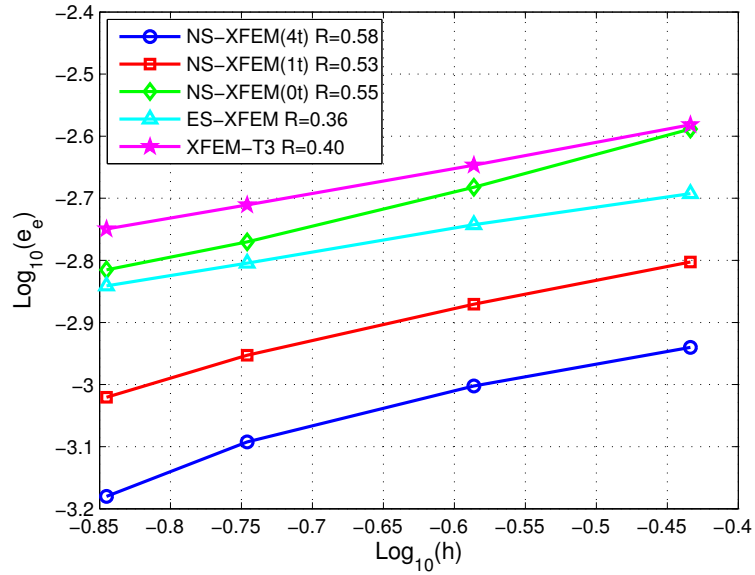


Figure 7.11: The convergence in the energy norm vs. h (mesh size) for plate with edge crack under shear.

tion of discontinuous approximation by transforming interior integration into boundary integration. More importantly, no derivatives of shape functions are needed to compute the stiffness matrix. As a result, the integration of singular functions is avoided when the Westergaard solution is inserted into the approximation.

7.4 Conclusions

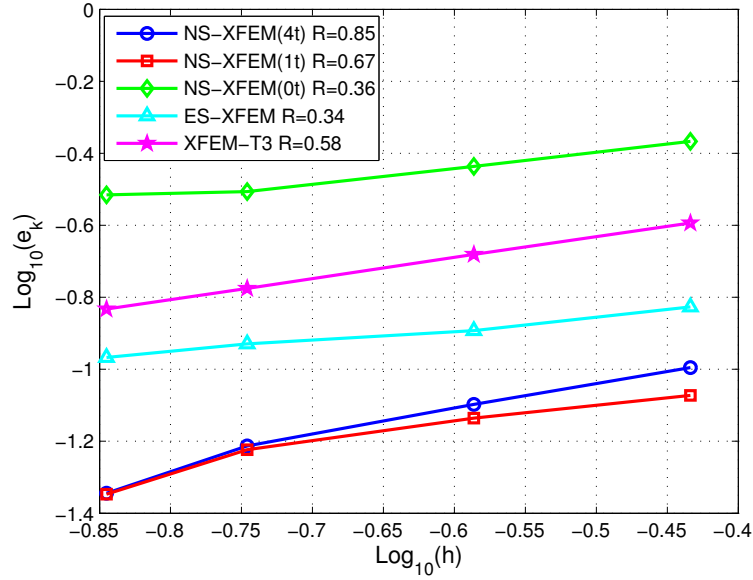


Figure 7.12: The convergence in the stress intensity factor K_I vs. h (mesh size) for plate with edge crack under shear.

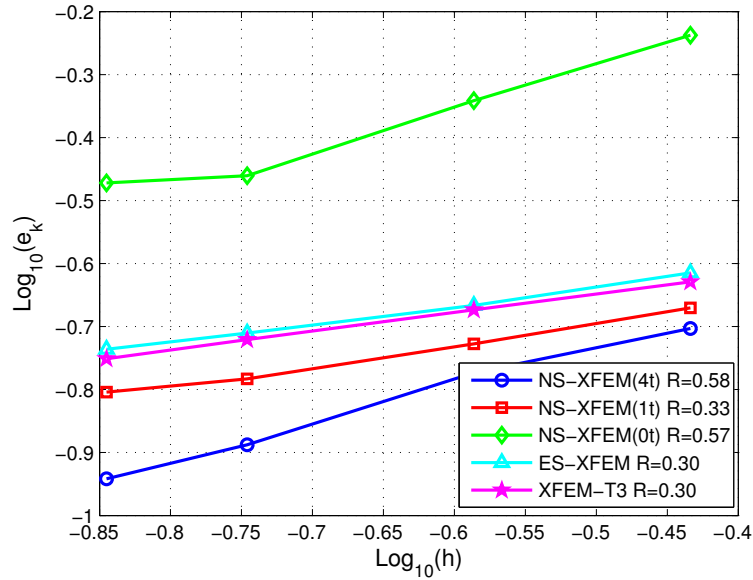


Figure 7.13: The convergence in the stress intensity factor K_{II} vs. h (mesh size) for plate with edge crack under shear.

Chapter 8

A phantom-node method with edge-based strain smoothing for linear elastic fracture mechanics

8.1 Introduction

The extended finite element method (XFEM) (BB99) has become a standard tool to model arbitrary crack growth. However, the implementation of XFEM in an existing finite element code requires severe modifications. An alternative method to model arbitrary crack growth was proposed by (HH04), subsequently implemented by (MK05) in a static setting and by (SAB06) in a dynamic setting. It was shown by (SAB06, AB05) that the method proposed by (HH04) is identical to a step-enriched XFEM; (SAB06) refer to this method as phantom node method. The main difference to the original XFEM is that the discontinuity jump is not obtained by introducing additional unknowns but by so called overlapping paired elements. In other words, a new 'overlapped' element is introduced to handle the crack kinematics when an underlying element is cracked. It is accomplished by integrating these overlapped elements up to the crack. Though it was shown by (SAB06) that the crack kinematics obtained with the phantom node method is identical to the step enriched XFEM, it has some advantages over step-enriched XFEM:

1. As no additional degrees of freedom are introduced, the implementation of the phantom node method in an existing finite element code is simpler. For example, arbitrary crack growths for non-linear materials and cohesive zone models even for multiple cracks in two and three dimensions have already been implemented in ABAQUS (SCL⁺10) while an additional plug-in (Duf11) is required to model crack growth using XFEM.

8.1 Introduction

2. No mixed terms (\mathbf{K}^{ua} and \mathbf{K}^{au}) occur improving conditioning.
3. Standard mass lumping schemes can be used due to the absence of an enrichment. There are several contributions to develop diagonalized mass matrices in standard XFEM (MRM⁺06, MRM⁺08) but they are based on certain assumptions.
4. The development of complex FE-formulations is much easier due to the lack of an enrichment. For example: When techniques such as EAS (Enhanced Assumed Strain) or ANS (Assumed Natural Strain) are used, special attention is required in a standard XFEM-formulation, particularly for problems with constraints. Those difficulties do not occur in the phantom node method (CZL⁺12).

The key drawback of the phantom node method compared to standard XFEM is its lower flexibility. It was developed for problems involving crack growth 'only'. However, avoiding a crack tip enrichment significantly facilitates the enrichment strategy and the crack tracking algorithm:

- A crack tip enrichment introduces more additional unknowns. It is well known that a topological enrichment is needed for accuracy reasons (LPRS05b) leading to a substantial increase of additional unknowns (compared to 'pure' step-enriched formulations) and increasing difficulties due to increasing the condition number.
- The non-polynomial (and singular) crack-tip enrichment complicates integration (BMMB05, VGB09, GWB08, BRN⁺08) and requires special attention (blending).
- The enrichment strategy and the crack growth algorithms are complicated, in particular in 3D.

Modeling crack growth with the phantom node method on the other hand is quite simple. Commonly, plane crack segments are introduced through the entire element though crack tip elements were developed (RZGW08) that allow cracks to close inside an element.

Recently, Liu *et al.* constructed a new class of finite element methods based on strain smoothing. Among those methods, the so-called ES-FEM (Edge-based Smoothed Finite Element Method) has been proven to be the most efficient and accurate one. In numerous application (LDN07, LNDL07, NRNB08), it was shown that particularly low-order SFEM-formulations are superior in terms of efficiency and accuracy over 'standard' low-order finite element formulations. In particular, it was shown for many applications (BN10, BRN⁺08) that results obtained by triangular ES-FEM elements are of the same accuracy as standard Q4-elements.

8.2 Edge-based strain smoothing phantom node method

Therefore, we propose to couple the ES-FEM with the phantom node method. We name the new element edge-based phantom node method (ES-Phantom node). In this manuscript, we focus on two-dimensional problems in linear elastic fracture mechanics (LEFM). However, our long term goal is to model fracture in non-linear materials in 3D. Numerical results show high reliability of the present method for analysis of fracture problems.

This chapter is organized as follows. The combination between the phantom-node method and the ES-FEM is elaborated in Section 2. Section 3 presents the integration technique. Benchmark numerical problems taken from linear elastic fracture mechanics are studied in Section 4. Finally, we give some concluding remarks.

8.2 Edge-based strain smoothing phantom node method

8.2.1 Displacement and strain field

The approximation of the displacement field is written similarly to Equation (2.40)

$$\mathbf{u}^h(\mathbf{x}) = \sum_{I \in S_1^{es-pht}} \underbrace{\mathbf{u}_I^1 N_I(\mathbf{x})}_{\mathbf{u}^1(\mathbf{x})} H(f(\mathbf{x})) + \sum_{I \in S_2^{es-pht}} \underbrace{\mathbf{u}_I^2 N_I(\mathbf{x})}_{\mathbf{u}^2(\mathbf{x})} H(-f(\mathbf{x})) \quad (8.1)$$

where S_1^{es-pht} and S_2^{es-pht} are nodes associated with smoothing domains 1 and 2, respectively, consisting of real nodes and phantom nodes illustrated in Figures 8.1 and 8.2. The associated nodes of the inner smoothing domain $\Omega^{(k)}$ (DEFG) and boundary smoothing domain $\Omega^{(m)}$ (ABC) are shown in Figure 2.14.

The connectivities of these superimposed smoothing domains which are cracked completely and the corresponding active parts are shown in Figure 8.1

$$\text{nodes of smoothing domain 1 } (\Omega_1^{(k)}) = [1, 2, \tilde{3}, \tilde{4}]$$

$$\text{nodes of smoothing domain 2 } (\Omega_2^{(k)}) = [\tilde{1}, \tilde{2}, 3, 4]$$

The connectivity of a superimposed smoothing domain containing the crack tip and the corresponding active parts is shown in Figure 8.2 so that crack tip is guaranteed to locate on the element's edge.

$$\text{nodes of smoothing domain 1 } (\Omega_1^{(k)}) = [1, 2, 4]$$

$$\text{nodes of smoothing domain 2 } (\Omega_2^{(k)}) = [\tilde{1}, 2, 4,]$$

Numerical integration is implemented on chosen Gauss points as illustrated in Figures 8.3 and 8.4 corresponding with split smoothing domain in Figure 8.1 and tip smoothing domain in Figure 8.2, respectively.

8.2 Edge-based strain smoothing phantom node method

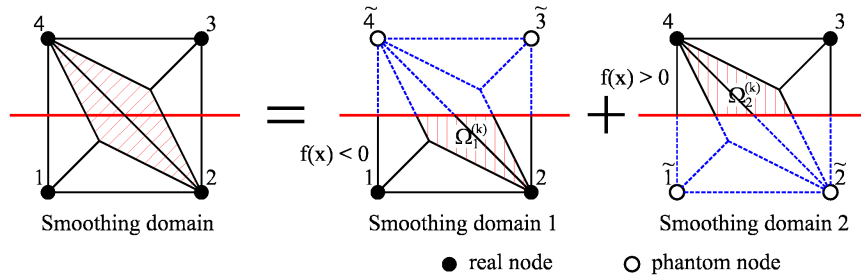


Figure 8.1: The decomposition of a completely cracked smoothing domain into two superimposed smoothing domains.

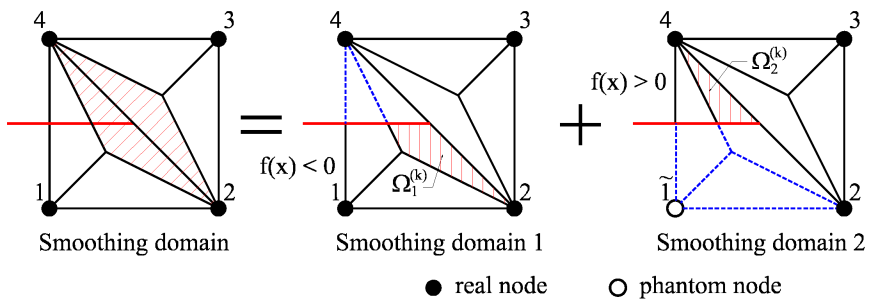


Figure 8.2: The decomposition of a cracked smoothing domain containing crack tip into two superimposed smoothing domains.

8.2 Edge-based strain smoothing phantom node method

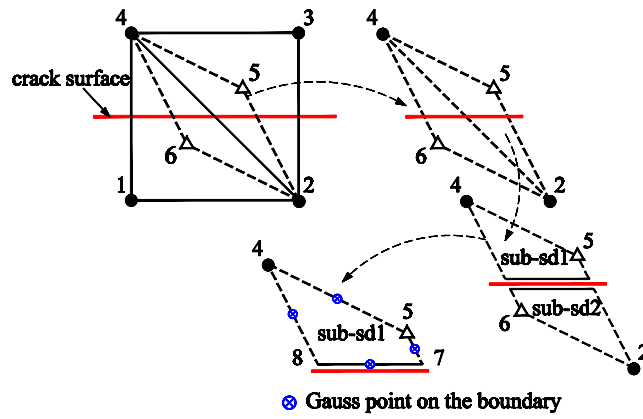


Figure 8.3: The decomposition of a completely cracked smoothing domain into two superimposed smoothing domains.

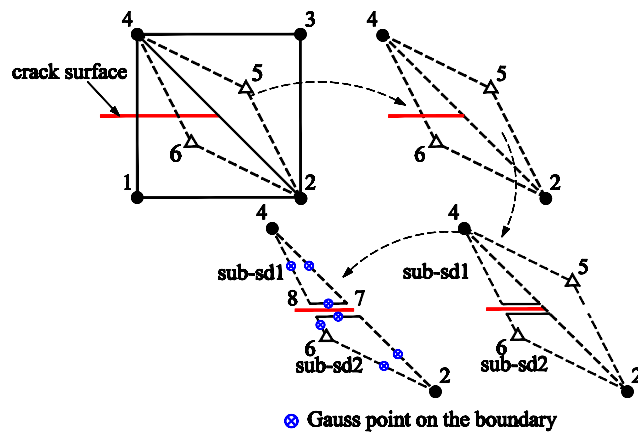


Figure 8.4: The decomposition of a cracked smoothing domain containing crack tip into two superimposed smoothing domains.

8.2 Edge-based strain smoothing phantom node method

Using the strain smoothing operation, the smoothed strain associated with edge k created from the displacement approximation in Equation (8.1) can be rewritten as:

$$\bar{\epsilon}_k = \sum_{I \in S_1^{es-phk}} \underbrace{\bar{\mathbf{B}}_I(\mathbf{x}_k) \mathbf{u}_I^1}_{\bar{\epsilon}^1(\mathbf{x})} H(-f(\mathbf{x})) + \sum_{I \in S_2^{es-phk}} \underbrace{\bar{\mathbf{B}}_I(\mathbf{x}_k) \mathbf{u}_I^2}_{\bar{\epsilon}^2(\mathbf{x})} H(f(\mathbf{x})) \quad (8.2)$$

where $\bar{\mathbf{B}}_I(\mathbf{x}_k)$ is the smoothed strain gradient matrix for the standard ES-FEM part. Those matrices write as follows

$$\bar{\mathbf{B}}_I(\mathbf{x}_k) = \begin{bmatrix} \bar{b}_{Ix}(\mathbf{x}_k) & 0 \\ 0 & \bar{b}_{Iy}(\mathbf{x}_k) \\ \bar{b}_{Iy}(\mathbf{x}_k) & \bar{b}_{Ix}(\mathbf{x}_k) \end{bmatrix} \quad (8.3)$$

In Equation (8.3), $\bar{b}_{Ih}(\mathbf{x}_k)$, $h \in x, y$ is computed by:

$$\bar{b}_{Ih}(\mathbf{x}_k) = \frac{1}{A_k^s} \int_{\Gamma_k^s} n_h(\mathbf{x}) N_i(\mathbf{x}) H((-1)^e f(\mathbf{x})) d\Gamma \quad (8.4)$$

Using Gauss-Legendre integration along the segments of boundary Γ_k^s , we have:

$$\bar{b}_{Ih} = \frac{1}{A_k^s} \sum_{m=1}^{N_{seg}} \left[\sum_{n=1}^{N_{gauss}} w_{m,n} N_i(\mathbf{x}_{m,n}) H((-1)^e f(\mathbf{x}_{m,n})) n_h(\mathbf{x}_{m,n}) \right] \quad (8.5)$$

where N_{seg} is the number of segments of the boundary Γ_k^s , N_{gauss} is the number of Gauss points used along each segment, $w_{m,n}$ are the corresponding Gauss weights, $\mathbf{x}_{m,n}$ is the n -th Gaussian point on the m -th segment of the boundary Γ_k^s , whose outward unit normal is denoted n_h , and the subscript "e" is either 1 or 2 as shown in Figure 8.1 and the superscript "e" indicates a domain restriction to element e.

The stiffness matrix $\bar{\mathbf{K}}$ associated with a smoothing domain is assembled by a similar process as in the FEM:

$$\bar{\mathbf{K}}_{IJ} = \sum_{k=1}^{N_s} \bar{\mathbf{K}}_{IJ,k}^s = \sum_{k=1}^{N_s} \int_{\Omega_k^s} (\bar{\mathbf{B}}_I^u)^T \mathbf{D} \bar{\mathbf{B}}_J^u d\Omega \quad (8.6)$$

All entries in matrix $\bar{\mathbf{B}}_I$ in Equation (8.3) with triangular meshes are constants over each smoothing domain; the stiffness matrix in Equation (8.6) is therefore calculated by:

$$\bar{\mathbf{K}}_{IJ} = \sum_{k=1}^{N_s} \bar{\mathbf{K}}_{IJ,k}^s = \sum_{k=1}^{N_s} (\bar{\mathbf{B}}_I^u)^T \mathbf{D} \bar{\mathbf{B}}_J^u A_k^s \quad (8.7)$$

8.2 Edge-based strain smoothing phantom node method

8.2.2 Weak formulation and discretized equation

We return to the two dimensional body in Figure 2.10. Since the smoothed strain over smoothing domains is variationally consistent as proven in (Liu09) and used by (CRL+10, VBNXC+11), the assumed displacement \mathbf{u}^h and the smoothed strains $\bar{\boldsymbol{\epsilon}}$ satisfies the "smoothed" Galerkin weak form: Find $\mathbf{u}^h \in V, \forall \delta \mathbf{u}^h \in V_0$ such that

$$\int_{\Omega} \delta(\bar{\boldsymbol{\epsilon}}(\mathbf{u}^h))^T \mathbf{D}(\bar{\boldsymbol{\epsilon}}(\mathbf{u}^h)) d\Omega - \int_{\Omega} (\delta \mathbf{u}^h)^T \mathbf{b} d\Omega - \int_{\Gamma} (\delta \mathbf{u}^h)^T \mathbf{t}_{\Gamma} d\Gamma = 0 \quad (8.8)$$

with $V = \{\mathbf{u} \mid \mathbf{u} \in H^1(\Omega \setminus \Gamma_c), \mathbf{u} = \bar{\mathbf{u}} \text{ on } \Gamma_u, \mathbf{u} \text{ discontinuous on } \Gamma_c\}$
and $V_0 = \{\delta \mathbf{u} \mid \delta \mathbf{u} \in H^1(\Omega \setminus \Gamma_c), \delta \mathbf{u} = 0 \text{ on } \Gamma_u, \delta \mathbf{u} \text{ discontinuous on } \Gamma_c\}$

Substituting the trial and test functions into Equation (8.8), we finally obtain the familiar equation:

$$\bar{\mathbf{K}} \bar{\mathbf{d}} = \mathbf{f} \quad (8.9)$$

where \mathbf{f} is the nodal force vector that is identical to that in the standard Phantom-node. The edge-based smoothed stiffness matrix $\bar{\mathbf{K}}$ for all sub-cells follows Equation (8.7).

The smoothed stress $\bar{\boldsymbol{\sigma}}^h$ is obtained in the same way from the $\bar{\boldsymbol{\epsilon}}^h$ in FEM, which is constant over a smoothing cell. In particular, for linear elastic problems, $\bar{\boldsymbol{\sigma}}^h = \mathbf{D} \bar{\boldsymbol{\epsilon}}^h$ is calculated on the level of the smoothing cell.

8.2.3 Crack growth and stress intensity factor

Fracture parameters such as mode I and mode II stress intensity factors (SIFs) are determined using the domain form (LSN85, MS87) of the interaction integral (YWC80). All the finite elements within a radius of $r_d = r_k h_e$ from the crack-tip are used. Herein, h_e is the crack-tip element size and r_k is a scalar.

In this chapter, crack growth is governed by the maximum hoop stress criterion (ES63, MB10), which assumes that the crack will propagate from its tip in the direction θ_c , where the circumferential (hoop) stress $\sigma_{\theta\theta}$ is maximum. The angle of crack propagation satisfies the following equation:

$$K_I \sin(\theta_c) + K_{II} (3 \cos(\theta_c) - 1) = 0 \quad (8.10)$$

Solving this equation, we have

$$\theta_c = 2 \arctan \left[\frac{-2 \left(\frac{K_{II}}{K_I} \right)}{1 + \sqrt{1 + 8 \left(\frac{K_{II}}{K_I} \right)^2}} \right] \quad (8.11)$$

Once K_I and K_{II} are known, Equation (8.11) may be used to compute the direction of propagation.

8.3 Numerical examples

8.3 Numerical examples

In all numerical examples, we are not using near-tip enrichment, i.e only discontinuous enrichment is used. This means that the best convergence rate attainable is $1/2$ in the H_1 norm and 1 in the L_2 norm ($\mathcal{O}(h^{1/2})$ and $\mathcal{O}(h)$, respectively, where h is the mesh size).

8.3.1 Sheet with an edge-crack under uniaxial tension

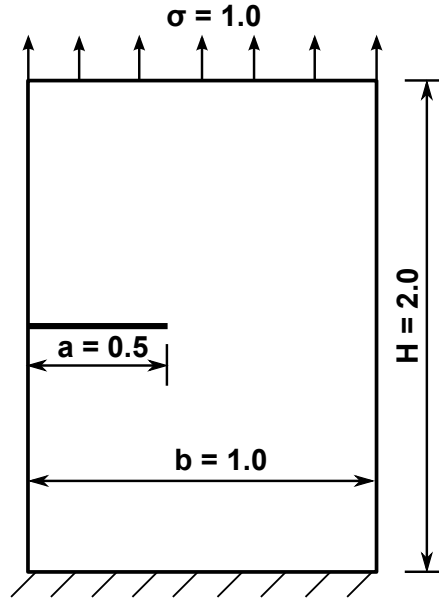


Figure 8.5: Sheet with edge crack under tension.

Consider a sheet under uniaxial tension as shown in Figure 8.5. The dimensions of sheet are in unit of [mm]. The material parameters are Young's modulus $E = 3 \times 10^7 Pa$, Poisson's ratio $\nu = 0.3$. The plane strain condition is assumed. The reference mode I SIF is given by:

$$K_I^{exact} = F\left(\frac{a}{b}\right) \sigma \sqrt{a\pi} = 1.6118Pa\sqrt{\text{mm}} \quad (8.12)$$

where $a = 0.5$ is the crack length, b is the sheet width and $F\left(\frac{a}{b}\right)$ is given by

$$F\left(\frac{a}{b}\right) = 1.12 - 0.231\left(\frac{a}{b}\right) + 10.55\left(\frac{a}{b}\right)^2 - 21.72\left(\frac{a}{b}\right)^3 + 30.39\left(\frac{a}{b}\right)^4 \quad (8.13)$$

8.3 Numerical examples

The strain energy and the error in the energy norm are defined as:

$$E_{(\Omega)} = \frac{1}{2} \int_{\Omega} \boldsymbol{\epsilon}^T \mathbf{D} \boldsymbol{\epsilon} d\Omega \quad (8.14)$$

$$e_e = \left| \frac{E_{(\Omega)}^{\text{num}} - E_{(\Omega)}^{\text{ref}}}{E_{(\Omega)}^{\text{ref}}} \right|^{1/2} \quad (8.15)$$

$$e_k = \left| \frac{K_{\text{sif}}^{\text{num}} - K_{\text{sif}}^{\text{ref}}}{K_{\text{sif}}^{\text{ref}}} \right|^{1/2} \times 100\%, \quad \text{sif} = I, II \quad (8.16)$$

where the superscript "ref" denotes the exact or reference solution, and "num" denotes the numerical solution.

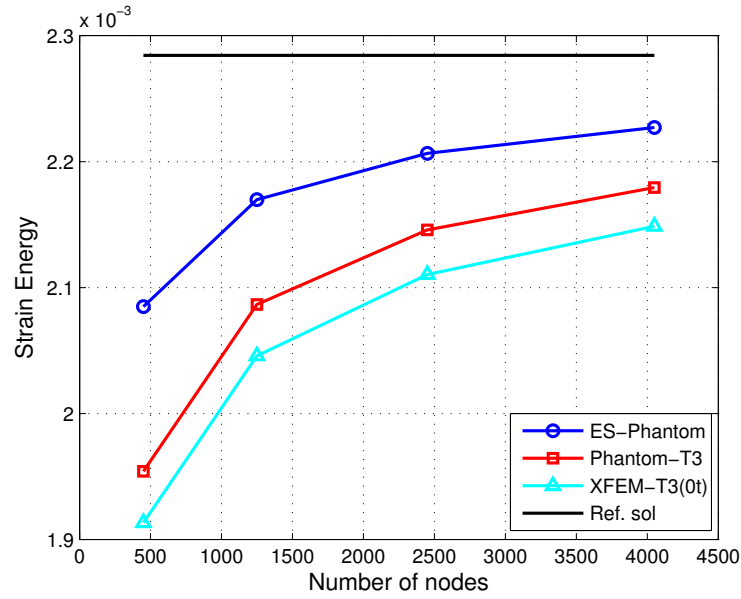


Figure 8.6: Strain energy for the sheet with edge crack under tension.

The results of the ES-Phantom node are compared with those of the standard Phantom-node using triangular meshes and the XFEM-T3(0t) (the "standard" XFEM formulation without tip enrichment that only employs the Heaviside enrichment of Equation (2.41)). Figure 8.6 shows that the strain energy of the ES-Phantom node method is more accurate than both the original Phantom-node and the XFEM-T3(0t). The convergence rates in terms of the strain energy and the stress intensity factor K_I are

8.3 Numerical examples

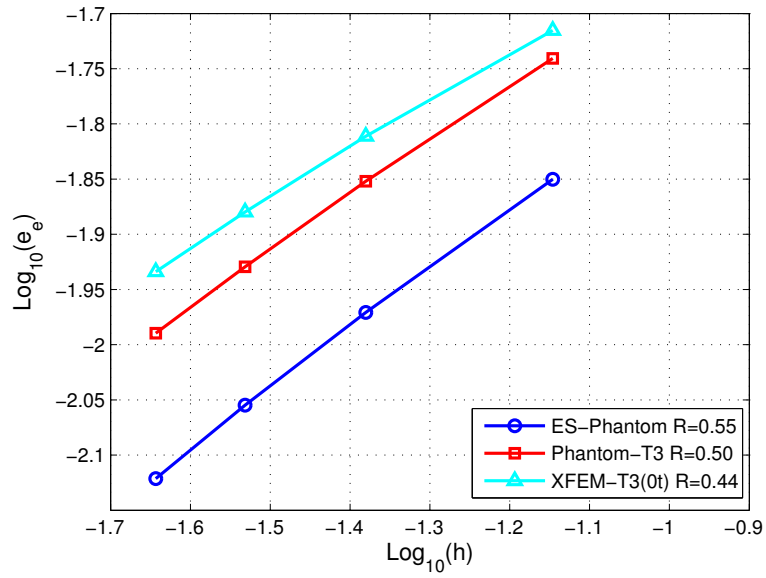


Figure 8.7: The convergence in the energy norm vs. h (mesh size) for the sheet with an edge crack under tension.

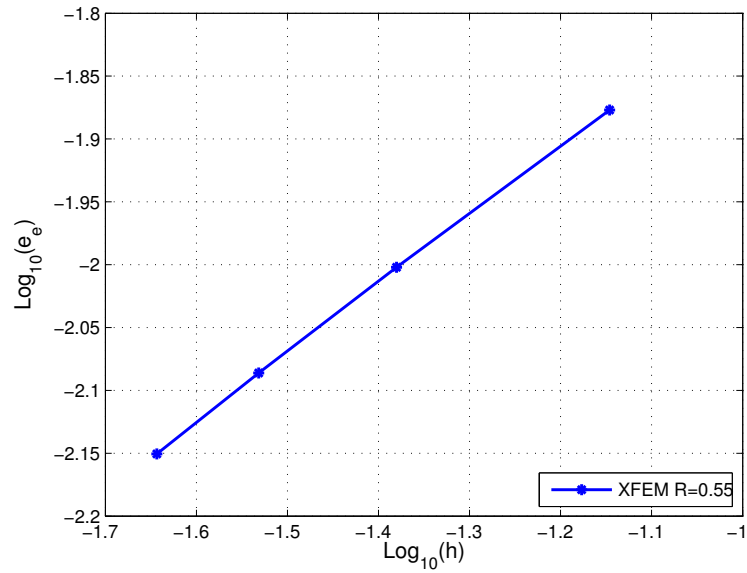


Figure 8.8: The convergence in the energy norm of XFEM vs. h (mesh size) for the sheet with an edge crack under tension.

8.3 Numerical examples

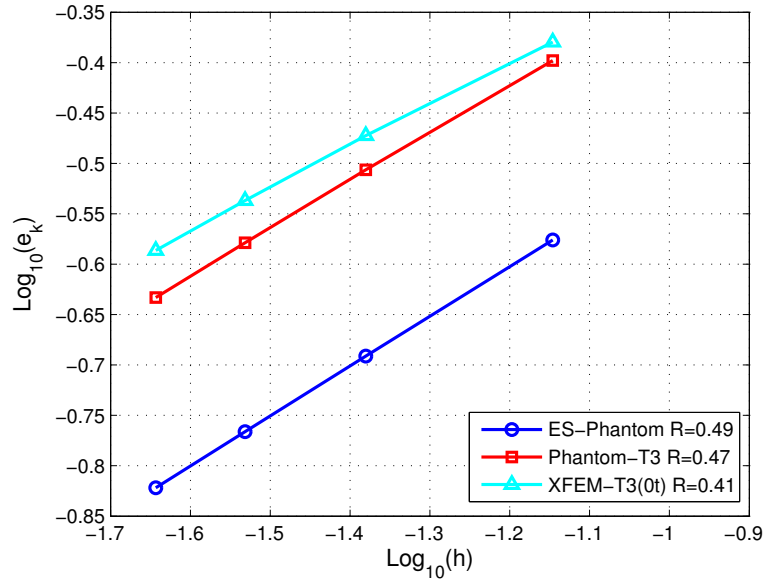


Figure 8.9: The convergence in the stress intensity factor K_I vs. h (mesh size) for the sheet with edge crack under tension.

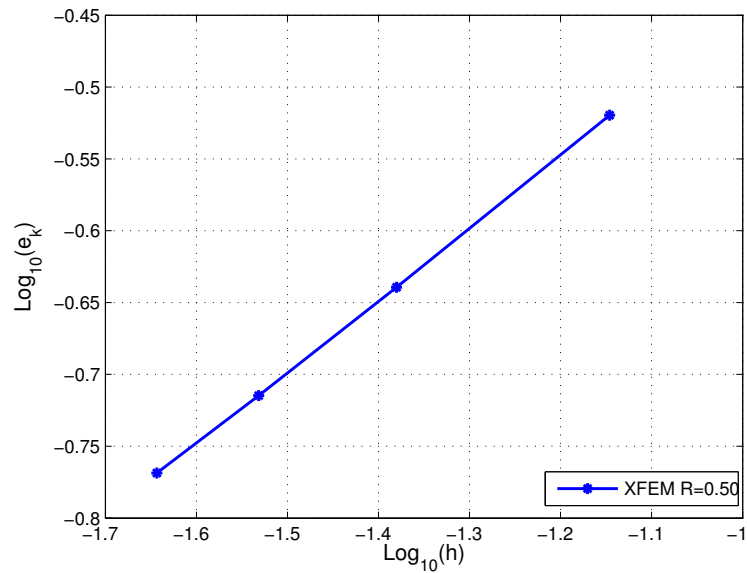


Figure 8.10: The convergence in the stress intensity factor K_I of XFEM vs. h (mesh size) for the sheet with edge crack under tension.

8.3 Numerical examples

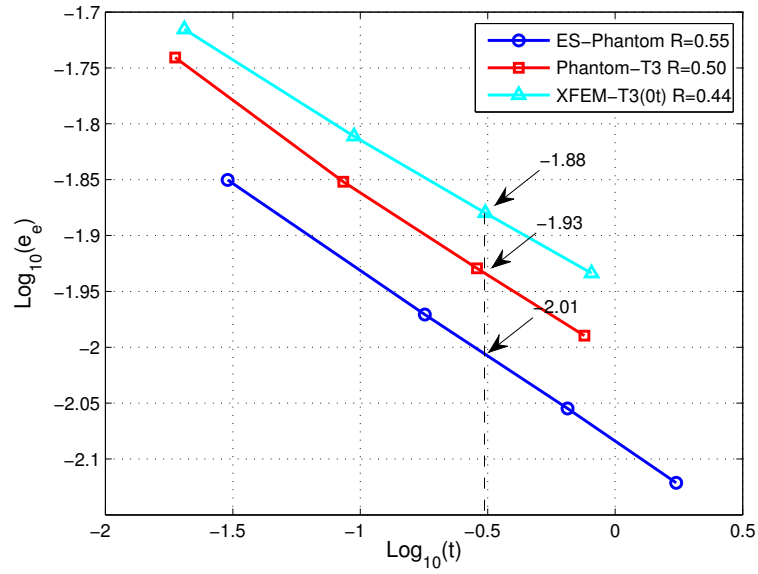


Figure 8.11: Computational efficiency of energy norm for the problem of a sheet with an edge crack under remote tension.

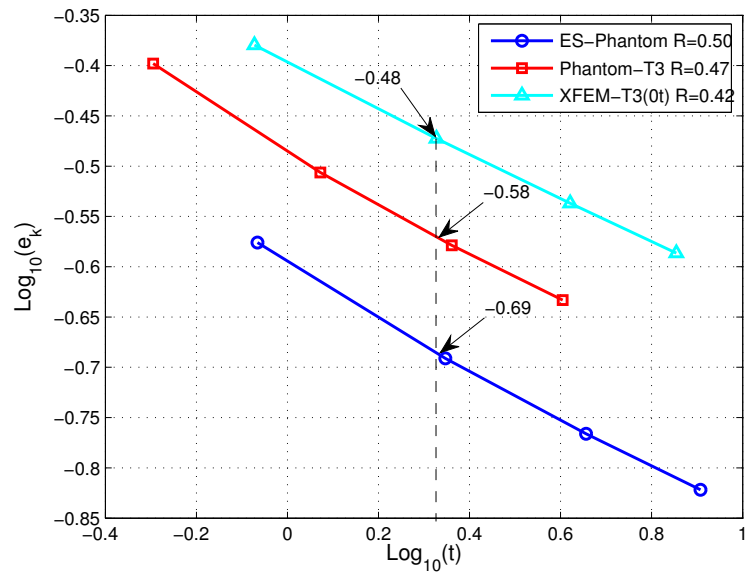


Figure 8.12: Computational efficiency of mode I SIF K_I for the problem of a sheet with an edge crack under remote tension.

8.3 Numerical examples

depicted in Figures 8.7 and 8.9, respectively. Furthermore, Phantom-node using triangular meshes (Phantom-T3) is superior to XFEM-T3(0t) although they are equivalent to each other. We also have included two more figures comparing the phantom-node method to the tip-enriched XFEM in Figures 8.8 and 8.10 as a reference, although it would not be fair to compare a method that includes the asymptotic crack tip enrichment to a method that models the crack in a much simpler way.

Note that the proposed method leads to a similar convergence rate to the standard XFEM and standard phantom-node, which is close to optimal (1/2) given the lack of tip enrichment. Also note that the error level of the proposed method is a fifth of an order of magnitude lower than the method compared with.

The computational efficiency in terms of the error in the energy norm and the relative error of K_I versus computation time (s) is compared for the ES-Phantom, the standard Phantom and the XFEM-T3 (0t). The results are plotted in Figure 8.11 and Figure 8.12, respectively. It is clear that the present method always produces higher computational efficiency, i.e., accuracy to computational time ratio, compared to the other methods. The accuracy of the present method is approximate (1) $\frac{ES-Phantom10^{-1.88}}{Phantom10^{-1.93}} = 1.12$ times as much as that of the standard Phantom, $\frac{ES-Phantom10^{-1.88}}{XFEM-T3(0t)10^{-2.01}} = 1.34$ times of the XFEM-T3(0t) in term of error in energy norm; (2) $\frac{ES-Phantom10^{-0.48}}{Phantom10^{-0.58}} = 1.26$ times as much as that of the standard Phantom and $\frac{ES-Phantom10^{-0.48}}{XFEM-T3(0t)10^{-0.58}} = 1.62$ times of the XFEM-T3(0t) in term of relative error for K_I .

8.3.2 Sheet with edge-crack under shear

In this example, we consider the edge crack geometry subjected to a shear load as shown in Figure 8.13. The material parameters are Young's modulus $E = 3 \times 10^7 Pa$ and Poisson's ratio $\nu = 0.25$. The exact stress intensity factors for this load case are given by (YWC80)

$$K_I = 34.0Pa\sqrt{mm}; K_{II} = 4.55Pa\sqrt{mm} \quad (8.17)$$

The results from Figure 8.14 to Figure 8.19 show that ES-Phantom node results are more accurate than both those of the standard Phantom-node and the XFEM-T3(0t). ES-Phantom node maintains slight superconvergent solutions in the strain energy. Furthermore, Phantom-node using triangular meshes (Phantom-T3) is superior to XFEM-T3(0t) although they are equivalent to each other with respect to the convergence in energy norm and the stress intensity factor K_I . Figure 8.16, Figure 8.18 and Figure 8.20 again are shown as a reference for readers.

8.3 Numerical examples

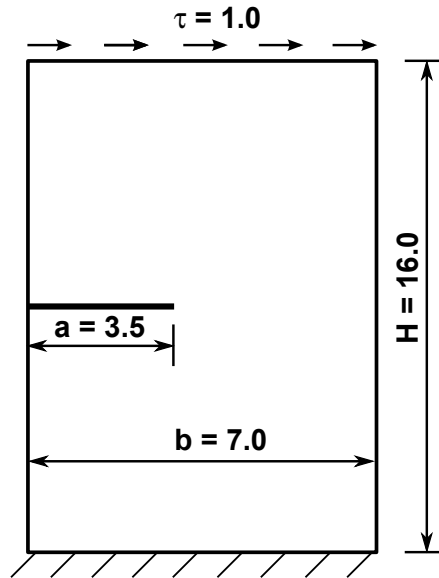


Figure 8.13: Sheet with edge crack under shear.

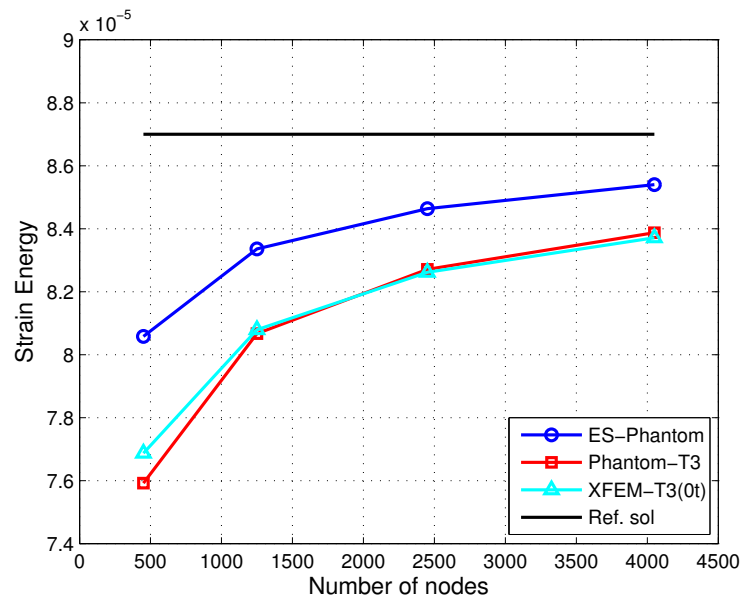


Figure 8.14: Strain energy for a sheet with an edge crack under shear.

8.3 Numerical examples

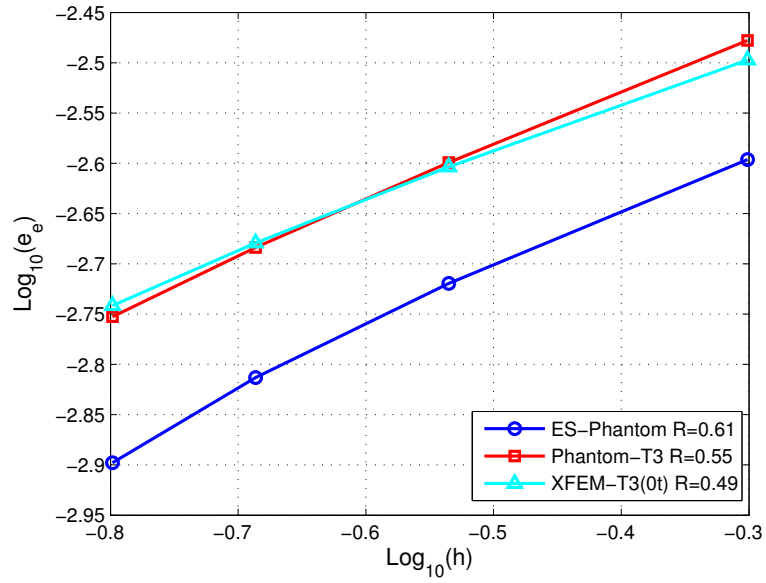


Figure 8.15: The convergence in the energy norm vs. h (mesh size) for a sheet with an edge crack under shear.

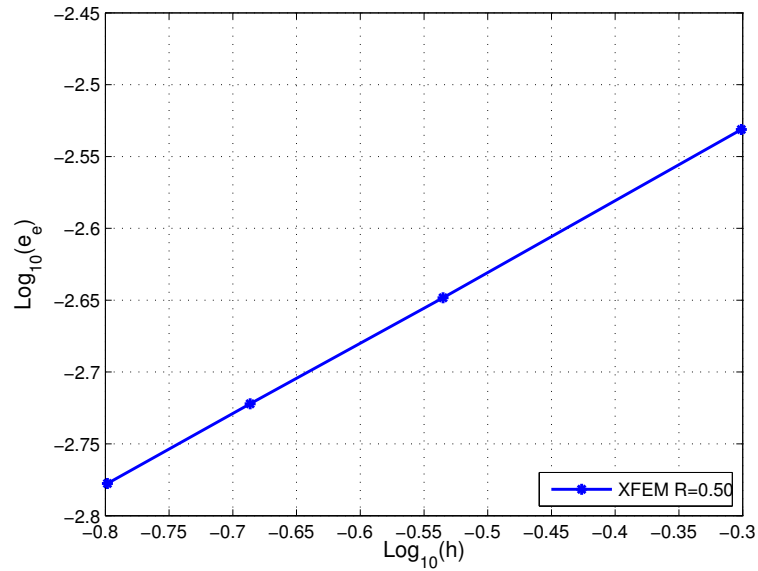


Figure 8.16: The convergence in the energy norm of XFEM vs. h (mesh size) for a sheet with an edge crack under shear.

8.3 Numerical examples

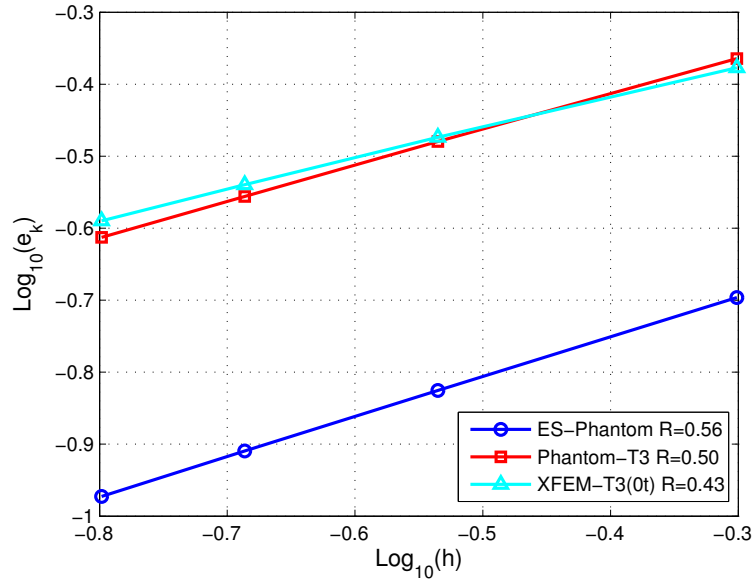


Figure 8.17: The convergence in the stress intensity factor K_I vs. h (mesh size) for a sheet with an edge crack under shear.

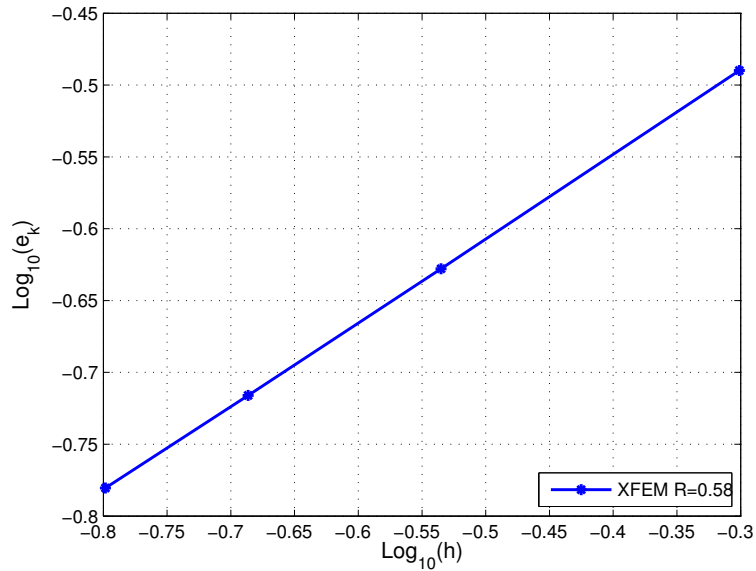


Figure 8.18: The convergence in the stress intensity factor K_I of XFEM vs. h (mesh size) for a sheet with an edge crack under shear.

8.3 Numerical examples

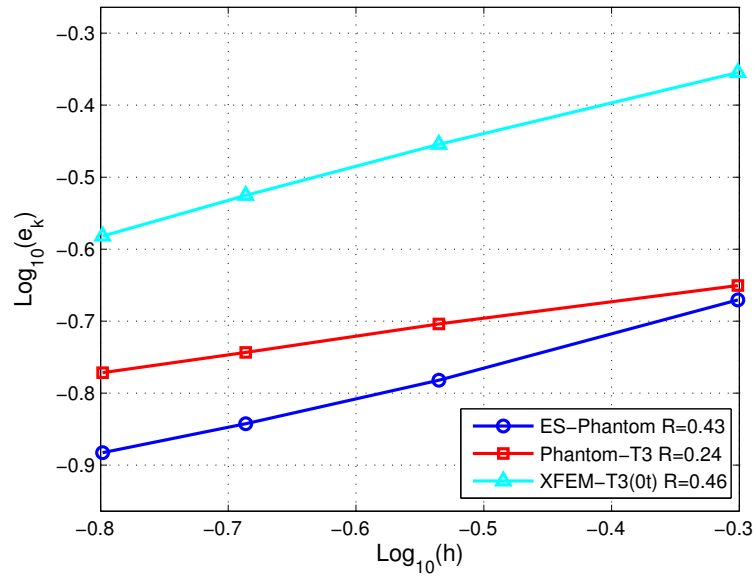


Figure 8.19: The convergence in the stress intensity factor K_{II} vs. h (mesh size) for sheet with edge crack under shear.

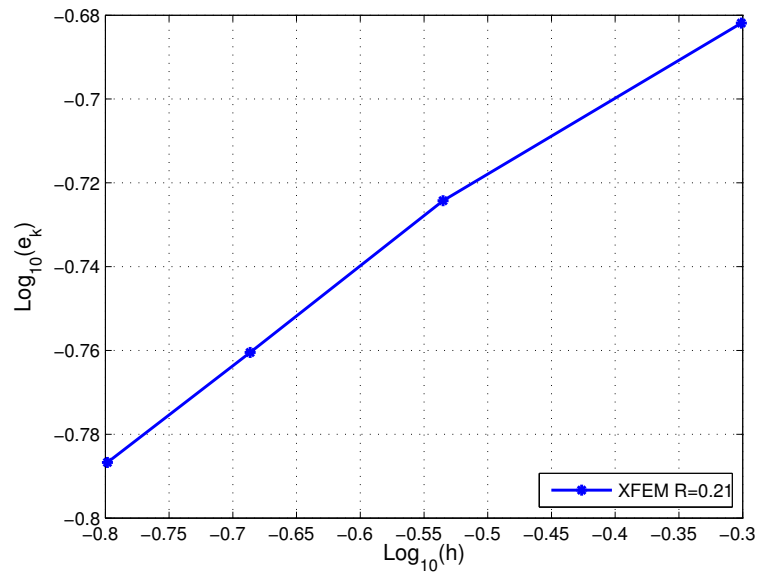


Figure 8.20: The convergence in the stress intensity factor K_{II} of XFEM vs. h (mesh size) for sheet with edge crack under shear.

8.3 Numerical examples

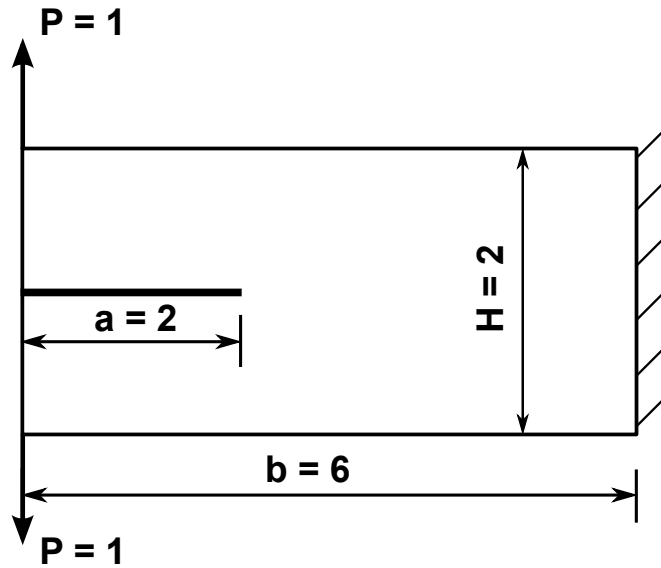


Figure 8.21: Double cantilever beam with an edge crack.

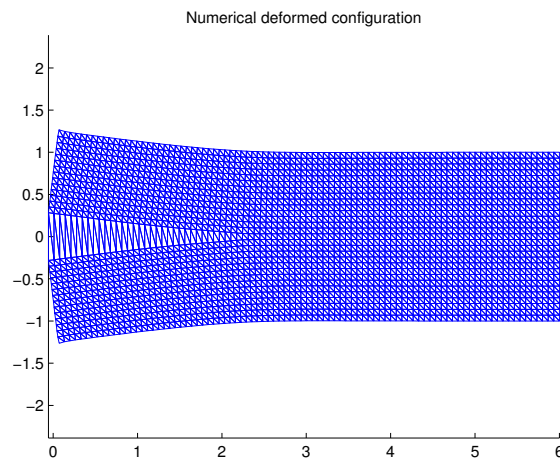
8.3.3 Crack growth simulation in a double cantilever beam

In this section, the ES-Phantom node with structured and unstructured meshes is used for crack growth simulation. The dimensions of the double cantilever beam Figure 8.21 are $6mm \times 2mm$ and an initial pre-crack with length $a = 2mm$ is considered. Plane stress conditions are assumed with Young's modulus, $E = 100MPa$ as well as the Poisson ratio, $\nu = 3$, and the load P is taken to be unity. By symmetry, a crack on the mid-plane of the cantilever beam is dominated by pure mode I and the crack would propagate in a straight line. We also have included simulations with a 'distorted' mesh and show that the crack path does not change.

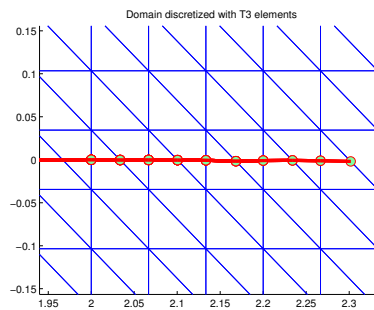
The crack growth increment, Δa , is taken so that the tip is always located at an element's edge and the crack growth is simulated for 10 steps. The domain is discretized with a structured and unstructured mesh of 2730 nodes. The crack path is simulated using both the proposed ES-Phantom node method and XFEM-T3(0t), and Figure 8.22 and Figure 8.23 show the deformed shape of the double cantilever beam with the magnification factor of 25×10^4 used to enable a clear description and the evolution of the crack path. The result shows that the crack path for an initial angle $\theta_c = 0$ agrees with the published results (BB99).

Distribution of the stress components σ_{xx} and σ_{yy} for and unstructured mesh are shown in Figure 8.24 and Figure 8.25, respectively.

8.3 Numerical examples



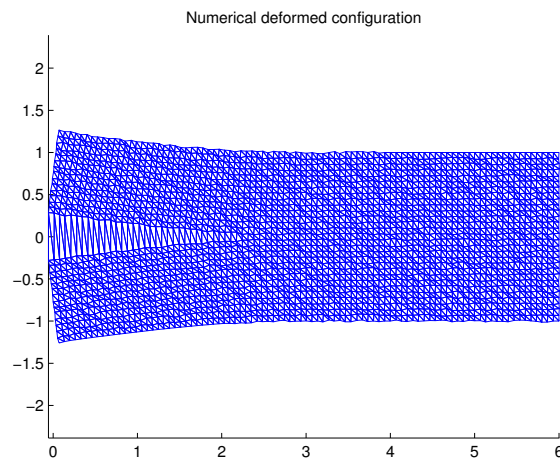
(a)



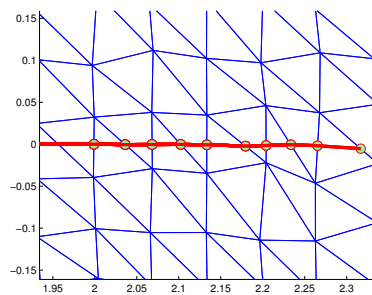
(b)

Figure 8.22: (a) Deformed shape of the double cantilever beam (structured mesh) and (b) Crack path simulated by ES-Phantom node method (structured mesh) after ten-step growing in which the filled circles are the new crack tip after each step.

8.3 Numerical examples



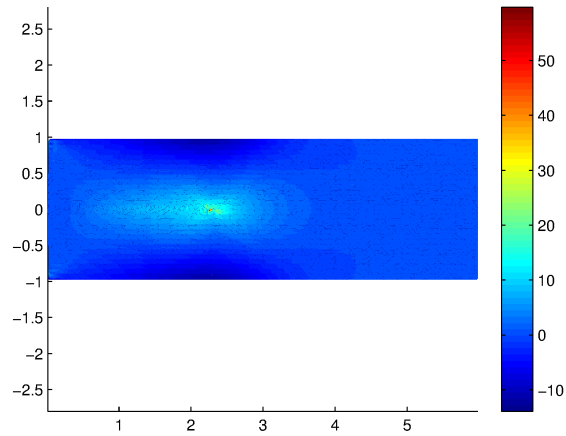
(a)



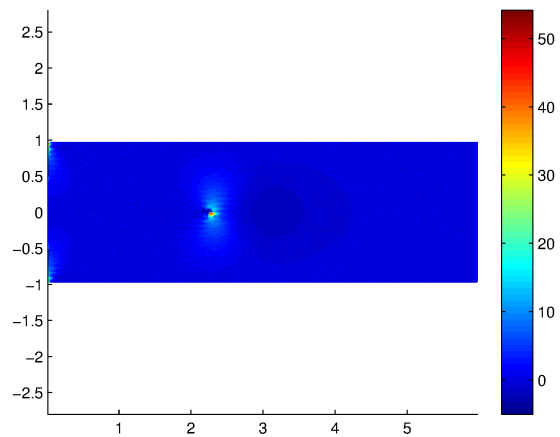
(b)

Figure 8.23: (a) Deformed shape of the double cantilever beam (unstructured mesh) and (b) Crack path simulated by ES-Phantom node method (unstructured mesh) after ten-step growing in which the filled circles are the new crack tip after each step.

8.3 Numerical examples



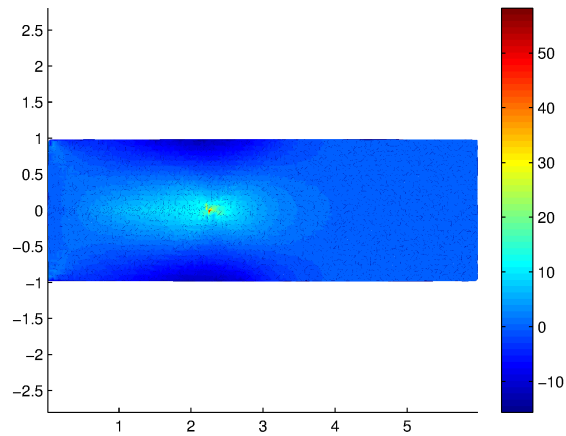
(a)



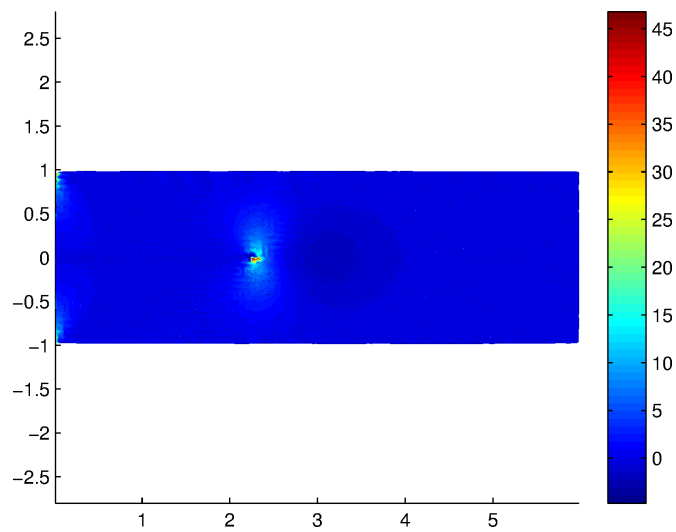
(b)

Figure 8.24: Stress (a) σ_{xx} and (b) σ_{yy} contours in the sheet (structured mesh) after the crack propagates.

8.3 Numerical examples



(a)



(b)

Figure 8.25: Stress (a) σ_{xx} and (b) σ_{yy} contours in the sheet (unstructured mesh) after the crack propagates.

8.4 Conclusions

A numerical Phantom-node method for analysis of two-linear elastic fracture problems was developed in framework of the ES-FEM to create the novel ES-Phantom node method. In this method, a cracked element is replaced by two superimposed elements and a set of additional phantom nodes. The two first examples were performed to investigate convergence rate in terms of strain energy and stress intensity factors. The results have shown that the ES-Phantom node is able to produce superconvergent solutions. Meanwhile, the last example has demonstrated the capability of the method to deal with the growing crack.

Chapter 9

Conclusions

9.1 Summary of achievements

This study proposes computational models at four length scales (nano-, micro-, meso-, macro-scales) and hierarchical upscaling approaches to predict the mechanical properties of PE and PNCs in dependent of fine scale features. This work is the first framework for uncertainty quantification (UQ) applied to quantify the key parameters associated with corresponding scale influencing on the macroscopic mechanical properties of PNCs was also presented. The results were verified and validated and they show agreement with previous simulations and experimental results.

All global SA methods predict the same effect of the input on the output.

The probability distribution of mechanical properties are characterized by using the probability plot method. Particularly, the Young's modulus of the PE is best characterized by the Weibull distribution while the Young's modulus of the PCNs is best fitted by the Log-normal distribution. Furthermore, the upper and lower bounds according to 95 % PIs were determined.

The surrogate models are robust as they can be constructed from a limited amount of available data. For the sake of simplicity, polynomial regression is sufficient to be used as the obtained coefficient of determination ≥ 0.8 . However, with respect to complex mechanical models which the linear and quadratic regression fail to approximate ($R^2 < 0.8$), the MLS, Hybrid, Kriging and penalized spline regression models could be used.

At *nano-scale*, the most influential parameter on the yield stress and the Young's modulus of the polyethylene (PE) is the temperature, followed by the strain rate. While the strain rate affects the yield stress, it barely influences the Young's modulus. The latter effect is best predicted by the variance-based methods while the partial derivatives and the elementary-effects method slightly overpredict this influence. The key

9.2 Future works

parameter influencing on the interfacial shear stress (ISS) of the PNCs is the SWCNT radius, followed by the temperature.

The key parameter influencing on the Young's modulus of the PNCs is the single-walled nanotube (SWNT) volume fraction *at macro-scale* followed by the SWNT curvature *at meso-scale* and the SWNT length *at micro-scale*, respectively. Meanwhile, SWNT curvature is the most significant parameter for the Poisson's ratio of the PNCs followed by the volume fraction and the SWNT length, respectively. The effect of the correlated input parameters (i.e. the SWNT length, the SWNT curvature) on the mechanical properties has been quantified. The effects of SWNT length, SWNT curvature on either Young's modulus or Poisson's ratio come from their mutual correlation rather than from themselves. The agglomeration parameters *at meso-scale* do not have a significant effect on the Young's modulus and Poisson's ratio.

The Young's modulus of exfoliated PCNs *at meso-scale* is governed by the stiffness of the polymer matrix. For examples studied, it seems that the most robust methods are the FAST and EFAST. The FAST approach, which allows all first-order indices to be computed from the single curve, requires a small number of model evaluations such that the first-order indices can also be directly estimated on the mechanical model.

With respect to the matrix combination method and the its improved formulas, a large number of model evaluations were required to compute the sensitivity indices as a price paid to capture the total-effect indices.

For both NS-XFEM and ES-Phantom node methods, no derivatives of shape functions are needed to compute the stiffness matrix by transforming interior integration into boundary integration. Consequently, the integration of singular functions is avoided. Furthermore, both methods can produce superconvergent solutions.

9.2 Future works

In the future, we aim to develop the work to the PNCs considering cohesive zone model *at micro-scale* in which both bulk properties of the polymer matrix and the interfacial properties (cohesive parameters) of the fibers and the polymer matrix can be extracted from our MD simulations. Then, a unified framework for the model selection will be developed. Graph theory could be employed to quantitatively assess the model quality and also the quality of those coupled partial models on different scales. Figure 9.1 illustrates partial models at different scales and a combination of partial models with different model qualities (e.g. $\hat{M}1$, $\hat{M}2$, $\tilde{M}1$, $\tilde{M}2$, ...) and sensitivity indices (S_{Ti}). At *nano-scale*, $\hat{M}1$ is the united atom model while $\tilde{M}1$ could be full atomistic model *at nano-scale*. At *micro-scale*, $\tilde{M}1$ is the current model (the CNTs are perfectly bonded to the polymer matrix) and $\tilde{M}2$ considers the polymer/CNT interface described by cohesive zone model, etc. The influence of model choice on the uncertainty of the predicted

9.2 Future works

mechanical properties and the quality of a combination of coupled partial models could be quantitatively estimated. The quantified result allows us to select the optimal model with the best compromise between model input and the model uncertainty.

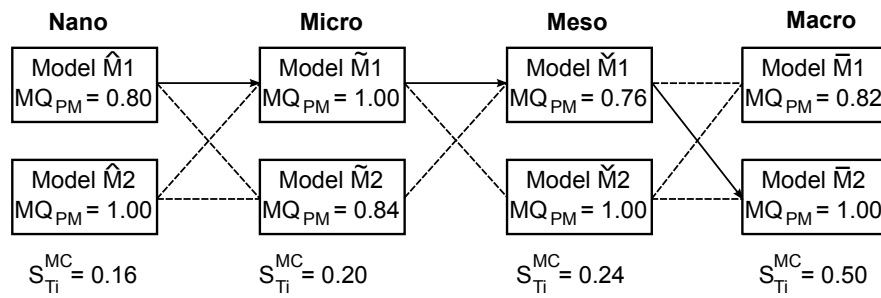


Figure 9.1: Model selection based on graph theory and sensitivity analysis.

References

- [AB05] P.M.A. Areias and T. Belytschko. A comment on the article: a finite element method for simulation of strong and weak discontinuities in solid mechanics. *CMAME*, 2005. [23](#), [181](#)
- [ABJ95] E.M. Arruda, M.C. Boyce, and R. Jayachandran. Effects of strain rate, temperature and thermomechanical coupling on the finite strain deformation of glassy polymers. *Mechanics of Materials*, 19:193–212, 1995. [89](#)
- [AG06] V. Anumandla and R.F. Gibson. A comprehensive closed form micromechanics model for estimating the elastic modulus of nanotube-reinforced composites. *Composites Part A: Applied Science and Manufacturing*, 37:2178–2185, 2006. [116](#)
- [AJR⁺99] R. Andrews, D. Jacques, A.M. Rao, T. Rantell, F. Derbyshire, Y. Chen, J. Chen, and R.C. Haddon. Nanotube composite carbon fibers. *Appl. Phys. Lett.*, 75:1329–1331, 1999. [1](#)
- [Ant95] A. Anthoine. Derivation of the in-plane elastic characteristics of masonry through homogenization theory. *Int. J. Solid Struct.*, 32:137–163, 1995. [142](#)
- [ASGR00] P.M. Ajayan, L.S. Schadler, S.C. Giannaris, and A. Rubio. Single-walled carbon nanotube polymer composites: Strength and weakness. *Adv. Mater.*, 12:3842–3844, 2000. [1](#), [91](#)
- [ASS97] G. Archer, A. Saltelli, and I.M. Sobol'. Sensitivity measures, anova-like techniques and the use of bootstrap. *Journal of Statistical Computation and Simulation*, 58:99–120, 1997. [158](#)
- [AT87] M.P. Allen and D.J. Tildesley. *Computer Simulation of Liquids*. Oxford University Press, New York, 1987. [7](#)

REFERENCES

- [BA00] M.C. Boyce and E.M. Arruda. Constitutive models of rubber elasticity: a review. *Rubber Chem. Technol*, 73:504–523, 2000. [65](#)
- [BB99] T. Belytschko and T. Black. Elastic crack growth in finite elements with minimal remeshing. 45:602–620, 1999. [21](#), [23](#), [163](#), [165](#), [181](#), [198](#)
- [BC91] D. Brown and J. Clarke. Molecular dynamics simulation of an amorphous polymer under tension. 1. phenomenology. *Macromolecules*, 24:2075–2082, 1991. [9](#), [68](#)
- [BCKW03] A.H. Barber, S.R. Cohen, S. Kenig, and H.D. Wagner. Measurement of carbon nanotubepolymer interfacial strength. *Applied Physics Letters*, 82:4140–4142, 2003. [91](#)
- [BCKW04] A.H. Barber, S.R. Cohen, S. Kenig, and H.D. Wagner. Interfacial fracture energy measurements for multi-walled carbon nanotubes pulled from a polymer matrix. *Compos. Sci. Technol.*, 64:2283–2289, 2004. [91](#)
- [Ben87] Y. Benveniste. A new approach to the application of mori-tanaka’s theory in composite materials. *Mechanics of Materials*, 6:147–57, 1987. [14](#)
- [BFB03] R.D. Bradshaw, F.T. Fisher, and L.C. Brinson. Fiber waviness in nanotube-reinforced polymer composites–ii: Modeling via numerical approximation of the dilute strain concentration tensor. *Compos. Sci. Technol.*, 63:1705–1722, 2003. [116](#), [129](#)
- [BG00] S.D. Burnside and E.P. Giannelis. Nanostructure and properties of polysiloxane layered silicate nanocomposites. *J. Polym. Sci. Pol. Phys.*, 38:1595–1604, 2000. [139](#)
- [Bin95] K. Binder. *Monte Carlo and molecular dynamics simulations in polymer science*. New York: Oxford University Press, 1995. [66](#)
- [BMMB05] E. Bechet, H. Minnebo, N. Moës, and B. Burgardt. Improved implementation and robustness study of the x-fem for stress analysis around cracks. *International Journal for Numerical Methods in Engineering*, 64:1033–1056, 2005. [182](#)
- [BN10] S. Bordas and S. Natarajan. On the approximation in the smoothed finite element method (sfem). 81:660–670, 2010. [164](#), [182](#)

REFERENCES

- [BND⁺07] S. Bordas, V.P. Nguyen, C. Dunant, D.H. Nguyen, and A. Guidoum. An extended finite element library. *71*(6):703–732, 2007. [23](#)
- [Bow01] D.I. Bower. *An Introduction to Polymer Physics*. Cambridge University Press, 2001. [68](#)
- [BRN⁺08] S. Bordas, T. Rabczuk, X.H. Nguyen, V.P. Nguyen, S. Natarajan, T. Bog, M.Q. Do, and V.H. Nguyen. Strain smoothing in FEM and XFEM. *Computers and Structures*, 88:1419–1443, 2008. [22](#), [169](#), [170](#), [182](#)
- [BSH⁺02] D.W. Brenner, O.A. Shenderova, J.A. Harrison, S.J. Stuart, B. Ni, and S.B. Sinnott. A second-generation reactive empirical bond order (rebo) potential energy expression for hydrocarbons. *Journal of Physics: Condensed Matter*, 14:783–802, 2002. [8](#), [93](#)
- [Buc09] C. Bucher. *Computational analysis of randomness in structural mechanics*. Structures and Infrastructures Book Series, Vol. 3 CRC Press, 2009. [56](#)
- [BWH⁺09] J.L. Bouvard, D.K. Ward, D. Hossain, S. Nouranian, E.B. Marin, and M.F. Horstemeyer. Review of hierarchical multiscale modeling to describe the mechanical behavior of amorphous polymers. *Journal of Engineering Materials and Technology*, 131:1–15, 2009. [1](#)
- [BWH⁺10] J.L. Bouvard, D.K. Ward, D. Hossain, E.B. Marin, D.J. Bammann, and M.F. Horstemeyer. A general inelastic internal state variable model for amorphous glassy polymers. *Acta Mechanica*, 213:71–96, 2010. [9](#)
- [BZR⁺05] M.F. Budyka, T.S. Zyubina, A.G. Ryabenko, S.H. Lin, and A.M. Mebel. Bond lengths and diameters of armchair single wall carbon nanotubes. *Chemical Physics Letters*, 407:266–271, 2005. [117](#)
- [CB99] F. Campolongo and R. Braddock. The use of graph theory in the sensitivity analysis of the model output: a second order screening method. *Reliability Engineering & System Safety*, 64:1–12, 1999. [54](#)
- [CBR02] F.M. Capaldi, M.C. Boyce, and G.C. Rutledge. Enhanced mobility accompanies the active deformation of a glassy amorphous polymer. *Phys. Rev. Lett.*, 89:175505–09, 2002. [65](#), [89](#)
- [CBR04] F.M. Capaldi, M.C. Boyce, and G.C. Rutledge. Molecular response of a glassy polymer to active deformation. *Polymer*, 45:1391–1399, 2004. [1](#), [65](#), [68](#)

REFERENCES

- [CE06] B. Chen and J.R.G. Evans. Elastic moduli of clay platelets. *Scripta Materialia*, 54:1581–1585, 2006. [145](#), [146](#)
- [CKG12] E.W.C. Coenen, V.G. Kouznetsova, and M.G.D. Geers. Novel boundary conditions for strain localization analyses in microstructural volume elements. *International Journal for Numerical Methods in Engineering*, 90:1–21, 2012. [142](#)
- [CLS78] R.I. Cukier, H.B. Levine, and K.E. Shuler. Nonlinear sensitivity analysis of multiparameter model systems. *Journal of Computational Physics*, 26:1–42, 1978. [38](#)
- [CNA⁺10] L.V. Canh, X.H. Nguyen, H. Askes, S. Bordas, T. Rabczuk, and V.H. Nguyen. A cell based smoothed finite element method for kinematic limit analysis. 46:679–701, 2010. [164](#)
- [CO07] S.C. Chowdhury and T. Okabe. Computer simulation of carbon nanotube pull-out from polymer by the molecular dynamics method. *Composites Part A: Applied Science and Manufacturing*, 38:747–754, 2007. [92](#)
- [CRL⁺02a] C.A. Cooper, D. Ravich, D. Lips, J. Mayer, and H.D. Wagner. Distribution and alignment of carbon nanotubes and nanofibrils in a polymer matrix. *Compos. Sci. Technol.*, 62:1105–1112, 2002. [91](#)
- [CRL⁺02b] C.A. Cooper, D. Ravich, D. Lips, J. Mayer, and H.D. Wagner. Load transfer in carbon nanotube epoxy composites. *Applied Physics Letters*, 81:3873–3875, 2002. [91](#)
- [CRL⁺10] L. Chen, T. Rabczuk, G.R. Liu, K.Y. Zeng, P. Kerfriden, and S. Bordas. Extended finite element method with edge-based strain smoothing (esm-xfem) for linear elastic crack growth. accepted, 2010. [171](#), [187](#)
- [CST97] K. Chan, A. Saltelli, and S. Tarantola. Sensitivity analysis of model output: Variance-based methods make the difference. In *Proceeding of the 1997 Winter Simulation Conference*, pages 261–268, 1997. [38](#)
- [CST00] K. Chan, A. Saltelli, and S. Tarantola. Winding stairs: A sampling tool to compute sensitivity indices. *Statistics and Computing*, 10:187–196, 2000. [35](#)
- [CWYY00] J.S. Chen, C.T. Wu, S. Yoon, and Y. You. A stabilized conforming nodal integration for galerkin meshfree method. *IJNME*, 50:435–466, 2000. [163](#)

REFERENCES

- [CZL⁺12] D.T. Chau, G. Zi, P.S. Lee, T. Rabczuk, and J.H. Song. Phantom-node method for shell models with arbitrary cracks. *Computers and Structures*, 92-93:242–256, 2012. [182](#)
- [Dai02] H. Dai. Carbon nanotubes: opportunities and challenges. *Surf. Sci.*, 500:218–241, 2002. [91](#), [115](#)
- [Den11] F. Deng. *Investigation of the interfacial bonding and deformation mechanism of the nano composites containing carbon nanotubes*. PhD thesis, Bauhaus-Universität Weimar, 2011. [91](#)
- [DH11] A.V. Desai and M.A. Haque. Mechanics of the interface for carbon nanotube–polymer composites. *Thin-Walled Structures*, 43:1854–1860, 2011. [91](#)
- [DLN7a] K.Y. Dai, G.R. Liu, and T.T. Nguyen. An n-sided polygonal smoothed finite element method (nSFEM) for solid mechanics. *Finite elements in analysis and design*, 43:847–860, 2007a. [164](#)
- [Duf11] M. Duflo. Industrial applications of xfem for 3d crack propagation with morfeo/crack and abaqus. *ECCOMAS thematic conference on XFEM, Cardiff (U.K.)*, 2011. [181](#)
- [ES63] F. Erdogan and G. Sih. On the crack extension in plates under plane loading and transverse shear. *Journal Basic Engineering*, 85:519–527, 1963. [187](#)
- [Esh57] J.D. Eshelby. The determination of the elastic field of an ellipsoidal inclusion, and related problems. *Proceedings of the Royal Society of London. Series A. Mathematical and Physical Sciences*, 241:376–396, 1957. [15](#)
- [FBB03] F.T. Fisher, R.D. Bradshaw, and L.C. Brinson. Fiber waviness in nanotube-reinforced polymer composites–i: Modulus predictions using effective nanotube properties. *Compos. Sci. Technol.*, 63:1689–1703, 2003. [116](#), [129](#)
- [FH03] S.J.V. Frankland and V.M. Harik. Analysis of carbon nanotube pull-out from a polymer matrix. *Surface Science*, 525:103–108, 2003. [92](#), [98](#)
- [FHO⁺03] S.J.V. Frankland, V.M. Harik, G.M. Odegard, D.W. Brenner, and T.S. Gates. The stress–strain behavior of polymer–nanotube composites from molecular dynamics simulation. *Compos. Sci. Technol.*, 63:1655–1661, 2003. [116](#)

REFERENCES

- [FMP02] R. Faller and F. Mueller-Plathe. Modeling of poly(isoprene) melts on different scales. *Polymer*, 43:621–628, 2002. [1](#)
- [FP03] T.D. Fornes and D.R. Paul. Modeling properties of nylon 6/clay nanocomposites using composite theories. *Polymer*, 44:4993–5013, 2003. [139](#)
- [FP07a] M. Fermeglia and S. Pricl. Multiscale modeling for polymer systems of industrial interest. *Progress in Organic Coatings*, 58:187–199, 2007. [2](#)
- [FP07b] M. Fermeglia and S. Pricl. Multiscale modeling for polymer systems of industrial interest. *Progress in Organic Coatings*, 58:187–199, 2007. [140](#)
- [FSK 1] A.I.J. Forrester, A. Sóbester, and A.J. Keane. *Engineering design via surrogate modeling: A practical guide*. John Wiley & Sons, Chichester, 2008, ISBN 978-0-470-06068-1. [60](#)
- [FTD02] H. Fukunaga, J. Takimoto, and M. Doi. A coarse-graining procedure for flexible polymer chains with bonded and nonbonded interactions. *Journal of Chemical Physics*, 116:8183–8190, 2002. [1](#)
- [Gel94] B.R. Gelin. *Molecular modeling of polymer structures and properties*. Verlag, Munich, 1994. [13](#)
- [GHT03] D. Gay, S.V. Hoa, and S.W. Tsai. *Composite Materials: Design and Applications*. CRC Press, 2003. [19](#)
- [Gib07] R.F. Gibson. *Principles of Composite Material Mechanics, second ed.* CRC Press, 2007. [115](#)
- [GK90] F.F. Gan and K.J. Koehler. Goodness-of-fit tests based on p–p probability plots. *Technometrics*, 32:289–303, 1990. [76](#), [146](#)
- [GMW⁺04] J. Gou, B. Minaei, B. Wang, Z. Liang, and C. Zhang. Computational and experimental study of interfacial bonding of single-walled nanotube reinforced composites. *Comp. Mater. Sci.*, 31:225–236, 2004. [12](#), [92](#), [94](#)
- [GWB08] R. Gracie, H. Wang, and T. Belytschko. Blending in the extended finite element method by discontinuous galerkin and assumed strain methods. *International Journal for Numerical Methods in Engineering*, 74:1645–1669, 2008. [182](#)

REFERENCES

- [GWFS] F.H. Gojny, M.H.G. Wichmann, B. Fiedler, and K. Schulte. Influence of different carbon nanotubes on the mechanical properties of epoxy matrix composites—a comparative study. [115](#)
- [Hal69] J.C. Halpin. Stiffness and expansion estimates for oriented short fiber composites. *Journal of Composite Materials*, 3:732–734, 1969. [139](#)
- [Has83] Z. Hashin. Analysis of composite materials. *J. Appl. Mech.*, 50:481–505, 1983. [142](#)
- [HD03] J.C. Helton and F.J. Davis. Latin hypercube sampling and the propagation of uncertainty in analyses of complex systems. *Reliability Engineering & System Safety*, 81:23–69, 2003. [29](#)
- [HdH85] M.F. Hutchinson and F.R. de Hoog. Smoothing noisy data with spline functions. *Numerische Mathematik*, 47:99–106, 1985. [61](#)
- [HE07] Y. Han and J. Elliott. Molecular dynamics simulations of the elastic properties of polymer/carbon nanotube composites. *Comp. Mater. Sci.*, 39:315–323, 2007. [116](#)
- [HH94] S. Hazanov and C. Huet. Order relationships for boundary conditions effect in heterogeneous bodies smaller than the representative volume. *J. Mech. Phys. Solids*, 42:1995–2011, 1994. [142](#)
- [HH04] A. Hansbo and P. Hansbo. A finite element method for the simulation of strong and weak discontinuities in solid mechanics. *CMAME*, 193:3523–3540, 2004. [23](#), [181](#)
- [Hil67] R. Hill. The essential structure of constitutive laws for metal composites and polycrystals. *J. Mech. Phys. Solids*, 15:79–95, 1967. [142](#)
- [HK92] S.J. Hollister and N. Kikuchi. A comparison of homogenization and standard mechanics analyses for periodic porous composites. *Computational Mechanics*, 10:73–95, 1992. [142](#)
- [Hoo85] W.G. Hoover. Canonical dynamics: Equilibrium phase-space distributions. *Phys. Rev. A*, 31:1695–1697, 1985. [7](#), [9](#)
- [HS96] T. Homma and A. Saltelli. Importance measures in global sensitivity analysis of model output. *Rel. Eng. Syst. Safety*, 52:1–17, 1996. [35](#)
- [HTW⁺10] D. Hossain, M.A. Tschopp, D.K. Ward, J.L. Bouvard, P. Wang, and M.F. Horstemeyer. Molecular dynamics simulations of deformation mechanisms of amorphous polyethylene. *Polymer*, 51:6071–6083, 2010. [1](#), [65](#), [66](#), [94](#), [97](#)

REFERENCES

- [HWC07] K. Hbaieb, Y.H.J. Wang, Q.X. Chia, and B. Cotterell. Modelling stiffness of polymer/clay nanocomposites. *Polymer*, 48:901–909, 2007. [139](#)
- [IC82] R.L. Iman and W.J. Conover. A distribution-free approach to inducing rank correlation among input variables. *Communications in Statistics - Simulation and Computation*, 11:311–334, 1982. [29](#), [30](#), [43](#), [51](#)
- [ISI⁺98] S. Izrailev, S. Stepaniants, B. Isralewitz, D. Kosztin, H. Lu, F. Molnar, W. Wriggers, and K. Schulten. *Steered Molecular Dynamics*, volume 4. Computational Molecular Dynamics: Challenges, Methods, Ideas, Lecture Notes in Computational Science and Engineering, 1998. [98](#)
- [Jan99] M.J.W. Jansen. Analysis of variance designs for model output. *Computer Physics Communications*, 117:35–43, 1999. [33](#), [34](#), [35](#)
- [Kar11] G. Karaki. *Assessment of coupled models of bridges considering time-dependent vehicular loading*. PhD thesis, Bauhaus-Universität Weimar, 2011. [59](#)
- [KGR⁺10] A.L. Kalamkarov, A.V. Georgiades, S.K. Rokkam, V.P. Veedu, and M.N. Ghasemi-Nejhad. Analytical and numerical techniques to predict carbon nanotubes properties. *Int. J. Solid Struct.*, 43:6832–6854, 2010. [14](#), [118](#)
- [KPL08] B.C. Kim, S.W. Park, and D.G. Lee. Fracture toughness of the nanoparticle reinforced epoxy composite. *Compos. Struct.*, 86:69–77, 2008. [1](#)
- [KTA12] S. Kucherenko, S. Tarantola, and P. Annoni. Estimation of global sensitivity indices for models with dependent variables. *Computer Physics Communications*, 183:937–946, 2012. [49](#), [161](#)
- [LC03] C.Y. Li and T.-W. Chou. Structural mechanics approach for the analysis of carbon nanotubes. *Int. J. Solids Struct.*, 40:2487–2499, 2003. [xvi](#), [13](#), [14](#), [18](#), [117](#), [118](#)
- [LC06] C.Y. Li and T.-W. Chou. Multiscale modeling of compressive behavior of carbon nanotube/polymer composites. *Compos. Sci. and Technol.*, 66:2409–2414, 2006. [2](#)

REFERENCES

- [LCN⁺10] G.R. Liu, L. Chen, T.T. Nguyen, K.Y. Zeng, and G.Y. Zhang. A novel singular node-based smoothed finite element method (ns-fem) for upper bound solutions of fracture problems. *IJNME*, 83:1466–1497, 2010. [174](#)
- [LDN07] G.R. Liu, K.Y. Dai, and T.T. Nguyen. A smoothed element method for mechanics problems. 39:859–877, 2007. [164](#), [182](#)
- [LGH06] K.T. Lau, C. Gu, and D. Hui. A critical review on nanotube and nanotube/nanoclay related polymer composite materials. *Compos. Part B – Eng.*, 37:425–436, 2006. [91](#), [115](#)
- [LGSea04] X. Li, H. Gao, W.A. Scrivens, and et al. Nanomechanical characterization of single-walled carbon nanotubes reinforced epoxy composites. *Nanotechnology*, 15:1416–1423, 2004. [115](#)
- [Liu09] G.R. Liu. A g space theory and weakened weak (w2) form for a unified formulation of compatible and incompatible methods: Part i theory and part ii application. accepted, 2009. [187](#)
- [LL01] K. Liao and S. Li. Interfacial characteristics of a carbon nanotube-polystyrene composite system. *Applied Physics Letters*, 79:4225–4227, 2001. [12](#), [92](#), [94](#)
- [LLP⁺11] Y. Li, Y. Liu, X. Peng, C. Yan, S. Liu, and N. Hu. Pull-out simulations on interfacial properties of carbon nanotube-reinforced polymer nanocomposites. *Computational Materials Science*, 50:1854–1860, 2011. [12](#), [92](#)
- [LMV⁺06] J. Li, T. Mulder, B. Vorselaars, A.V. Lyulin, and M.A.J. Michels. Monte carlo simulation of uniaxial tension of an amorphous polyethylene-like polymer glass. *Macromolecules*, 39:7774–7782, 2006. [1](#)
- [LNLDL07] G.R. Liu, T.T. Nguyen, K.Y. Dai, and K.Y. Lam. Theoretical aspects of the smoothed finite element method (SFEM). 71:902–930, 2007. [163](#), [182](#)
- [LNL09] G.R. Liu, T.T. Nguyen, and K.Y. Lam. An edge-based smoothed finite element method (ES-FEM) for static, free and forced vibration analyses of solids. *Journal Sound and Vibration*, 320:1100–1130, 2009. [27](#), [164](#)

REFERENCES

- [LNNL09] G.R. Liu, T.T. Nguyen, X.H. Nguyen, and K.Y. Lam. A node-based smoothed finite element method (NS-FEM) for upper bound solutions to solid mechanics problems. 87:14–26, 2009. [164](#)
- [LPRS05a] P. Laborde, J. Pommier, Y. Renard, and M. Salaun. High-order extended finite element method for cracked domains. 64:354–381, 2005. [166](#), [171](#)
- [LPRS05b] P. Laborde, J. Pommier, Y. Renard, and M. Salaun. High-order extended finite element method for cracked domains. *International Journal for Numerical Methods in Engineering*, 64:354–381, 2005. [182](#)
- [LS86] P. Lancaster and K. Salkauskas. *An introduction: Curve and surface fitting*. Academic Press, 1986. [58](#)
- [LSN85] F.Z. Li, C.F. Shih, and A. Needleman. A comparison of methods for calculating energy rates. 21(2):405–421, 1985. [171](#), [187](#)
- [LW85] K.S. Lee and G. Wegner. Linear and cyclic alkanes ($c_n h_{2n+2}$, $c_n h_{2n}$) with $n \geq 100$. synthesis and evidence for chain-folding. *Makromol. Chem., Rapid Commun.*, 6:203–208, 1985. [68](#)
- [MB97] J.M. Melenk and I. Babuška. The partition of unity finite element method: basic theory and applications. *CMAME*, 40:727–758, 1997. [163](#)
- [MB05] T. Most and C. Bucher. A moving least squares weighting function for the element-free galerkin method which almost fulfills essential boundary conditions. *Structural Engineering and Mechanics*, 21:315–332, 2005. [58](#)
- [MB10] A. Menk and S. Bordas. Crack growth calculations in solder joints based on microstructural phenomena with x-fem. *Computational Materials Science*, 50:1145–1156, 2010. [187](#)
- [MCB79] M.D. McKay, W.J. Conover, and R.J. Beckmann. A comparison of three methods for selecting values of input variables in the analysis of output from a computer code. *Technometrics*, 21:239–245, 1979. [29](#)
- [MCP⁺07] D.L. McDowell, H.J. Choi, J. Panchal, R. Austin, J. Allen, and F. Mistree. Plasticity-related microstructure-property relations for materials design. *Key Engineering Materials*, 340–341:21–30, 2007. [2](#)
- [MDB99] N. Möes, J. Dolbow, and T. Belytschko. A finite element method for crack growth without remeshing. 46:131–150, 1999. [22](#), [163](#)

REFERENCES

- [MK05] J. Mergheim and Steinmann P. Kuhl, E. and. A finite element method for the computational modeling of cohesive cracks. *IJNME*, 63(2):276–289, 2005. [181](#)
- [ML13] S. Marzban and T. Lahmer. Variance-based sensitivity analysis: The method of slices. *Rel. Eng. Syst. Safety*, submitted, 2013. [36](#)
- [MLLM07] T. Mulder, J. Li, A.V. Lyulin, and M.A.J. Michels. Monte carlo simulation of uniaxial deformation of polyethylene-like polymer glass: Role of constraints and deformation protocol. *Macromolecular Theory and Simulations*, 16:348–358, 2007. [1](#)
- [MM02] R.H. Myers and D.C. Montgomery. *Response surface methodology process and product optimization using designed experiments*. 2nd ed. New York: John Wiley, 2002. [55](#)
- [MOG90] S.L. Mayo, B.D. Olafson, and W.A. Goddard. Dreiding: A generic force field for molecular simulations. *Journal of Physical Chemistry*, 94:88–97, 1990. [7](#)
- [Mor91] M.D. Morris. Factorial sampling plans for preliminary computational experiments. *Technometrics*, 33:161–174, 1991. [54](#), [55](#)
- [Mos12] T. Most. Variance-based sensitivity analysis in the presence of correlated input variables. In *Proceedings 5th International Conference on Reliable Engineering Computing (REC)*, Brno, 2012. [46](#), [48](#), [124](#)
- [MP02] F. Mueller-Plathe. Coarse-graining in polymer simulation: From the atomistic to the mesoscopic scale and back. *ChemPhysChem*, 3:754–769, 2002. [1](#)
- [MRM⁺06] T. Menouillard, J. Rethore, N. Moës, A. Combescure, and H. Bung. Efficient explicit time stepping for the extended finite element method (x-fem). *International Journal for Numerical Methods in Engineering*, 68:911–939, 2006. [182](#)
- [MRM⁺08] T. Menouillard, J. Rethore, N. Moës, A. Combescure, and H. Bung. Mass lumping strategies for x-fem explicit dynamics: Application to crack propagation. *International Journal for Numerical Methods in Engineering*, 74:447–474, 2008. [182](#)
- [MS87] B. Moran and C.F. Shih. Crack tip and associated domain integrals from momentum and energy balance. *27(6):615–641*, 1987. [171](#), [187](#)

REFERENCES

- [MSR10] T. Most, A. Saltelli, and M. Ratto. Estimating total effect sensitivity indices in the presence of correlated input variables. In *Internal report, GRK 1462, Bauhaus-Universität Weimar*, 2010. [46](#), [124](#)
- [MT73] T. Mori and K. Tanaka. Average stress in matrix and average elastic energy of materials with misfitting inclusions. *Acta Metall.*, 21:571–574, 1973. [15](#), [139](#)
- [MT12] T.A. Mara and S. Tarantola. Variance-based sensitivity indices for models with dependent inputs. *Rel. Eng. Syst. Safety*, 107:115–121, 2012. [32](#), [50](#), [161](#)
- [NBN08] X.H. Nguyen, S. Bordas, and D.H. Nguyen. Smooth finite element methods: Convergence, accuracy and properties. *74*:175–208, 2008. [164](#)
- [NLLZ09] T.T. Nguyen, G.R. Liu, K.Y. Lam, and G.Y. Zhang. A face-based smoothed finite element method (FS-FEM) for 3d linear and nonlinear solid mechanics problems using 4-node tetrahedral elements. *78*:324–353, 2009. [164](#)
- [Nos84] S. Nose. A molecular dynamics method for simulations in the canonical ensemble. *Mol. Phys.*, 50:255–268, 1984. [7](#), [9](#)
- [NRN⁺10] X.H. Nguyen, T. Rabczuk, T.N. Nguyen, T.T. Nguyen, and S. Bordas. A node-based smoothed finite element method with stabilized discrete shear gap technique for analysis of reissner-mindlin plates. *CM*, 46:679–701, 2010. [164](#)
- [NRNB08] T.N. Nguyen, T. Rabczuk, X.H. Nguyen, and S. Bordas. A smoothed finite element method for shell analysis. *CMAME*, 198:165–177, 2008. [163](#), [182](#)
- [NRNB09] T.N. Nguyen, T. Rabczuk, X.H. Nguyen, and S. Bordas. An alternative alpha finite element method with discrete shear gap technique for analysis of mindlin-reissner plates. in *Proof*, 2009. [164](#)
- [NRNXB10] T.N. Nguyen, T. Rabczuk, H. Nguyen-Xuan, and S. Bordas. An alternative alpha finite element method (a’fem) free and forced vibration analysis of solids using triangular meshes. *233(9)*:2112–2135, 2010. [164](#)

REFERENCES

- [NVRNX10] T.T. Nguyen, D.H.C. Vu, T. Rabczuk, and H. Nguyen-Xuan. A node-based smoothed finite element method (ns-fem) for upper bound solution to visco-elastoplastic analysis of solids using triangular and tetrahedral meshes. *CMAME*, 199:3005–3027, 2010. [164](#)
- [OGW⁺03] G.M. Odegard, T.S. Gates, K.E. Wise, C. Park, and E.J. Siochi. Constitutive modeling of nanotube-reinforced polymer composites. *Compos. Sci. and Technol.*, 63:1671–1687, 2003. [1](#), [2](#), [115](#)
- [Pig95] M.R. Piggott. A new model for interface failure in fibre-reinforced polymers. *Compos. Sci. Technol.*, 55:269–276, 1995. [91](#)
- [Pli95] S.J. Plimpton. Fast parallel algorithms for short-range molecular dynamics. *Journal of Computational Physics*, 117:1–19, 1995. [8](#), [11](#), [66](#), [93](#)
- [Pli10] E. Plischke. An effective algorithm for computing global sensitivity indices (easi). *Rel. Eng. Syst. Safety*, 95:354–360, 2010. [40](#), [41](#)
- [PS04] S. Park and K. Schulten. Calculating potentials of mean force from steered molecular dynamics simulations. *Journal of Chemical Physics*, 120:5946–5961, 2004. [12](#)
- [PSS12] P. Paruolo, M. Saisana, and A. Saltelli. Ratings and rankings: voodoo or science? *The Royal Statistical Society: Journal Series A*, 176:1–26, 2012. [31](#)
- [PYS95] W. Paul, D.Y. Yoon, and G.D. Smith. An optimized united atom model for simulations of polymethylene melts. *The Journal of Chemical Physics*, 103:1702–1709, 1995. [1](#)
- [QDAR00] D. Qian, E.C. Dickey, R. Andrews, and T. Rantell. Load transfer and deformation mechanisms in carbon nanotube-polystyrene composites. *Applied Physics Letters*, 20:2868–2870, 2000. [1](#), [91](#)
- [Qia] Qiao. Polymer lecture. *Department of Structural Engineering & Program of Materials Science and Engineering University of California – San Diego*. [68](#)
- [RA06] T. Rabczuk and P.M.A. Areias. A meshfree thin shell for arbitrary evolving cracks based on an external enrichment. *Computer Modeling in Engineering and Sciences*, 16(2):115–130, 2006. [163](#)

REFERENCES

- [RAB07] T. Rabczuk, P.M.A. Areias, and T. Belytschko. A simplified meshfree method for shear bands with cohesive surfaces. *International Journal for Numerical Methods in Engineering*, 69(5):993–1021, 2007. [23](#)
- [RB04] T. Rabczuk and T. Belytschko. Cracking particles: A simplified mesh-free method for arbitrary evolving cracks. 61(13):2316–2343, 2004. [22](#), [163](#)
- [RB06] T. Rabczuk and T. Belytschko. Application of meshfree particle methods to static fracture of reinforced concrete structures. *International Journal of Fracture*, 137(1-4):19–49, 2006. [23](#)
- [RB07a] T. Rabczuk and T. Belytschko. A three dimensional large deformation meshfree method for arbitrary evolving cracks. *CMAME*, 196(29-30):2777–2799, 2007. [23](#)
- [RB07b] T. Rabczuk and T. Belytschko. A three dimensional large deformation meshfree method for arbitrary evolving cracks. *CMAME*, 196(29-30):2777–2799, 2007. [163](#)
- [RBZ07] T. Rabczuk, S. Bordas, and G. Zi. A three dimensional meshfree method for static and dynamic multiple crack nucleation/propagation with crack path continuity. *CM*, 40(3):473–495, 2007. [22](#), [163](#)
- [RCC92] A.K. Rappe, C.J. Casewit, and K.S. Colwell. A full periodic-table force-field for molecular mechanics and molecular dynamics simulations. *Journal of American Chemical Society*, 114:10024–10035, 1992. [13](#)
- [RE06] T. Rabczuk and J. Eilb. Modelling dynamic failure of concrete with meshfree methods. *International Journal for Impact Engineering*, 32(2):1878–1897, 2006. [163](#)
- [RM91] S.H. Robert and O.R. Mark. Strain hardening of polymer glasses: Effect of entanglement density, temperature, and rate. *Journal of Polymer Science: Part B: Polymer Physics*, 2006, 1991. [65](#)
- [RMV⁺03] D. Ratna, N.R. Manoj, R. Varley, R.K.S. Raman, and G.P. Simon. Clay-reinforced epoxy nanocomposites. *Polym. Int.*, 52:1403–1407, 2003. [139](#)
- [RRP⁺13] R. Rafiee, T. Rabczuk, R. Pourazizi, J. Zhao, and Y. Zhang. Challenges of the modeling methods for investigating the interaction between the cnt and the surrounding polymer. *Advances in Materials Science and Engineering*, Article ID 183026, 2013. [92](#)

REFERENCES

- [RS08] T. Rabczuk and E. Samaniego. Discontinuous modelling of shear bands with adaptive meshfree method. *CMAME*, 197(6-8):641–658, 2008. [163](#)
- [RW06] T. Rabczuk and W.A. Wall. Extended finite element and meshfree methods. *Technical University of Munich, Germany*, WS200/2007, 2006. [21](#), [165](#)
- [RWC62] D. Ruppert, M.P. Wand, and R.J. Carroll. *Semiparametric regression*. ambridge University Press, 2003, ISBN: 0521785162. [61](#), [63](#)
- [RZ07] T. Rabczuk and G. Zi. A meshfree method based on the local partition of unity for cohesive cracks. *Computational Mechanics*, 39(6):743–760, 2007. [174](#)
- [RZGW08] T. Rabczuk, G. Zi, A. Gerstenberger, and W.A. Wall. A new crack tip element for the phantom node method with arbitrary cohesive cracks. *IJNME*, 75:577–599, 2008. [182](#)
- [SAA⁺10] A. Saltelli, P. Annoni, I. Azzini, F. Campolongo, M. Ratto, and S. Tarantola. Variance based sensitivity analysis of model output. design and estimator for the total sensitivity index. *Computer Physics Communications*, 181:259–270, 2010. [33](#), [34](#), [35](#), [158](#)
- [SAB06] J.H. Song, P.M.A. Areias, and T. Belytschko. A method for dynamic crack and shear band propagation with phantom nodes. *IJNME*, 67(6):868–893, 2006. [23](#), [181](#)
- [Sal02] A. Saltelli. Making best use of model valuations to compute sensitivity indices. *Computer Physics Communications*, 145:280–297, 2002. [34](#), [35](#), [153](#)
- [SARA02] J.-L. Sauvajol, E. Anglaret, S. Rols, and L. Alvarez. Phonons in single wall carbon nanotube bundles. *Carbon*, 40:1697–1714, 2002. [117](#)
- [SBC00] J.T. Strouboulis, I. Babuška, and K. Copps. The design and analysis of the generalized finite element method. *CMAME*, 181:43–96, 2000. [163](#)
- [SBP⁺04] N. Sheng, M.C. Boyce, D.M. Parks, G.C. Rutledge, J.I. Abes, and R.E. Cohen. Multiscale micromechanical modeling of polymer/clay nanocomposites and the effective clay particle. *Polymer*, 45:487–506, 2004. [139](#)

REFERENCES

- [SCL⁺10] J. Shi, D. Chopp, J. Lua, N. Sukumar, and T. Belytschko. Abaqus implementation of extended finite element method using a level set representation for three-dimensional fatigue crack growth and life predictions. *Engineering Fracture Mechanics*, 77:2840–2863, 2010. [181](#)
- [SDR02] J.P. Salvétat-Delmotte and A. Rubio. Mechanical properties of carbon nanotubes: a ber digest for beginners. *Surf. Sci.*, 40:1729–1734, 2002. [91](#)
- [SFH⁺04] D.L. Shi, X.Q. Feng, Y.Y. Huang, K.C. Hwang, and H. Gao. The effect of nanotube waviness and agglomeration on the elastic property of carbon nanotube-reinforced composites. *Transactions of the ASME. Journal of Engineering Materials and Technology*, 126:250–257, 2004. [14](#), [15](#), [16](#), [17](#), [18](#), [116](#), [124](#)
- [SGA98] L.S. Schadler, S.C. Giannaris, and P.M. Ajayan. Load transfer in carbon nanotube epoxy composites. *Applied Physics Letters*, 73:3842–3844, 1998. [1](#), [91](#)
- [She06] J.E. Shepherd. *Multiscale modeling of the deformation of semi-crystalline polymers*. PhD thesis, Georgia Institute of Technology, 2006. [66](#), [93](#)
- [SK95] P.R. Sundararajan and T.A. Kavassalis. Molecular dynamics study of polyethylene chain folding: the effects of chain length and the torsional barrier. *J. Chem. Soc., Faraday Trans.*, 91:2541–2549, 1995. [68](#)
- [SK08] P.D. Spanos and A. Kotsos. A multiscale monte carlo finite element method for determining mechanical properties of polymer nanocomposites. *J. Probab. Eng. Mech.*, 23:456–470, 2008. [2](#), [116](#)
- [Sob93] I.M. Sobol'. Sensitivity estimates for nonlinear mathematical models. *Mathematical Modelling and Computational Experiment 1*, pages 407–414, 1993. [33](#), [35](#), [50](#), [116](#)
- [Soban] I.M. Sobol'. Global sensitivity analysis indices for the investigation of nonlinear mathematical models. *Matematicheskoe Modelirovanie*, 19:23–24, 2007 (in Russian). [34](#), [35](#)
- [SPD⁺07] G. Scocchi, P. Posocco, A. Danani, S. Pricl, and M. Fermeglia. To the nanoscale, and beyond! multiscale molecular modeling of polymer-clay nanocomposites. *Fluid Phase Equilibria*, 261:366–374, 2007. [140](#)

REFERENCES

- [SR10a] M.M. Shokrieh and R. Rafiee. Investigation of nanotube length effect on the reinforcement efficiency in carbon nanotube based composites. *Compos. Struct.*, 92:2415–2420, 2010. [14](#), [18](#), [115](#), [118](#)
- [SR10b] M.M. Shokrieh and R. Rafiee. Prediction of mechanical properties of an embedded carbon nanotube in polymer matrix based on developing an equivalent long fiber. *Mechanics Research Communications*, 37:235–240, 2010. [xxiv](#), [18](#), [115](#), [118](#), [120](#)
- [SR10c] M.M. Shokrieh and R. Rafiee. Stochastic multi-scale modeling of cnt/polymer composites. *Computational Materials Science*, 50:437–446, 2010. [18](#), [116](#), [117](#), [118](#), [120](#), [122](#), [123](#)
- [SRA⁺08] A. Saltelli, M. Ratto, T. Andres, F. Campolongo, J. Cariboni, D. Gatelli, M. Saisana, and S. Tarantola. *Global Sensitivity Analysis. The Primer*. John Wiley and Sons, 2008. [31](#), [52](#), [54](#), [55](#)
- [SS 9] P.E. Spencer and J. Sweeney. Modeling of polymer clay nanocomposites for a multiscale approach. In: *Nano- and Micromechanics of Polymer Blends and Composites, München (Carl Hanser Verlag GmbH & Co. KG)*, pages 545–578, 2009, eBook ISBN: 978-3-446-43012-9. [20](#), [141](#), [143](#)
- [STC99] A. Saltelli, S. Tarantola, and K. Chan. A quantitative model independent method for global sensitivity analysis of model output. *Technometrics*, 41:39–56, 1999. [37](#), [38](#), [155](#)
- [STG⁺07] I.M. Sobol', S. Tarantola, D. Gatelli, S. Kucherenko, and W. Mauntz. Estimating the approximation error when fixing unessential factors in global sensitivity analysis. *Rel. Eng. Syst. Safety*, 92:957–960, 2007. [34](#)
- [STH00] S.J. Stuart, A.B. Tutein, and J.A. Harrison. A reactive potential for hydrocarbons with intermolecular interactions. *Journal of Chemical Physics*, 112:6472–6486, 2000. [8](#)
- [STLS92] I.M. Sobol', S. Turchaninov, V. Levitan, and B.V. Shukhman. Quasi-random sequence generators. *Keldysh Inst. Appl. Maths RAS Acad. Sci.*, 1992. [29](#), [153](#)
- [STZR⁺13] M. Silani, H. Talebi, S. Ziaei-Rad, P. Kerfriden, S.P.A. Bordas, and T. Rabczuk. Stochastic modeling of clay/epoxy nanocomposites. *Composite Structures*, submitted, 2013. [140](#), [146](#)

REFERENCES

- [SW99] M.S.P. Shaffer and A.H. Windle. Fabrication and characterization of carbon nanotube/poly(vinyl alcohol) composites. *Adv. Mater.*, 11:937–941, 1999. [91](#), [115](#)
- [SZRET12] M. Silani, S. Ziaei-Rad, M. Esfahanian, and V.B.C. Tan. On the experimental and numerical investigation of clay/epoxy nanocomposites. *Composite Structures*, 94:3142–3148, 2012. [140](#), [145](#), [146](#)
- [TBW⁺14] M.A. Tschopp, J.L. Bouvard, D.K. Ward, D.J. Bammann, and M.F. Horstemeyer. Influence of ensemble boundary conditions (thermostat and barostat) on the deformation of amorphous polyethylene by molecular dynamics. *arXiv:1310.0728 [cond-mat.mtrl-sci]*, 2014. [1](#)
- [TGM06] S. Tarantola, D. Gatelli, and T.A. Mara. Random balance designs for the estimation of first order sensitivity indices. *Rel. Eng. Syst. Safety*, 91:717–727, 2006. [39](#)
- [TJP⁺10] Y. Tian, H. Jiang, J.v. Pfaler, Z. Zhu, A.G. Nasibulin, T. Nikitin, B. Aitchison, L. Khriachtchev, D.P. Brown, and E.I. Kauppinen. Analysis of the size distribution of single-walled carbon nanotubes using optical absorption spectroscopy. *The Journal of Physical Chemistry Letters*, 1:1143–1148, 2010. [97](#), [101](#)
- [TL99] C.L. Tucker and E. Liang. Stiffness predictions for unidirectional short-fiber composites: review and evaluation. *Compos. Sci. Technol.*, 59:655–671, 1999. [139](#)
- [TLC05] E.T. Thostenson, C. Li, and T-W. Chou. Nanocomposites in context. *Compos Sci Technol*, 65:491–516, 2005. [115](#)
- [TLP02] C.S. Triantafillidis, P.C. LeBaron, and T.J. Pinnavaia. Thermoset epoxy-clay nanocomposites: The dual role of alpha,omega-diamines as clay surface modifiers and polymer curing agents. *J. Solid. State. Chem.*, 167:354–362, 2002. [139](#)
- [Tsa10] C.H. Tsai. *Elastic property prediction and variation quantification for buckypaper-polymer nanocomposites: modeling and experimental validation*. PhD thesis, The Florida State University College of Engineering, 2010. [121](#), [123](#)
- [TWBH11] M.A. Tschopp, D.K. Ward, J.L. Bouvard, and M.F. Horstemeyer. Atomic scale deformation mechanisms of amorphous polyethylene under tensile loading. In *The Minerals, Metals & Materials Society (TMS)*, pages 789–794, 2011. [xxiv](#), [9](#)

REFERENCES

- [UKK⁺93a] A. Usuki, Y. Kojima, M. Kawasumi, A. Okada, Y. Fukushima, T. Kurauchi, and O. Kamigaito. Mechanical properties of nylon 6-clay hybrid. *J. Mater. Res.*, 8:1185–1189, 1993. [139](#)
- [UKK⁺93b] A. Usuki, Y. Kojima, M. Kawasumi, A. Okada, Y. Fukushima, T. Kurauchi, and O. Kamigaito. Synthesis of nylon 6-clay hybrid. *J. Mater. Res.*, 8:1179–1184, 1993. [139](#)
- [USK⁺85] G. Ungar, J. Stejny, A. Keller, A.I. Bidd, and Whiting M.C. The crystallization of ultralong normal paraffins: the onset of chain folding. *Science*, 229:386–389, 1985. [68](#)
- [UT98] A. Uhlherr and D. N. Theodorou. Hierarchical simulation approach to structure and dynamics of polymers. *Current Opinion in Solid State and Materials Science*, 3:544–551, 1998. [1](#)
- [Val08] P.K. Valavala. *Multiscale constitutive modeling of polymer materials*. PhD thesis, Michigan Technology University, 2008. [1](#)
- [VBLK⁺14] N. Vu-Bac, T. Lahmer, H. Keitel, J. Zhao, X. Zhuang, and T. Rabczuk. Stochastic predictions of bulk properties of amorphous polyethylene based on molecular dynamics simulations. *Mechanics of Materials*, 68:70–84, 2014. [94](#), [97](#)
- [VBLZ⁺14] N. Vu-Bac, T. Lahmer, Y. Zhang, X. Zhuang, and T. Rabczuk. Stochastic predictions of interfacial characteristic of polymeric nanocomposites (pnCs). *Composites Part B: Engineering*, 59:80–95, 2014. [139](#)
- [VBNXC⁺11] N. Vu-Bac, H. Nguyen-Xuan, L. Chen, S. Bordas, P. Kerfriden, R.N. Simpson, G.R. Liu, and T. Rabczuk. A node-based smoothed extended finite element method (ns-xfem) for fracture analysis. *CMES*, 1898:1–25, 2011. [187](#)
- [Ver67] L. Verlet. Computer experiments on classical fluids. i. thermodynamical properties of lennard-jones molecules. *Phys. Rev.*, 159:98–103, 1967. [7](#)
- [VGB09] G. Ventura, R. Gracie, and T. Belytschko. Fast integration and weight function blending in the extended finite element method. *International Journal for Numerical Methods in Engineering*, 77:1–29, 2009. [182](#)
- [VM07] R.G. Villoria and A. Miravete. Mechanical model to evaluate the effect of the dispersion in nanocomposites. *Acta Mater.*, 55:3025–3031, 2007. [116](#)

REFERENCES

- [VPN03] T. Vanorio, M. Prasad, and A. Nur. Elastic properties of dry clay mineral aggregates, suspensions and sandstones. *Geophysical Journal International*, 155:319–326, 2003. [145](#)
- [WCW⁺05] K. Wang, L. Chen, J. Wu, M.L. Toh, C. He, and A.F. Yee. Epoxy nanocomposites with highly exfoliated clay: mechanical properties and fracture mechanisms. *Macromolecules*, 38:788–800, 2005. [140](#), [145](#), [146](#)
- [Wei06] C. Wei. Adhesion and reinforcement in carbon nanotube polymer composite. *Applied Physics Letters*, 88:93–108, 2006. [92](#)
- [WJ98] G.D. Wyss and K.H. Jorgensen. A user’s guide to lhs: Sandia’s latin hypercube sampling software. technical report sand98-0210. Technical report, Sandia National Laboratories, Albuquerque, NM, 1998. [29](#)
- [WLWZ06] S. Wang, Z. Liang, B. Wang, and C. Zhang. Statistical characterization of single-wall carbon nanotube length distribution. *Nanotechnology*, 17:634–639, 2006. [122](#), [123](#)
- [WM10] J.M. Wernik and S.A. Meguid. Multiscale modeling of the nonlinear response of nano-reinforced polymers. *Acta Mechanica*, 217:1–16, 2010. [2](#)
- [WP98] Z. Wang and T.J. Pinnavaia. Nanolayer reinforcement of elastomeric polyurethane. *Chem. Mater.*, 10:3769–3771, 1998. [139](#)
- [WP04] J. Wang and R. Pyrz. Prediction of the overall moduli of layered silicate-reinforced nanocomposites - part i: basic theory and formulas. *Compos. Sci. Technol.*, 64:925–934, 2004. [139](#)
- [WSC02] C. Wei, D. Srivastava, and K. Cho. Thermal expansion and diffusion coefficients of carbon nanotube-polymer composites. *Nano Letters*, 2:647–650, 2002. [92](#), [93](#), [97](#)
- [WWC⁺06] L. Wang, K. Wang, L. Chen, C. He, and Y. Zhang. Hydrothermal effects on the thermomechanical properties of high performance epoxy/clay nanocomposites. *Polymer Engineering & Science*, 46:215–221, 2006. [140](#)
- [WWW⁺05] K. Wang, L. Wang, J. Wu, L. Chen, and C. He. Preparation of highly exfoliated epoxy/clay nanocomposites by slurry compounding: process and mechanisms. *Langmuir*, 21:3613–3618, 2005. [140](#), [145](#), [146](#)

REFERENCES

- [XG07] C. Xu and G. Gertner. Extending a global sensitivity analysis technique to models with correlated parameters. *Computational Statistics & Data Analysis*, 51:5579–5590, 2007. [36](#), [43](#)
- [XG08] C. Xu and G.Z. Gertner. Uncertainty and sensitivity analysis for models with correlated inputs. *Rel. Eng. Syst. Safety*, 93:1563–1573, 2008. [44](#), [45](#), [130](#)
- [YSM93] D.Y. Yoon, G.D. Smith, and T. Matsuda. A comparison of a united atom and an explicit atom model in simulations of polymethylene. *The Journal of Chemical Physics*, 98:10037–10043, 1993. [1](#)
- [YWC80] J.F. Yau, S.S. Wang, and H.T. Corten. A mixed-mode crack analysis of rectilinear anisotropic solids using conservation laws of elasticity. 16(3):247–59, 1980. [171](#), [176](#), [187](#), [193](#)
- [ZNZ10] J. Zhao, S. Nagao, and Z. Zhang. Thermo-mechanical properties dependence on chain length in bulk polyethylene: coarse-grained molecular dynamics simulations. *Journal of Materials Research*, 25:537–544, 2010. [65](#)
- [ZSS06] S.C. Zunjarrao, R. Sriraman, and R.P. Singh. Effect of processing parameters and clay volume fraction on the mechanical properties of epoxy-clay nanocomposites. *Journal of Materials Science*, 41:2219–2228, 2006. [145](#)
- [ZWX⁺11] Z.Q. Zhang, D.K. Ward, Y. Xue, H.W. Zhang, and M.F. Horstemeyer. Interfacial characteristics of carbon nanotube-polyethylene composites using molecular dynamics simulations. *ISRN Materials Science*, page 10 pages, 2011. [xviii](#), [92](#), [97](#), [98](#)
- [ZXX⁺09] Q. Zheng, D. Xia, Q. Xue, K. Yan, X. Gao, and Q. Li. Computational analysis of effect of modification on the interfacial characteristics of a carbon nanotube-polyethylene composites system. *Applied Surface Science*, 255:3524–3543, 2009. [92](#)
- [ZYL08] Q.H. Zeng, A.B. Yu, and G.Q. Lu. Multiscale modeling and simulation of polymer nanocomposites. *Prog. Polym. Sci.*, 33:191–269, 2008. [115](#)
- [ZZW⁺13] Y. Zhang, J. Zhao, N. Wei, J.W. Jiang, and T. Rabczuk. Effects of the dispersion of polymer wrapped two neighbouring single walled carbon nanotubes (swnts) on nanoengineering load transfer. *Composites Part B: Engineering*, 45:1714–1721, 2013. [11](#)

Academic Curriculum Vitae

Nam Vu-Bac

Institute of Structural Mechanics
Bauhaus-Universität Weimar
Marienstraße 15, 99423 Weimar, Germany
Email: bac.nam.vu@uni-weimar.de

Education

- Ph.D: Institute of Structural Mechanics, Bauhaus-University Weimar, Germany, 2014.
- M.Eng: Master at Ho Chi Minh City University of Technology, Vietnam, 2006.
- B.Eng: Bachelor at University of Transport and Communications, Hanoi, Vietnam, 2003.

Research Interests

- Computational materials design
- Multiscale methods
- Stochastic modeling
- Uncertainty quantification
- Molecular dynamics
- Polymer nanocomposites
- Fracture mechanics

REFERENCES

Scientific Activities

Reviewer for international journals:

- Computational Materials Science
- International Journal of Impact Engineering
- International Journal of Fracture
- International Journal of Computational Methods
- Journal of Civil Engineering (KSCE)
- Mathematical Problems in Engineering
- Frontiers of Structural and Civil Engineering

Skills and Expertise

Fortran, C++, Matlab, LAMMPS, Ansys, Abaqus, Latex, Numerical simulations.

Publications Refereed Journal Articles

Journal Publications

1. **Vu-Bac, N.**; Nguyen-Xuan, H. ; Chen, L. ; Bordas, S. ; Kerfriden, P. ; Simpson, R. N. ; Liu, G. R and Rabczuk, T. A node-based smoothed extended finite element method (NS-XFEM) for fracture analysis. *Computer Modeling In Engineering & Sciences*, (73) 331–355, 2011.
2. **Vu-Bac, N.**; Nguyen-Xuan, H., Chen, L., Lee, C. K., Zi, G., Zhuang, X., Liu, G. R and Rabczuk, T. A phantom-node method with edge-based strain smoothing for linear elastic fracture mechanics. *Journal of Applied Mathematics*, vol. 2013, Article ID 978026, 2013.
3. **Vu-Bac, N.**; Lahmer, T. ; Keitel, H. ; Zhao, J. ; Zhuang, X. and Rabczuk, T. Stochastic predictions of bulk properties of amorphous polyethylene based on molecular dynamics simulations. *Mechanics of Materials*, (68) 70–84, 2014.

REFERENCES

4. **Vu-Bac, N.**; Lahmer, T. ; Zhang, Y. ; Zhuang, X. and Rabczuk, T. Stochastic predictions of interfacial characteristic of polymeric nanocomposites (PNCs). *Composites Part B: Engineering*, (59) 80–95, 2014.
5. **Vu-Bac, N.**; Silani, M. ; Lahmer, T. ; Zhuang, X. and Rabczuk, T. A unified framework for stochastic predictions of mechanical properties of polymeric nanocomposites. *Computational Materials Science*, (96) 520–535, 2015.
6. **Vu-Bac, N.**; Rafiee, R. ; Zhuang, X. ; Lahmer, T. and Rabczuk, T., Uncertainty quantification for multiscale modeling of polymer nanocomposites with correlated parameters. *Composites Part B: Engineering*, (68) 446–464, 2015.
7. **Vu-Bac, N.**; Bessa, M. A. ; Rabczuk, T. and Liu, W. K., A multiscale model for the quasi-static thermo-plastic behavior of highly cross-linked glassy polymers, *Macromolecules*, (48) 6713–6723, 2015.
8. **Vu-Bac, N.**; Lahmer, T.; Nguyen-Thoi, T.; Zhuang, X. ; and Rabczuk, T., A software framework for uncertainty analysis for complex models, under review.

Presentations

1. **Vu-Bac, N.** Comparison of different strategies for sensitivity analysis with applications in material modeling, Graduiertenkolleg 1462, Bauhaus-Universität Weimar, 2014.